



THE HONG KONG
POLYTECHNIC UNIVERSITY

香港理工大學

Pao Yue-kong Library

包玉剛圖書館

Copyright Undertaking

This thesis is protected by copyright, with all rights reserved.

By reading and using the thesis, the reader understands and agrees to the following terms:

1. The reader will abide by the rules and legal ordinances governing copyright regarding the use of the thesis.
2. The reader will use the thesis for the purpose of research or private study only and not for distribution or further reproduction or any other purpose.
3. The reader agrees to indemnify and hold the University harmless from and against any loss, damage, cost, liability or expenses arising from copyright infringement or unauthorized usage.

IMPORTANT

If you have reasons to believe that any materials in this thesis are deemed not suitable to be distributed in this form, or a copyright owner having difficulty with the material being included in our database, please contact lbsys@polyu.edu.hk providing details. The Library will look into your claim and consider taking remedial action upon receipt of the written requests.

**ON INVESTIGATION OF ACOUSTIC WAVES AND ITS
APPLICATIONS IN NOISE AND AIR STUDIES**

YITING ZHANG

PhD

The Hong Kong Polytechnic University

2022

The Hong Kong Polytechnic University

Department of Civil and Environmental Engineering

**On Investigation of Acoustic Waves and Its Applications in
Noise and Air Studies**

Yiting Zhang

A Thesis Submitted in Partial Fulfillment of the Requirements for the
Degree of Doctor of Philosophy

August 2021

CERTIFICATE OF ORIGINALITY

I hereby declare that this thesis is my own work and that, to the best of my knowledge and belief, it reproduces no material previously published or written, nor material that has been accepted for the award of any other degree or diploma, except where due acknowledgement has been made in the text.

_____ (Signed)

YITING ZHANG (Name of student)

To my family
for their love and support

ABSTRACT

Explosive population growth and increasing migration have led to a boom in mega-cities, posing technological challenges in urban development. To meet long-term sustainability targets and environmental regulations, developing innovative technologies for providing a comfortable, green and safe living environment is of prominent need. The intensive investigation of acoustic waves in both theoretical and experimental studies is largely due to their extensive applications in various engineering fields. In an attempt to minimize the impact of environmental noise and intervene the degradation of indoor air quality, we strive to explore multiple applications of acoustic waves in noise and air studies in this work.

This thesis is mainly divided into two parts. The first part focuses on the investigation of acoustic wave characteristics and noise mitigation strategies. Due to hectic construction activities under a rapid urbanization process in densely populated cities (e.g., Hong Kong), construction noise generated from various powered mechanical equipment (e.g., drillers, hammers and excavators) is a major problem. A long-term exposure in noise can cause an adverse impact on psychological health, life quality and working efficiency. To alleviate this problem, a passive noise control (PNC) approach (e.g., noise barriers) and an active noise control (ANC) method (e.g., generation of anti-noise signals) are commonly conducted to mitigate the unwanted noise. For PNC, the performance of passive-type sound barriers greatly depends on several factors, including material types, design dimensions, surface conditions, and geometric configurations. Nevertheless, the use of PNC approach alone is not practical for the attenuation of low-frequency noise, while ANC method shows advantages in low-frequency range. Motivated by this idea, the combination of both PNC and ANC strategies are investigated.

With the development of digital signal processing, it enables the feasibility of control algorithm for active control. In this work, a learning and forecasting approach is utilized as a pre-treatment process, which combines a Bayesian approach and a dynamic linear model (DLM). Comprising the statistical strategy and descriptive time series, the proposed pre-treatment system is conducive to raw-signal pre-processing and can concurrently generate a predicted signal as a reference signal. The predicted signals based on prior information and Bayesian inference afford an alternative to the normal costs of the secondary path, such as those associated with electro-acoustic signal conversions and computation efforts in the control algorithm. To demonstrate the feasibility of this pre-treatment system, illustrative examples coupling with the existing control algorithms, e.g., the conventional filtered-x least mean square (FxLMS) algorithm and a new convex structure via an FxLMS/F algorithm (C-FxLMS/F), are studied. Making use of the present forecasting technique, stationary signals are acquired for analysis. The updating characteristic “*forecast-observation-analysis*” loop is advantageous for the implementation of signal processing for an ANC system.

To establish a noise mitigation device, using passive barriers is an effective way for construction sites. With consideration of environmental-friendly barriers, it is preferable to use low-cost, recyclable and lightweight materials. Recycling use of waste wood and rubber materials from construction sites is investigated as their good tensile modulus and mechanical strength. A laminated configuration, which consists of: (i) one-thick-layer recycled composite panel with a mixture of wood pellets and rubber particles, and (ii) a thin-film layer of polyvinylidene fluoride (PVDF) material, is examined. The wood-rubber composite panels are designed for wideband frequency control, while the PVDF thin-film layer as a supplementary part is to eliminate the peak narrowband low-frequency component. Compared to conventional loudspeakers with bulky coils and diaphragms, piezoelectric thin-film materials are flexible and

lightweight with strong piezoelectric and ferroelectric properties to couple with passive panels. A scale-down model is fabricated and tested in the in-house semi-anechoic chamber to examine the effectiveness. The barrier shows good performance in noise attenuation (i.e., a reduction of sound pressure levels (SPLs) at average 10dB).

To go beyond the potential application of acoustic waves, the second part focuses on acoustic manipulation technique and thermo-acoustic (TA) wave devices. Acoustic manipulation (e.g., acoustic trapping) is an active but contact-free technique, which utilizes acoustic waves to exert radiation forces on manipulating objects in air. To maintain indoor air quality, heating, ventilation and air-conditioning (HVAC) systems play a crucial role. Through the ventilation duct, viruses and bacteria can spread through the air on dust and microscopic particles within enclosed buildings. Epidemiological evidence reveals that a good ventilation control strategy can reduce the possibility of airborne viral transmission and infection. Generally, particle filters inside mechanical ventilation ductworks having a minimum efficiency rating value (MERV) (ANSI/ASHRAE, 1999) are frequently used, but they are limited of capturing airborne particles at a sub-micron scale (0.3–1.0 μm). Hence, a combination of acoustic-driven pre-filtering techniques and commercial coarse filters is an alternative to enhance filtration efficiency for sub-micron particles.

A U-shaped acoustic-driven pre-filtering device is proposed to enhance the working efficiency of coarse filters for capturing sub-micron particles (0.3–1.0 μm). The U-shaped device can optimize spatial homogeneity to improve the removal coefficient of airborne particles under lower sound intensity requirements, which can circumvent the existing problem of using high-intensity sound pressure for acoustic manipulation. Experimental studies are conducted to examine the efficiency of the present pre-filtering device. The results show that an overall filtration efficiency of up to 89% for 1.0- μm airborne particles can be achieved when the acoustic-driven device

is coupled together with a low-grade MERV-6 coarse filter. As a standalone device, the acoustic effect works well for the sub-micron particles with a filtration efficiency of up to 61% under a sound pressure level of 116 dB, which is lower than those SPLs as reported in the literature. The design has a high level of flexibility to work with various MERV filters. In the analysis, the influence of relevant parameters (e.g., airflow rates, acoustic frequencies, and sound intensities) on various particle sizes is investigated.

To further develop an acoustic-wave emitter with high sensitivity, the application of thermo-acoustic device is a new direction to go beyond the limitations of vibration-based speakers. Advances in nanomaterials (e.g., carbon nanotube (CNT) and graphene) over the last decade have realized the “*thermophone*” concept that was discovered a century ago, it basically differs from the working mechanism of conventional acoustic devices to generate sound by mechanical vibration. The operating mechanism of this TA-based technique can be described by providing an alternating current to CNT- or graphene-based thin-film materials, causing the surrounding medium (air) to be heated periodically. An oscillation of the temperature field induced in air can result in thermal expansion and contraction to generate acoustic waves. This next-generation acoustic technique can be scalable to deliver a flat-band frequency range as well as a high-intensity sound pressure level. Test samples of the TA-based emitter are fabricated to characterize its acoustic performance.

The research findings of this work can provide a further understanding of the nature of acoustic waves and its potential applications in various engineering fields. The acoustic-based technologies can contribute better resource efficiency to maintain a healthy, resilient and pleasant urban environment.

LIST OF PUBLICATIONS

Journal Papers:

Y.T. Zhang, S.K. Lai, J.C.W. Yu, H. Guo and C.W. Lim, A novel U-shaped acoustic-manipulated design to enhance the performance of low-efficiency filters for sub-micron particles, *Powder Technology*, 392, 412–423, 2021.

S.K. Lai, **Y.T. Zhang** and J.Q. Sun, Application of probabilistic assessment for optimal prediction in active noise control algorithms, *Applied Acoustics*, 173, 107675, 2021.

Conference Papers:

S.K. Lai, **Y.T. Zhang**, J.C.W. Yu and Y.G. Li, A new approach for an induced coagulation of particulate matter through thermo-acoustic agglomeration, *Proceedings of Inter-Noise 2020 E-Congress*, Seoul, Korea, 23–26 Aug 2020.

S.K. Lai, **Y.T. Zhang**, J.M. Wang, S.Y. Leu and J.Q. Sun, Investigation of a smart noise barrier for dual active and passive control of construction noise, *Proceedings of Inter-Noise 2020 E-Congress*, Seoul, Korea, 23–26 Aug 2020.

S.K. Lai and **Y.T. Zhang**, Real-time prediction of noise signals for active control based on Bayesian forecasting and time series analysis, *Proceedings of Inter-Noise 2019 Congress*, Madrid, Spain, 16–19 Jun 2019.

Y.T. Zhang, L.H. Zhang, S.K. Lai and Y.Q. Ni, Free vibration analysis of cracked rectangular plates using the DSC method, *Proceedings of Cross-Strait Symposium on Dynamical Systems and Vibration*, Hong Kong, 10–17 Dec 2017.

ACKNOWLEDGEMENTS

I would like to express my sincere gratitude to all my friends and colleagues who have been helping me and assisting me during my doctoral study. This study would not be so smooth without your presence.

First of all, I wish to express my sincerest gratitude and profound appreciation to my chief supervisor, Dr. Siu-Kai Lai, for his unceasing support, outstanding teaching, valuable experience, recommendation, enthusiastic insightful guidance and encouragement throughout the whole period of my PhD study at The Hong Kong Polytechnic University (PolyU). With his wisdom, patience, preeminent research keenness and rich practical experience have motivated me in my research. Besides, I would also like to express my sincere thanks to my co-supervisor, Prof. Yi-Qing Ni, for his insightful comments and continuous support during my PhD study.

I would like to give my deepest thanks to Dr. Jerry Yu for his recommendations, generous guidance and valuable advice beneficial to my research. I am very lucky to learn and share his passions, visions, and insights in this period. His vast backgrounds and comprehensive knowledge have been great invaluable for me.

I would like to address special thanks to my groupmates, Dr. Chen Wang, Dr. Xin Yang, Dr. Lin-Hao Zhang, Dr. Qi Hu, Ms. Jia-Mei Wang at PolyU for their recommendations and valuable advice beneficial to my research. I thank them very much for the enjoyable discussions on a variety of research topics and research methods. I also would like to express my thanks to Dr. Caiyi Xiong, Mr. Hao-Xian Lu, Mr. Hao-Ran Fan, Mr. Yan-Hui Liu, Mr. Tian-Hang Zhang for their great help in conducting experiments.

I would like to express my sincere appreciation to Prof. Hai Guo, who is professor of the Department of Civil and Environmental Engineering of PolyU, and Prof. Jian-Qiao Sun, who is professor at University of California Merced, for their great support and valuable suggestions in my present research work. I also wish to take this opportunity to present my cordial appreciation to Dr. Xin-Yan Huang, who is assistant professor of the Department of Building Environment and Energy Engineering of PolyU, who gave me great support in experimental studies.

I would like to express my sincere thanks to Ms. Emily Fung who is the technician of Noise and Safety Laboratory at Department of Civil and Environmental Engineering, Mr. W. S. Lam and Mr. Y. H. Chan who are the technicians of Water and Waste Research Laboratory at Department of Civil and Environmental Engineering, Mr. Michael Fung who is the technician of Fire Engineering Laboratory at the Department of Building Environment and Energy Engineering. Special thanks should go to their advice and assistance on experimental studies.

It is with great sincerity that I acknowledge the financial support of the Research Studentship offered from The Hong Kong Polytechnic University. In addition, the work described in this thesis was supported by the General Research Fund (Project No.: PolyU 152008/19E) from the Research Grants Council of Hong Kong and the Environment and Conservation Fund (Project No.: ECF Project 83/2017) of the Hong Kong Special Administrative Region. These funding supports are greatly appreciated.

Last but not least, I am deeply grateful to my parents who always support me, understand me and encourage me throughout my life. This thesis is dedicated to my most beloved family with gratitude for their everlasting love, encouragement and support.

CONTENTS

CERTIFICATE OF ORIGINALITY	i
ABSTRACT.....	iii
LIST OF PUBLICATIONS.....	vii
ACKNOWLEDGEMENTS	viii
CONTENTS.....	x
LIST OF FIGURES	xiv
LIST OF TABLES.....	xxv
LIST OF SYMBOLS.....	xxvi
LIST OF ABBREVIATIONS	xxxii
CHAPTER 1	1
INTRODUCTION.....	1
1.1 Research motivation.....	1
1.2 Research objectives.....	9
1.3 Thesis outline	11
CHAPTER 2	13
LITERATURE REVIEW.....	13
2.1 Overview of passive noise control technique	13
2.1.1 Sound insulation measure	13
2.1.2 Materials and performance of PNC barriers	15
2.2 Overview of active noise control strategies	19
2.2.1 Adaptive control algorithm	20
2.2.2 Active anti-noise devices	27
2.3 Acoustic manipulation technique	29
2.3.1 Mechanism of acoustic manipulation	30

2.3.2 Potential application of acoustic-based particle manipulation.....	33
2.4 Thermal-acoustic sound emitter.....	36
2.5 Concluding remarks	39
CHAPTER 3.....	42
APPLICATION OF PROBABILISTIC ASSESSMENT FOR NOISE SIGNAL	
PRE-PROCESSING IN ACTIVE NOISE CONTROL.....	42
3.1 Introduction.....	42
3.2 Research methodology.....	44
3.2.1 Dynamic linear model.....	45
3.2.2 Bayesian forecasting	46
3.2.3 Adaptive FxLMS control algorithm.....	51
3.3 Proposed ANC system with pretreatment process	55
3.4 Illustrative case studies	59
3.4.1 In-situ noise signal recording.....	59
3.4.2 Case 1: Conventional FxLMS algorithm with Bayesian inference	61
3.4.3 Case 2: C-FxLMS/F algorithm with Bayesian inference.....	67
3.4.4 Complexity analysis of various signal forms.....	72
3.5 Concluding remarks	76
CHAPTER 4.....	78
INVESTIGATION OF A DUAL-FUNCTION BARRIER FOR NOISE	
CONTROL	78
4.1 Introduction.....	78
4.2 Characterization of acoustic properties of wood-rubber composites.....	81
4.2.1 Two-microphone method	81
4.2.2 Four-microphone method.....	83
4.2.3 Samples preparation and experimental setup.....	88
4.2.4 Soundproofing performance of wood-rubber composites	93
4.3 Characterization of the PVDF thin-film materials.....	105

4.3.1	Fabrication of a PVDF thin-film speaker.....	105
4.3.2	Experimental setup and testing condition.....	106
4.3.3	Response analysis of PVDF thin-film speaker	107
4.4	Design and implementation of scale-down model.....	111
4.4.1	Sound field simulation	111
4.4.2	Barrier implementation and measurement setup.....	114
4.4.3	Effectiveness of barrier	118
4.5	Concluding remarks	131
CHAPTER 5	133
	ACOUSTIC-MANIPULATED DEVICE TO ENHANCE FILTRATION	
	REMOVAL OF SUB-MICRON PARTICLES	133
5.1	Introduction.....	133
5.2	Theoretical analysis and experimental studies.....	137
5.2.1	Working principle	137
5.2.2	Numerical modeling.....	142
5.2.3	Device fabrication and experimental setup.....	145
5.3	Results and discussion	152
5.3.1	Numerical analysis.....	152
5.3.2	Experimental results.....	159
5.4	Concluding remarks	175
CHAPTER 6	177
	FABRICATION AND CHARACTERIZATION OF NANO-THINFILM	
	THERMO-ACOUSTIC DEVICES	177
6.1	Introduction.....	177
6.2	Gap effects for nano-thinfilmm TA device	183
6.3	Experimental procedures	188
6.3.1	Substrate preparation	188
6.3.2	TA device fabrication	190

6.3.3 Sound measurement setup.....	198
6.4 Results and discussion	199
6.5 Concluding remarks	202
CHAPTER 7.....	204
CONCLUSIONS AND RECOMMENDATIONS	204
7.1 Conclusions.....	204
7.2 Limitations and recommendations for future work	206
REFERENCES.....	209

LIST OF FIGURES

Fig. 2.1: (a) Alteration of noise paths by a noise barrier; and (b) Noise barrier diffraction (Maekawa, 1968; EPD, 2003).....	17
Fig. 2.2: Principle of active noise control.	19
Fig. 2.3: Schematic diagram of ANC system in a duct system (Kuo and Morgan, 1999): (a) Single-channel broadband feedforward ANC system; and (b) Adaptive filter identification framework.	21
Fig. 2.4: Schematic of an ANC system considering secondary-path effects (Kuo, 1996).	22
Fig. 2.5: Schematic of the FxLMS algorithm (Widrow and Stearns, 1985).	23
Fig. 2.6: Illustration of aerosol particulate transport under an acoustic wave (Ng et al., 2017).	31
Fig. 2.7: Application forecast of graphene-based TA devices and their industrialization time from 2019 to 2030 (Qiao et al., 2020).	38
Fig. 3.1: Block diagram of a conventional FxLMS algorithm (Kuo, 1995).	51
Fig. 3.2: Block diagram of a convex combination of adaptive filters based on an FxLMS/F algorithm (Song and Zhao, 2019).	53
Fig. 3.3: Evaluation of noise reduction performance.....	56
Fig. 3.4: Block diagram of a conventional single channel feedforward FxLMS algorithm with Bayesian inference based on DLM as a pre-processing procedure for signal processing.	57
Fig. 3.5: Block diagram of a convex structure with Bayesian inference based on DLM as a pre-processing procedure for signal processing.....	57
Fig. 3.6: Flow chart of the proposed pre-processing system.	58

Fig. 3.7: Frequency responses of acoustic paths used in computer simulations. (a) Magnitude response and (b) Phase response.	59
Fig. 3.8: (a) Digging machine and transportation vehicles at a construction site near Austin MTR Station; (b) Noise measurement equipment with microphone, accelerometer, recorder and amplifier, and (c) Time-history of raw data.....	60
Fig. 3.9: Comparison of the inference and observation signals (Inference signal is denoted by a distribution with $K=5$).	62
Fig. 3.10: Time domain signals (a) with and (b) without Bayesian inference: Desired signal (blue line); Control signal (green line); Residual signal (red line).....	63
Fig. 3.11: Evolution of learning curves for processing in-situ measurement data based on the ANR index.....	63
Fig. 3.12: Evolution of learning curves for processing in-situ measurement data based on the MNR index.....	64
Fig. 3.13: Performance of the proposed ANC system (FxLMS algorithm) with or without Bayesian approach as a pre-processing procedure.	65
Fig. 3.14: Evolution of learning curves for processing in-situ measurement data based on the ANR index.....	66
Fig. 3.15: Evolution of learning curves for processing in-situ measurement data. based on the MNR index.....	66
Fig. 3.16: Performance of the proposed ANC system (conventional FxLMS algorithm combined with Bayesian approach) with various K-step values.	67
Fig. 3.17: Comparison of the inference and measurement signals (Inference signal is denoted by a distribution with $K=5$).	68
Fig. 3.18: Time domain signals (a) with and (b) without Bayesian inference: Desired signal (blue line); Control signal (green line); Residual signal (red line).....	69
Fig. 3.19: Evolution of learning curves for processing in-situ measurement data based on the ANR index.....	70
Fig. 3.20: Evolution of learning curves for processing in-situ measurement data based	

on the MNR index.....	70
Fig. 3.21: Performance of the proposed ANC system (C-FxLMS/F algorithm) with or without Bayesian approach as a pre-processing procedure.	70
Fig. 3.22: Evolution of learning curves for processing in-situ measurement data based on the ANR index.....	71
Fig. 3.23: Evolution of learning curves for processing in-situ measurement data based on the MNR index.....	71
Fig. 3.24: Performance of the proposed ANC system (C-FxLMS/F algorithm combined Bayesian approach) with various K -step values.....	72
Fig. 3.25: Evolution of learning curves for a Gaussian signal input (FxLMS algorithm with various step-size).	73
Fig. 3.26: Evolution of learning curves for a Gaussian signal input (FxLMS/F algorithm).....	73
Fig. 3.27: Evolution of learning curves for a Gaussian signal input (C-FxLMS/F algorithm).....	74
Fig. 3.28: Evolution of learning curves for a combined sinusoidal and Gaussian signal (FxLMS algorithm).....	74
Fig. 3.29: Evolution of learning curves for a combined sinusoidal and Gaussian signal (FxLMS/F algorithm).....	75
Fig. 3.30: Evolution of learning curves for a combined sinusoidal and Gaussian signal (C-FxLMS/F algorithm).....	75
Fig. 3.31: Evolution of learning curves for in-situ measurement noise (FxLMS, FxLMS/F and C-FxLMS/F algorithm with an optimal parameter).	76
Fig. 4.1: Schematic diagram of two-microphone impedance tube (Bolton et al., 1997).	81
Fig. 4.2: Transmission loss measurement by impedance tube (B&K, 2007).....	84
Fig. 4.3: Preparation procedures of test samples.	89

Fig. 4.4: Experimental setup of impedance tube. (a) Semi-anechoic chamber; (b) and (c) Impedance tube test system including microphones (<i>Type 2690</i>), amplifier (<i>Type 2735</i>) and generator module (<i>Type 3160-A-042</i>).	89
Fig. 4.5: Test samples of wood-rubber composite materials.....	90
Fig. 4.6: Comparison of the acoustic absorption performance of the test specimens with the same thickness but different wood-rubber ratio. (a) Thickness of 10 mm; (b) Thickness of 15 mm; (c) Thickness of 20 mm; and (d) Thickness of 25 mm.	94
Fig. 4.7: Comparison of the acoustic absorption performance of the test specimens with the same wood-rubber ratio but different thickness: (a) Pure-wood samples; (b) Wood-rubber ratio 2:1; (c) Wood-rubber ratio 1:1; and (d) Wood-rubber ratio 1:2. (* Specimen numbers are from 1 to 16).	95
Fig. 4.8: Comparison of the acoustic absorption performance of the test specimens with the same wood-rubber ratio but different thickness: (a) and (b) wood-rubber ratio 2:1; (c) and (d) Wood-rubber ratio 1:1; (e) and (f) Wood-rubber ratio 1.5:1; (g) Pure-wood samples for control experiments; and (h) Pure-rubber samples for control experiment. (*Sample numbers are 17–52).	96
Fig. 4.9: SEM images of wood particles: (a) and (b) Microstructure of coarse-wood particles (3–6 mm in diameter); (c) and (d) Microstructure of fine-wood particles (1–2 mm in diameter).	97
Fig. 4.10: Absorption coefficient of samples fabricated by different kinds of wood particle with 1:1 wood-rubber ratio. (a) Thickness of 10 mm; (b) Thickness of 15 mm; (c) Thickness of 20 mm; and (d) Thickness of 25 mm.....	98
Fig. 4.11: Absorption coefficient of the samples with different amounts of epoxy resin.	99
Fig. 4.12: Transmission loss of the testing samples with same wood-rubber ratio but different thickness. (a) Wood-rubber ratio 2:1; (b) Wood-rubber ratio 1.5:1; (c) Wood-rubber ratio 1:1; (d) Pure-wood samples and (e) Pure-rubber samples. .	101

Fig. 4.13: Comparison of acoustic transmission loss of various test samples with same thickness. (a) Thickness of 10 mm; (b) Thickness of 15 mm; (c) Thickness of 20 mm; and (d) Thickness of 25 mm.	102
Fig. 4.14: Acoustic performance comparison. (a) Absorption coefficient index: including kenaf fiber specimen (Lim et al., 2018), paper-polyethylene specimen (Buratti et al., 2016), wool-paper specimen (Buratti et al., 2016), waste paper specimen (Buratti et al., 2016), extruded polystyrene panel (Buratti et al., 2016)) and recycled wood-rubber composite sample (i.e., thickness 25mm, wood-rubber ratio 2:1 and thickness 25mm, wood-rubber ratio 1:1), and (b) Transmission loss index: including hybrid fiber metal laminate panels (MLSP-I and MLSP-II) (Pai et al., 2021) and recycled wood-rubber composite samples (i.e., 1:1 and 25 mm).	104
Fig. 4.15: (a) Schematic diagram of a PVDF thin-film speaker; and (b) A fabricated PVDF thin-film speaker.	106
Fig. 4.16: Experimental setup for acoustic response testing of the PVDF thin-film speaker. (a) Schematic diagram of setup; (b) and (c) Pictures of microphones and the PVDF thin-film speaker position within the semi-anechoic chamber.	107
Fig. 4.17: (a) Steady-state responses and harmonic distortion of the PVDF thin-film speaker; and (b) Relationship between input signals (at 1 kHz) and harmonic distortion levels of a PVDF thin-film speaker.	109
Fig. 4.18: Frequency response curves of a PVDF thin-film speaker.	109
Fig. 4.19: Directivity of PVDF thin-film speaker.	110
Fig. 4.20: General configuration in the numerical model.	112
Fig. 4.21: Schematic diagram of dual-function barrier. (a) A U-like supporting frame with an inserted wood-rubber composite panel and an embedded PVDF thin-film speaker and (b) Schematic diagram of a 3-by-3 array dual-function noise barrier.	115
Fig. 4.22: Experimental setup of scale-down model: (a) and (b) Schematic diagram of	

<p>a scale-down model setup for performance identification of the dual-function noise barrier; (c) and (d) A dual-function barrier setup in the semi-anechoic chamber; and (e) Acoustic measurement for the scale-down model experiment. </p>	117
Fig. 4.23: SPLs at measurement point A with different separation distance (d_1).....	118
Fig. 4.24: Numerical simulation of sound fields at 1500 Hz: (a) without a passive noise barrier; and (b) with a passive noise barrier.	119
Fig. 4.25: Insertion loss with presence of a passive noise barrier (0.1–10 kHz). (a) Distance from the barrier 0.5 m; (b) Distance from the barrier 0.6 m; (c) Distance from the barrier 0.7 m; (d) Distance from the barrier 0.8 m; (e) Distance from the barrier 0.9 m, and (f) Distance from the barrier 1.0 m.....	122
Fig. 4.26: Contour profiles of SPL distribution under two cases: (i) without any barrier; and (ii) with a passive barrier only at (a) 2000 Hz, (b) 2500 Hz, (c) 3150 Hz, (d) 4000 Hz, (e) 5000 Hz, (f) 6300 Hz, (g) 8000 Hz, and (h) 10000 Hz.....	124
Fig. 4.27: Variation of SPLs at microphone height 0.3 m under three various conditions at different separation distance between the sound barrier and the microphone: (a) 0.5 m, (b) 0.7 m, (c) 0.9 m, (d) 1.1 m, and (e) 1.3 m.	125
Fig. 4.28: Variation of SPLs microphone height 0.4 m under three various conditions at different separation distance between the sound barrier and the microphone: (a) 0.5 m, (b) 0.7 m, (c) 0.9m, (d) 1.1m, and (e) 1.3 m.	125
Fig. 4.29: Variation of SPLs at microphone height 0.5 m under three various conditions at different separation distance between the sound barrier and the microphone: (a) 0.5 m, (b) 0.7 m, (c) 0.9 m, (d) 1.1 m, and (e) 1.3 m.	126
Fig. 4.30: Variation of SPLs at microphone height 0.6 m under three various conditions at different separation distance between the sound barrier and the microphone: (a) 0.5 m, (b) 0.7 m, (c) 0.9 m, (d) 1.1 m, and (e) 1.3 m.	126
Fig. 4.31: Variation of insertion loss results at microphone height 0.3 m under three various conditions at different separation distance between the sound barrier and	

the microphone: (a) 0.5 m, (b) 0.7 m, (c) 0.9 m, (d) 1.1 m, and (e) 1.3 m. 127

Fig. 4.32: Variation of insertion loss results at microphone height 0.4 m under three various conditions at different separation distance between the sound barrier and the microphone: (a) 0.5 m, (b) 0.7 m, (c) 0.9 m, (d) 1.1 m, and (e) 1.3 m. 127

Fig. 4.33: Variation of insertion loss results at microphone height 0.5 m under three various conditions at different separation distance between the sound barrier and the microphone: (a) 0.5 m, (b) 0.7 m, (c) 0.9 m, (d) 1.1 m, and (e) 1.3 m. 128

Fig. 4.34: Variation of insertion loss results at microphone height 0.6 m under three various conditions at different separation distance between the sound barrier and the microphone: (a) 0.5 m, (b) 0.7 m, (c) 0.9 m, (d) 1.1 m, and (e) 1.3 m. 128

Fig. 4.35: Contour profiles of SPL distribution under three cases: (i) without any barrier; (ii) with the passive barrier only; and (iii) with the dual-function noise barrier at (a) 1100 Hz, (b) 1250 Hz, (c) 1300 Hz, (d) 1400 Hz, and (e) 1500 Hz. 129

Fig. 4.36: Overall assessment results: the SPL reduction profiles (a) at high-frequency range; and (b) at low-to-medium frequency range. 131

Fig. 5.1: A typical schematic diagram of HVAC system in commercial building (Zheng et al., 2021). 134

Fig. 5.2: Illustration of aerosol particulate transport under the acoustic effects: (a) A loudspeaker is mounted at the top of a ventilation duct (Ng et al., 2017); and (b) A loudspeaker is mounted at the sidewall of a ventilation duct. 138

Fig. 5.3: (a) Schematic diagram (top view) of the U-shaped acoustic-driven device; (b) Photo of the fabricated acoustic-driven device (top view); (c) Schematic diagram of a ventilation duct with the U-shaped acoustic-driven device (top view); (d) Experimental setup (side view) of a ventilation tube with the U-shaped acoustic-driven device; (e) Experimental setup (top view) comprises of an aerosol source, a trapping zone, a MERV commercial filter (*PureFit, Pleated Filter MERV 6*

<i>Furnace Filter</i>) and a power fan.....	148
Fig. 5.4: Measured distribution of sprayed particles from aerosol generator.	149
Fig. 5.5: (a) Preparation of a sample sheet (10-by-10-mm square sample sheet); (b) Attaching the sample sheets on a PTFE thin-film; and (c) Placing the PTFE thin- film at the bottom of the acoustic-driven device.	152
Fig. 5.6: A schematic diagram of ventilation ducting with 120 cm length for simulation.....	153
Fig. 5.7: A 2D model simulation of a ventilation duct of different height: (a) 10 cm, (b) 15 cm and (c) 20 cm under 10287 Hz.....	154
Fig. 5.8: A 2D model simulation of a ventilation duct at 15cm size at different frequencies: (a) 6858 Hz, (b) 10287 Hz and (c) 20574 Hz.....	155
Fig. 5.9: A 2D model showing the particle trajectory of PM10 sized matter as introduced into the tube at a flow rate of (a) 0, (b) 0.1, (c) 0.3 and (d) 0.5 m/s. Arrows indicate the direction of moving particles across the tube and a snapshot is captured at 3s.....	156
Fig. 5.10: A 2D numerical simulation. (a) the airflow speed contour map under a steady-state condition; and (b) the particle trajectory of a laminar flow occurs within the chambers with a minimal airflow resistance.....	158
Fig. 5.11: A 2D numerical simulation of the device operating at 836 Hz and 116 dB: (a) Formations of a standing wave and a pressure differential (at 10 cm location) to facilitate particle trapping; (b) Variation of sound pressure along the length direction of the resonant chambers at 836 Hz; and (c) Trapping of particles at the pressure nodes.....	159
Fig. 5.12: Preliminary test of wood powders generated from sandpapering balsa wood (<i>Ochroma pyramidale</i> ; density = 116 kg/m ³): (a) Balsa wood within the resonant chamber under 116 dB and 836 Hz; (b) Particles concentrated at the pressure node; and (c) A multi-line pattern of wood powders under acoustic standing waves within the resonant chamber (the interval between two lines ~ 2.43 mm).	

.....	161
Fig. 5.13: Particle number concentration under various operating frequencies (836–4183 Hz) and 116 dB: (a) fine particles (0.3 to 1.0 μm); and (b) coarse particles (2.5 to 10.0 μm).	162
Fig. 5.14: Removal coefficient of under various resonant frequencies (between 836 Hz and 4183 Hz) at 116 dB.....	163
Fig. 5.15: Influence of particle size distributions with and without the acoustic effect under 836 Hz and 108–116 dB: (a) fine particle (0.3 to 2.5 μm); and (b) coarse particle (2.5 to 10.0 μm).	164
Fig. 5.16: Removal coefficient of particles at 836 Hz under different SPLs.....	165
Fig. 5.17: Removal coefficient of particles under the inlet flow speed ranged from 0.45–0.75 m/s.....	166
Fig. 5.18: Influence of particle size distributions with and without a MERV filter under 116 dB and 836 Hz: fine particles between (a) 0.3–0.8 μm , (b) 1.0–2.0 μm ; and coarse particles between (c) 2.5–4.0 μm and (d) 5.0–10.0 μm	169
Fig. 5.19: Removal coefficient as determined from a MERV-6 filter (green dash line), present technique (blue dash line), and a MERV filter with the present technique (red solid line).	170
Fig. 5.20: Performance comparison between MERV-6 filter coupling with the present U-shaped device, cabin filter (Xu et al., 2011), MERV-13 filter (Dols et al., 2020), fine filter (F6 class) (Zhao et al., 2020), and low-grade filter (35–45% and 60–65%) (NIOSH, 2003).....	171
Fig. 5.21: SEM images of particles precipitation at the bottom of the U-shaped acoustic resonant chamber: (a) Clean sample sheets as a control group; (b) Sample sheets placed at the bottom of the acoustic-driven device without an acoustic effect; and (c) Sample sheets placed at the bottom of the acoustic-driven device with an acoustic effect.	174

Fig. 6.1: (a) Graphene: a monolayer of carbon atoms tightly bound in a hexagonal honeycomb lattice and (b) Single-walled carbon nanotube (SWCNT): a graphene layer seamlessly rolled into a tubular structure (Onorato, 2011; Vidu et al., 2014; Yan et al., 2019).	178
Fig. 6.2: (a) Schematic diagram of an encapsulated TA transducer; and (b) Schematic diagram of a four-TA-transducer shunt-wound array.....	184
Fig. 6.3: A 50- μm gap silicon substrate preparation. (a) a 5-inch covered mask design for photolithography and physical vapor deposition; (b) Procedure of wafer treatment including wafer coating and photolithography; and (c) a 4-inch wafer cutting into four substrates (3 cm \times 3 cm)	190
Fig. 6.4: (a) SEM image of a graphene thin-film layer; and (b) SEM image of an anodic aluminum oxide template.	191
Fig. 6.5: Schematic structure of an AAO template onto a 50- μm gap Si/SiO ₂ substrate.	193
Fig. 6.6: Transfer procedures of a graphene thin film from a polymer substrate to a 50- μm gap Si/SiO ₂ substrate.....	196
Fig. 6.7: Procedures of graphene thin-film layer transfer onto a prepared substrate (50- μm gap Si/SiO ₂ substrate with AAO template) in the in-house Cleanroom.	196
Fig. 6.8: SEM image of a CNT thin film.	197
Fig. 6.9: Fabrication procedures of a CNT-based TA device.	198
Fig. 6.10: Acoustic performance testing: (a) Schematic of the experimental setup; (b) measurement equipment; (c) CNT-based TA device; and (d) graphene-based TA device.	199
Fig. 6.11: Sound pressure levels of a CNT-based TA device measured at a distance of 1 cm and comparison with F-MWNT-F TA device (Aliev et al., 2015).	200
Fig. 6.12: Sound pressure levels under various AC power with different microphone distances.	201

Fig. 6.13: Temperature variation of a CNT-based TA device with different input power levels.	201
Fig. 6.14: Sound pressure levels of a graphene-based TA device with various input power.....	202

LIST OF TABLES

Table 2.1: A partial summary of relevant experimental works of using acoustic agglomeration (Ng et al., 2017).	35
Table 4.1: Configuration and weight of test samples (Group 1).....	91
Table 4.2: Configuration and weight of test samples (Group 2).....	92
Table 4.3: Comparison of epoxy resin usage in sample fabrication.	99
Table 5.1: Filtration efficiency of particle concentrations under various parameters.	167

LIST OF SYMBOLS

The main abbreviations used in this thesis are listed below:

Chapter 2

A_t	Diffraction of a half-infinite open space
A, B	Probability events
a	Distance from sound screen to sound source
b	Distance from sound screen to receiver
$C(v)$	Fresnel's integral for variable v
$d(n)$	Ideal primary disturbance
$E(z)$	z -transform expression of error signal $e(n)$
$e(n)$	Error signal
H_e	Effective height of semi-infinite sound screen
$P(z)$	Transfer function of primary path
$S(v)$	Fresnel's integral for variable v
$S(z)$	Transfer function of secondary path
$\hat{S}(z)$	Estimated secondary filter
TL	Transmission loss
W_i	Acoustic power of incident wave
W_t	Acoustic power of transmitted wave
$W(z)$	Adaptive filter
$X(z)$	z -transform expression of reference signal $x(n)$
$x(n)$	Reference signal
$y(n)$	Secondary signal
Z_s	Acoustic impedance of a sample material
Z_a	Acoustic impedance of air
α	Absorption coefficient
λ	Sound wavelength

Chapter 3

$A(n)$	Inner adaptation
D_t	Observation vector
$d(n)$	Desired signal vector
$e(n)$	Residual error signal
F_t	Regression matrix of known values of independent variables
G_t	State evolution transfer matrix
$J(n)$	Cost function
K	Prediction step size
L	Length of adaptive filter
$P(z)$	Transfer function of primary path
$S(z)$	Transfer function of secondary path
$\hat{S}(z)$	Estimated secondary filter
V_t	Observational variance matrix
V_t, W_t	Unknown covariance matrices
v_t, w_t	Independent Gaussian random vectors
$v(n)$	Gaussian noise
W_t	Evolution variance
$w(n)$	Weighted vector of adaptive filter
$x(n)$	Reference signal vector
Y_t	Observation value
θ_t	State space vector
α_t	Current level of parameter value
β_t	Current level of gradient
μ_t	Prior information
Φ	Positive threshold parameter
$\gamma(n)$	Mixing coefficient
σ^+	Control algorithm parameter
κ	Forgetting factor

Chapter 4

A, B, C, D	Complex amplitudes of plane wave components
c	Speed of sound
c_c	Speed of sound in a medium
d_1	Distance between sound source and noise barrier
d_2	Distance between noise barrier and receiver
d_{src}	Distance from a source to the intensity I_{rms} is specified
H_l, H_i, H_r	Transfer functions
I_{rms}	Sound intensity
IL	Insertion loss
k	Wave number
l	Distance between the first microphone location and the front of sample
P_1, P_2, P_3, P_4	Complex sound pressure
$P(x, \omega)$	Complex pressure
P_s	Time-averaged sound pressure
p_i	Sound pressure of incident wave
p_r	Sound pressure of reflected wave
$p(x)$	Sound pressure
p_t	Total pressure of sound
$p(t)$	Instantaneous sound pressure
P_{ref}	Reference sound pressure
Q_m	Monopole domain source
q_d	Dipole domain source
R	Reflection coefficient
Re	Real part
R_a	Normal incidence
S	Monopole amplitude
s	Space between microphones
T_a	Plane wave reflection
T_{ij}	Transfer matrix components
TL	Transmission loss

T	Sampling time
$V(x, \omega)$	Complex particle velocity
V_1, V_2	Complex particle velocities
$v(x, t)$	Particle velocity
Z_i	Acoustic impedance
α	Absorption coefficient
α_n	Normal absorption coefficient
ρ_0	Fluid density
ω	Angular frequency
ξ_0	Coordinate of an inner PML boundary
ρ_c	Density of medium
ω	Angular frequency
ϕ	Phase of sound source
$\delta(x-x_0)$	Delta function

Chapter 5

C_1	Particle concentration in the absence of an acoustic effect
C_2	Particle concentration in the presence of an acoustic effect
$C_{\epsilon 1}, C_{\epsilon 2}$	Non-dimensional constants
C_μ	Flow constant
C_d	Drag coefficient
c_p	Velocity of small particles
c_0	Speed of sound in a carrier medium
c	Speed of sound in air
d	Distance between particles
f	Acoustic frequency
F_a	Acoustic radiation force
F_s	Secondary radiation force
F_g	Gravitational force
F_d	Drag force
k	Turbulent kinetic energy

L	Length of resonant chamber
m	Harmonic number of emitted frequency
m_p	Particle mass
P_{rms}	Root-mean-square pressure
P_{ref}	Reference sound pressure
P_A	Sound pressure amplitude
\bar{p}	Mean pressure of the fluid flow
P_k	Production term
p_i	Sound pressure amplitude of incident wave
p_r	Sound pressure amplitude of reflected wave
$p_s(x)$	General form of sound pressure
p_t	Total pressure of sound
q_d, Q_m	Dipole and monopole domain sources, respectively.
R	Equivalent radius of small spherical particles
Re_r	Relative Reynolds number
S	Projection area of the particle perpendicular to the direction of propagation of acoustic waves
t	Temporal variable
U_r	Relative velocity between airflow and particle
u	Average flow velocity
\bar{u}_i	Mean flow velocity
v_A	Velocity amplitude in acoustic standing wave
$v_p(x)$	Velocity of particles
x	Spatial variable
α	Removal coefficient
β_p, β_0	Compressibility factors of particle and air
λ	Wavelength of sound
ϕ_1, ϕ_2	Acoustic contrast factors
ρ_p	Density of small particles
ρ_0	Density of sound in a carrier medium
Φ	Modified acoustic contrast factor
θ	Angular between the angular velocity from the center of two particles and the propagation direction of an acoustic wave

ω	Angular velocity of the air carrier medium
ν	Fluid kinematic viscosity
τ_{ij}	Reynolds-stress term
μ_T	Dynamic viscosity
ε	Turbulent dissipation rate
$\sigma_k, \sigma_\varepsilon$	Non-dimensional constants

Chapter 6

a	Thin-film area
c_0	Isothermal speed of sound
f	Frequency of sound
g	Gap distance between a thin film and a substrate
j	Imaginary number
\bar{P}_j	Average electric power
$P_j(t)$	Joule power
P_1	Acoustic pressure
P_{in}	Effective input power
S_1	Heat source
T	Temperature
T_0	Ambient temperature of medium
t	Time
R	Reflection coefficient of thermal wave
R_0	Rayleigh distance
x	Perpendicular direction to a thin-film surface
α_1	Diffusion constant of medium (typically air)
α_2	Thermal diffusion constant of substrate
κ_1	Heat conductivity of medium
ρ_0	Density of surrounding medium
$\delta(x - g)$	Dirac Delta function

LIST OF ABBREVIATIONS

The main abbreviations used in this thesis are listed below:

AAO	Anodic aluminum oxide
AC	Alternating current
ANC	Active noise control
ANR	Average noise reduction index
C-FxLMS/F	Convex combination filter via FxLMS/F algorithm
CNT	Carbon nanotube
CVD	Chemical vapor deposition
DLM	Dynamic linear model
FxLMS	Filtered-x least mean square
FxLMS/F	Filtered-x least mean square/fourth
HCPUA	Heat capacity per unit area
HD	Harmonic distortion
HEPA	High-efficiency particulate air
HVAC	Heat, ventilation, and air conditioning
ICP	Inductively coupled plasma etcher
IL	Insertion loss
LMS	Least mean square
MERV	Minimum efficiency rating value
MNR	Mean noise reduction index
MWCNT	Multi-walled carbon nanotube
NFB-FxLMS	Normalized frequency-domain block filtered-x least mean square
PDMS	Polydimethylsiloxane
PET	Polyethylene terephthalate
PML	Perfect match layer
PMMA	Polymethyl methacrylate
PM	Particulate matter
PNC	Passive noise control

PTFE	Polytetrafluoroethylene
PVD	Physical vapor deposition
PVDF	Polyvinylidene fluoride
RANS	Reynolds-averaged Navier–Stokes
SEM	Scanning electron microscope
SPL	Sound pressure level
SSR	Steady-state response
SWCNT	Single-walled carbon nanotube
TA	Thermo-acoustic
TL	Transmission loss
UV	Ultraviolet

CHAPTER 1

INTRODUCTION

1.1 Research motivation

According to a 2019 report by the United Nations, 55% of the world's population resides in urban areas, a proportion estimated to increase to 68% by 2050 (DESAPD, 2019). This explosive population growth in the urban population and the resulting dynamic shift in urban sprawl inevitably pose great challenges in pollution control in urban environment. Data related to nuisance complaints in Hong Kong show that most disputes and complaints from citizens are related to noise and air pollution (EPD, 2019). According to “Hong Kong 2030+: Planning Vision and Strategy Transcending 2030” (LCPD, 2016), the Hong Kong Government not only plans to pursue economic growth but also improves comfort and attractiveness of the urban living environment. Hence, to help realize a comfortable, green, and safe urban living environment, researchers are increasingly focusing on developing effective and innovative technique for mitigation pollutions. In this work, with the objective of simulating sustainable development, we attempt to explore alternative approaches to mitigating noise and improving indoor air quality by using acoustic-based technologies.

Acoustic noise problems increase with urbanization. A report from the World Health Organization (WHO) assessing the burden of disease (WHO, 2011) highlighted that noise pollution is a severe issue in Western Europe contributing to early deaths. Another report (UWE, 2015) valued the loss of healthy life due to noise exposure at more than one billion pounds. In Hong Kong, disputes and complaints

related to noise accounted for over 20% of all citizen grievances, making noise the second most common among the six major types of pollution complaints. The aforementioned regional reports indicate that noise pollution negatively affects human life in cities across the world. Therefore, sustainable urban planning and technological development are essential for improving and preserving the acoustic environment.

The ongoing COVID-19 pandemic has directly caused the stagnation of the global economy. To spur economic recovery, cities are fast-tracking infrastructure projects as the construction industry has long been an effective driver of the economy. Therefore, continuous and long-term construction is likely to be an essential part of urban development. Construction noise mainly arises from the operation of powered mechanical equipment, such as piling rigs, drillers, rollers, mechanical saws, hammers, and pumps. The relevant environmental regulation (EPD, 2018) provides statutory controls to restrict and lessen the nuisance caused by construction activities. In addition, the issuance of noise permits for general construction and piling works includes strict assessments and acoustical stipulations (EPD, 1997,1998,2001).

Prolonged exposure to noise, even at levels well below statutory limits, can threaten human health. Noise has been shown to have various psychological effects such as poor concentration, depression, annoying, stress, fatigue from lack of sleep, and even physiological effects, such as cardiovascular disease, tinnitus and hearing impairment (Hahad et al., 2019). The sound power level of some powered mechanical equipment can exceed 90 dB(A), with that of piling equipment exceeding 120 dB(A). Moreover, construction noise generated from powered mechanical equipment is dominated by low-frequency sound components (DEFRA, 2006). The challenges associated with the acoustic characteristic of construction noise are the loudness of construction machinery and the difficulty in implementing noise-control measures.

A common solution to this severe noise problem is to block the acoustic

transmission paths between polluting sources and sensitive receivers, which is typically achieved by erecting noise barriers or acoustical enclosures around construction sites or powered mechanical equipment. Such passive noise control measures are also used to insulate sound pathways, for example, by using barriers along expressways. This approach is practicable, mature, and low in cost. The more rigid and the thicker the barrier we have, the better the insulation performance is. However, thick and rigid sound barriers (e.g., concrete walls) have poor aesthetics. Furthermore, sound barriers composed of environment-friendly materials with innovative designs that improve portability warrant investigation. Finally, passive noise control (PNC) measures are effective for insulating against high-frequency noise components but not low-frequency components, such as construction noise.

The other approach to attenuate noise, especially low-frequency noise, is active noise control (ANC). In this approach, which is based on the principle of superposition, a new source (i.e., a secondary source) is introduced to suppress the acoustic pressure suspension of the undesired noise (i.e., the primary source). In ANC systems, noise signals are first sampled and processed using digital signal processing (DSP) hardware (i.e., DSP chips) and adaptive control algorithms (Widrow et al., 1975). Then, using electroacoustic or electromechanical transducers, a new sound wave with the same amplitude as the processed noise but with the phase inverted is generated, thus achieving noise attenuation. The weighting coefficients can be continually adjusted using adaptive control algorithms to minimize residual noise, thus resulting in optimal noise reduction.

The most common algorithms for residual noise signal processing are those based on the least mean square (LMS) theory. The standard LMS algorithm (Widrow and Stearns, 1985) was the first processable adaptive algorithm, but it incurs a significant cost through its introduction of a secondary path. To overcome this drawback, a filtered-x LMS (FxLMS) algorithm (Kuo, 1995; Kuo and Morgan, 1999)

was proposed for estimating the secondary path. Time-domain FxLMS algorithms offer easy implementation and high robustness but are limited by their convergence speed and sensitivity to environmental disturbances (Hosur and Tewfik, 1997). FxLMS algorithms in the frequency domain (Kuo et al., 2008) and a hybrid time and frequency domain (Padhi et al., 2018) have also been investigated. Furthermore, highly modified adaptive control algorithms with complex hierarchical structures have been proposed to process time-varying unstable sound signals (e.g., impulse noise).

When an ANC system is deployed in real applications, many practical problems arise, such as those related to its fundamental performance, practical constraints, performance–complexity balance, and practical design architectures (Kurakata et al., 2008; Helzner et al., 2011). Considering feasibility and practicality, the fundamental performance and real-time capabilities of the kernel adaptive control algorithm are the most important and therefore have been extensively studied. Many studies focusing on improving the performance of control algorithms have produced complicated algorithms, which entail a high computational burden and thus have less utility because of their cost and difficulty of implementation. Hence, increasing the real-time capacity of ANC systems is crucial for improving their practicability.

To maintain the stability and feasibility of the real-time process, a preprocessing procedure utilizing a Bayesian inference-based dynamic linear model (DLM) was considered for filtering raw signals. Bayesian forecasting is extensively used for statistical analysis in numerous disciplines, such as econometrics, structural dynamics, and aerospace engineering (Yuen, 2010). In a broadband time-varying feed-forward control system, Bayesian inference can be used to provide a fuzzy reference signal. Noise signal processing entails many parametric uncertainties. A Bayesian-based statistical model has high potential for use in signal parameter identification. The basic elements of a Bayesian updating model are prior information, a likelihood

function, and posterior information. Bayesian models have been widely adopted to determine the decision rules used to classify data patterns and as a way to infer unknown parameters from known measurements. A DLM is a mathematical tool for time series analysis and can be used to describe a routine way of viewing a context that changes with time. Another advantage of the Bayesian approach is that the preprocessing system can be treated as a filter. As is well known, ANC systems struggle to achieve broadband frequency noise attenuation. Therefore, using a preprocessing system to make decisions during ANC operation prevents interference from cumbersome environmental disturbances. Furthermore, inference from noise model parameters can be identified using a “short-time” prediction. Using statistical strategy-based data prediction is a promising technique for improving the efficiency of signal processing by compensating for the time-delay effects introduced by multiple signal conversion in the secondary path of ANC algorithms (e.g., analog-to-digital and digital-to-analog signal transitions).

In this work, innovative and environmentally friendly concepts are adopted to establish alternative, effective and practical measures against construction noise. Specifically, passive and active control measures are integrated in a dual approach to develop a retractable and movable noise barrier capable of attenuating both low- and high-frequency noise. Deploying barriers or enclosures is a common solution in engineering sites requiring noise insulation because of the ease of implementation and low cost of these measures. In addition, composite panels made of recycled materials such as wood pellets and rubber particles are used for passive control. The use of wood-rubber composites is a sustainable and environmentally friendly approach that offers a high level of noise insulation against middle- and high-frequency noise. Moreover, soft and porous materials are highly effective in insulating against medium and high-frequency noise components because the pores create friction against the movement of air particles at high velocities. Therefore, owing to their porous internal structure, wood–rubber composites have excellent acoustic absorption characteristics.

Composite panels made of recycled materials provide fairly good high-frequency noise attenuation. However, machine operations primarily generate low-frequency noise. Therefore, in such situations, integrating active and passive control measures can lead to better sound insulation performance. The development of new and smart materials such as polyvinylidene fluoride (PVDF) and innovations in loudspeaker technology are facilitating the realization of compact devices with better acoustic response. PVDF is a light, flexible, and transparent material with characteristics ideal for sound attenuation. Unlike conventional loudspeakers with bulky coils and diaphragms, smart and thin-film speakers fabricated using PVDF materials facilitate active control owing to their strong piezoelectric, ferroelectric, and lightweight characteristics. Therefore, in this work, PVDF thin-film sound devices with high sensitivity and low distortion are investigated for the further optimization of acoustic wave devices. In particular, recycled wood–rubber composite panels are coupled with a PVDF thin-film speaker to realize a dual-function laminated barrier that offers two lines of defense against noise.

In addition to noise attenuation, acoustic manipulation has great potential in the field of particulate removal, especially in the removal of fine and ultrafine particles. Acoustic manipulation is an active and contact-free technique for capturing particles (e.g., aerosols, dust, and hazardous particles), in which acoustic waves are used to exert an acoustic radiation force to levitate tiny objects. By creating a standing wave field, fine particles can be forced into and trapped within a specific zone and then filtered. Furthermore, the standing wave field forces these particles to oscillate periodically, causing them to collide and adhere to each other and thus form larger structures in a phenomenon called “acoustic agglomeration”. Temkin (1994) and Hoffmann (2000) defined acoustic agglomeration as an orthokinetic and aerodynamic process in which an acoustic wave induces particle coalescence (Ng, et al., 2017). Given the advantages of acoustic trapping in manipulating fine and ultrafine particulates, its adoption in indoor ventilation systems is of great research interest.

Heating, ventilation and air-conditioning (HVAC) systems play an important role in ensuring the sufficient flow of fresh air in buildings, thus reducing exposure to outdoor particles and maintaining good indoor air quality and thermal comfort. Although outdoor and indoor air pollutants interact via building envelopes and ventilation systems (Jaakkola et al., 1991), the degradation of indoor air quality may be worse than that of outdoor air because contained areas can catalyze the accumulation of potential pollutants. Low airborne particulate matter (PM) transmission in confined indoor spaces has been associated with a reduced risk of viral infection transmission, which is especially crucial during severe outbreaks such as that of COVID-19 (Qian et al., 2021). It is plausible that infectious viruses carried by PM can be disseminated throughout buildings via the recirculated air pumped by HVAC systems (Morawska et al., 2020).

Low-grade filters (e.g., those with a minimum efficiency rating value (MERV) of 6–9) are generally installed inside air ventilation ductworks. These filters typically comprise an activated carbon air-filter medium, a polyurethane foam air-filter, and polyester impingement materials. These low-grade filters are ineffective in capturing fine and ultrafine (sub-micrometer) particles. The use of high-efficiency particulate air (HEPA) filters, however, requires compliance with the mandatory ventilation and fire protection policies of the NFPA-96 (2021) and ANSI/ASHRAE-62 standards (2019). The resulting upgrades (e.g., upgrading extraction fans in high-rise buildings) are expensive and increase the overall energy consumption and maintenance costs of buildings. In addition, high-grade filters would severely restrict airflow, and therefore is considered not suitable for some ventilation systems due to airflow resistance.

Acoustic manipulation technique is a complementary air-filtering approach that not only effectively removes fine particles from indoor air but also is sustainable in the long term. However, acoustic-based particle removal techniques may require a relatively high sound pressure level (SPL), which is a potential obstacle restricting

their application. Further study to improve the removal efficiency of airborne fine particles (especially sub-micron particles) at low SPLs is thus of great research interest. In this work, by applying the concept of acoustic trapping, a novel configuration (i.e., a U-shaped design) is developed for acoustic-manipulated devices for removing submicron particles at low SPLs. In addition, the efficiency of air purification in ventilation ducts is significantly improved by coupling the acoustic-manipulated device with low-grade coarse filters (e.g., a MERV-6 grade filter) for pre-filtration.

Acoustic manipulation is applied as an efficient pre-treatment technique for promoting the formation of particle clusters, which in turn can be easily captured by the low-grade filters in mechanical ventilation systems. However, existing acoustic-based devices for particulate filtering are dogged by the following difficulties. Electromagnetic acoustic transducers are not sufficiently sensitive to generate swift and precise responses, which can cause unsteady airflows inside ventilation ducts. Piezoelectric and electrostatic acoustic devices are typically large, limiting their applicability in commercial engineering solutions. Nevertheless, this problem can be addressed using nanomaterials such as carbon nanotubes (CNTs) and graphene. Unlike conventional acoustic devices, thermoacoustic (TA) devices adopt the concept of a thermophone (Prevenslik, 2010) and generate sound by mechanical vibration. Specifically, providing an alternating current to CNT- or graphene-based thin-film materials causes the surrounding medium (e.g., air) to be heated periodically. This periodicity in turn causes the temperature field induced in the air to oscillate, and the resulting thermal expansion and contraction can generate acoustic waves. Using these principles, in this work, a smart, small-scale, high-sound-intensity, and sensitivity acoustic wave emitter is developed.

1.2 Research objectives

Stimulated by the challenges mentioned above, this work focuses on developing an acoustic-based technique for mitigating noise and improving air quality. There are two main objectives of this work, the first of which is related to investigating acoustic characteristics and noise mitigation strategies. Specifically, the tasks related to this objective are summarized as follows.

- Optimize the ANC algorithm for practical engineering applications: A learning and forecasting approach based on the Bayesian statistical framework is investigated as a pre-treatment system. The combined application of this statistical strategy and a descriptive time series (DLM) enables the preprocessing of raw signals and the concurrent generation of a predicted signal as a reference signal. This framework, together with the conventional control algorithm FxLMS and a new convex structure, the C-FxLMS/F algorithm (Song and Zhao, 2019), provides a promising way to enhance the real-time capacity of ANC systems. The convergence performance and complexity of the algorithms are comparatively evaluated against different types of reference signals.
- Investigate the use of smart materials (e.g., PVDF) in the active control of low-frequency noise: The investigation of the secondary source is another major task. Theoretically, a perfect controller is a combination of an optimized digital processing algorithm and a perfect secondary source array with high sensitivity. Such a controller can overcome the current challenges in the active control of noise. A smart, flexible, and transparent PVDF thin-film acoustic device is fabricated and its acoustic performance in terms of steady-state response and harmonic distortion is investigated under three configurations.
- Implement a hybrid barrier with active and passive noise control measures

specifically against construction noise: The use of recycled composite materials (wood pellets and rubber particles) in the attenuation of medium- and high-frequency noise is experimentally examined. An acoustic device is fabricated using recycled composite panels and PVDF thin films, and its effectiveness is examined via a scaled-down indoor experiment. An optimized configuration of this device with a retractable and portable design is also presented.

The second objective is to develop an acoustic-based technique for the contact-free filtration of sub-micron particulates. Developing an innovative, small-scale, yet high-intensity acoustic wave device is crucial, as is addressing the requirements for high-efficiency acoustic-particle interaction mechanisms. The tasks to achieve this objective can be summarized as follows.

- Improve the removal efficiency of airborne fine particles (especially for sub-micron particles) at lower SPLs: A simple U-shaped device (i.e., a device with double resonant acoustic chambers) that realizes acoustic trapping and works at lower SPLs is developed to achieve the filtering of sub-micron particulates. The parallel airflow within the resonant acoustic chambers enhances the acoustic-particle interaction, immobilizing particulates within a specific region. Using this device for pre-filtration, together with low-grade coarse filters, substantially improves the efficiency of air purification within ventilation ducts.
- Deliver a flat-band frequency range and a high-intensity SPL output: Novel nano-based materials with low heat capacity per unit area (e.g., CNTs and graphene) are studied from the perspective of TA. Prototypes of CNT- and graphene-based TA devices are fabricated, and their acoustic performance tested.

1.3 Thesis outline

This thesis is composed of seven chapters.

Chapter 1 summarizes the relevant environmental pollution issues in compact cities and briefly introduces acoustic-based techniques by referring to environmental assessment reports, statistical data, and relevant technical reports.

Chapter 2 reviews the research on noise control techniques, acoustic wave devices, acoustic manipulation techniques in particle clusters, and the application of nanomaterials in acoustic devices.

Chapter 3 introduces the combined use of the Bayesian approach and DLM as a pre-filter to improve the performance of the adaptive ANC algorithm. Numerical simulations and convergence analysis are presented. Case studies with different primary sources, (i) Gaussian noise, (ii) sinusoidal and Gaussian noise, and (iii) (measured) in-situ noise, are presented to illustrate performance of the ANC system.

Chapter 4 proposes a dual-function barrier with active and passive noise control measures for mitigating noise. The acoustic performance of recycled composite panels (passive control) and piezoelectric thin-film acoustic devices (active control) are investigated. The barrier is assembled and tested via a scale-down experiment in a semi-anechoic chamber. The effectiveness of the barrier is characterized.

Chapter 5 investigates a U-shaped acoustic-manipulated device for improvement the removal efficiency of sub-micron particulates in a ventilation system. Numerical simulations are presented to discuss the sound field and flow field, and a prototype is fabricated to examine the filtration efficiency of this device.

Chapter 6 explores the use of new materials, i.e., CNTs and graphene, in the development of a small-scale and high-intensity TA device.

Chapter 7 summarizes the main achievements of the present work, discusses its advantages and limitations, and recommends future research directions.

CHAPTER 2

LITERATURE REVIEW

To provide background for our investigation of acoustic waves and their potential applications in noise control and air filtration, this chapter presents a relevant review of the following topics:

- noise control strategies, including passive noise control (PNC) and active noise control (ANC), and their implementations;
- the mechanism of the acoustic-based particle manipulation technique and its potential application for air purification; and
- thermoacoustic (TA) effects and the fabrication of a novel TA sound emitter.

2.1 Overview of passive noise control technique

This section provides a literature review of passive noise control strategies. Most methods of noise control related to structure-borne sound can be broadly classified into two groups: passive control and active control. In the passive approach, noise is reduced by separating the sources of noise from noise-sensitive uses, resulting in noise reduction along the transmission path. In this obvious approach, noise barriers or enclosures are often used to interrupt the acoustic wave propagation path.

2.1.1 Sound insulation measure

PNC methods dissipate propagating sound waves in the absence of an external supply of control energy. Some examples include mufflers, barriers, and sound-

absorbent materials. The use of distributed sound-absorbent layers is among the most common, inexpensive, and reliable methods of reducing noise related to building structures and vehicles. The realization of PNC within the absorbent layer relies mainly on the material properties and configuration (Bies, 2018). Specifically, a foam structure is an important strategy to achieve better sound insulation (Tiuc et al., 2016). In noise control applications that use passive foam layers, the air molecules in the interstices of the porous material oscillate with the resonant frequency of the inserted sound wave, which results in frictional losses. The irregular pores within the porous structure cause variations in the flow direction as well as the expansion and contraction of the fluid, resulting in a further loss of momentum in the direction of wave propagation. In the high-frequency range, massive sound energy is lost due to these coincidental phenomena (Gentry-Grace, 1998).

To determine the acoustic anti-noise performance, the absorption coefficient and transmission loss are measured with a two- or four-microphone transfer function method (Chung and Blaser, 1980b; Nobile, 1984; B&K, 2007). An impedance tube is commonly used for acoustic characteristic testing. The absorption coefficient in standard ISO 10534-2 (1998) can be expressed as follows:

$$\alpha = 1 - \left(\frac{Z_s - Z_a}{Z_s + Z_a} \right)^2 \quad (2.1)$$

where α is the absorption coefficient, Z_s is the acoustic impedance of the sample material, and Z_a is the impedance of air. The transmission loss can be expressed as TL (B&K, 2007):

$$TL = 10 \log_{10} \left| \frac{W_i}{W_t} \right| \quad (\text{dB}) \quad (2.2)$$

where W_i is the acoustic power of the incident wave traveling toward a defined area, and W_t is the acoustic power of the transmitted wave traveling away from a defined area. A higher absorption coefficient and a higher transmission loss value represent

better sound insulation performance.

2.1.2 Materials and performance of PNC barriers

The performance of passive noise insulation depends on the use of the most economic material package with the best anti-noise performance. Many studies have investigated sound absorption in various materials. Nechita and Năstac (2018) investigated low-density and low-environmental-impact products composed of cellulose composite materials for sound insulation. The porous structure of these composites led to a higher absorption coefficient compared with existing extruded polystyrene absorbers. Pedreño-Rojas et al. (2017) developed new false ceiling plates made of gypsum and wood waste material with improved sound absorption and thermal conductivity, leading to their use in new building structures. However, most synthetic materials are made from petrochemicals, and the extensive use of synthetic materials leads to the depletion of resources and energy. Moreover, these non-biodegradable materials produce pollutants, such as refractory organics, and greenhouse gases (Putra et al., 2013). With growing awareness of environmentally friendly development, research into sustainable and recycled materials as alternatives have attracted considerable research interest (Asdrubali et al., 2012).

The huge amount of waste products generated by various industrial processes has created an environmental problem, according to a report from Hong Kong's Environmental Protection Department (2021). Vast quantities of industrial and living waste are inert in nature. Typically, waste products are disposed of in landfills or are incinerated, which increases greenhouse gas emission, land pollution, and ecological destruction (Rabl et al., 2008). Reusing waste materials can be an effective measure to mitigate the waste problem. Therefore, the recycling and reuse of waste products as anti-noise materials have been brought into focus, not only to deal with waste recycling but also to contribute to noise mitigation.

Natural materials are generally defined as materials composed of natural and renewable constituent materials, with a low level of environmental pollution emitted during their production (Pervaiz and Sain, 2003) or with low embodied energy (Zabalza Bribián et al., 2011). Many studies have reported noise insulation with various natural and recycled materials. Berardi and Iannace (2015) investigated fiber materials, including kenaf, wool, hemp, coconut, cork, cane, cardboard, and sheep wool, as the basic components of a sound absorption panel and identified their acoustic insulation properties. Yang et al. (2003) investigated the acoustic insulation performance of composite boards fabricated using rice straw–wood particles and measured relevant factors, such as the weight proportion of the particles. Putra et al. (2013) developed sound absorbers made of natural fibers from sugarcane waste. The absorbers presented good acoustic performance at 1.2 to 4.5 kHz, with an average absorption coefficient of 0.65. Schiavi et al. (2006) utilized the flexible property of rubber to enhance sound absorption. They found that rubber used as a resilient underlayer in a floating floor is effective in protecting against sound and vibration propagation in structures. They further analyzed the thickness under load and the compression behavior of the rubber underlayer. Gil-Lopez et al. (2017) mixed shredded palm tree pruning waste with dampened topsoil to act as a noise barrier against roadside noise. This ecofriendly waste material prototype not only provided significant sound absorption benefits but also delivered a large-shaded area.

Studies have examined waste and reused materials as a feasible alternative for synthetic materials in sound absorption treatment. Secchi et al. (2016) investigated the use of cardboard waste in the fabrication of acoustic insulation panels; through impedance tube testing and life cycle assessment, they found that their panels have better acoustic properties than commercial products. Ersoy and Küçük (2009) measured the acoustic absorption coefficient of industrial waste fibers arising from the processing of tea leaves and indicated that these waste fibers achieved great sound absorption in the low-frequency range. Zhao et al. (2010) investigated the sound

insulation properties of a composite panel manufactured with waste wood particles, rubber crumbs, and commercial adhesive in various proportions. Overall, natural and waste materials have good sound insulation properties and exert no detrimental effects on health and thus possess advantages over synthetic materials. Furthermore, the fabrication of sound absorbers with waste material presents an alternative approach to waste product disposal.

Noise barriers are commonly used in practical engineering applications as a PNC measure. The performance of passive-type noise barriers depends strongly on several factors, such as material type, design dimension, surface condition, and geometric configuration (Morgan and Kay, 2001; Ishizuka and Fujiwara, 2004; Samsudin et al., 2016). Maekawa (1968) summarized the effectiveness of noise insulation screens. For assessing sound insulation performance, an experimental test was established for the diffraction analysis of a free sound field with a semi-infinite plan screen. Fig. 2.1 illustrates the alteration of sound wave with presence of noise barrier.

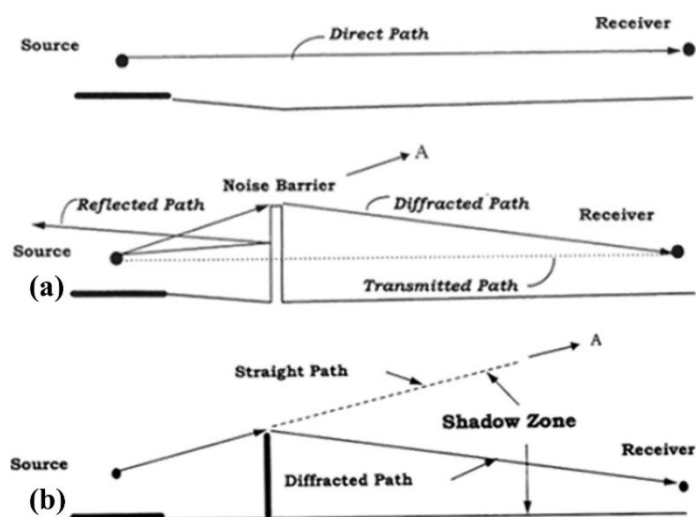


Fig. 2.1: (a) Alteration of noise paths by a noise barrier; and (b) Noise barrier diffraction (Maekawa, 1968; EPD, 2003).

The shielding effect of a semi-infinite screen can be identified by applying Kirchoff's diffraction theory (Max, 2019), as follows:

$$A_t = -10 \log_{10} \frac{1}{2} \left[\left(\frac{1}{2} - C(v) \right)^2 + \left(\frac{1}{2} - S(v) \right)^2 \right] \quad (2.3)$$

where A_t denotes the diffraction of a half-infinite open space, and $C(v)$ and $S(v)$ are Fresnel's integral for the variable v as follows:

$$v = H_e \sqrt{\frac{2}{\lambda} \left(\frac{1}{a} + \frac{1}{b} \right)} \quad (2.4)$$

where H_e denotes the effective height of the semi-infinite screen, λ denotes the sound wave length and a and b are the distances from the screen to the source and the receiver, respectively. To reconcile the actual and perceived effectiveness of the noise barrier, Mital and Ramakrishnan (1997) conducted a comprehensive survey to gather residents' responses and recommended that a reduction of more than 11 dB(A) in the sound pressure level (SPL) would provide acoustic comfort. Furthermore, Sánchez-Dehesa et al. (2011) designed a noise barrier made of perforated metal shells and waste rubber crumbs. Arenas et al. (2013) further evaluated the applicability of waste ash mixed with Portland cement for noise barriers in highway roads.

Passive strategies to obstruct the propagation of noise by deploying a noise barrier and enclosure have been demonstrated in the aforementioned studies. However, passive strategies are limited in their isolation of low-frequency noise, especially noise below 1 kHz. Conventional passive noise barriers, even those made of aluminum, concrete, acrylic sheets, or recycled materials, cannot effectively block noise of a wide range frequency range (Nilsson and Berglund, 2006), because the long acoustic wavelength of the low-frequency components facilitates their long-distance travel with less energy loss. The high-frequency components of noise are strongly susceptible to distance attenuation. Thus, the reduction of low-frequency noise components is worthy of greater attention. Studies of the health impact of noise effects have indicated that low-frequency noise has a tremendous effect on human health (Berglund et al., 1999; Mirowska and Mroz, 2000; Leventhall, 2004;

Pawlaczyk-Luszczyniska et al., 2005; Nilsson and Berglund, 2006; Baliatsas et al., 2016) and that older adults are especially sensitive to low-frequency noise (Kurakata et al., 2008; Helzner et al., 2011). Therefore, the ANC strategy was proposed as an alternative approach to address low-frequency noise problems.

2.2 Overview of active noise control strategies

In the active method, protection is provided at the receiver end by applying the concept of sound wave superposition to achieve noise attenuation. The ANC strategy was first proposed in a patent (Lueg, 1936) presenting a design in which a microphone and an electronic loudspeaker are used to generate a secondary source for noise attenuation. The development of digital electro technology has enabled the development of active anti-noise devices that can be governed digitally and automatically (Ise et al., 1991). With this technology, noise signals can be transformed in real time via the integration of an electroacoustic transducer system and a digital signal processing system. In the 1990s, the development of smart chips aided the implementation of adaptive algorithms (Eriksson, 1993), accelerating the widespread application of adaptive ANC systems (Kuo, 1996). Fig. 2.2 illustrates the principle of active noise control strategy.

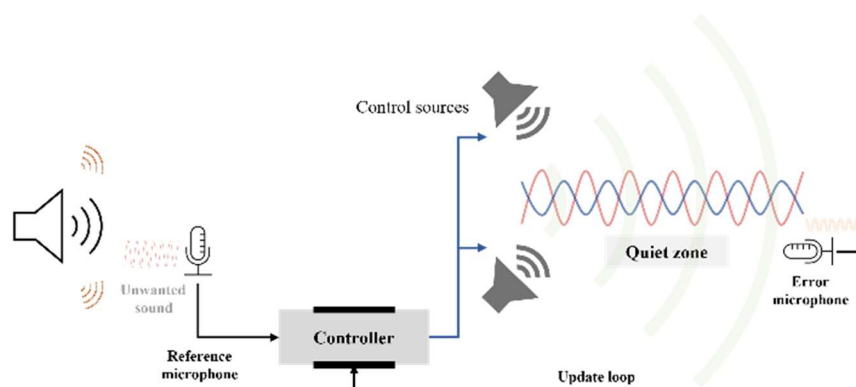


Fig. 2.2: Principle of active noise control.

The early ANC systems (Nelson, 1993; Kuo, 1996; Hansen, 2013) were

electroacoustic systems used to generate anti-noise sounds with the same amplitude as the noise but with the opposite phase, thereby resulting in the cancellation of both noises. Thereafter, adaptive systems were developed to cope with variations in noise by considering the time-varying frequency, amplitude, and phase characteristics of the environmental disturbance. Later ANC systems integrated an adaptive processing system with an electroacoustic transducer system.

2.2.1 Adaptive control algorithm

Adaptive filters play an important role within the processing system. According to the adaptive characteristics, the coefficients of filters enable their adjustment to optimize a cost function or to satisfy some predetermined optimization criteria (Kuo and Morgan, 1999). An adaptive filter not only allows automatic adaptation in the face of changing environments but also enables training for optimal decision-making performance under specific requirements. These characteristics enable an adaptive filter to achieve prompt parameter estimation and signal processing in time-varying and nonstationary conditions. Fig. 2.3(a) is a schematic of a basic feedforward ANC system, and Fig. 2.3(b) illustrates the framework of an adaptive filter within the ANC system.

A single-channel ANC system normally consists of a reference microphone, a cancelling speaker, and an error microphone (Kuo, 1996; Kuo and Morgan, 1999; Hansen, 2013), as shown in Fig. 2.3. The reference microphone is used to pick up the information from the noise source (reference signal: $x(n)$), and the error microphone is used to monitor the performance of the ANC system by sampling the residual noise signal (error signal: $e(n)$) and sending feedback. The kernel of an ANC system is the adaptive filter for reference signal processing and secondary signal ($y(n)$) manipulation. Specifically, the adaptive filter $W(z)$ is used to estimate the unknown primary path $P(z)$ of the acoustic response from the reference microphone to the error

microphone. The ideal primary disturbance $d(n)$ is the acoustic response after the reference signal passes through an unknown plant $P(z)$. Theoretically, the adaptive filter $W(z)$ enables minimization of the error signal $e(n)$ via multiple iterations until zero is reached. This approach assumes that $X(z) \neq 0$ and $E(z) = 0$, where $X(z)$ and $E(z)$ are the z -transform expression of reference signal $x(n)$ and error signal $e(n)$, respectively. Sufficient iterations of adaptive filter $W(z)$ allows us to obtain the optimal results of $W(z) = P(z)$, resulting in $d(n) = y(n)$. Accordingly, perfect cancellation of both the primary and secondary sound waves can be achieved based on the principle of superposition.

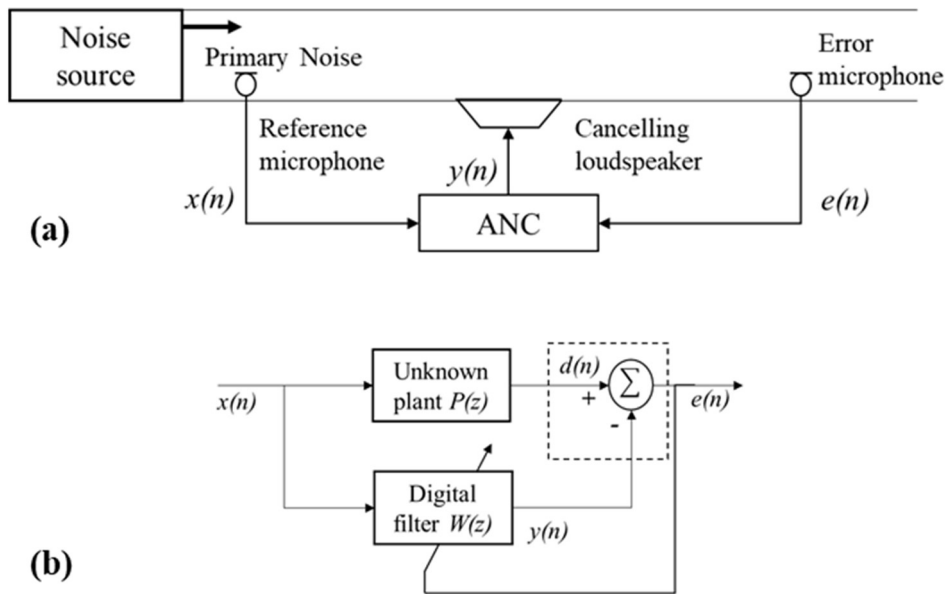


Fig. 2.3: Schematic diagram of ANC system in a duct system (Kuo and Morgan, 1999): (a) Single-channel broadband feedforward ANC system; and (b) Adaptive filter identification framework.

Nevertheless, secondary path effects, which are acoustic responses from a secondary source to the error microphone, are inevitable. Fig. 2.4 illustrates the framework of an adaptive filter considering the secondary-path effects, which can be demonstrated via the secondary-path transfer function $S(z)$. This function considers the cost of a digital-to-analog converter, a reconstruction filter, an amplifier, an

electroacoustic transducer, an acoustic path from the speaker to the error microphone, and an analog-to-digital converter. Therefore, the numerical expression of the adaptive loop is:

$$E(z) = [P(z) - S(z)W(z)]X(z) \quad (2.5)$$

where $E(z)$ and $X(z)$ are the z -transform expression of error signal $e(n)$ and $x(n)$, respectively, and $P(z)$ and $S(z)$ are the primary and secondary paths, respectively. Assuming $E(z)=0$ and $X(z)\neq 0$, the ideal expression of $W(z)$ after adaptive filter convergence can be expressed as follows:

$$W(z) = \frac{P(z)}{S(z)} \quad (2.6)$$

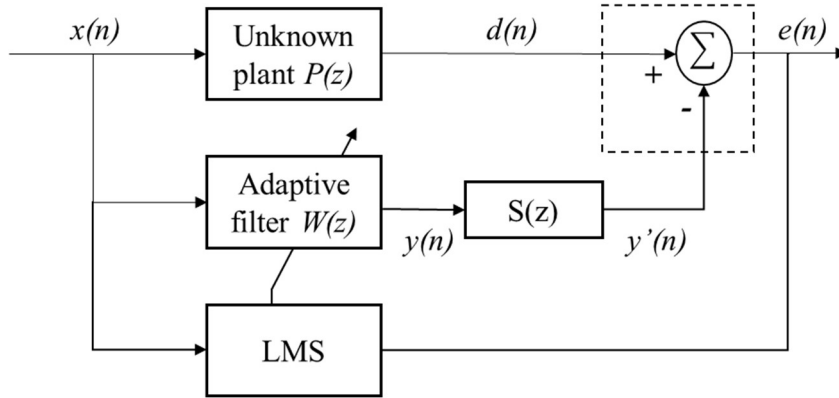


Fig. 2.4: Schematic of an ANC system considering secondary-path effects (Kuo, 1996).

To achieve more adaptive control algorithms, Widrow et al. (1975) proposed a standard least mean square (LMS) algorithm, in which the least-mean-square criterion is treated as a cost function. However, the time-delay effect induced by the secondary-path transfer function must be compensated for (Elliot and Nelson, 1985). Widrow et al. (1981) further proposed the filtered-x LMS (FxLMS) algorithm, which includes an estimated filter $\hat{S}(z)$ in the reference signal path to compensate for the secondary-path

effects in the LMS algorithm. Burgess (1981) investigated the feasibility of the FxLMS algorithm within an ANC system. Widrow and Stearns (1985) proposed an online secondary-path modeling approach that avoids the preliminary estimation of the secondary path via offline secondary-path modeling. The FxLMS algorithm presents acceptable results if the adaptation is slow (i.e., if the step size is fixed and limited to a small value), as shown in Fig. 2.5.

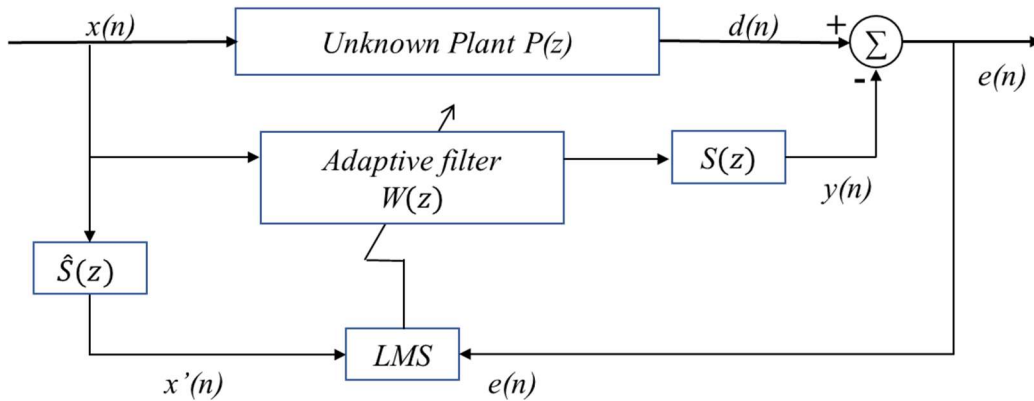


Fig. 2.5: Schematic of the FxLMS algorithm (Widrow and Stearns, 1985).

The FxLMS-based adaptive algorithm had to be modified for processing complex dynamic signals. To process dynamic disturbances within the adaptive process, Boucher et al. (1991) derived the optimum step size and convergence time for the FxLMS algorithm, and further explorations of the time-domain algorithm have also been reported (Kuo and Ji, 1996; De Diego et al., 2004). Such time-domain FxLMS algorithms enable the processing of stationary (Widrow et al., 1976; Bershad, 1991) and nonstationary noise (Tahir Akhtar and Mitsuhashi, 2009). However, their limitations, such as the relatively high computational complexity and slow convergence (Kuo, 1996), restrict their practicability. To enhance the calculation velocity, Zhang et al. (2019) proposed a novel normalized frequency-domain block FxLMS (NFB-FxLMS) algorithm that can reduce the computational complexity, and Tang and Lee (2012) also proposed a time–frequency domain FxLMS algorithm. To investigate the effort weighting of time-domain techniques versus frequency-domain

techniques, Friot (2017) discussed and analyzed the effort-weighting parameters via error index comparison. Tu and Fuller (2000) reported an optimum multiple-channel ANC system in the frequency domain. Although the algorithms in the frequency domain (Rees and Elliott, 2006; Patel et al., 2017) have always been effective in suppressing stationary noise, they may be unstable against nonstationary disturbances or frequency modulation rate signals. In summary, Wang et al. (2020b) mentioned that frequency-domain algorithms fail to eliminate nonstationary signals, whereas time-domain algorithms entail high computational complexity and low convergence speed (Kuo, 1996).

To further address the aforementioned issues, tremendous efforts have been made to achieve faster convergence, lower computational complexity, and greater adaptivity. By applying discrete wavelet transformation, Wang et al. (2020b) and Qiu et al. (2016) developed a frequency-domain algorithm (i.e., the discrete wavelet transformation–FxLMS algorithm) to process both stationary and nonstationary signals. Some novel algorithms have been proposed to cancel impulse noise, including a convex mixture of algorithms (Arenas-Garcia et al., 2003; 2006; Song and Zhao, 2018) and modified conventional algorithms (Sun et al., 2006; Tahir Akhtar and Mitsuhashi, 2009; Akhtar and Mitsuhashi, 2011; Zhou et al., 2013; Sun et al., 2015). Kurian et al. (2017) presented a theoretical learning approach for the robust improvement of adaptive algorithms. With the FxLMS/F algorithm (Lim and Harris, 1997) and the idea of a convex structure that includes two adaptive filters (Ferrer et al., 2013; George and Gonzalez, 2014; Al Omour et al., 2016), a convex combination filter via the FxLMS/F algorithm (C-FxLMS/F) (Song and Zhao, 2019) has been presented as a variable step-size algorithm.

Many studies have proposed modifications of the control algorithm. Indeed, a robust algorithm is important for the control result and should be tested against various input signals, such as stationary, impulse, and tonal signals. However, real-

world (in-situ) measured data are more complicated and likely represent a mixture of multiple signals, which cannot yet be effectively processed. Furthermore, due to the time-delay effects within the ANC system, the computational effort in the controller, signal conversion, and secondary source response needs to be further investigated. To accommodate a wide range of applications, an effective preprocessing system for the reference signal is likely important to enhance the real-time performance of the adaptive filter. An ANC system with preprocessing that uses a combination of a dynamic linear model (DLM) and Bayesian inference to reduce operating machine noise in a construction site is worthy of exploration.

Bayesian inference is a method of statistical inference, in which Bayes' theorem is adopted to update the probability for a hypothesis. Assuming A and B to denote two events, the condition probability of the event A to provide the occurrence of the event B can be given by (Yuen, 2010):

$$P(A|B) = \frac{P(A \wedge B)}{P(B)} \quad (2.7)$$

where symbol \wedge denotes the logical operator for two (or more) events, so $P(A \wedge B)$ denotes the probability of the occurrence of both events if $P(B) > 0$. (If $P(B) = 0$, then $P(A \wedge B) = 0$ and $P(A|B)$ is meaningless). For discrete events, the theorem is obtained as follows:

$$P(A|B) = \frac{P(B|A)P(A)}{P(B)} \quad (2.8)$$

for $P(B) > 0$. If the event A is partitioned into N mutually exclusive events, i.e., A_1, A_2, \dots, A_N , the probability $P(B)$ in the denominator can be replaced by:

$$P(A_n | B) = \frac{P(B | A_n)P(A_n)}{\sum_{n=1}^N P(A_n)P(B | A_n)} \quad (2.9)$$

for $n=1, 2, \dots, N$.

Bayesian forecasting is among the most widely used approaches in statistical analysis. It has been adopted in multiple disciplines, such as econometrics, structural dynamics, and aerospace engineering (Yuen, 2010). The basic elements of a Bayesian updating model include prior information, a likelihood function, and posterior information. This forecasting approach has been widely adopted for decision rules used to classify data patterns and as a means to infer unknown parameters from known measurements. A DLM is a mathematical tool for time series analysis that can be used to describe a routine method of viewing a context that changes over time. Bayesian inference has been used to estimate frequency periodic information in a narrowband ANC system (Han et al., 2019). Prediction information has contributed significantly to enhancing the performance for a specific periodic noise signal. A Bayesian estimation approach (Ardekani et al., 2016) was used to recast the problem of online secondary path modeling in the form of a statistical inverse problem. A novel approach to ANC based on Bayesian estimation theory (Ardekani et al., 2017) was investigated using the statistical property for the optimization of parameters. Various structures and theories of dynamic models that incorporate Bayesian forecasting have also been reviewed in the literature (Pole, 1994; West and Harrison, 1997). The versatility and applicability of Bayesian methods make them suitable for many other applications in mechanical and structural engineering. For instance, (Lipowsky et al., 2009) combined Bayesian forecasting with DLM for assessing the performance of gas turbines, and Zhang et al. (2018c) and Wang et al. (2017, 2020c) used a combination of time series analysis and Bayesian inference for assessing the structural responses of high-speed trains and cable-stayed bridges.

2.2.2 Active anti-noise devices

Instead of building on the control algorithm, some researchers have focused on modeling effective ANC systems to control noise in large spaces. Multi-input multi-output ANC systems have been examined (Krahe, 2005; Berthilsson et al., 2012; Eder et al., 2017). As the name suggests, an ANC system consists of multiple anti-noise sources and sensors. A bottleneck in the development of multi-input multi-output ANC systems is the increasing computational load imposed by the controller and the increased cost incurred in meeting this requirement. As an alternative system, Murao et al. (2016) proposed an array of ANC units on the basis of the active acoustic shielding technique and implemented such an array using collocating reference microphones and speakers. In this decentralized system, each ANC unit is relatively independent and disconnected, and by applying the Huygens–Fresnel principle, the array of collocated units can produce the same wavefront pattern as the noise passes through it. Murao et al. (2016) claimed that such a decentralized system could realize a large quiet zone behind the array and that it could work against any noise source. Efforts to optimize this approach have focused on the enhancement of the secondary source array. For example, Elliott et al. (2018) first proposed an approach for normal incidence plane wave analysis with a clear indication of the optimal cut-off frequency, and they recommended that the distance between each secondary source should be shorter than one-half of the wavelength of a sound wave. Wang et al. (2015) evaluated the integration of sound masking techniques by embedding active noise mitigation elements in passive control barriers.

Other techniques to achieve ANC by embedding anti-noise elements in windows have been described in the literature (Huang et al., 2011; Pàmies et al., 2014; Lam et al., 2017). The limitation of such array-based ANC systems is that noise reduction relies greatly on the density of the secondary speakers, and a quiet large room occupied by such an array system has low practicability. Considering commercial and

artistic requirements, conventional speakers within the array ANC system have gradually been substituted with flexible, lightweight, and smart materials because the former are bulky, costly, and unaesthetic.

Unlike conventional speakers with coils and diaphragms, polyvinylidene fluoride (PVDF) (Sugimoto et al., 2009) is a new, smart, lightweight, and thin-film material with strong piezoelectric (Kawai, 1969) and ferroelectric (Lolla et al., 2016) properties. PVDF thin-film materials are not affected by electromagnetic interference or iron filling, and they can be driven directly by an integrated circuit with high energy exchange efficiency (Kim et al., 2011). The acoustic characteristics and surface vibration modes of transparent and flexible devices, for example, a sandwiched membrane structure driven by PVDF, have been investigated (Sugimoto et al., 2009; Wang et al., 2015). Moreover, a new-shape structures which uses a folded zigzag-tack shape bimorph sheet of PVDF have been explored (Ohga et al., 2010; Kim et al., 2012) to improve the efficiency of piezoelectric speakers in low-frequency wideband signals. As an implementation of PVDF devices in ANC systems, a foam-PVDF smart skin was developed for noise control in aircraft interiors (Guigou and Fuller, 1999). To address the noise transmission issue from windows, Yu et al. (2007) used PVDF thin film coated with compliant carbon nanotube (CNT) conductors as actuators of the control system. Hu et al. (2012,2013) proposed a wave separation technique to eliminate the disturbance and implemented an anti-noise system via a PVDF secondary source for directional noise cancellation. The performance of transparent thin-film speakers attached to the surface of a window as a secondary source was tested experimentally by Sharifzadeh Mirshekarloo et al. (2018); they also performed a numerical simulation to illustrate the overall active control performance within the testing room and reported an average SPL of 6.3 dB.

Despite the foregoing efforts reported in the literature, significant barriers remain, blocking the widespread adoption of ANC techniques. The bottlenecks of active

mitigation in a large space include but are not limited to the following: the large scale of the secondary source array, the limits of the low-frequency response of the PVDF speakers, the complexity of the spatial sound field, and the effectiveness of the system. Overall, considerable room remains for the further improvement of noise mitigation. To this end, hybrid ANC and PNC strategies have been proposed and examined (Lee et al., 2002; Remington et al., 2005; George and Panda, 2012; Murao et al., 2019). For example, Lee et al. (2002) presented a hybrid panel to reduce transmitted noise; in their study, the use of a sound-absorbing material and an air gap proved effective against high frequencies, whereas an active approach was found to be effective against lower resonant modes. Considering the complexity of the spatial sound field, such a hybrid strategy has high potential for application in broadband frequency noise reduction.

2.3 Acoustic manipulation technique

In addition to noise control, nonlinear acoustic effects have another potential application, that is, in the removal of aerosol particles (Yuen et al., 2014). As a contact-free technique, acoustic manipulation enables the realization of a noninvasive aerosol removal process (Yuen et al., 2014). In most filtration and aerosol removal systems, particles are removed from the main air stream via deposition (Niu et al., 2020). For example, separators such as cyclones use external centripetal force to displace particles from the main air stream and then collect them by deposition via inertial impaction. In a passive filter, fibers introduce sudden changes in the airflow velocity, and the particles are deposited onto them via interception and impaction. The capture of submicron particles, such as pollen, dirt, dust moisture, bacteria, virus, and liquid aerosol droplets, requires a high-efficiency particulate air (HEPA) filter, in which four collection mechanisms are implemented: diffusion, interception, inertial impaction, and electrostatic attraction. These systems require that either a high airflow

velocity or a high-pressure drop be overcome within the air duct, resulting in high energy consumption (Thomas et al., 1999; Jang et al., 2008). Acoustic agglomeration was introduced in the 1930s (Patterson and Cawood, 1931). Mednikov (1965) developed an innovative aerosol removal technique with the use of nonlinear acoustic effects, which has great potential to be developed into an energy-efficient and smart aerosol removal technique (Yuen et al., 2014, 2016, 2017).

2.3.1 Mechanism of acoustic manipulation

Many research papers have reported the effectiveness of sound waves in causing large-scale particle polymerization, thereby decreasing the particulate concentration. (Hoffmann et al., 1993; Gallego-Juárez et al., 1999; Liu et al., 2011). Several agglomeration mechanisms have been discussed to determine the particles' motions and interactions in a sound wave field (Mednikov, 1965; Song et al., 1994; Zhang et al., 2012; Zhou et al., 2017; Kačianauskas et al., 2018). However, no consensus has yet been reached regarding the mechanism governing particle agglomeration, which is of great research interest. The basic mechanism of acoustic-particle interaction is shown in Fig. 2.6. Acoustic agglomeration can be illustrated as a process in which acoustic waves are used to manipulate the motion of airborne particles (Chou et al., 1980; Lee et al., 1981; Tiwary et al., 1984; Temkin and Ecker, 1989), promoting the occurrence of collision leads to the formation of agglomerates or clustering (Ng et al., 2017). Forces acting on airborne fine particles include viscous force, acoustic pressure gradient force and inertia force (Yan et al., 2016).

discrete element method model for particle agglomeration and concluded that the acoustic wake effect was a major mechanism and that orthokinetic collision was inconsequential. The same claim was made by Zhang et al. (2018b) in their proposal of a new model, in which they concluded that the acoustic wake effect was dominant during the acoustic agglomeration process. However, differing opinions have been presented. Dong et al. (2006) claimed that the acoustic wake effect was stronger at high frequencies and that orthokinetic interaction was more obvious at low frequencies during the agglomeration process. Fan et al. (2017) showed that the joint effects induced from orthokinetic interaction and gravity sedimentation were dominant.

The controversy over the dominant mechanism has spurred considerable research on acoustic agglomeration. Shen et al. (2018) experimentally examined acoustic agglomeration and fragmentation and found that the agglomeration efficiency was greatly affected by two factors: the particle size distribution and the volume fraction of fine particles. Zhang et al. (2018a) used the addition of liquid droplets to enhance the effectiveness of agglomeration. Direct observation of particle motion in a sound wave field with an extremely-high-speed camera was examined for further investigation of acoustic agglomeration. A new technique (Hoffmann and Koopmann, 1994,1996) has been examined to observe particle movement via a charge-coupled device camera with a high-resolution video system, but this method failed in acquiring the particle size and velocity. More recently, Zhou et al. (2017) captured particle trajectories using a high-speed camera and track analysis. The vibration speed and amplitude were calculated and were shown to be consistent with the numerical simulation. Lu et al. (2019) applied high-precision microscopic visualization and high-speed photography to observe the agglomeration and separation phenomena of fly-ash particles.

2.3.2 Potential application of acoustic-based particle manipulation

A particular pattern of constructive and destructive interference is called a standing wave. With two traveling sound waves propagating in opposite directions, the two waves combine to create a resultant wave that appears to stand still at certain resonant frequencies called modes. These modes generally correspond with harmonic partials, with the first mode producing the fundamental. By using acoustic standing wave field, aerosol manipulation can achieve the regular motion.

To further explore the potential application of this technique in an air purification system, independent experiments have been conducted to explore the feasibility of the acoustic manipulation technique. According to the existing publications in developing such an particle manipulation techniques, Sarabia et al. (1986) used high-intensity sound pressure to investigate the ultrasonic agglomeration effect on micron-size aerosol particles under a high-intensity standing wave. Ng et al. (2017) used acoustic agglomeration as a preconditioning device in the ventilation system to enhance the PM_{2.5} filtration efficiency at 6.4 kHz and 140 dB. Shi et al. (2017) constructed a resonant structure for the removal of fine particles at SPLs greater than 145 dB. Furthermore, phase-control acoustic manipulation has been presented as an alternative approach. Qiao et al. (2015,2017) applied fine particle manipulation with a two-dimensional acoustic standing field emitted by two pairs of Helmholtz resonators above 130 dB and concluded that aerosols can be manipulated by multiple acoustic wave packets under resonance conditions. Similarly, Greenhall (2013) examined micro-particle manipulation within a reservoir via the phase control of bulk acoustic waves. They succeeded in experimental manipulation of particles trapped at a predetermined location based on two regimes: the ray acoustic regime and the Rayleigh regime.

To further demonstrate practicability, Guo et al. (2012) investigated the

combined effects of acoustic effects and gas-solid jet action on particle agglomeration. They concluded that the joint effects enhanced particle collision and that the optimal frequency was 1416 Hz at a lower SPL of 120 dB. Other important research on acoustic manipulation has concerned the levitation of micro- and macro-particles in air (Weber et al., 2009; Foresti et al., 2012; Foresti et al., 2013). Indeed, acoustic manipulation has distinct advantages for micron particle filtration, which enable its use as a prefilter or even a standalone filter for air purification. However, relative to the rich body of work on acoustic-based particle manipulation, the application of this technique in particulate matter removal has been sluggish. Karpul et al. (2010) summarized the relevant factors for filter design when using acoustic force. They concluded that acoustic filtering is a working form of filtration but one that requires an unfeasibly large amount of power. They mentioned that further novel configurations to achieve acoustic-based filtration are essential to adapt to an environment with a higher volume flow rate. Moreover, Yao et al. (2010) published a comprehensive review of particulate matter control strategies, including acoustic agglomeration, from an industrial application perspective. Acoustic manipulation enables the realization of innovative devices capable of prolonged, energy-efficient, and effective removal of fine particles (Yuen et al., 2014; Yuen et al., 2016,2017). Although the literature shows good progress, such devices still require an extremely high SPL, a potential obstacle that restricts their application. A partial summary of relevant works in using acoustic-particle manipulation is listed in Table 2.1.

As shown in Table 2.1, in order for acoustics agglomeration to be effective, high SPLs are required in the range of 120 to 160 dB, which may cause a noise problem. The problem of high SPLs may become a potential barrier to restrict the application of acoustic-driven techniques in actual building scenes. Hence, a further study and notable breakthrough, to improve the removal efficiency of airborne fine particles (especially for sub-micron particles) under lower SPLs, is of current focus. Therefore, future studies should focus on improving the removal efficiency of aerosol

particulates at a low SPL via acoustic-based particle manipulation. Also, the improvement of purification effectiveness is among the most anticipant aspects of providing safe, comfortable, and efficient indoor environments (Kelly and Fussell, 2019).

Table 2.1: A partial summary of relevant experimental works of using acoustic agglomeration (Ng et al., 2017).

Reference	Particle size and distribution	Frequency (kHz)	Intensity (dB)	Performance
Boulaud et al. (1984)	Monodisperse	0.54 and 1.02	140 to 160	Shifted mean from 1.5 μm to 4.5 μm and shifted σ from 1.75 to 5.
Gallego-Juarez et al. (1996)	Polydisperse	10 and 20	152	Number concentration of micron & sub-micron particles reduced by 70% and 30%, respectively.
Hoffmann et al. (1993)	Fly ash & limestone as sorbent	0.044	160	Mass concentration of particles < 11 μm reduced by 23%.
Liu et al. (2009a)	Fly ash	1.4	147	Number concentration of $\text{PM}_{2.5}$ reduced by 75.6%.
Guo et al. (2012)	Fly ash	1.416	120	Mass concentration of particles 3.3 μm reduced around 35% from combined acoustics, 23 ms^{-1} jet gas & seed particles of 150 μm to 250 μm .
Zhou et al. (2015)	Fly ash	1.4	142	Number concentration reduced by 35%.
Ng et al. (2017)	Polydisperse	6.4	140	Number concentration of particles ranged from 0.4 to 0.5 μm reduced by 16%.

2.4 Thermal-acoustic sound emitter

Acoustic manipulation has been investigated as an efficient pretreatment technique to produce particle clusters, which in turn can be easily captured by low-grade filters in mechanical ventilation systems. However, existing sound emitters are dogged by difficulties such as insufficient sensitivity and bulky size, which limit their applicability in commercial engineering solutions. This problem is likely to be addressed with the development of nanomaterials with high thermal and electrical conductivity. A TA sound emitter is a novel type of device that enables the generation of TA pressure waves. This emitter adopts the concept of a thermophone (Prevenslik, 2010) and generates sound via interaction among temperature, density, and pressure variations of the surrounding medium.

Although TA-induced oscillation was first observed centuries ago, TA theory was not fully realized until the late 1990s. Rayleigh (1945) gave a qualitative explanation of the TA phenomena; he stated a criterion for TA oscillation, relating the occurrence of TA phenomena to heat-induced variations in air density. Kramers (1949) then presented a formal theoretical study of TA phenomena, in which he generalized the Kirchhoff theory of sound attenuation at constant temperature to the case of attenuation with a temperature gradient. Feldman (1968) classified TA phenomena as Rijke oscillation and Sondhauss oscillation. However, the detailed heat transfer mechanism was not discussed in depth. A great breakthrough was made by Rott (1969), who developed a linear theory to model TA phenomena. Swift (1988) summarized the fundamentals of TA engines built as an energy-conversion device. To obtain a comprehensive understanding of TA technologies, relevant reviews (Avent and Bowen, 2015; Jin et al., 2015; Zolpakar et al., 2016; Iniesta et al., 2018; Timmer et al., 2018; Tartibu, 2019; Chen et al., 2021) were conducted on specific topics, including advances in practical implementations, options for transducers, and the optimization of TA refrigerators and multiphysics coupling effects within TA devices.

In general, two aspects of the TA effects lay the foundation for a TA sound emitter. First, an alternating current input is induced into solid materials, which have good thermal conductivity, to increase the temperature differential. Second, the temperature differential produces spontaneous oscillations (Wheatley et al., 1983) of nearby compressible fluid under the continuous excitation of alternating current (Helmholtz, 1878). Due the temperature gradient, acoustic waves propagate along the direction of expansion and compression of the carrier medium. The thermodynamic analysis approach (Tiwatane and Barve, 2014) is commonly used to describe specific TA properties such as permeability, heat capacity, and thermodynamic equilibrium.

A TA sound emitter, also referred to as a TA standing-wave generator or a TA speaker, is an important application of TA effects. One of the most highly cited studies in this field is based on flexible, stretchable, transparent CNT thin-film loudspeakers. Xiao et al. (2008) demonstrated that such CNTs can be fabricated and removed from well-aligned arrays grown on 4-inch silicon wafers. They measured CNT materials with wide frequency range responses from 1 to 30 kHz and high SPL responses above 70 dB. Furthermore, this CNT loudspeaker device has been examined in other theoretical and modeling studies. For example, Lim et al. (2013) developed a TA radiation analytical model using suspended CNT films and identified a flat frequency response as the TA source. Suzuki et al. (2011) examined the use of CNTs as TA loudspeakers in a web configuration. In addition, Xiao et al. (2011) investigated the dependence of gases and the relevant frequency response of CNT thin films for loudspeakers, and Tong et al. (2013) studied gas-filled encapsulated TA transducers. Kozlov et al. (2009) reported a comparative analysis of suspended multi-walled CNT sheets and multi-walled CNT-type forests grown on Si wafers; the multi-walled CNT sheets illustrated better sound intensity performance. Other studies on near-field acoustic holography have been performed (Hall et al., 2014; Asgarisabet et al., 2016). The high thermal conversion capability of CNT- or graphene-based thin-film TA devices enables the rapid transfer of a temperature difference to allow the conversion

of electrical energy to acoustic energy. The advantages of such a device include an improved sensitive acoustic response (Magri and Juniper, 2013), high sound intensity outputs (Tiwatane and Barve, 2014), a flat frequency response (Hu et al., 2012a), and a compact structure (Xiao et al., 2008; Tian et al., 2011b; Tian et al., 2011c; Aliev et al., 2015; Asgarisabet and Barnard, 2017; Sbrockey et al., 2018; Torraca et al., 2018).

An expectation of the graphene-based TA devices and their industrialization time is shown in Fig. 2.7 (Qiao et al., 2020). Many graphene TA theory models and devices have been demonstrated. To fabricate such TA devices, there are still many advantages by using graphene materials which have not been fully explored. Therefore, in-depth investigations on it are still of great research interest.

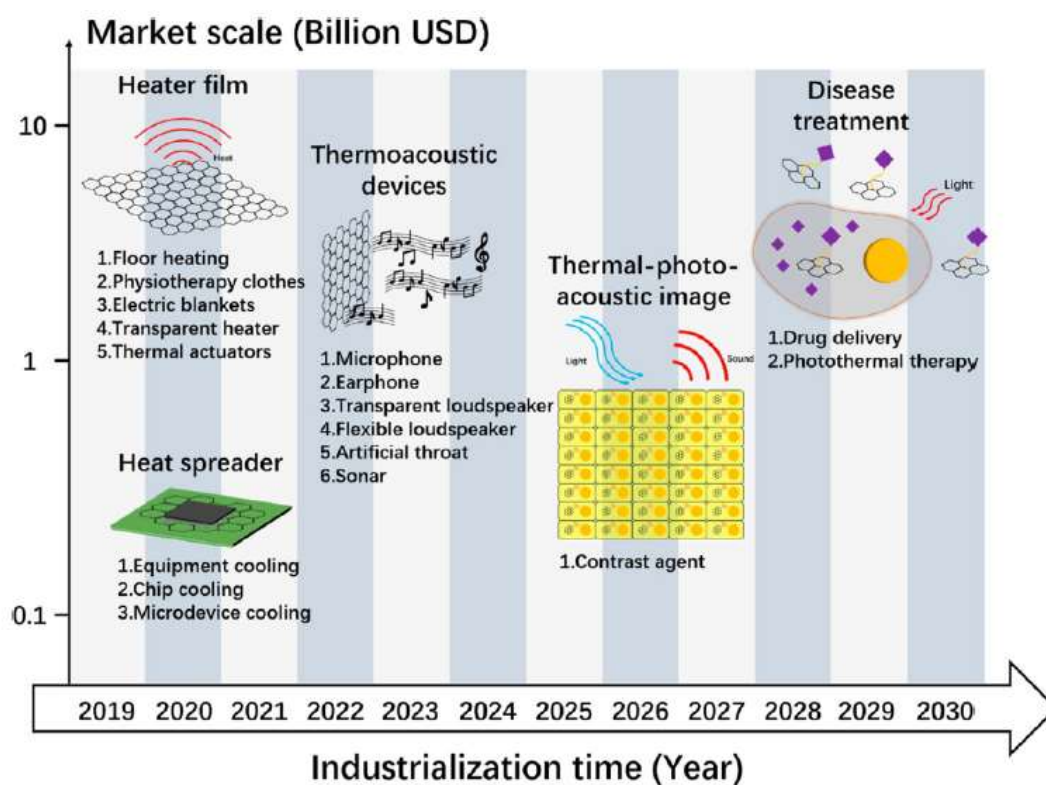


Fig. 2.7: Application forecast of graphene-based TA devices and their industrialization time from 2019 to 2030 (Qiao et al., 2020).

2.5 Concluding remarks

This chapter reviews the important concepts relevant to this thesis. This work focuses on the development of effective acoustic-based devices for the mitigation of noise and improvement of air quality. This work has two main objectives. The first is to investigate acoustic characteristics and noise mitigation strategies, and the second is to develop a contact-free particulate filtration device that uses acoustic waves. Aiming to realize high-efficiency acoustic-particle interactions, we also attempted to develop an innovative, small-scale, yet high-intensity TA sound emitter based on CNT and graphene.

Regarding the first objective, we investigated acoustic characteristics and noise mitigation strategies. In this regard, we proposed a preprocessing approach that includes a Bayesian inference-based DLM for raw-signal filtering, enabling integration with an adaptive ANC system. Several studies have exploited effective noise defensive strategies that include both passive and active approaches. Specific to ANC, many studies of the control algorithm problem have sought to develop complicated algorithms. They enhance the control algorithm performance but introduce computational burdens. Moreover, such intricate systems have inherently less utility in terms of their cost and the feasibility of their implementation. In a broadband time-varying feed-forward control system, Bayesian inference enables a fuzzy reference signal to be provided. Noise signal processing includes many parametric uncertainties. A statistical model can be used for signal parameter identification, and this method has the great potential in this respect. Another advantage is that a preprocessing system can be treated as a filter when using a Bayesian approach.

It is well known that ANC systems struggle to achieve broadband frequency noise attenuation, but decisions made by a preprocessing system while the ANC

system is in operation prevent interference from cumbersome disturbances from the environment, thereby acting as a filter to narrow the frequency bandwidth. Meanwhile, the inference from the noise model parameters can be identified with a “short-time” prediction. Many investigations have focused on the convergence speed and robustness of control algorithms but have ignored the complicated signal conversion in the secondary path of ANC algorithms. Hence, such a preprocessing system provides a promising method to enhance the efficiency of signal processing, which should lead to an improvement in the performance of the ANC system.

The establishment of an effective anti-noise device is another focus in noise control investigations. To this end, we developed a dual-function noise barrier with both active and passive control approaches as an anti-noise device. Considering the complexity of the spatial sound field in the construction noise issue, a hybrid control strategy is more advantageous. Conventional barriers are typically made of masonry, steel, concrete, and wood materials. Consider concrete as an example, using which simple construction and acceptable aesthetics are difficult to achieve (Hong and Jeon, 2014). In contrast, the use of low-cost, lightweight, and recyclable materials is preferred in the design of environmentally friendly noise barriers. Wood and rubber composite materials have shown great potential as candidates for advanced barrier design because they can increase the tensile modulus and mechanical strength. However, the use of passive noise barriers (e.g., aluminum, metal, timber, acrylic, or vegetation) alone is not effective in covering a wide range of frequency bandwidth, especially low-frequency components (Nilsson and Berglund, 2006); this is mostly because the acoustic wavelength of low-frequency noise is significantly longer than the thickness dimension of the barrier structures, which leads to an inefficient coupling effect. To address this challenging task, we used smart piezoelectric thin-film as a layer embedded inside the noise barrier made of recycled composite materials. A noise barrier made with such laminated structures allows the delivery of two defensive lines for wide-frequency noise attenuation.

To further investigate nonlinear acoustic effects and their potential application in the filtration of submicron particulates, we developed a prototype that enabled submicron particulate filtration at a lower sound intensity based on the concept of acoustic trapping. Relevant studies have demonstrated significant achievements in acoustic agglomeration at high SPLs (i.e., 130 to 140 dB). However, the requirement of high SPLs is a problem that could restrict the practical application of acoustic-driven techniques in construction sites. Hence, a study to improve the removal efficiency of airborne fine particles (especially submicron particles) at lower SPLs warrants attention. Moreover, the development of an innovative, small-scale, yet high-intensity acoustic wave device is crucial, as is addressing the requirements for high-efficiency acoustic-particle interaction mechanisms.

The achievement of TA manipulation requires a novel loudspeaker in lieu of conventional mechanical acoustic transducers. It requires novel flexible materials with a low heat capacity per unit area. A significant breakthrough was achieved with CNT-based loudspeakers (Xiao et al., 2008) that exhibited exemplary sound emitting properties, and single-walled CNT films were reported thereafter (Nasibulin et al., 2011). TA chips with CNT thin yarn arrays have been reported (Wei et al., 2013), and many materials have been identified for use as loudspeakers (Aliev et al., 2015). Recently, the main focus has turned to 2D materials such as graphene. For example, Tian et al. (2011a) and Suk et al. (2012) developed TA speakers with monolayer graphene which is nanometer in thickness. Newer designs for TA devices have shown broadband signal responses (Tong et al., 2017), demonstrating that high performance can be achieved with gap separation between the loudspeaker material and the substrate (Tong et al., 2015). We thus developed two prototypes, namely CNT-based and graphene-based TA devices and tested their acoustic performance.

CHAPTER 3

APPLICATION OF PROBABILISTIC

ASSESSMENT FOR NOISE SIGNAL PRE-

PROCESSING IN ACTIVE NOISE CONTROL

3.1 Introduction

Technical challenges of construction noise control are the loudness of construction machines and the difficulty of implementing noise-control measures. The deployment of barriers and enclosures is a common solution because of easier implementation and lower cost. Whilst barrier insulation provides fairly good high-frequency noise control, in machine operations low frequencies are dominant, and passive noise control has limited efficacy. Moreover, construction noise generated from various powered mechanical equipment with a broadband sound power spectrum is more complicated than other noise types, such air-borne noise can induce annoyance to human beings (Lee et al., 2015). To achieve an effective active noise attenuation, it is necessary to consider particularly annoying characteristics within construction noise, such as low-frequency sound components, intermittent noise, impulsive elements, and audible tones (DEFRA, 2006; Murphy and King, 2014).

To process such a time-varying noise signal, we attempted to investigate a feasible pre-processing model which enable to cooperate with ANC system for

construction noise signal attenuation. The use of PNC approaches is hardly to resist the effect of low-frequency noise, as the acoustic wavelength is significantly longer than the dimension of barrier structures to cause inefficient coupling. Hence, an active cancellation system is of particular interest for low-frequency noise. Based on the principle of superposition of sound, an anti-noise speaker is adopted to emit sound waves with the same amplitude but with inverted phase to reduce undesired noise. In this work, a pre-processing procedure, utilizing a Bayesian inference-based dynamic linear model (DLM), was used for raw-signal filtering before the ANC system. Bayesian forecasting is one of the most widely used approaches in statistical analysis. It has been adopted in multiple disciplines, such as econometrics, structural dynamics, and aerospace and mechanical engineering (Yuen, 2010), while DLM is a mathematical tool for time series analysis that can be used to describe a routine way of viewing a context that changes with time (Pole, 1994).

Bayesian inference is a pre-processing filter based on statistical characteristics and the control algorithm retains a least-mean-square (LMS) foundation. In a broadband time-varying feed-forward control system, Bayesian inference enables to provide a fuzzy reference signal. Noise signal processing contains many parametric uncertainties. A statistical model can be used for signal parameter identification, and this method possesses great potential on this aspect. For example, Bayesian inference was adopted to estimate frequency periodic information in a narrowband ANC system (Han et al., 2019). Prediction information contributed a lot to enhance the performance for a specific periodic noise signal. A Bayesian estimation approach (Ardekani et al., 2016) was adopted to recast the problem of online secondary path modeling in the form of a statistical inverse problem. A novel approach to active noise control based on Bayesian estimation theory (Ardekani et al., 2017) was investigated utilizing the statistical property for the optimization of parameters. Various structures and theories of dynamic models that incorporate Bayesian forecasting have also been reviewed (Pole, 1994; West and Harrison, 1997).

In real-life engineering applications, time-delay effects introduced by a multiple signal conversion in the secondary path of ANC algorithms such as analog-to-digital and digital-to-analog signal transitions are important factors that can directly affect the control algorithm performance. Plenty of investigations have focused on the convergence speed and robust of control algorithms, but the complicated signal conversion in the secondary path of ANC algorithms is still a problem. Hence, the use of data prediction based on a statistical strategy is an alternative way to enhance the efficiency of signal processing.

In this work, the prediction signal is a “*K-step estimation*” of the observation in a Bayesian approach. A time series model was adopted to simulate the observational signal characteristic as it enabled modeling of the dynamic behavior. The combination of the Bayesian approach and a time series model is a characteristic strategy for providing the reference signal for an ANC system ahead of time. To investigate the pre-processing system, a reference signal was acquired from in-situ measurement on a construction site, which contained environmental disturbance. The derivations of Bayesian inference for this signal, based on a DLM, are presented in Section 3.2. The pre-processing method is presented in Section 3.3. Simulations were performed using a conventional control algorithm FxLMS (Widrow and Stearns, 1985) and a new convex structure C-FxLMS/F algorithm (Song and Zhao, 2019). In addition, we used two cases to illustrate the possibility of three types of reference signals processing, i.e., (i) Gaussian noise; (ii) sinusoidal and Gaussian noise; and (iii) in-situ measurement data. We also discussed the convergence performance and complexity of the whole processing procedure in Section 3.4. Finally, we summarized the findings and limitations of this work and illustrated the future research direction in Section 3.5.

3.2 Research methodology

The proposed method is presented in the subsequent sections. For ANC

algorithms, time-delay effects, including controller computation and secondary source response, can restrict the control performance of adaptive filters. To provide early signal processing in an active control algorithm, Bayesian forecasting is utilized to predict the next few steps to reduce the time consumption of the complicated secondary path. Furthermore, Bayesian inference is incorporated with time series analysis to express the variation in the observation signal with time. The combination of Bayesian inference and a DLM can be considered as a pre-processing system to appropriately modify the complicated signal before it enters the active control algorithm, which partly reduced the time delay effects.

3.2.1 Dynamic linear model

DLMs form the basis of time series analysis methods. To describe a time series such as an observational signal, the general state-space function is utilized to express the current status using mathematical elements, e.g., values, gradients, curvature, etc. We focus on statements about the future development of a time series that is conditional on existing information. Hence, mathematical and statistical representations are the connection that provides communication between the forecaster, model and decision makers.

According to the information available in time cycle $(t-1)$, the guess value in time t for the parameter can be calculated through the model function. For the general normal DLM, it can be characterized by a quadruple (Pole, 1994; West and Harrison, 1997; Lipowsky et al., 2010; Lai and Zhang, 2019) as follows:

$$\{F_t, G_t, V_t, W_t\} \quad (3.1)$$

where F_t is a known $(p \times r)$ matrix that acts as a regression matrix of known values

of independent variables, G_t is the known ($p \times p$) system or state evolution transfer matrix, and V_t and W_t are the observational variance matrix and evolution variance, respectively.

The equations of the model can be expressed as (Pole, 1994; West and Harrison, 1997; Zhang et al., 2018c; Wang and Ni, 2020c; Wang et al., 2020d):

$$\text{Observation Equation: } Y_t = F_t^T \cdot \theta_t + v_t, v_t \sim N[0, V_t] \quad (3.2)$$

$$\text{System Equation: } \theta_t = G_t \cdot \theta_{t-1} + w_t, w_t \sim [0, W_t]$$

$$\theta_t = \begin{pmatrix} \alpha_t \\ \beta_t \end{pmatrix}, F_t = \begin{pmatrix} 1 \\ 0 \end{pmatrix}, G_t = \begin{pmatrix} 1 & 1 \\ 0 & 1 \end{pmatrix} \quad (3.3)$$

$$W_t = \begin{pmatrix} \sigma_{level}^2 & 0 \\ 0 & \sigma_{trend}^2 \end{pmatrix}, V_t = \sigma_{observation}^2$$

where the guess vector θ_t contains two elements, α_t and β_t , which denote the current level of parameter value and gradient, respectively. v_t and w_t are two independent Gaussian random vectors with mean zero and unknown covariance matrices V_t and W_t . The evolution error-free case is assumed with $W_t = 0$ for all t so that $\theta_t = G_t \cdot \theta_{t-1}$.

3.2.2 Bayesian forecasting

Bayesian forecasting proceeds according to the known information as its principle of management. Routine forecasting from a model is used directly, while the occurrence of non-routine events alters the parameters of the model to reflect the circumstances. Based on Bayes' rule (Pole, 1994; Yuen, 2010), the prior density provides concise and coherent transferred information to the posterior probability of a model parameter. With a time-varying observed process, this can be formed using a

probability density function based on the assumption of Gaussian distribution. It is noted that Bayesian method is available for all distributional assumptions.

The observational distribution with density can be described as (Pole, 1994)

$$p(Y_t | \mu_t, D_{t-1}) \quad (3.4)$$

and the prior for μ_t given D_{t-1} has the density,

$$p(\mu_t | D_{t-1}) \quad (3.5)$$

According to Bayes' theorem (Lipowsky et al., 2010; Yuen, 2010), the posterior for μ_t can be obtained:

$$\begin{aligned} p(\mu_t | D_t) &= p(\mu_t | D_{t-1}, Y_t) \\ &= \frac{p(\mu_t | D_{t-1}) p(Y_t | \mu_t, D_{t-1})}{p(Y_t | D_{t-1})} \end{aligned} \quad (3.6)$$

The notation of the guess vector θ_t is given by (Pole, 1994; West and Harrison, 1997; Lipowsky et al., 2010; Zhang et al., 2018c; Lai and Zhang, 2019):

$$(\theta_t | D_t) \sim N[m_t, C_t] \text{ with } D_t = Y_1, Y_2, \dots, Y_t \quad (3.7)$$

where $\{D_t = Y_1, Y_2, \dots, Y_t\}$ are the observations. On the basis of these, Bayes' rule provides a formula for the probability estimation of the next time step, which represents the state space vector θ_t that obeys the Gaussian distribution. The function $\{D_t = Y_1, Y_2, \dots, Y_t\}$ expresses the known information at the time cycle t , and m_t and C_t are the mean value and variance, respectively.

The Bayesian updating approach is utilized for signal filtering and short-term forecasting of noise signal inference. It is worth noting that the noise signals processed must be relatively stable and regular construction noise patterns, such as automobile engines or turbine motors. The combination of Bayesian inference and a DLM can provide a “*forecast-observation-analysis*” cycle. The logic of Bayesian inference equations is presented in Eqs. (3.8)–(3.11), the derivations of these can be referred to the works (Pole, 1994; West and Harrison, 1997).

Given that the state space function at time step (t) is

$$(\theta_t | D_t) \sim N[m_t, C_t] \quad (3.8)$$

where $\{D_t = Y_1, Y_2, \dots, Y_t\}$ denotes the state of knowledge at time t . Prior information on the state space function for the next time step ($t+1$) is summarized as follows

$$(\theta_{t+1} | D_t) \sim N[a_{t+1}, R_{t+1}] \quad (3.9)$$

According to the prior information and observation equation (i.e., Eq. (3.2)), Y_{t+1} can be obtained in the following form

$$(Y_{t+1} | D_t) \sim N[f_{t+1}, Q_{t+1}] \quad (3.10)$$

where the means and variances are given by (Pole, 1994):

$$\begin{aligned} a_{t+1} &= G_{t+1} \cdot m_t \\ f_{t+1} &= F_{t+1}^T \cdot a_{t+1} \\ R_{t+1} &= G_{t+1} C_t G_{t+1}^T + W_{t+1} \\ Q_{t+1} &= F_{t+1}^T R_{t+1} F_{t+1} + V_{t+1} \end{aligned} \quad (3.11)$$

If a forecast of the next K time steps is of interest, the K -step forecasting equations are given by (Pole, 1994). For a constant observational factor $F_t = F = \begin{pmatrix} 1 \\ 0 \end{pmatrix}$ and evolution factor $G_t = G = \begin{pmatrix} 1 & 1 \\ 0 & 1 \end{pmatrix}$, forecasting several steps ahead requires the prior information to be projected into the future through repeated application of the system equation. Given the prior for time $(t+1)$, the implied prior for time $(t+2)$ from the same standpoint, with no additional information, is $p(\theta_{t+1} | D_t)$. This prior is obtained by applying Eqs. (3.12) and (3.13) below:

$$(\theta_{t+K} | D_t) \sim N[a_t(K), R_t(K)] \quad (3.12)$$

$$(Y_{t+K} | D_t) \sim N[f_t(K), Q_t(K)] \quad (3.13)$$

with the following parameters:

$$\begin{aligned} a_t(K) &= G^{K-1} \cdot a_{t+1} \\ f_t(K) &= F_{t+K}^T \cdot a_t(K) \\ R_t(K) &= G^{K-1} R_{t+1} (G^{K-1})' + \sum_{j=2}^K G^{K-j} W_{t+j} (G^{K-j})' \\ Q_{t+K} &= F_{t+K}^T R_t(K) F_{t+K} + V_{t+K} \end{aligned} \quad (3.14)$$

The state vector θ_t , which comprises n elements, is extracted to enable identification of the time series. Accordingly, the mean response function μ_t affords knowledge of the state vector. The μ_t can be expressed as follows (West and Harrison, 1997).

$$\mu_t = T \cdot \theta_t \quad (3.15)$$

$$T = \begin{pmatrix} F_t^T \\ F_t^T \cdot G_t \\ \dots \\ F_t^T \cdot G_t^{n-1} \end{pmatrix} \quad (3.16)$$

$$\theta_t = T^{-1} \cdot \mu_t$$

where the matrix T must have a full rank n to satisfy the requirements of observability in model design.

Consider the observability and the forecasting function, for a time-domain DLM, the mean response function μ_{t+k} defines the implied form of the time series in model design where the K value is the step ahead index. With the state vector and evolution error $\theta_t = \begin{pmatrix} \alpha_t \\ \beta_t \end{pmatrix}$ and $w_t = \begin{pmatrix} w_{t1} \\ w_{t2} \end{pmatrix}$, respectively, we have

$$\begin{aligned} Y_t &= \alpha_t + v_t \\ \alpha_t &= \alpha_{t-1} + \beta_{t-1} + w_{t1} \\ \beta_t &= \beta_{t-1} + w_{t2} \end{aligned} \quad (3.17)$$

The expectation of state space at time cycle $(t-1)$ is given as $E[\theta_t | D_t] = m_t$. With

$m_t = \begin{pmatrix} m_{t1} \\ m_{t2} \end{pmatrix}$, the forecasting function is $f_t(K) = (m_{t1} + Km_{t2})$.

3.2.3 Adaptive FxLMS control algorithm

The block diagram of an adaptive active single-channel feed-forward ANC system is shown in Fig. 3.1 (Kuo, 1996). The primary path is denoted by the transfer function $P(z)$, and the secondary path is $S(z)$. $W(z)$ is the ANC controller weight coefficient, which is updated through the process. Variable $y(n)$ is the adaptive filter response and $e(n)$ is the residual error. $\hat{S}(z)$ is the estimation of the secondary path that can be obtained by adaptive filtering using either offline or online modeling.

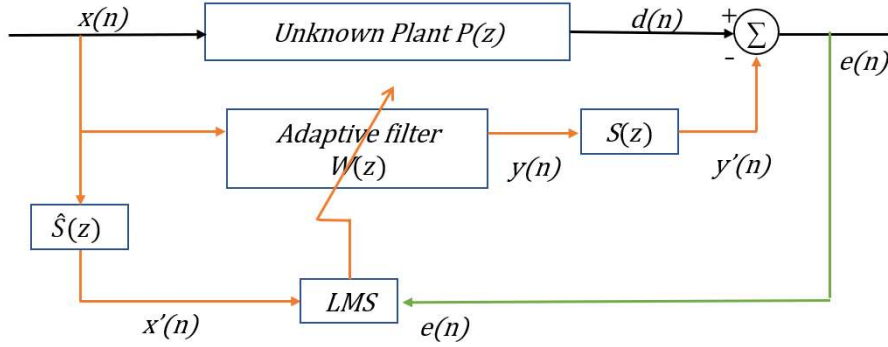


Fig. 3.1: Block diagram of a conventional FxLMS algorithm (Kuo, 1995).

The adaptive filter output signal $y(n)$ is given by

$$y(n) = w^T(n)x(n) \quad (3.18)$$

where $x(n) = [x(n), x(n-1), \dots, x(n-L+1)]^T$ is the reference signal vector and $w(n) = [w_0(n), w_1(n), \dots, w_{L-1}(n)]^T$ is the weighted vector of the adaptive filter. The expression for the residual error $e(n)$ is computed as follows:

$$e(n) = d(n) - y'(n) \quad (3.19)$$

where $d(n) = x(n) * p(n)$ represents the primary noise signal, $y'(n) = y(n) * s(n)$ is the secondary cancelling signal, and $s(n)$ is the impulse response of $S(z)$. The symbol “*” denotes the discrete convolution operator. The corresponding weighting equation can be updated by:

$$w(n+1) = w(n) + \mu x'(n)e(n) \quad (3.20)$$

where μ is the fixed step-size value.

To improve the noise reduction performance of a single-channel feed-forward ANC system, the filtered-x least-mean square/fourth (FxLMS/F) algorithm was introduced (Widrow and Stearns, 1985). Convex combination structures based on an LMS algorithm (Arenas-Garcia et al., 2006; Ni and Li, 2010) were developed to improve the filter performance. After this, a combination of a convex filter structure and an FxLMS/F algorithm was developed to solve the complicated parameter-setting problem and improve the convergence rate (Song and Zhao, 2019).

In general, the cost function of the LMS/F algorithm is given by (Lim and Harris, 1997; Li et al., 2016)

$$J(n) = \frac{1}{2} e^2(n) - \frac{1}{2} \phi \ln(e^2(n) + \phi) \quad (3.21)$$

where ϕ is a positive threshold parameter that controls the convergence speed and the noise reduction performance. The updated equation for FxLMS/F is different from the FxLMS algorithm, as shown below

$$\begin{aligned}
 w(n+1) &= w(n) + \mu \frac{e^3(n)}{e^2(n) + \phi} [x(n) * s(n)] \\
 &= w(n) + \frac{\mu}{1 + \phi / e^2(n)} e(n) x'(n)
 \end{aligned}
 \tag{3.22}$$

The block diagram for the convex combination with an FxLMS/F algorithm is shown in Fig. 3.2 (Song and Zhao, 2019). The convex combination is utilized for improving the convergence rate with two adaptive filters.

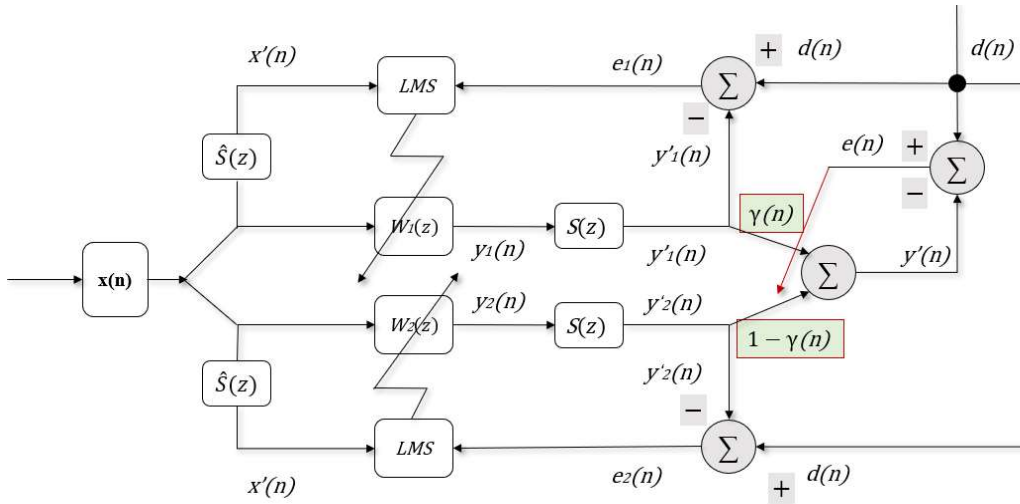


Fig. 3.2: Block diagram of a convex combination of adaptive filters based on an FxLMS/F algorithm (Song and Zhao, 2019).

The output of the overall combined filter is given by the following equation

$$y'(n) = \gamma(n)y_1'(n) + (1 - \gamma(n))y_2'(n)
 \tag{3.23}$$

where $\gamma(n)$ is a mixing coefficient ranging from 0 to 1. This coefficient is used to control the combination of two adaptive filters at each signal iteration, and its explicit form is shown via a sigmoid activation function (Arenas-Garcia et al., 2006):

$$\gamma(n) = \frac{1}{1 + e^{-A(n)}} \quad (3.24)$$

where $A(n)$ is an inner adaptation according to the gradient descent method. It ranges from $[-\sigma^+, \sigma^+]$ where σ^+ is a parameter to be determined by the control algorithm.

The explicit form is given by (George and Panda, 2012; Al Omour et al., 2016):

$$\begin{aligned} A(n+1) &= A(n) - \mu_a \frac{\partial J(n)}{\partial A(n)} \\ &= A(n) + \mu_a \left[\frac{e^3(n)}{e^2(n) + \phi} \right] (y_1'(n) - y_2'(n)\gamma(n)(1 - \gamma(n))) \end{aligned} \quad (3.25)$$

Then, the updated equation for the convex filter structure combined with an FxLMS/F algorithm can be obtained as below

$$w(n) = \gamma(n)w_1(n) + (1 - \gamma(n))w_2(n) \quad (3.26)$$

In the convex filter structure combined with an FxLMS/F algorithm (i.e., C-FxLMS/F), the filter performance for active control revealed enhancement in three case studies in terms of the Gaussian input signal, sinusoidal wave input signal and impulse noise with a symmetric alpha distribution signal (Song and Zhao, 2019). In terms of signal processing, the time-domain algorithm contains instabilities under an unpredictable disturbance. The proposed system with pretreatment procedures and Bayesian inference processed via a C-FxLMS/F algorithm is illustrated in the next section. The reference signal was derived from the in-situ measurement data.

A pretreatment procedure is used to enable reference signal processing. An ANC

system is utilized as a secondary source to highlight the desired signal, which means that the response time of the path is an important factor. The response time of the secondary path is also considered as a time-delay effect in an ANC system, which directly affects the converged performance of a control system as it requires complicated computation and conversion of signal form. A pre-processing system based on a characteristic strategy and having a low computational loss is required not only to reduce the time-delay compromise, but also to prevent the sudden disturbance of the reference signal.

3.3 Proposed ANC system with pretreatment process

In this section, the use of the Bayesian inference approach based on DLM as the pre-processing procedure before the ANC structure is described, as a way to solve the abovementioned problems. Given that the reference signal is acquired from an in-situ microphone measurement, the observation signal was modeled with DLM. K-step prediction data can be calculated ahead of the current time. The inference signal replaced the reference signal in the ANC system. In this study, we attempted to pre-process the inference signal based on the measurement data and treated it as a reference signal for adaptive prediction in ANC algorithms. In Eq. (3.2), the observation (measurement) equation contains the state parameter (θ_t) and the unknown variable (v_t). To investigate the dynamic change of the whole dataset, we assumed that the random noise (i.e., v_t) still obeys a normal distribution. With a smaller value of v_t , the estimation of the posterior parameters relies more heavily on the observation data. The posterior parameters can be updated via the inference loop given in Eqs. (3.8)–(3.11) as time goes on.

To investigate the performance of noise reduction, a simple diagram is presented for illustration in Fig. 3.3. To determine the learning process of this control algorithm, both average noise reduction (ANR) (Song and Zhao, 2019) and mean noise reduction

(MNR) indices are used. Furthermore, the performance of noise reduction can be evaluated by the power spectrum of noise residual (Bouchard and Quednau, 2000; Bouchard and Yu, 2001).

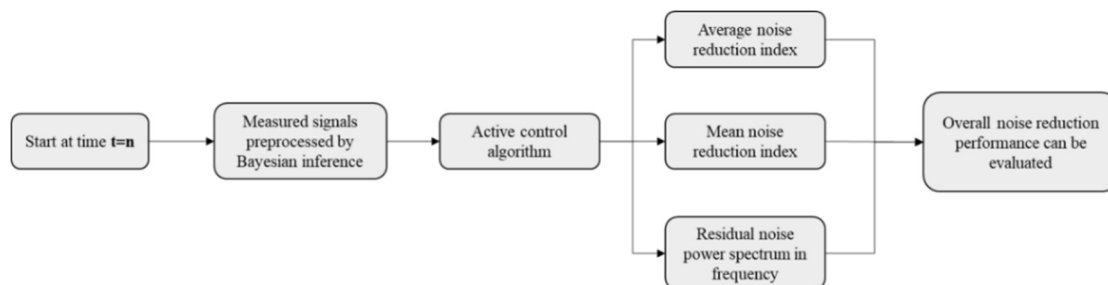


Fig. 3.3: Evaluation of noise reduction performance.

The block diagrams of the active control algorithms (conventional FxLMS algorithm and the C-FxLMS/F algorithm) are illustrated in Figs. 3.4 and 3.5, respectively. The measured noise signals from in-situ measurement of construction machines were processed by the proposed technique as shown in Fig. 3.6. It contains two processing loops, Bayesian inference loop for online measured data pre-processing and secondary source generation loop. In the pre-processing procedure, a second-order DLM was formulated to model the noise signal series. Then, the Bayesian forecasting approach was applied to conduct a K -step prediction prior to the next K -step observation as the reference signal for the ANC system, with the aim of reducing the time-delay effects of secondary source production. The noise signal acquired from in-situ measurement of machinery such as concrete mixers and road crushers were used as the primary source. The results of various simulations are conducted to validate the effectiveness of the proposed method for the primary noise attenuation. The performance evaluations were carried out using the following averaged noise reduction index (Song and Zhao, 2019)

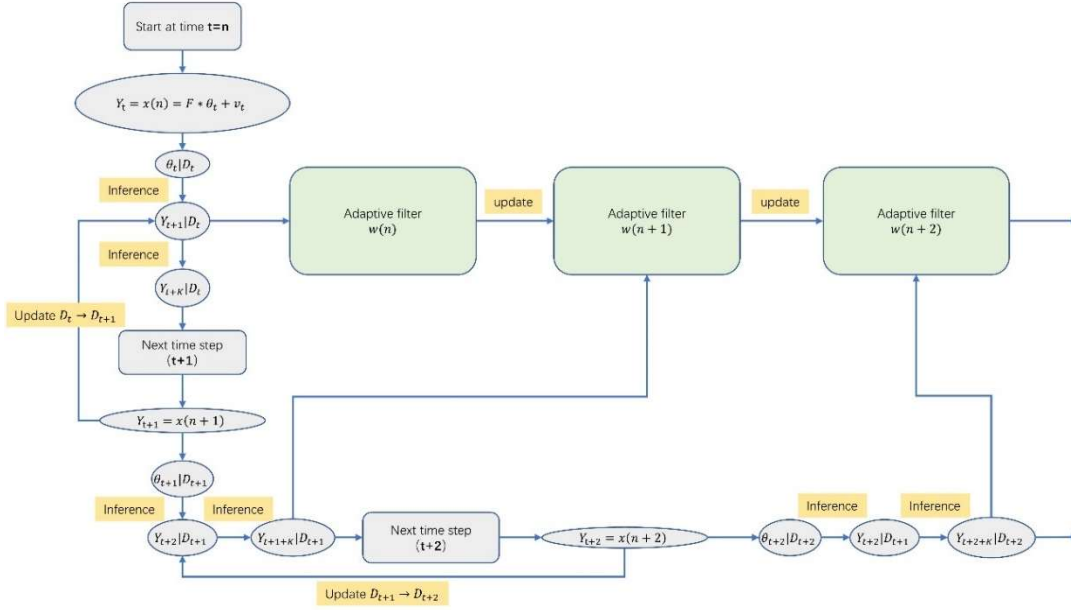


Fig. 3.6: Flow chart of the proposed pre-processing system.

The convergence performance of various algorithms is compared on the basis of mean noise reduction, which is defined as the ratio of average residual error signal power and average disturbance signal power (Bouchard and Quednau, 2000; Bouchard and Yu, 2001)

$$MNR(n) = 10 \log \left(\frac{E[e^2(n)]}{E[d^2(n)]} \right) \text{ (dB)} \quad (3.28)$$

The ANR and MNR curves for the various methods discussed here are presented in sub-subsequent section. To evaluate the performance of the proposed system, the secondary path $S(z)$ and its estimate $\hat{S}(z)$ were assumed to be the same. The adaptive filters were designed with a length of $L = L' = L'' = 128$, where the primary path $P(z)$ and secondary path $S(z)$ were modeled by a finite impulse response filter of length $N=256$. The primary and secondary paths can be estimated in the in-house laboratory. White noise signals were utilized as excitations. Then, the characteristics of the

transfer functions and their impulse responses can be investigated using two fixed position microphones. According to the impulse responses, the corresponding frequency and phase responses are shown in Fig. 3.7.

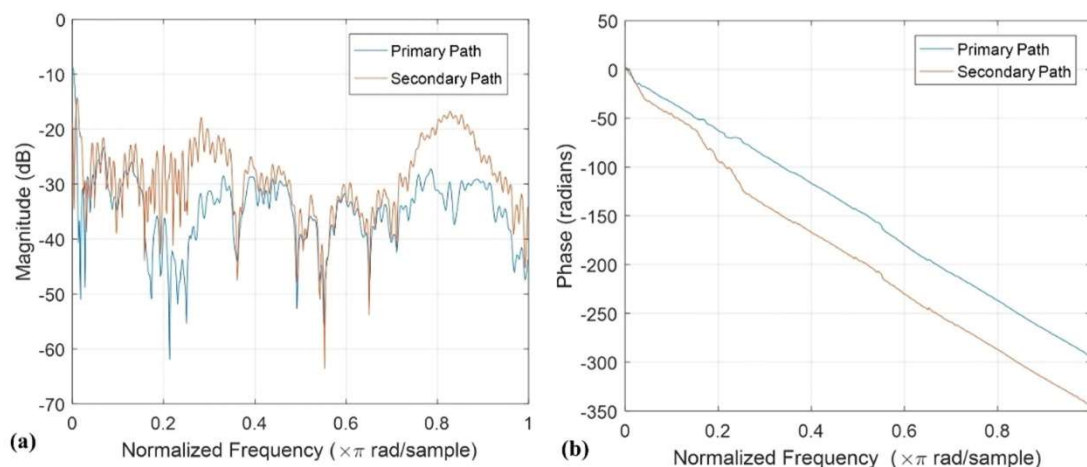


Fig. 3.7: Frequency responses of acoustic paths used in computer simulations. (a) Magnitude response and (b) Phase response.

3.4 Illustrative case studies

3.4.1 In-situ noise signal recording

In this study, the reference data were obtained from in-situ noise field measurement. Fig. 3.8 shows the measurement setup and data. The audio recordings of construction machines are registered by acoustic instruments including a binaural microphone (*Type B&K 4189*), a recorder (*Sony DAT Recorder*) and a microphone amplifier (*ENDEVCO 4416B*). According to the standardized procedures for measuring exterior noise levels of construction machines (SAE, 1976), the height of the microphone was set to 1.2 m from the ground.

The sampling rate of the data was 44,100 Hz. The sound pressure signals were stored by a recording tape and re-acquired using an analog-to-digital card in the

in-house laboratory. For the auditory experiments, 1-min audio samples of construction machine were excerpted from the recordings. The amplitude of digital signals represents the voltage of output signals. The processing signals below, i.e., Bayesian inference, are based on these raw signals that are plotted in Fig. 3.8(c).

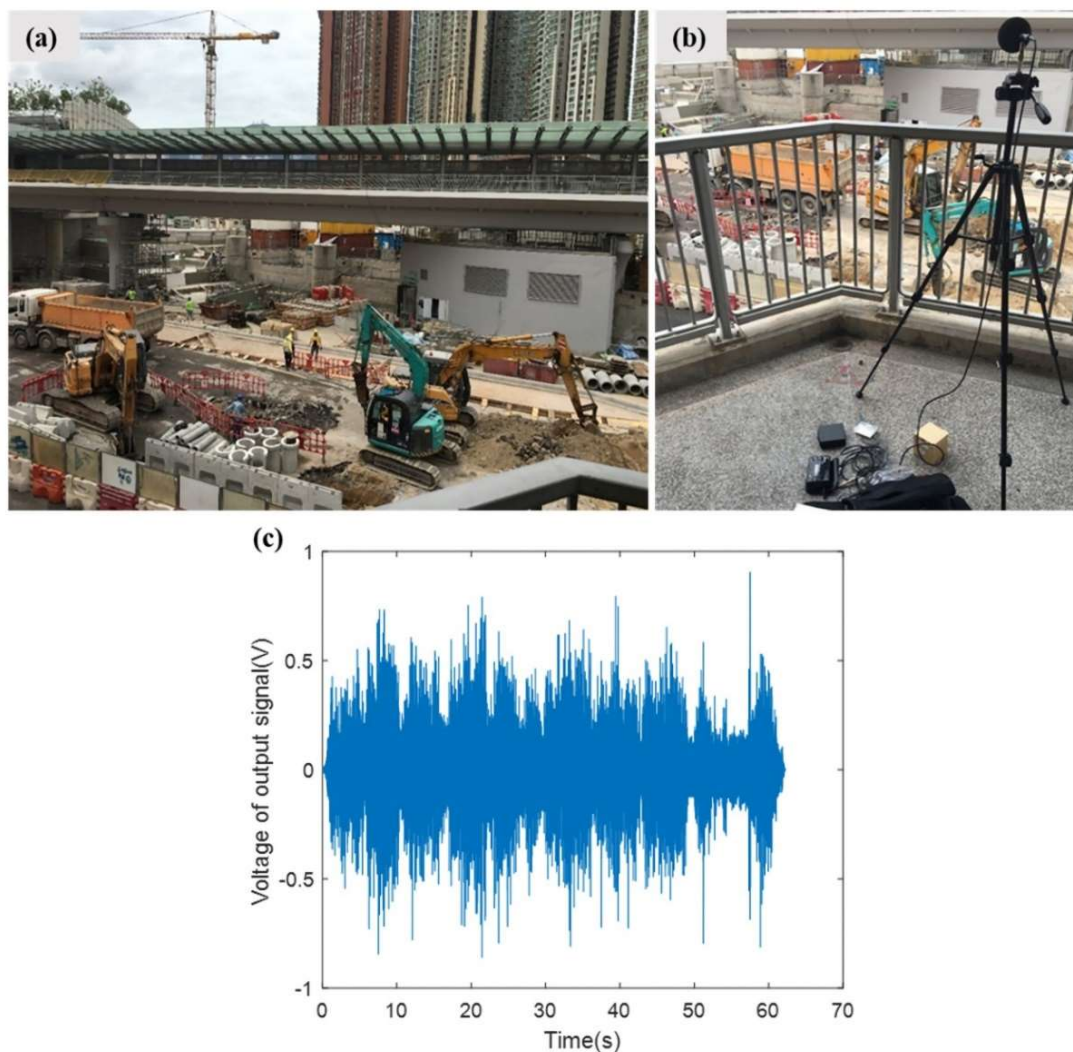


Fig. 3.8: (a) Digging machine and transportation vehicles at a construction site near Austin MTR Station; (b) Noise measurement equipment with microphone, accelerometer, recorder and amplifier, and (c) Time-history of raw data.

3.4.2 Case 1: Conventional FxLMS algorithm with Bayesian inference

The various simulation parameters used in the case were the conventional FxLMS algorithm with $\mu=0.01$. The Bayesian inference approach was applied to conduct K -step predictions prior to the current time. In the DLM, the parameter setting was as below:

$$F_t = \begin{pmatrix} 1 \\ 0 \end{pmatrix}, \quad G_t = \begin{pmatrix} 1 & 1 \\ 0 & 1 \end{pmatrix}, \quad K = 5 \quad (3.29)$$

In Fig. 3.9, the grey area depicts the predicted distribution at each iteration when $K = 5$. This means that according to the current observational data, the next five steps of data can be obtained via a time series model. The predicted information was presented as a distribution with a mean value and standard deviations. All of the original signals can be covered within the grey area at a 90% confidence interval. Next, the fuzzy prediction data were obtained as a reference signal for ANC control algorithm processing.

In an active control system, the reference signal is important as a reference in the secondary control path. However, most research has focused on the enhancement of the control algorithm and ignored the reference signal impact. The fuzzy prediction signal may not be identical to the observational data, but this will not affect ANC system performance. Moreover, the advantage of Bayesian inference is obvious: it considers the “*time-delay*” effect on the secondary path. In Fig. 3.9, the blue line is almost coincident with the middle of the grey area, which means that when $K=5$ the prediction data are almost the same as the observational data. With the increase in K , the prediction data contain greater uncertainty. Moreover, a greater computational effort would be required in the pre-processing step.

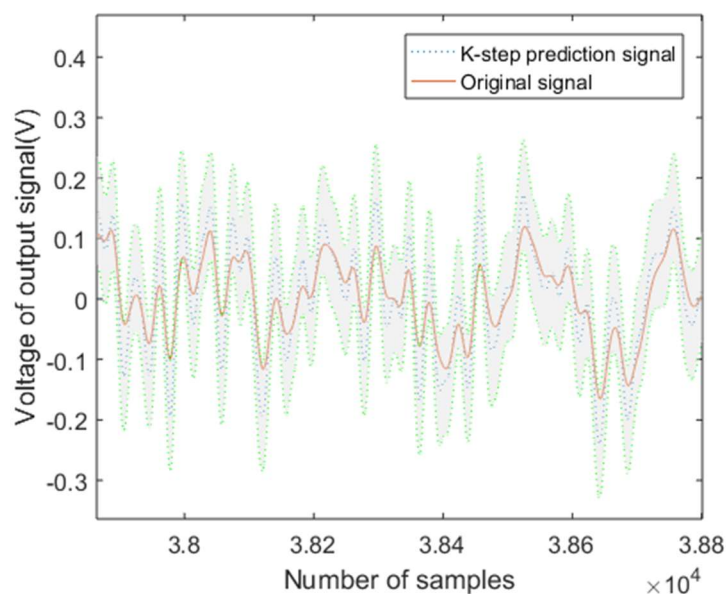


Fig. 3.9: Comparison of the inference and observation signals (Inference signal is denoted by a distribution with $K=5$).

The time-domain signal attenuation results with and without the use of the Bayesian inference pretreatment procedure are presented in Fig. 3.10. From time-domain analysis, it is clear that both systems can be converged. The convergence curves via the ANR index learning process with and without Bayesian inference are presented in Fig. 3.11, and the MNR learning curves are shown in Fig. 3.12; from these data it can be observed that systems using Bayesian inference achieved a higher convergence speed. Unless specified in the context, the term “*without prediction*” refers to the original signals measured from the construction site.

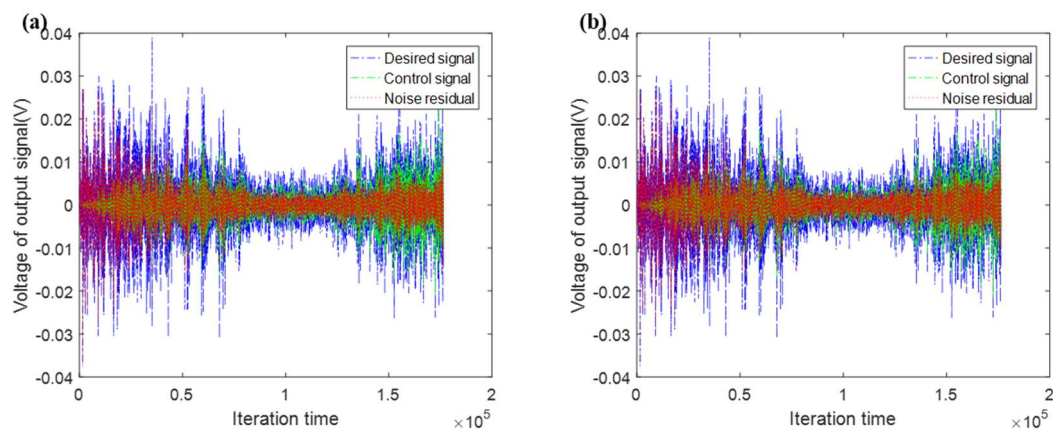


Fig. 3.10: Time domain signals (a) with and (b) without Bayesian inference: Desired signal (blue line); Control signal (green line); Residual signal (red line).

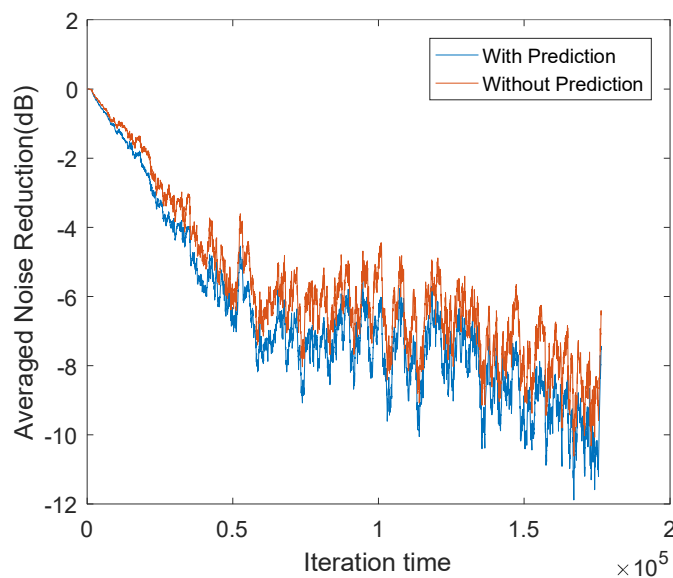


Fig. 3.11: Evolution of learning curves for processing in-situ measurement data based on the ANR index.

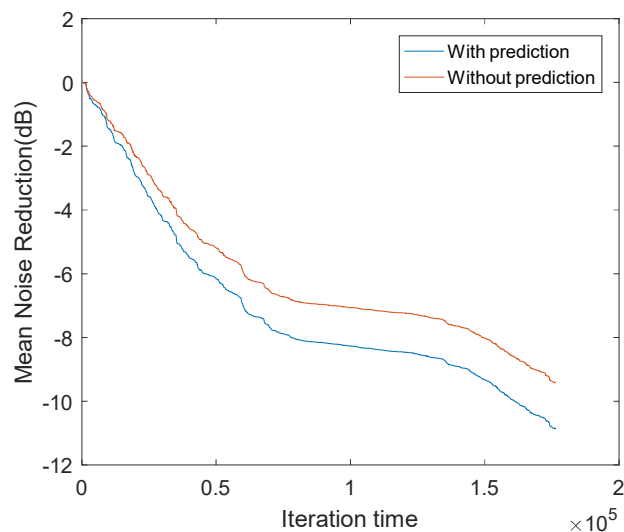


Fig. 3.12: Evolution of learning curves for processing in-situ measurement data based on the MNR index.

The same noise reduction performance with and without Bayesian inference is shown in Fig. 3.13. The unit of the time-domain signals was transformed as a sound pressure (Pa). Compared with the reference pressure ($P_{ref} = 20 \times 10^{-6}$ Pa), the signals were converted to a frequency domain via Welch's power spectral density estimation. The orange line representing data acquired using Bayesian inference and the yellow line data representing data acquired without Bayesian inference are coincident. The fact that our proposed system achieved a similar noise reduction performance as the conventional algorithm under the same parameter setting revealed obvious advantages can be realized. Primarily, it means that time-delay effects on the secondary path can be considered in the control algorithm; in addition, determining the convergence speed with the prediction data as a reference signal can give better results.

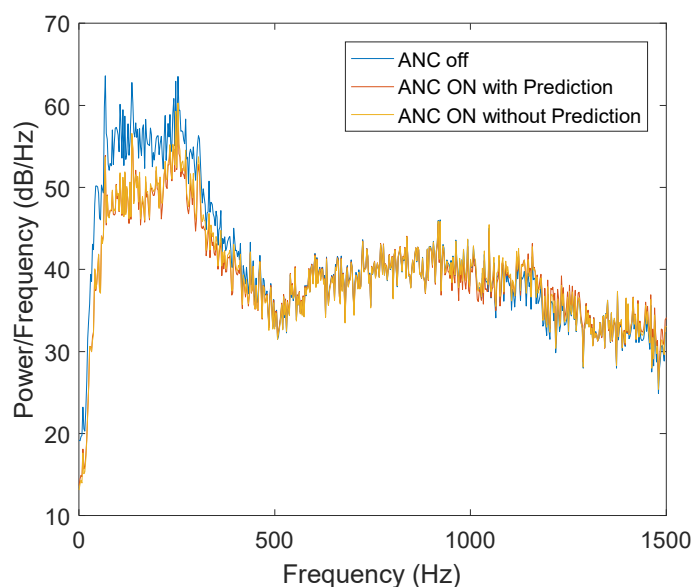


Fig. 3.13: Performance of the proposed ANC system (FxLMS algorithm) with or without Bayesian approach as a pre-processing procedure.

Figures 3.14–3.16 present the K value impact of the proposed ANC system. With K value increasing from five to eight steps, the convergence performance is better shown in the ANR index and the MNR index. Fig. 3.16 shows the noise attenuation performance in the frequency spectrum. It is obvious that the K value has less effect on the final noise reduction. In this figure, we also observe that the results with and without the use of the Bayesian inference pretreatment procedure are almost identical, thereby verifying the correctness of the proposed pretreatment procedure. By comparing the data without ANC processing (i.e., “ANC off”), the performance of the ANC system (with and without prediction) is dominant at the low-frequency region (\approx below 500 Hz), this is mainly due to the effect of the FxLMS algorithm.

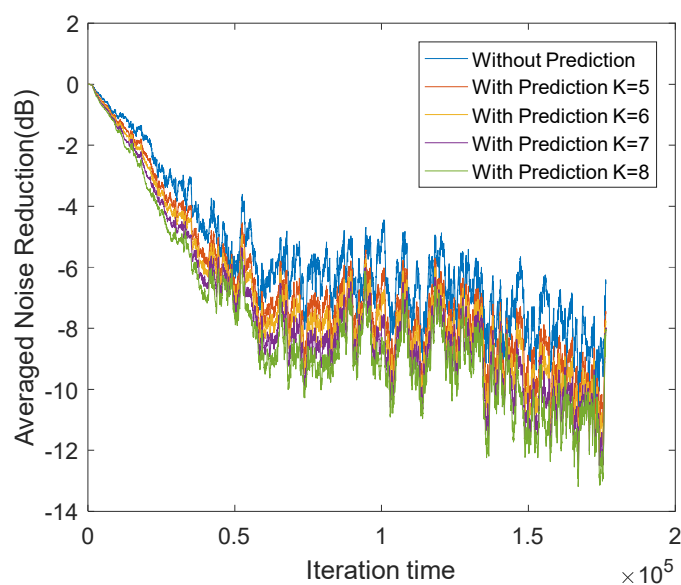


Fig. 3.14: Evolution of learning curves for processing in-situ measurement data based on the ANR index.

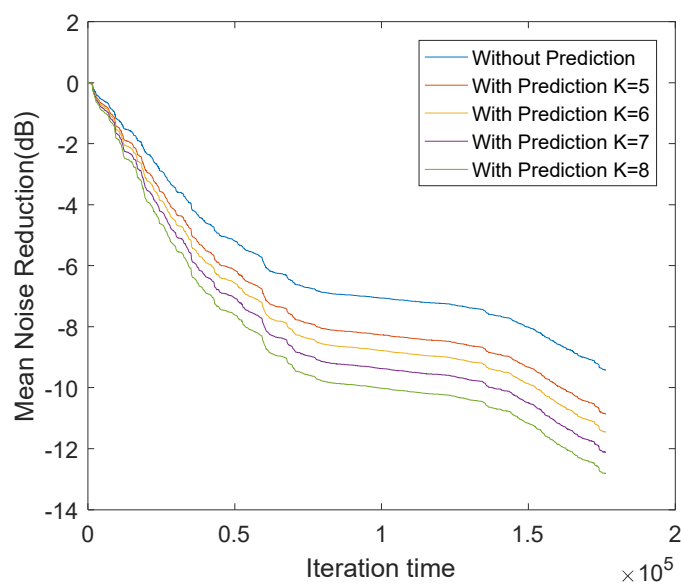


Fig. 3.15: Evolution of learning curves for processing in-situ measurement data. based on the MNR index.

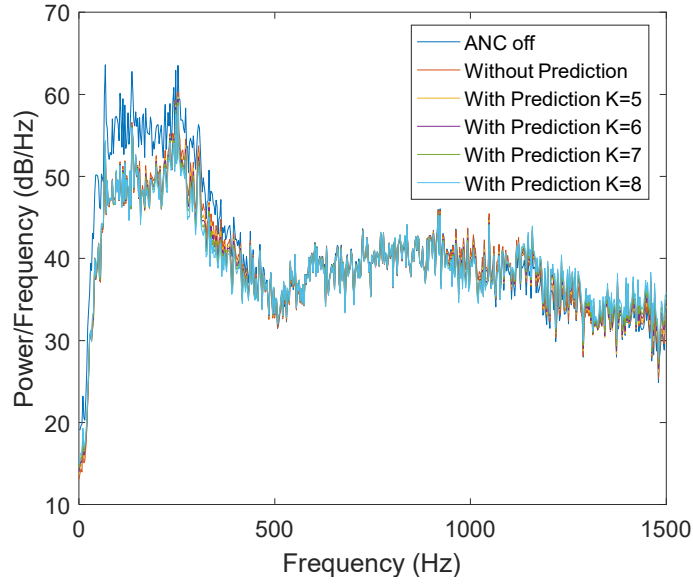


Fig. 3.16: Performance of the proposed ANC system (conventional FxLMS algorithm combined with Bayesian approach) with various K-step values.

3.4.3 Case 2: C-FxLMS/F algorithm with Bayesian inference

In a time-domain system, a conventional FxLMS algorithm contains distinct restrictions, and thus many researchers have investigated the time-domain control algorithm modification. The C-FxLMS/F algorithm was proposed (Song and Zhao, 2019); it utilized two adaptive filters for convex structure. The FxLMS/F algorithm was adopted as the cost function to reduce the limitations of the FxLMS algorithm. To investigate the practical effects of the Bayesian approach in this case, the C-FxLMS/F algorithm was utilized as a control algorithm. The reference signals were from in-situ measurement noise, as shown in Fig. 3.8. The various simulation parameters used in the case were (Song and Zhao, 2019):

$$\mu_a = 10, \mu_1 = 0.05, \mu_2 = 0.003, \Phi = 0.0001, \lambda_0 = 0, A_0 = 0, \sigma^+ = 4 \quad (3.30)$$

The Bayesian inference approach was applied to conduct K -step prediction information prior to the study. In the dynamic linear model, the parameter settings were the same as presented in Eq. (3.29).

In Fig. 3.17, the grey area shows the predicted distribution at each iteration where K is 5. By comparing the orange line and grey area, it can be seen that all the original signals can be covered by the grey area at a 90% confidence interval. The fuzzy prediction data were thus used as a reference signal for the ANC control-algorithm processing.

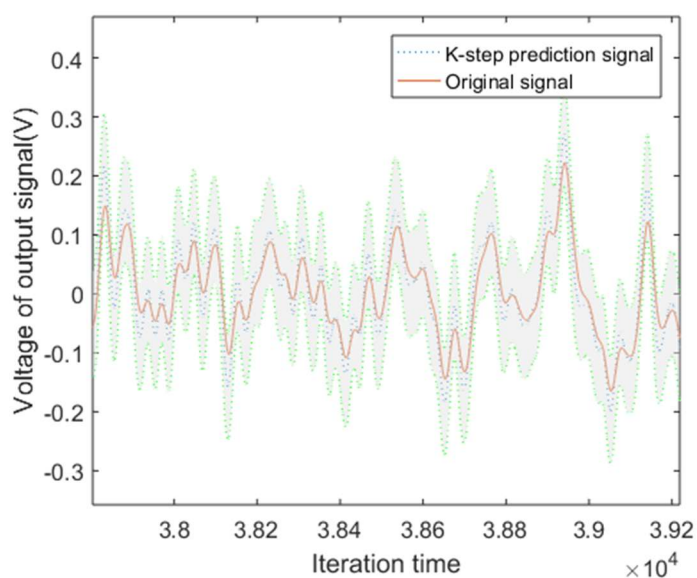


Fig. 3.17: Comparison of the inference and measurement signals (Inference signal is denoted by a distribution with $K=5$).

The time-domain signal attenuation results, with and without a Bayesian inference pretreatment procedure, are presented in Fig. 3.18. From time-domain analysis, it is obvious that both systems can be converged. The convergence curves via the ANR learning process with and without Bayesian inference are presented in Fig. 3.19, and the MNR learning curves are shown in Fig. 3.20; this reveals that the system treated with Bayesian inference can achieve a higher convergence speed. The

same noise reduction achievement with and without Bayesian inference is shown in Fig. 3.21.

To evaluate the parameter effects in the ANC system, the comparison results are shown in Figs. 3.22–3.24. It can be seen that with increasing K value, the convergence performance is faster, as illustrated in the ANR and MNR indexes. The noise reduction performance in the frequency spectrum coincides with the performance of the ANC system without Bayesian inference, as shown in Fig. 3.24. In this figure, the results with and without the use of the Bayesian inference pretreatment procedure are almost identical to each other, this shows again the correctness of the proposed pretreatment procedure. By comparing the data without ANC processing (i.e., “ANC off”), the performance of the ANC system (with and without prediction) is still pronounced at the low-frequency region (\approx below 500 Hz), this is mainly due to the effect of the C-FxLMS/F algorithm.

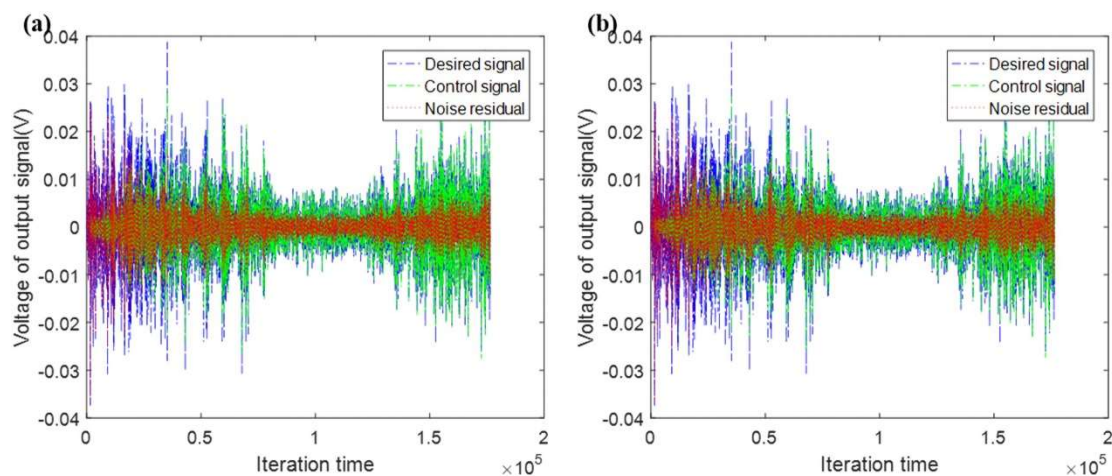


Fig. 3.18: Time domain signals (a) with and (b) without Bayesian inference: Desired signal (blue line); Control signal (green line); Residual signal (red line).

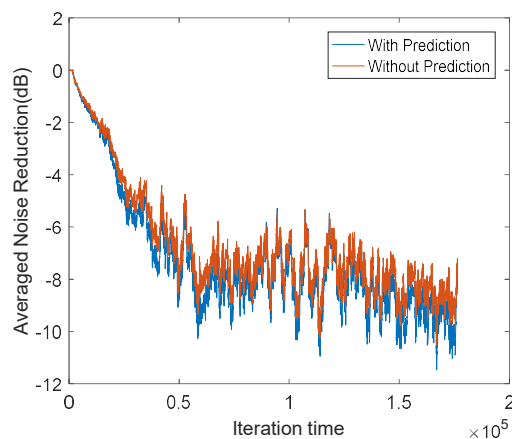


Fig. 3.19: Evolution of learning curves for processing in-situ measurement data based on the ANR index.

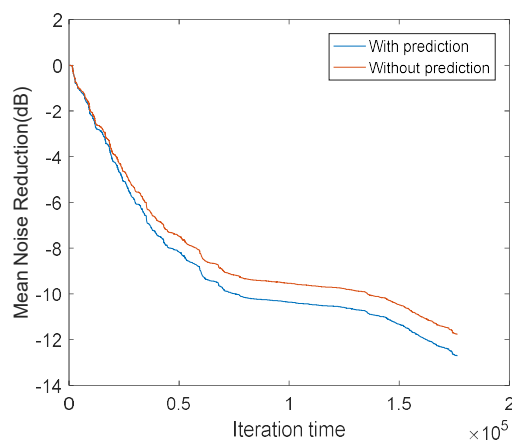


Fig. 3.20: Evolution of learning curves for processing in-situ measurement data based on the MNR index.

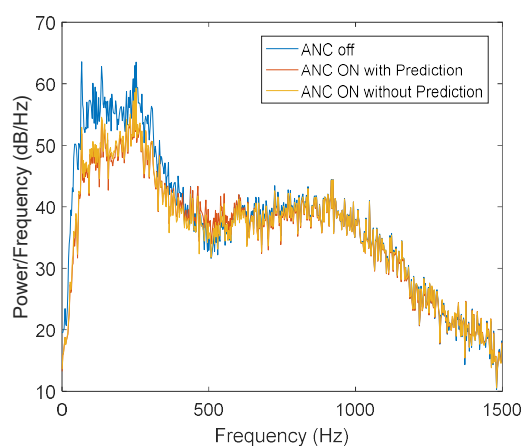


Fig. 3.21: Performance of the proposed ANC system (C-FxLMS/F algorithm) with or without Bayesian approach as a pre-processing procedure.

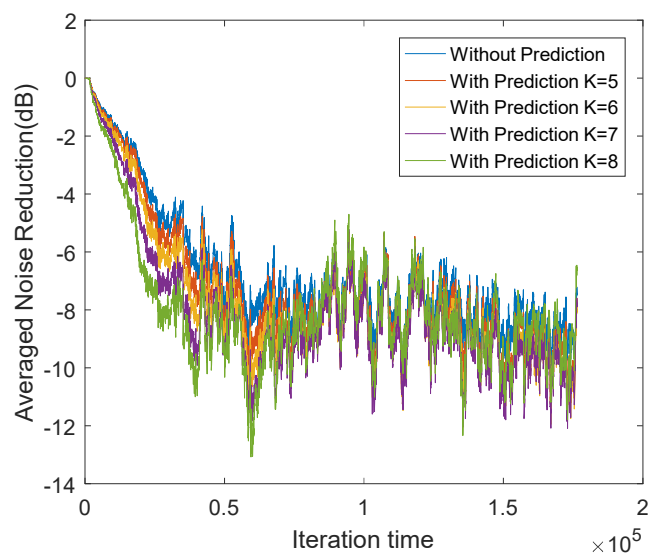


Fig. 3.22: Evolution of learning curves for processing in-situ measurement data based on the ANR index.

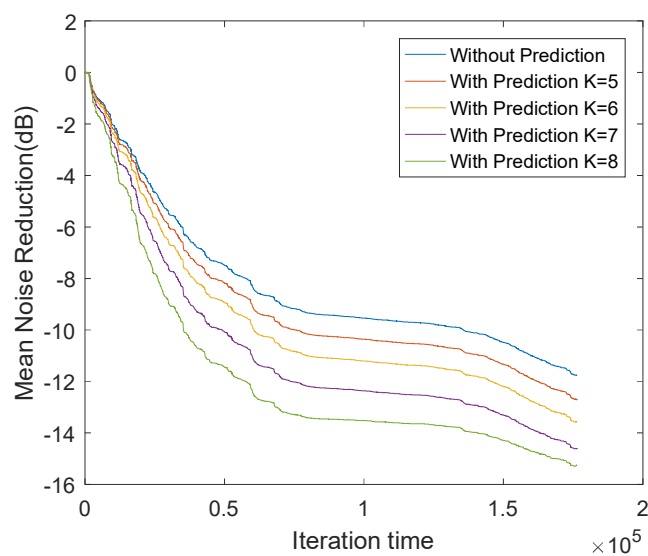


Fig. 3.23: Evolution of learning curves for processing in-situ measurement data based on the MNR index.

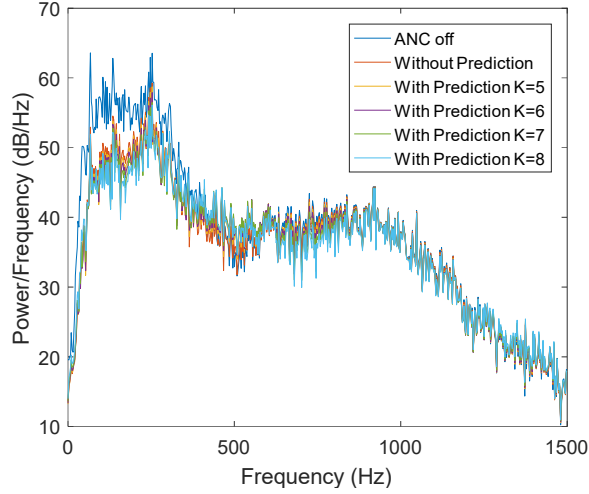


Fig. 3.24: Performance of the proposed ANC system (C-FxLMS/F algorithm combined Bayesian approach) with various K -step values.

3.4.4 Complexity analysis of various signal forms

To evaluate the effectiveness of this pre-processing process, three signal forms (i.e., (i) Gaussian noise; (ii) sinusoidal and Gaussian noise; and (iii) in-situ measurement data) are also tested for comparison. In Figs. 3.25–3.27, the convergence speed is examined by the ANR index. Only a Gaussian noise input was fed into an ANC system with and without Bayesian inference. The results show that the convergence performance is better with the presence of this pre-processing system. Figs. 3.28–3.30 further present a good convergence performance under the effect of both sinusoidal and Gaussian noise signals. In this case, the reference noise signal $x(n)$ is a sinusoidal wave of 500 Hz and the sampling rate is 8000 Hz as follows:

$$x(n) = \sin\left(\frac{2\pi \times 500 \times n}{8000}\right) + v(n) \quad (3.31)$$

where $v(n)$ represents a Gaussian noise. In Figs. 3.27 and 3.30, the C-FxLMS/F algorithm with and without the pre-processing system presents a similar convergence performance. In Fig. 3.31, using the in-situ measurement noise input, we observe that

the results with Bayesian inference are better than that of those without such a process for the FxLMS, FxLMS/F and C-FxLMS/F algorithms.

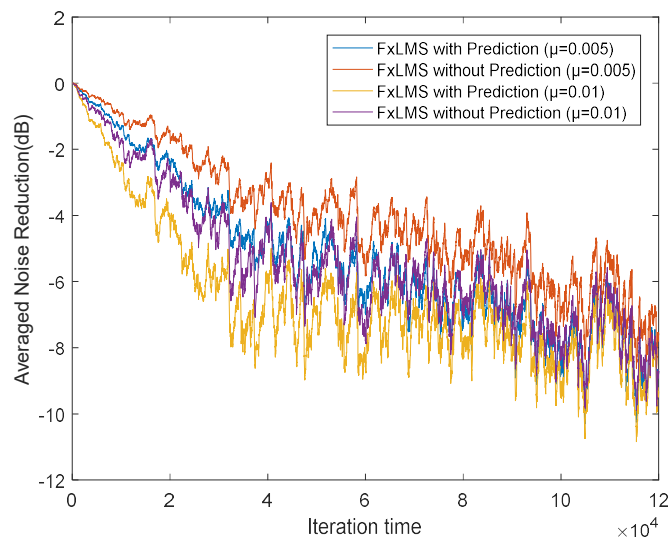


Fig. 3.25: Evolution of learning curves for a Gaussian signal input (FxLMS algorithm with various step-size).

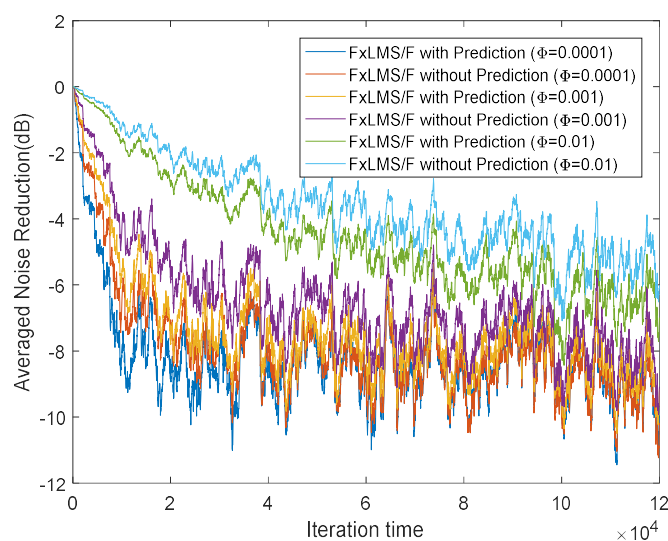


Fig. 3.26: Evolution of learning curves for a Gaussian signal input (FxLMS/F algorithm).

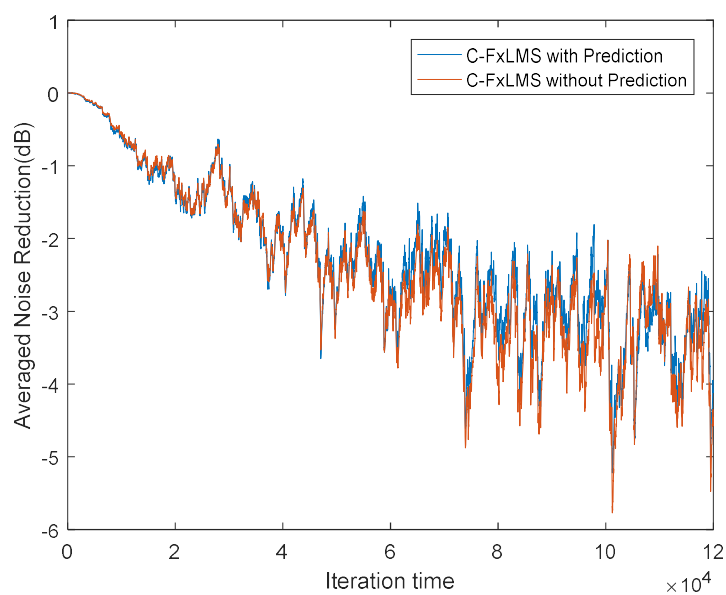


Fig. 3.27: Evolution of learning curves for a Gaussian signal input (C-FxLMS/F algorithm).

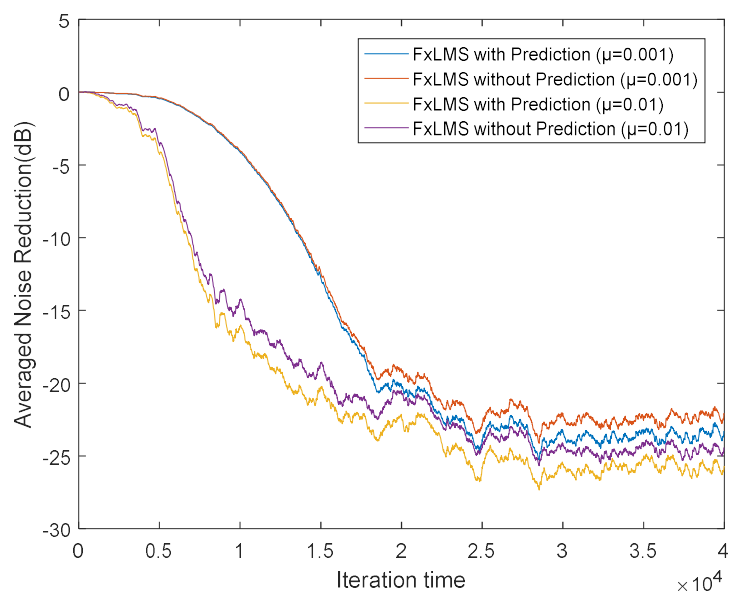


Fig. 3.28: Evolution of learning curves for a combined sinusoidal and Gaussian signal (FxLMS algorithm).

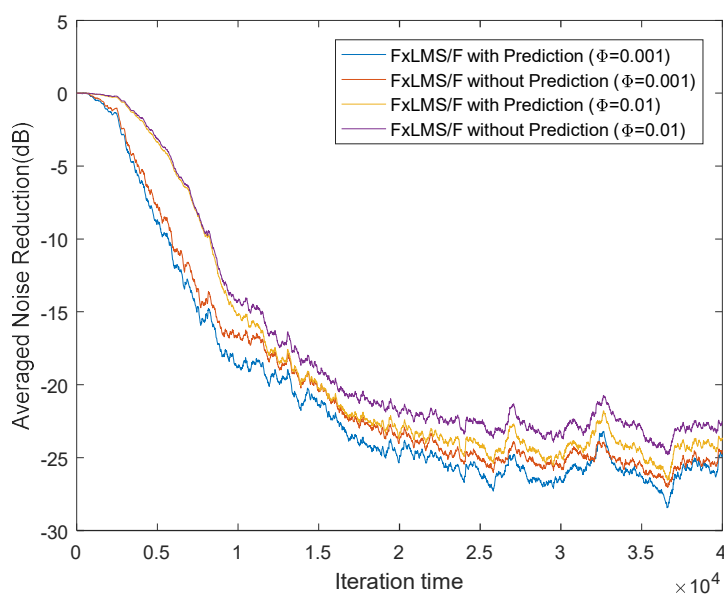


Fig. 3.29: Evolution of learning curves for a combined sinusoidal and Gaussian signal (FxLMS/F algorithm).

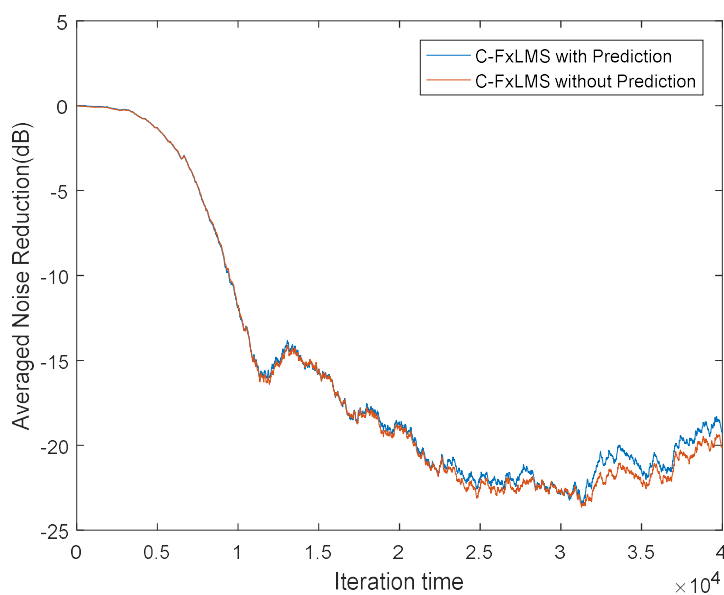


Fig. 3.30: Evolution of learning curves for a combined sinusoidal and Gaussian signal (C-FxLMS/F algorithm).

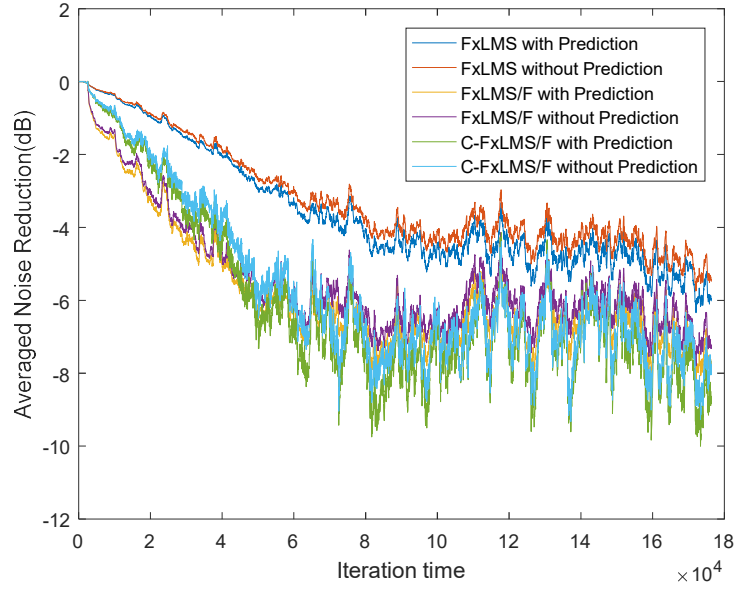


Fig. 3.31: Evolution of learning curves for in-situ measurement noise (FxLMS, FxLMS/F and C-FxLMS/F algorithm with an optimal parameter).

3.5 Concluding remarks

In this study, a DLM with Bayesian inference was adopted as a means of raw signal pretreatment in the ANC system. We summarized the major findings of this work as follows:

- This pre-processing system shows a higher convergence speed. A pretreatment process combined with the conventional FxLMS algorithm and a new C-FxLMS/F algorithm was investigated for its applicability to various time-domain control algorithms.
- To enhance the control performance, the cost of the secondary path was considered from various aspects in previous literatures, such as secondary path estimation and online modeling of the secondary path. In this study, a DLM combined Bayesian inference can provide a time-step compensation for utilizing the prediction function. The combination of prior information and updated

observation leads to an updated fuzzy estimation for the future values. The estimation was in some steps dependent on the value of K ahead of the then-current time, which can reduce the time-delay effects in the control algorithm.

- The present approach, as a pretreatment process, can be coupled for various ANC algorithms. The updating characteristic “*forecast-observation-analysis*” loop is advantageous for the implementation of signal processing for an ANC system. This method requires less parameter identification that is an advantage for many engineering applications. Besides, it is also suitable for different types of noise signals, i.e., (i) Gaussian noise; (ii) sinusoidal and Gaussian noise; and (iii) in-situ measurement data, as investigated herein.

In this work, two case studies are used to provide a feasibility study for the preprocessing system in cooperating with ANC system. Noise effects from general construction machines are considered herein. Yet, to meet the requirements of widely application, various noise signals shall be considered for further improvement. This method is still limited to process the impulse/unstable noise signal (e.g., impact noise generated from piling driven machines). Due to the sharp and instantaneous properties, the impulse noise attenuation is a tricky point and needs to be further investigated in the future work. Also, the computational effort would be inevitably increased when the Bayesian-based approach is incorporated with ANC system. This problem may be fixed by designing an ad-hoc intelligent controller that can reduce the computational complexity. Further investigation will also focus on the complexity analysis of information inference.

CHAPTER 4

INVESTIGATION OF A DUAL-FUNCTION BARRIER FOR NOISE CONTROL

4.1 Introduction

Construction noise generated from various powered mechanical equipment is mainly dominated by high-intensity noise that can adversely threaten the public health. More seriously, the combined noise effects from equipment machines operating simultaneously are highly annoying (Lee et al., 2015). Hence, inspiring an innovative technology design for noise mitigation is of great interest. Typically, noise barriers or acoustic enclosures are often used to surround the sound emission sources in construction sites. Critical factors concerning the performance of passive-type sound barriers are strongly dependent on material types, structural dimensions, surface conditions, and geometric configurations (Morgan and Kay, 2001; Ishizuka and Fujiwara, 2004; Samsudin et al., 2016). In general, conventional barrier types made of masonry, steel, and concrete materials (EPD, 2003) are hard concurrently to fulfill the requirements of functional and aesthetic designs (Hong and Jeon, 2014).

To design environmentally friendly noise barriers, using low-cost, recyclable and lightweight materials is an alternative approach. These examples include wood and rubber composite materials that are promising choices for barrier design, because they can provide high tensile modulus and mechanical strength (Yang et al., 2003; Zhu et

al., 2013; Sim et al., 2014; Buratti et al., 2016; Peng, 2017; Raj et al., 2020). In this aspect, Zhao et al. (2010) investigated the use of wood-waste tire rubber composite panels for sound-insulated materials by presenting a modified four-microphone method, from which the transmission loss (*TL*) behavior was illustrated and compared with two other types of sound barriers. More recently, Thai et al. (2020) studied the performance of rubber aerogels that can be extracted from recycling tires for sound insulation. Because of the viscoelastic characteristic, wood-rubber composite materials can perform an elastic deformation with the movement of rubber molecule chains (Zhao et al., 2010), when the macromolecular polymers are subjected to alternating stresses (e.g., vibration stress or incident sound wave). It can be characterized by a remarkable lag of deformation with the stress change. The movement of deformation may overcome the resistance by converting them into heat energy and dissipating into environment, thereby resulting in a high-level soundproofing capacity. In this study, we attempt to present a comprehensive study of acoustic investigation for wood-rubber composites.

Nevertheless, making use of passive sound barriers (e.g., aluminum, metal, timber, acrylic, or vegetation) is not sufficient for the reduction of low-frequency components (Nilsson and Berglund, 2006). The major reason is the acoustic wavelength of low-frequency noise is significantly longer than the thickness dimension of barrier structures, resulting in an inefficient coupling effect. To alleviate this issue, acoustic metamaterial structures (Assouar et al., 2016; Iannace et al., 2021) have been proposed as a viable solution for low-frequency sound attenuation. As an alternative, unwanted sound can be cancelled based on the principle of superposition by generating an anti-phase acoustic wave, which is also called an active noise control (ANC) technique (Chakravarthy and Kuo, 2006; Kuo and Gireddy, 2007; Lam et al., 2021). Zhang and Qiu (2017) proposed an active partition which an integrated active and passive control modulus for snoring noise attenuation, a fairly good sound level reduction of around 10–15 dB can be achieved under 500–1000 Hz. Murao et al.

(2019) focused on the coupling use of an ANC system and a passive silencer to attenuate noise from openable windows. To simulate the attenuation of noise in open fields, the integration of sound masking techniques has been evaluated by embedding active noise mitigation elements in passive control barriers. Yet, as an active anti-noise device, conventional electromagnetic speakers with bulky coils and diaphragms can cause complex installation problems in a limited space. To overcome this technical challenge, polyvinylidene fluoride (PVDF) is a new, smart and thin-film material that can exhibit strong piezoelectric (Kawai, 1969) and ferroelectric (Lolla et al., 2016) effects. Searching the relevant information on this aspect, Mirshekarloo et al. (2016; 2018) examined the performance of transparent thin-film PVDF speakers attaching on the surface of a window as the secondary source of an ANC system. This ANC approach has also been discussed by theoretical, simulation, and experimental studies (Omoto and Fujiwara, 1993; Omoto et al., 1997; Duhamel et al., 1998; Han and Qiu, 2007; Liu and Niu, 2008; Chen et al., 2011).

In this work, we attempt to design a retractable and movable barriers for noise mitigation. The recycled composite materials (i.e., waste wood and tyre rubber) are inert in nature. Such materials are investigated for the design of a passive noise barrier. Compared with synthetic materials, recycle composites can be an alternative for satisfying the low-cost and environmental-friendly requirements in the barrier design. In addition, we utilize the flexible and lightweight features of PVDF thin-film as an anti-noise generator. Integrating composite panels and PVDF thin-film speaker, a dual-function barrier is investigated. The wood-rubber panel as a resilient layer appears to provide a global sound attenuation at a wideband frequency range, while the PVDF thin-film as an auxiliary component can be used for mitigating the peak narrowband low-frequency components. To investigate the feasibility of dual-function barrier, we implement a scale-down model, and conduct test in a semi-anechoic chamber. The rest parts of this chapter are organized as follows: Section 4.2 characterizes the soundproofing performance of wood-rubber composites. Section 4.3

demonstrates the fabrication and frequency response analysis of a PVDF thin-film speaker. In Section 4.4, we present the experimental study via a simplified two-dimensional sound field analysis. The major findings of this work are summarized in Section 4.5.

4.2 Characterization of acoustic properties of wood-rubber composites

4.2.1 Two-microphone method

The two-microphone method is commonly used for the measurement of acoustic properties of materials (Åbom, 1991; ASTM, 2009,2010,2016), which can measure the absorption coefficients utilizing an impedance tube. A stable and closed sound field is generated inside the tube with two microphones for data acquisition. The absorption parameters can thus be determined by transfer functions. A schematic diagram of the two-microphone impedance tube is shown in Fig. 4.1. To characterize the acoustic absorption behavior of a test sample, the two-microphone method can be implemented for direct measurement.

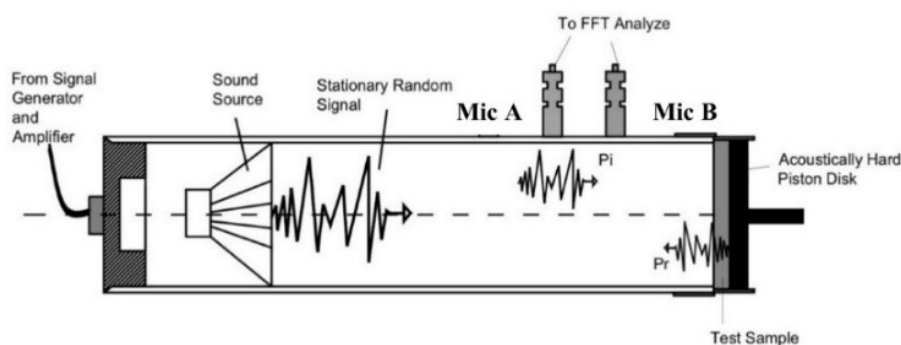


Fig. 4.1: Schematic diagram of two-microphone impedance tube (Bolton et al., 1997).

In Fig. 4.1, the incident wave (p_i) and reflected wave (p_r) are the critical components of a broadband stationary random signal. Acoustic wave fields in the tube

can be characterized by the acoustic pressure $p(x)$ of the incident wave $p_i(x)$ and the reflected wave $p_r(x)$ from the sample:

$$p(x) = p_i(x) + p_r(x) = Ae^{-jkx} + Be^{jkx} \quad (4.1)$$

where A and B are the amplitudes of the acoustic pressures of the incident and reflected wave, j is an imaginary component, k is the wave number, and x is the spatial variable.

Regarding the working mechanism, a loudspeaker is installed inside the tube to generate one-dimensional acoustic waves traveling inside the tube at normal incidence. The incident wave is reflected from the test sample placed at the tube end. Within the tube, the occurrence of phase interference may be resulted due to the incident and reflected waves, thereby resulting in the formation of a standing wave pattern. If 100% of the incident wave can be reflected, the incident and reflected waves have the same amplitude, resulting in a zero pressure at the nodes and a maximum pressure amplitude at the antinodes. If a portion of the incident wave is absorbed by the sample, then the incident and reflected waves have different amplitudes, implying that the nonzero of sound pressure at the nodes within the tube. Usually, a standing wave ratio is used to reflect the ratio between the maximum pressure (at anti-node position) and the minimum pressure (at node position). The reflection factor (R) and absorption coefficient (α) can be determined using this standing wave ratio.

The reflection fact (R) can be expressed as $R=B/A$, which is equal to the ratio of pressure amplitude of the reflected and incident waves. According to the transfer functions, the reflection factor can be expressed as follows (Chung and Blaser, 1980b; Sim et al., 2014; Labašová and Ďuriš, 2019):

$$R = \left(\frac{H_1 - H_i}{H_r - H_1} \right) e^{2jk(l+s)} \quad (4.2)$$

in which k is the wave number, l is the distance between the position of Mic B (see Fig. 4.1) and the front of the sample (in mm), and s is the spacing between the microphones (in mm), and j is an imaginary. H_i and H_r can be expressed as e^{-jks} and e^{jks} , respectively. H_1 is the transfer function between the microphone positions from Mic A to Mic B, which can be calculated by $H_1 = S_{12}/S_{11}$. S_{12} denotes the cross power spectral density of the signal (from Mic A to Mic B), while S_{11} denotes the auto-spectral density of the signal (from the Mic B). The sound absorption coefficient (α) can be obtained as follows (Bolton et al., 1997):

$$\alpha = 1 - |R|^2 \quad (4.3)$$

4.2.2 Four-microphone method

On the basis of the plane wave theory (Chung and Blaser, 1980a), the transfer-matrix method can be used to compute the transmission loss (TL) of materials. The testing material samples are considered as a complex vibration system. Fig. 4.2 shows the schematic diagram of a four-microphone impedance tube setup. Test samples are placed in the middle of the tube.

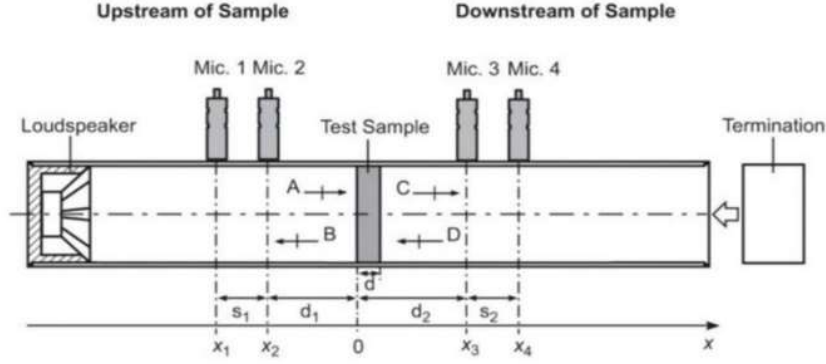


Fig. 4.2: Transmission loss measurement by impedance tube (B&K, 2007).

The sound pressure $p(x, t)$ and particle velocity $v(x, t)$ in the up- and downstream tube sections can be written as (Pierce and Beyer, 1990; Kinsler, 2000):

$$p(x, t) = \text{Re} \{ P(x, \omega) e^{j\omega t} \} = \begin{cases} \text{Re} \{ (A(\omega) e^{-jkx} + B(\omega) e^{jkx}) e^{j\omega t} \} & x \leq 0 \\ \text{Re} \{ (C(\omega) e^{-jkx} + D(\omega) e^{jkx}) e^{j\omega t} \} & x \geq l \end{cases} \quad (4.4)$$

$$v(x, t) = \text{Re} \{ V(x, \omega) e^{j\omega t} \} = \begin{cases} \text{Re} \left\{ \frac{(A(\omega) e^{-jkx} + B(\omega) e^{jkx})}{\rho_0 c} e^{j\omega t} \right\} & x \leq 0 \\ \text{Re} \left\{ \frac{(C(\omega) e^{-jkx} + D(\omega) e^{jkx})}{\rho_0 c} e^{j\omega t} \right\} & x \geq l \end{cases} \quad (4.5)$$

where $\text{Re} \{ \}$ means the real part, $P(x, \omega)$ is the complex pressure, $V(x, \omega)$ is the complex particle velocity, A to D represent the complex amplitudes of the plane wave components. ρ_0 is the fluid density, c is the speed of sound, ω is the angular frequency, k is the wave number, $k = (\omega/c) - j\alpha$, which is complex to consider the impact of viscous and thermal dissipation. l denotes the thickness of a test sample. The terms $e^{j\alpha t}$ and $e^{-j\alpha t}$ are complex exponential representations, which depend on the travelling directions, i.e., forward or backward, respectively. It can be interpreted as the phase increasing or decreasing with time. The complex sound pressures at the four-

microphone locations (Mic 1 to Mic 4) can be expressed as:

$$\begin{aligned}
 P_1 &= Ae^{-jkx_1} + Be^{jkx_1} \\
 P_2 &= Ae^{-jkx_2} + Be^{jkx_2} \\
 P_3 &= Ce^{-jkx_3} + De^{jkx_3} \\
 P_4 &= Ce^{-jkx_4} + De^{jkx_4}
 \end{aligned}
 \tag{4.6}$$

The coefficients A to D in terms of the four measured sound pressures can be calculated as follows (Olivieri et al., 2006; B&K, 2007):

$$\begin{aligned}
 A &= \frac{j(P_1e^{jkx_2} - P_2e^{jkx_1})}{2 \sin k(x_1 - x_2)} \\
 B &= \frac{j(P_2e^{jkx_1} - P_1e^{-jkx_2})}{2 \sin k(x_1 - x_2)} \\
 C &= \frac{j(P_3e^{jkx_4} - P_4e^{jkx_3})}{2 \sin k(x_3 - x_4)} \\
 D &= \frac{j(P_4e^{jkx_3} - P_3e^{-jkx_4})}{2 \sin k(x_3 - x_4)}
 \end{aligned}
 \tag{4.7}$$

A transfer matrix (Pierce and Beyer, 1990; Kinsler, 2000) is thus utilized to relate the complex pressure (P) and the complex normal acoustic particle velocities (V) which can be expressed by the following equation as follows:

$$\begin{bmatrix} P \\ V \end{bmatrix}_{x=0} = \begin{bmatrix} T_{11} & T_{12} \\ T_{21} & T_{22} \end{bmatrix} \begin{bmatrix} P \\ V \end{bmatrix}_{x=d}
 \tag{4.8}$$

where T_{ij} ($i, j = 1, 2$) are the transfer matrix components that are the ratio of the up-stream and down-stream quantities (i.e., pressure and velocity) (Song and Bolton,

2000). P and V of two faces of the test sample can be obtained by the decomposition of sound fields into incident and outgoing plane wave components for both sections:

$$\begin{aligned}
 P|_{x=0} &= A + B \\
 V|_{x=0} &= \frac{A - B}{\rho_0 c} \\
 P|_{x=d} &= Ce^{-jkd} + De^{jkd} \\
 V|_{x=d} &= \frac{Ce^{-jkd} - De^{jkd}}{\rho_0 c}
 \end{aligned} \tag{4.9}$$

where $\rho_0 c$ is the characteristic impedance in air. With the measurement results from the impedance test, the complex pressures at the four microphone positions are obtained, therefore, the pressure and velocities can be determined. Utilizing the two-load method (Munjal, 2014), to solve the four unknowns in Eq. (4.8), T_{11} , T_{12} , T_{21} , and T_{22} , two additional equations are formed. In a matrix form, the two independent measurements can be expressed as:

$$\begin{bmatrix} P_1 & P_2 \\ V_1 & V_2 \end{bmatrix}_{x=0} = \begin{bmatrix} T_{11} & T_{12} \\ T_{21} & T_{22} \end{bmatrix} \begin{bmatrix} P_1 & P_2 \\ V_1 & V_2 \end{bmatrix}_{x=d} \tag{4.10}$$

where the subscripts 1 and 2 on the complex pressure (P) and the complex particle velocity (V) denote two different termination conditions. One is a reflected termination, and the other one is an absorption termination condition. Therefore, the transfer matrix elements can be determined as follows (Olivieri et al., 2006; B&K, 2007):

$$\begin{aligned}
 \begin{bmatrix} T_{11} & T_{12} \\ T_{21} & T_{22} \end{bmatrix} &= \frac{1}{P_{1|x=d}V_{2|x=d} - P_{2|x=d}V_{1|x=d}} \\
 &\times \begin{bmatrix} P_{1|x=0}V_{2|x=d} - P_{2|x=0}V_{1|x=d} & -P_{1|x=0}P_{2|x=d} + P_{2|x=0}P_{1|x=d} \\ V_{1|x=0}V_{2|x=d} - V_{2|x=0}V_{1|x=d} & -P_{2|x=d}V_{1|x=0} + P_{1|x=d}V_{2|x=0} \end{bmatrix}
 \end{aligned} \tag{4.11}$$

Under certain circumstances, the transfer matrix elements can be simplified. When the plane wave reflection and transmission coefficient from two surfaces of a test sample are the same, the reciprocal nature of the layer can be considered to generate two additional equations, which can reduce a second set of measurements. It is also called as the one-load implementation.

$$\begin{aligned}
 T_{11} &= T_{22} \\
 T_{11}T_{22} - T_{12}T_{21} &= 1
 \end{aligned} \tag{4.12}$$

$$\begin{aligned}
 \begin{bmatrix} T_{11} & T_{12} \\ T_{21} & T_{22} \end{bmatrix} &= \frac{1}{P_{1|x=0}V_{2|x=d} + P_{2|x=d}V_{1|x=0}} \\
 &\times \begin{bmatrix} P_{1|x=d}V_{2|x=d} + P_{2|x=0}V_{1|x=0} & P_{1|x=0}^2 - P_{2|x=d}^2 \\ V_{1|x=0}^2 - V_{2|x=d}^2 & P_{1|x=d}V_{2|x=d} + P_{2|x=0}V_{1|x=0} \end{bmatrix}
 \end{aligned} \tag{4.13}$$

Consider the situation of a perfectly anechoic termination, the sample with a certain depth, the transmission coefficient (D) (see Eq. 4.7) can be idealized to zero in the down-stream tube section. Therefore, we can assume that the incident plane wave with a unit amplitude, the sound pressure and particle velocity expressions on the two surfaces of the porous layer (see Eq. 4.9) can be further written as (Olivieri et al., 2006; B&K, 2007):

$$\begin{aligned}
 P|_{x=0} &= 1 + R_a \\
 V|_{x=0} &= \frac{1 - R_a}{\rho_0 c} \\
 P|_{x=d} &= T_a e^{-jkd} \\
 V|_{x=d} &= \frac{T_a e^{-jkd}}{\rho_0 c}
 \end{aligned} \tag{4.14}$$

where $R_a=B/A$ and $T_a=C/A$ are the normal incidence and plane wave reflection, respectively. Using the transfer matrix components to represent T_a , we obtain (Olivieri et al., 2006; B&K, 2007):

$$\begin{aligned}
 T_a &= \frac{2e^{jkd}}{T_{11} + \frac{T_{12}}{\rho_0 c} + \rho_0 c T_{21} + T_{22}} \\
 R_a &= \frac{T_{11} + \frac{T_{12}}{\rho_0 c} - \rho_0 c T_{21} - T_{22}}{T_{11} + \frac{T_{12}}{\rho_0 c} + \rho_0 c T_{21} + T_{22}}
 \end{aligned} \tag{4.15}$$

The transmission loss (TL) of a test sample at normal incidence as follows (B&K, 2007):

$$TL = 10 \log_{10} \frac{1}{|T_a|^2} \tag{4.16}$$

4.2.3 Samples preparation and experimental setup

Wood-waste crumbs and tire rubber particles were prepared cylinder samples for acoustic material test. The simple fabrication procedures were presented in Fig. 4.3. Recycled wood-waste and tire rubber were cut into small crumbs. The composite

particles (i.e., wood particles and rubber crumbs) were mixed and bonded by epoxy resin. The important factors, which may affect the sound insulation properties (Zhao et al., 2010; Ghofrani et al., 2016; Lee et al., 2020), include: (i) the microstructure of wood particles, (ii) wood-to-rubber ratio, and (iii) thickness of samples. Two kinds of wood particles with different microstructures (i.e., *fine wood particle with 1–2 mm in diameter* and *coarse wood particle with 3–6 mm in diameter*) and rubber crumbs (*1–3 mm in diameter*) were used to prepare various test samples in a cylindrical mold shape with different thickness, i.e., 10, 15, 20 and 25 mm. The impedance tube system was tested in the in-house semi-anechoic chamber, as shown in Fig. 4.4 (a)–(c). Pure-wood and pure-rubber specimens were also prepared for control experiments. Fig. 4.5 shows a total number of 56 samples. Among all specimens, the diameter was set as 98 mm to fit the internal size of the standard impedance tube (i.e., 100 mm in diameter, *B&K Type 4206*). Tables 4.1 and 4.2 shows the information of all fabricated samples.

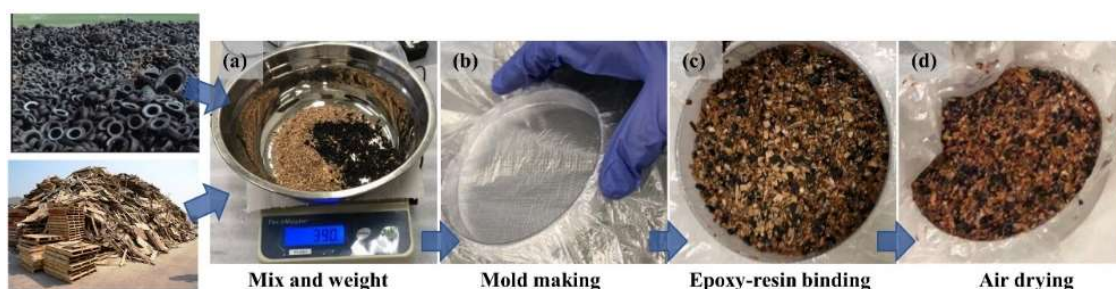


Fig. 4.3: Preparation procedures of test samples.

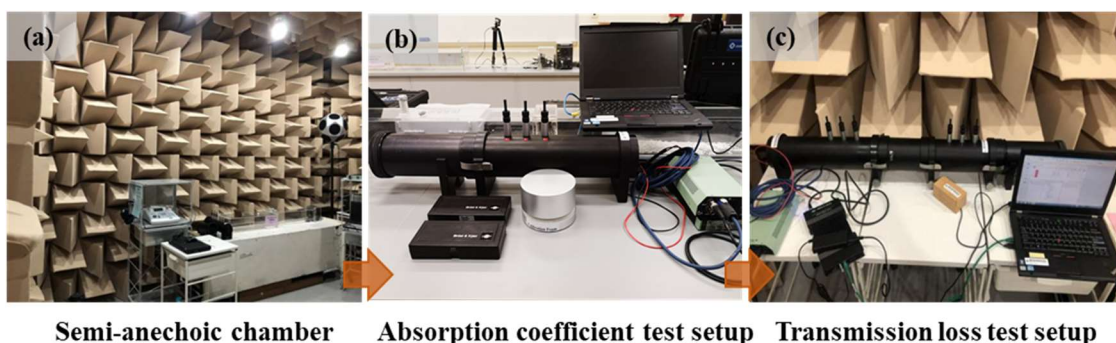


Fig. 4.4: Experimental setup of impedance tube. (a) Semi-anechoic chamber; (b) and (c) Impedance tube test system including microphones (*Type 2690*), amplifier (*Type 2735*) and generator module (*Type 3160-A-042*).



Fig. 4.5: Test samples of wood-rubber composite materials.

Table 4.1: Configuration and weight of test samples (Group 1)

Wood/Rubber Weight Ratio	Sample No.	Thickness (mm)	Weight of material (g)	Weight of epoxy resin adhesion (g)
Pure wood	1	10	21.4	29.1
	2	15	27.8	38.0
	3	20	36.7	49.5
	4	25	44.1	57.1
2:1	5	10	25.8	31.1
	6	15	35.3	34.7
	7	20	45.6	50.7
	8	25	58.0	58.6
1:1	9-1	10	29.8	34.9
	10-1	15	40.1	42.4
	11-1	20	55.4	47.5
	12-1	25	65.2	54.6
1:1	9-2	10	29.9	40.6
	10-2	15	40.9	67.6
	11-2	20	55.1	77.9
	12-2	25	65.6	98.2
1:2	13	10	35.0	37.5
	14	15	52.3	52.4
	15	20	65.8	62.8
	16	25	84.1	73.6

* Test samples were made of coarse wood particles (grain diameter: 3–6 mm).

Table 4.2: Configuration and weight of test samples (Group 2)

Wood-rubber weight ratio	Number	Thickness (mm)	Weight of dry material (g)	Weight of epoxy resin adhesion (g)
2:1	17	10	27.5	35.0
	18		27.9	35.0
	19	15	39.0	50.1
	20		41.7	53.0
	21	20	54.9	39.9
	22		54.5	36.2
	23	25	70.1	49.0
	24		70.3	41.6
1.5:1	25	10	28.0	24.1
	26		26.7	23.3
	27	15	38.1	30.2
	28		38.0	31.4
	29	20	58.2	35.0
	30		55.0	40.3
	31	25	68.4	51.6
	32		68.3	50.0
1:1	33	10	32.0	30.6
	34		30.4	31.1
	35	15	44.9	39.9
	36		45.3	38.4
	37	20	54.6	47.8
	38		52.6	45.4
	39	25	76.6	59.6
	40		77.8	55.0
Pure wood	41	10	21.2	24.5
	42		21.0	21.6
	43	15	33.6	39.2
	44		33.4	38.0
	45	20	47.2	57.5
	46		47.5	60.6
	47	25	55.7	73.1
	48		55.7	66.6
Pure rubber	49	10	62.1	29.1
	50	15	76.9	32.8
	51	20	102.8	43.0
	52	25	115.7	52.2

* Test samples were made of fine wood particles (grain diameter: 1–2 mm).

4.2.4 Soundproofing performance of wood-rubber composites

4.2.4.1 Absorption coefficient analysis

Absorption coefficient is used to evaluate the sound absorption efficiency of materials. It is regarded as the proportion of absorbed energy to incident energy (see Eq. (4.3)). Relevant figures are plotted below to show the acoustic absorption performance among test specimens. The variables, i.e., thickness of specimens, ratio of wood and rubber particles, and microstructure of wood particles, are considered as influencing factors to determine the sound absorption performance. We discuss the three factors subsequently. The relationship between the absorption coefficient and the sound frequency is studied. Herein, our main focus is to investigate the acoustic performance of recycled materials at a frequency range of 0–1600 Hz, because powered mechanical equipment normally generates low-frequency noise in this range.

In Fig. 4.6, four graphs from (a) to (d) correspond to the specimens with thickness of 10 mm, 15 mm, 20 mm, and 25 mm, respectively. In each graph, five types of samples with different wood-rubber ratios are compared. The proportion on the legends in the graphs represent the wood-rubber ration, e.g., (2:1 10 mm) denotes 2:1 of wood-rubber ratio and 10 mm in thickness. The results illustrate that a better acoustic absorption performance is in the case of 2:1 wood-rubber ratio, see graphs (a), (b) and (c). The absorption coefficient increases with a higher proportion of wood particles in the specimens. In the pure rubber samples, the absorption coefficient is relatively low as most of the incident wave would be reflected.

Figs. 4.7 and 4.8 compare the acoustic characteristics of the test samples with the same wood-rubber ratio but different thickness. In Fig. 4.7, referring to graphs (b), (c) and (d), with the thickness increasing, the moving trend of peaks is at a low-frequency range. In graphs (c) and (d), the wave crests are not salient as the acoustic absorption performance is weak with a lower proportion of wood particles. In Fig. 4.8, the

acoustic absorption performance is preferable with increasing thickness (see the solid lines) (i.e., thickness = 25 mm).

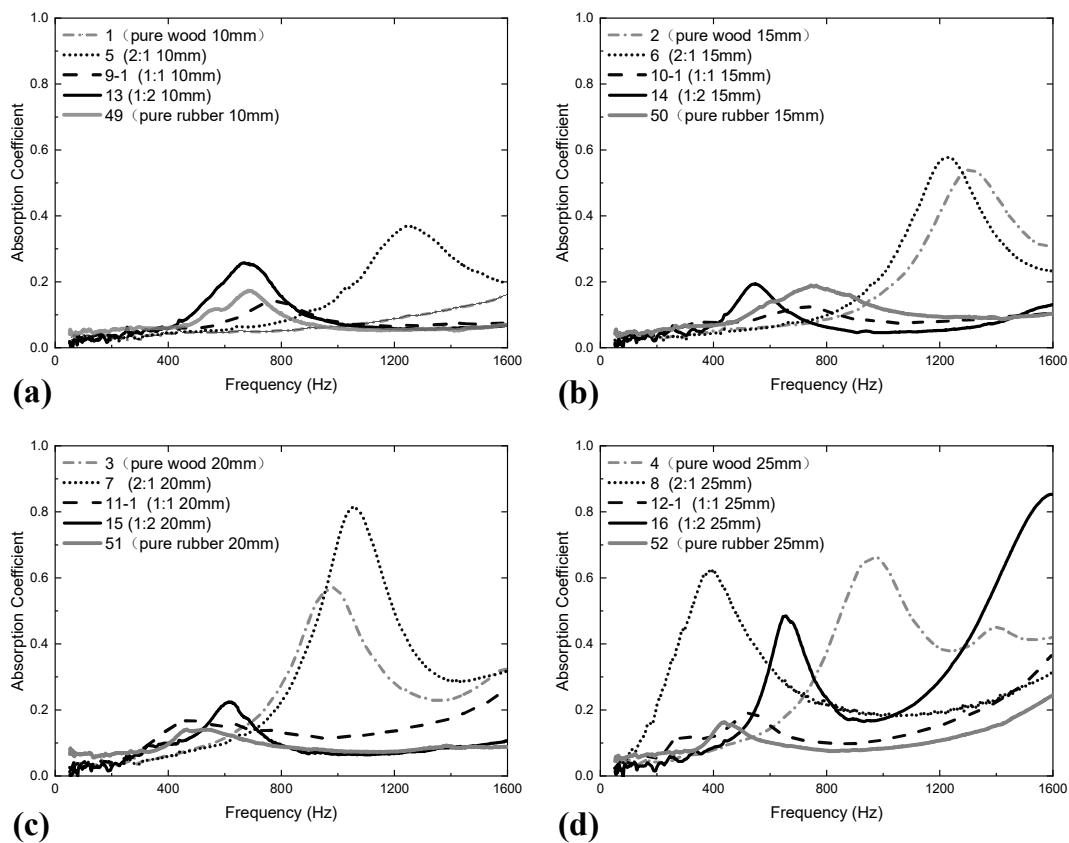


Fig. 4.6: Comparison of the acoustic absorption performance of the test specimens with the same thickness but different wood-rubber ratio. (a) Thickness of 10 mm; (b) Thickness of 15 mm; (c) Thickness of 20 mm; and (d) Thickness of 25 mm.

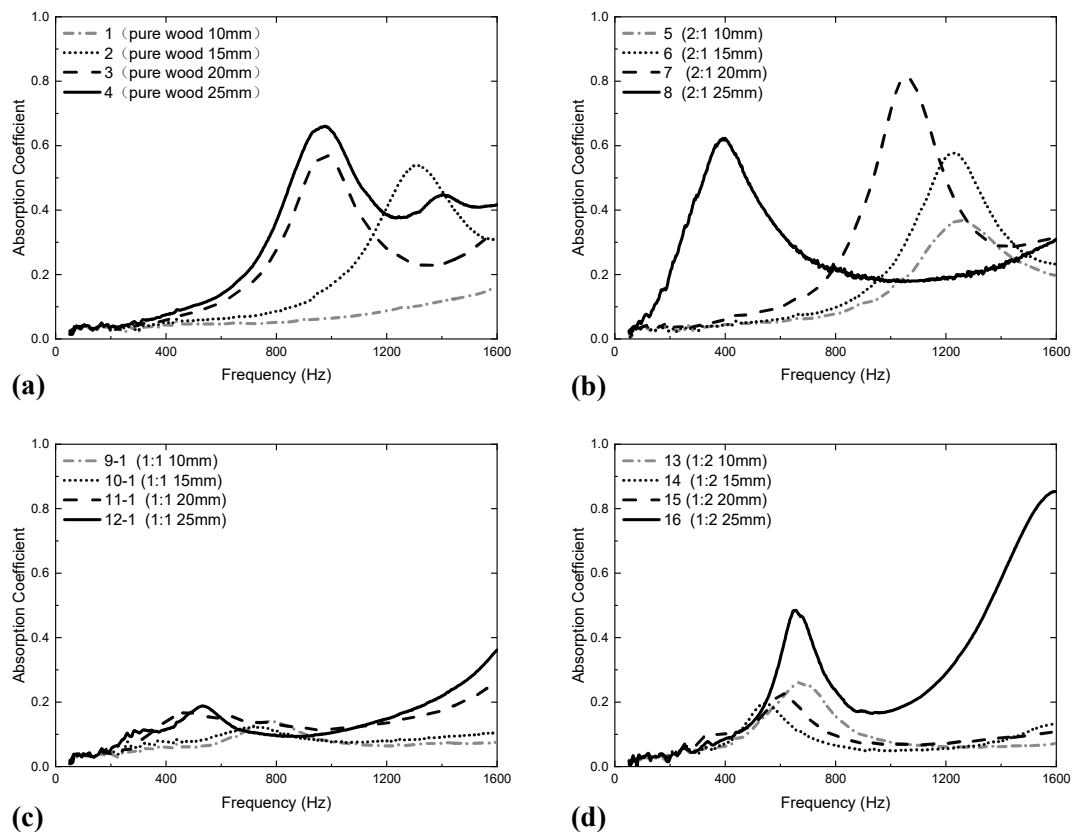


Fig. 4.7: Comparison of the acoustic absorption performance of the test specimens with the same wood-rubber ratio but different thickness: (a) Pure-wood samples; (b) Wood-rubber ratio 2:1; (c) Wood-rubber ratio 1:1; and (d) Wood-rubber ratio 1:2. (* Specimen numbers are from 1 to 16).

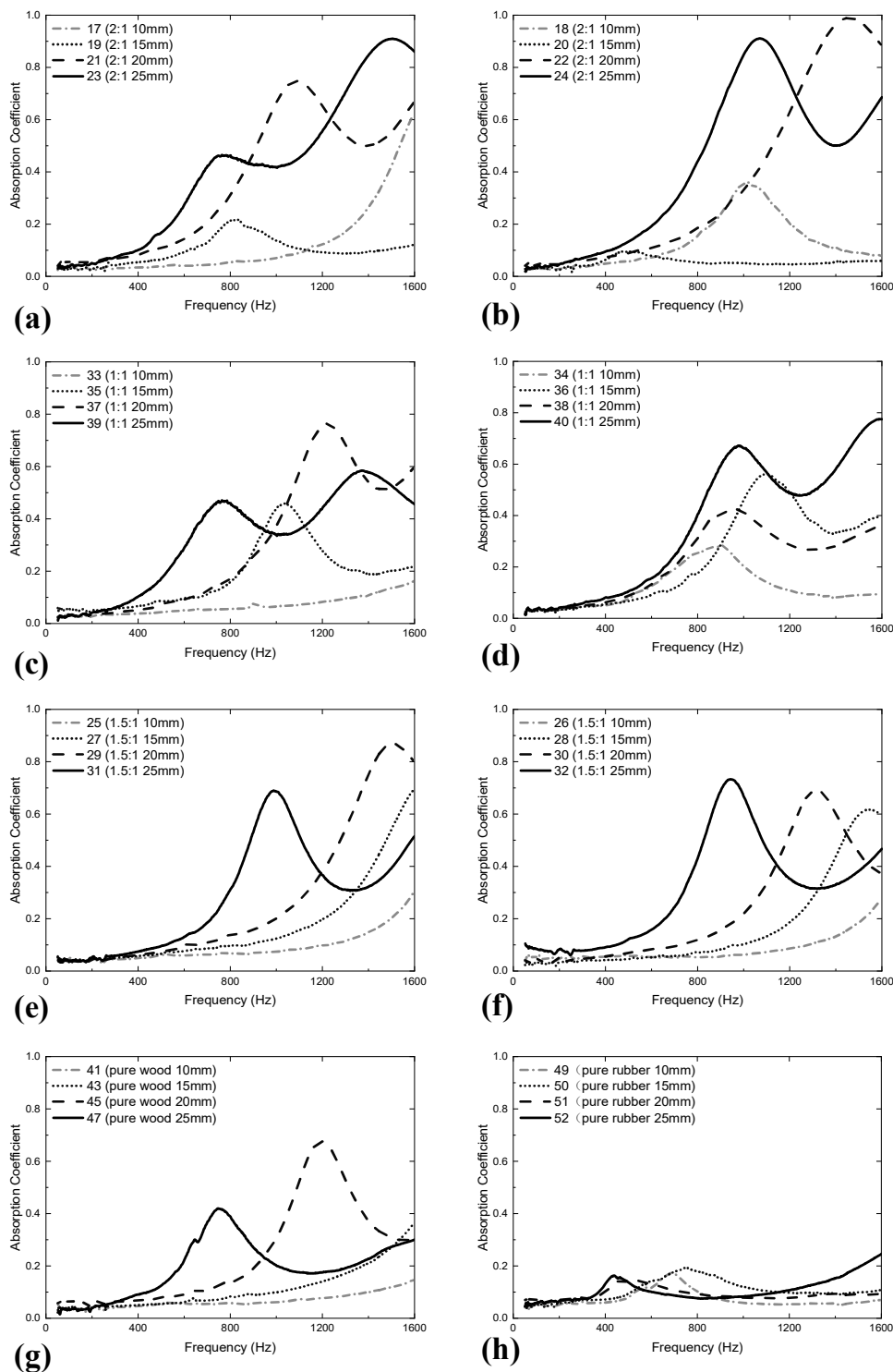


Fig. 4.8: Comparison of the acoustic absorption performance of the test specimens with the same wood-rubber ratio but different thickness: (a) and (b) wood-rubber ratio 2:1; (c) and (d) Wood-rubber ratio 1:1; (e) and (f) Wood-rubber ratio 1.5:1; (g) Pure-wood samples for control experiments; and (h) Pure-rubber samples for control experiment. (*Sample numbers are 17–52).

To further investigate the microstructure effect of wood particles, two sets of samples are studied by scanning electron microscope (SEM). Fig. 4.9 shows the microstructures of two wood particle types (i.e., coarse and fine particles). The coarse-wood particles present a stratified structures (see graphs (a) and (b)), while the fine-wood particles show porous structures (see graphs (c) and (d)). Fig. 4.10 presents the comparison of absorption coefficient for these two type materials. According to the results, we observe the acoustic absorption coefficients of the fine-wood-particle samples are better than the coarse type (the solid and dash lines represent fine-wood-particle samples, while the dash-dot line represents coarse-wood-particle samples). It implies that porous structure of wood particles can improve ability of sound energy dissipation, in particular for high-frequency sound components (Neithalath et al., 2005; Yang and Sheng, 2017).

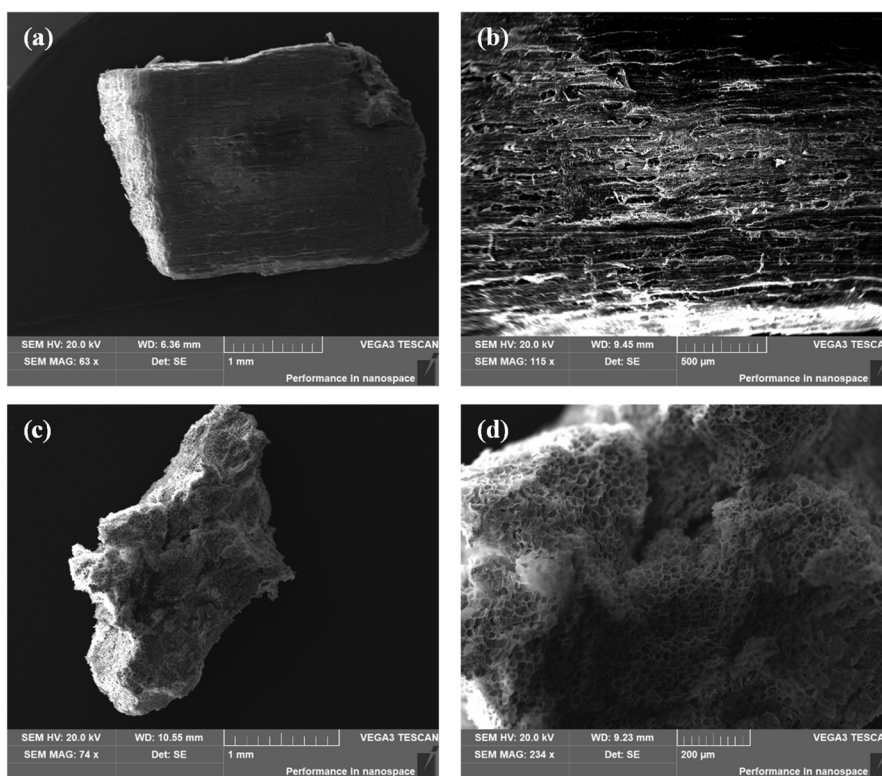


Fig. 4.9: SEM images of wood particles: (a) and (b) Microstructure of coarse-wood particles (3–6 mm in diameter); (c) and (d) Microstructure of fine-wood particles (1–2 mm in diameter).

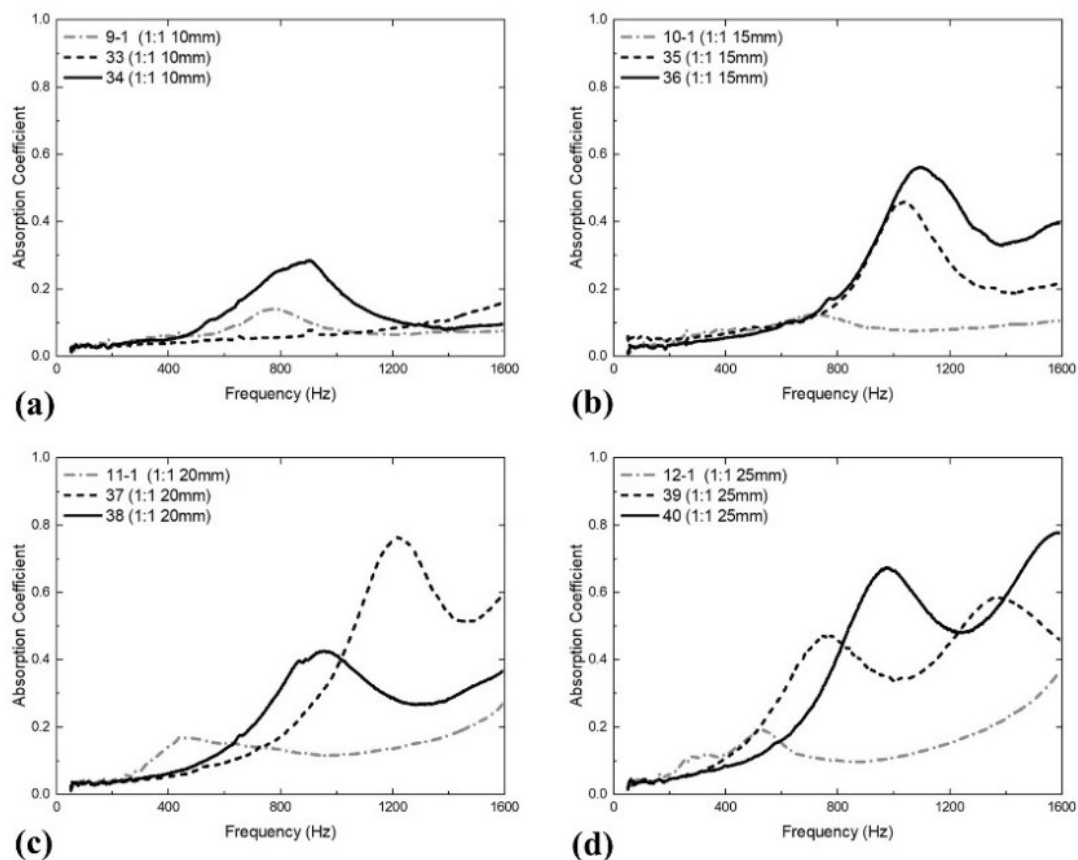


Fig. 4.10: Absorption coefficient of samples fabricated by different kinds of wood particle with 1:1 wood-rubber ratio. (a) Thickness of 10 mm; (b) Thickness of 15 mm; (c) Thickness of 20 mm; and (d) Thickness of 25 mm.

The influence of the amount of epoxy resin usage is presented in Fig. 4.11 and Table 4.3. The production processes for the test samples, i.e., thickness and wood-rubber ratio, are exactly the same, except for the weight amount of epoxy resin. As a result, we found that there is no dramatic change between these two data sets. In other words, the acoustic absorption coefficient would not be much affected by the amount of epoxy resin usage for binding the wood and rubber particles in the test samples.

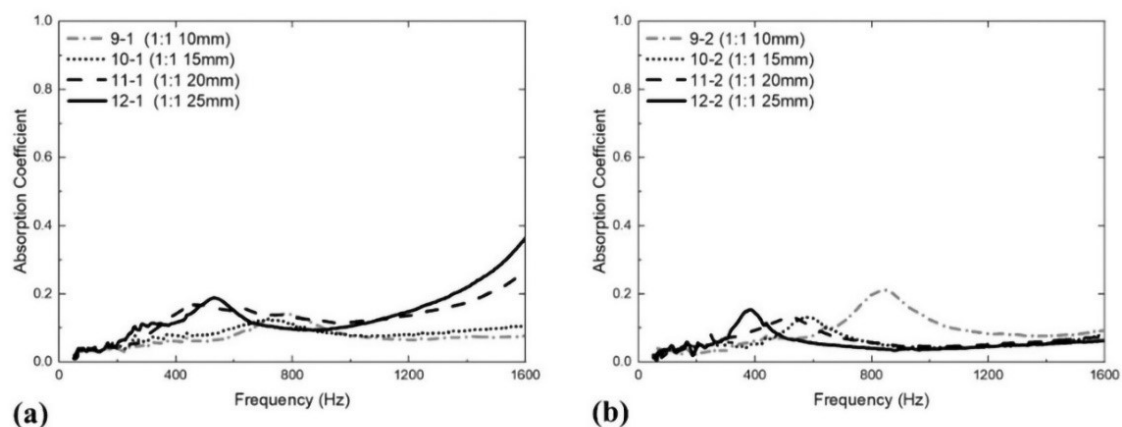


Fig. 4.11: Absorption coefficient of the samples with different amounts of epoxy resin.

Table 4.3: Comparison of epoxy resin usage in sample fabrication.

Sample No.	Dosage of epoxy resin (g)	Dosage increased (%)	Sample No.	Dosage of epoxy resin (g)	Dosage increased (%)
9-1	34.9		11-1	47.5	47.5%
9-2	40.6	16.3%	11-2	77.9	47.5%
10-1	42.4	59.4%	12-1	54.6	54.6%
10-2	67.6		12-2	98.2	

4.2.4.2 Transmission loss analysis

In general, the transmission loss (TL) of materials describes the accumulated decrease in the intensity of a waveform energy as a wave propagates outwards from a source, or as it propagates through a certain area or through a certain type of structure. Mathematically, transmission loss index can be obtained by the four-microphone transfer function matrix (see Eq. (4.16)). The larger the transmission loss value is, the better the sound insulation characteristics of the samples are. Relevant figures are plotted to illustrate the effectiveness of transmission loss among various test samples. Noted that the details of samples can be found in Tables 4.1 and 4.2.

Fig. 4.12 shows a comparison of various samples with the same wood-rubber

ratio but different thickness values, while Fig. 4.13 shows a comparison of samples with the same thickness but different wood-rubber ratios. The thicker samples naturally lead to a higher TL value, resulting in a better sound insulation performance. The TL values would increase with sound frequency and reach to the maximum for each type at 150, 450, 1100 and 1400 Hz. A general tendency of TL data would go up as the thickness of the samples increases. For the wood-rubber composite samples, the 1:1 ratio samples have a better sound insulation performance with over 10 dB (see Fig. 4.12(c)). Compared to the pure-rubber samples, the latter one has a peak value of 54 dB. It implies that larger amount of rubber particles can improve the TL value.

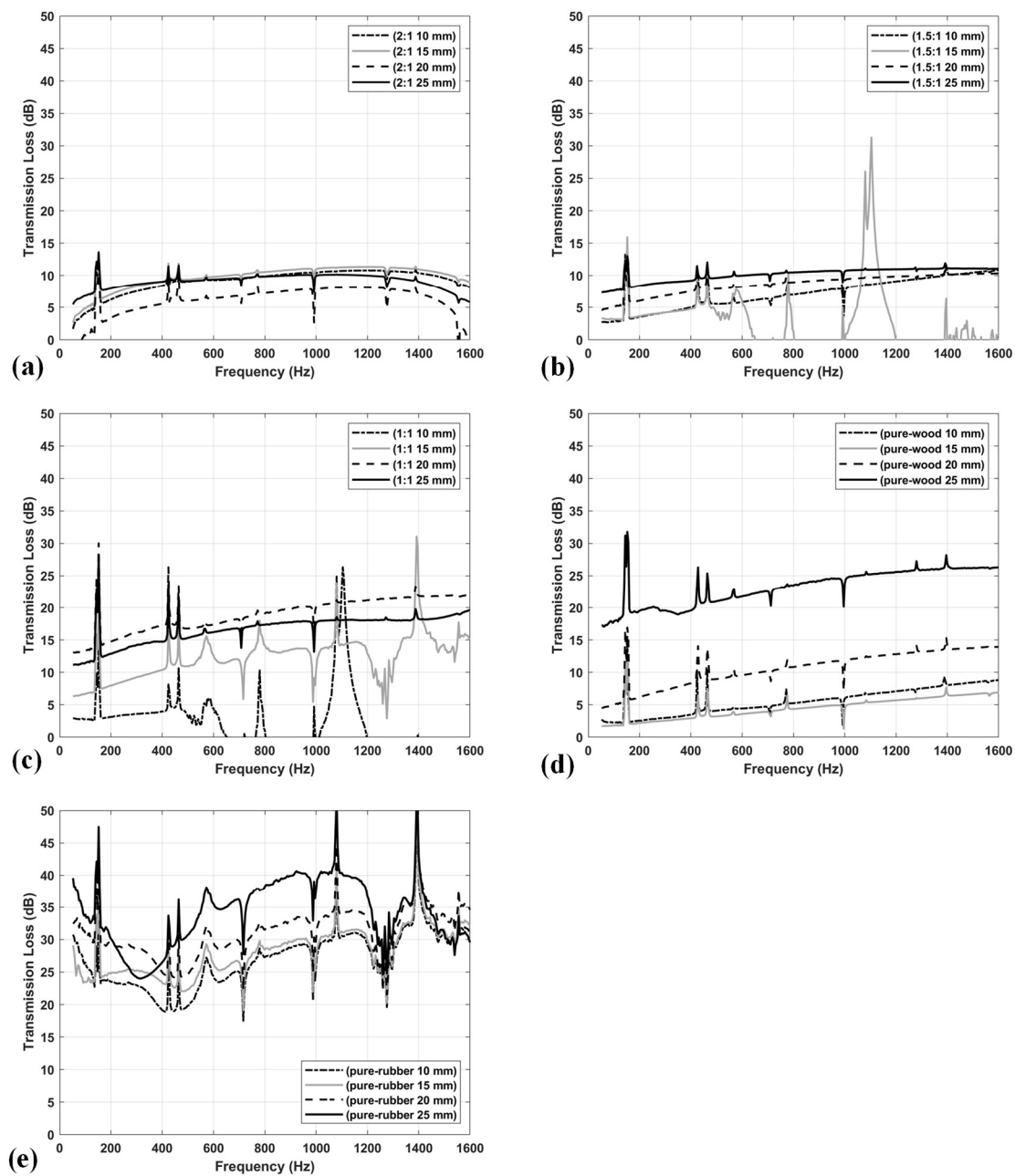


Fig. 4.12: Transmission loss of the testing samples with same wood-rubber ratio but different thickness. (a) Wood-rubber ratio 2:1; (b) Wood-rubber ratio 1.5:1; (c) Wood-rubber ratio 1:1; (d) Pure-wood samples and (e) Pure-rubber samples.

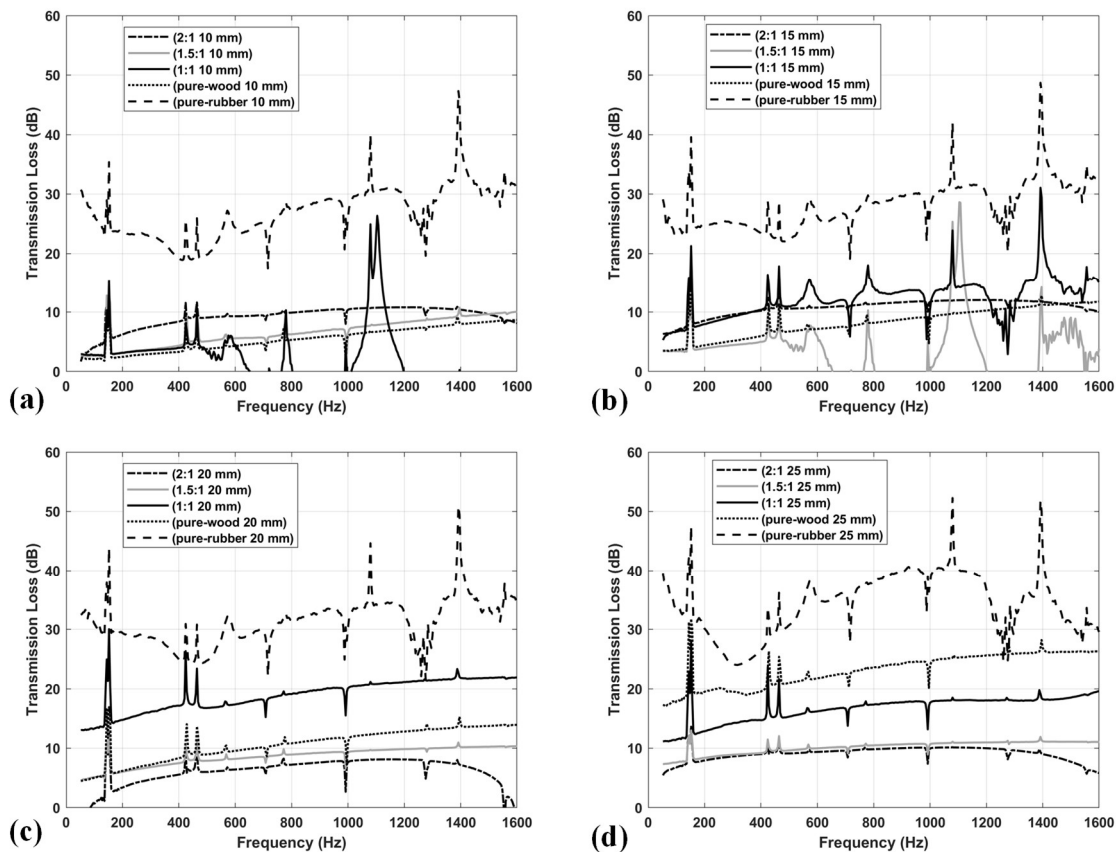
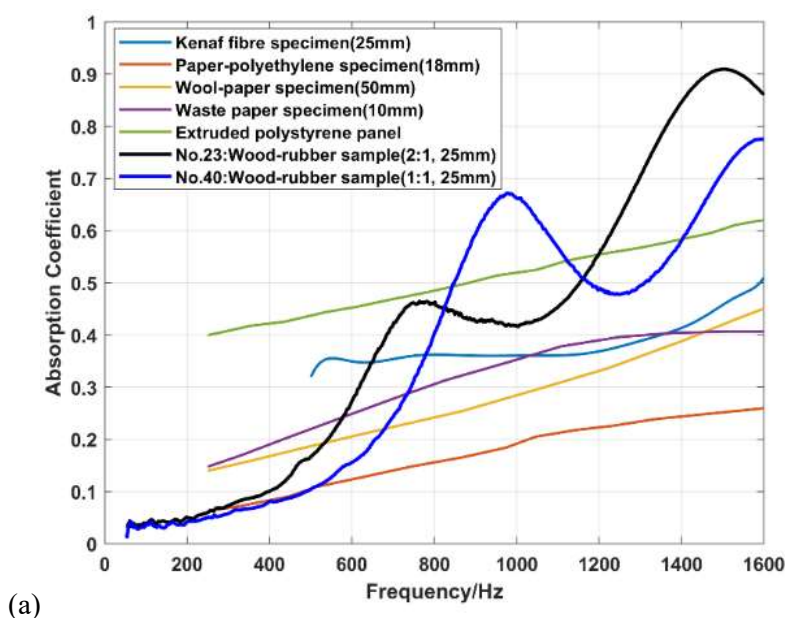


Fig. 4.13: Comparison of acoustic transmission loss of various test samples with same thickness. (a) Thickness of 10 mm; (b) Thickness of 15 mm; (c) Thickness of 20 mm; and (d) Thickness of 25 mm.

4.2.4.3 Comparison study of acoustic performance

In order to compare the innovative solutions with standard materials available on the market, a comparison study is presented herein. Fig. 4.14(a) presents acoustic absorption values about the sustainable panels, including kenaf fiber specimen (Lim et al., 2018), paper-polyethylene specimen (Buratti et al., 2016), wool-paper specimen (Buratti et al., 2016), waste paper specimen (Buratti et al., 2016), extruded polystyrene panel (Buratti et al., 2016)) and recycled wood-rubber composite sample (i.e., thickness 25mm, wood-rubber ratio 2:1 and thickness 25mm, wood-rubber ratio 1:1). According to the results, the wood-rubber composite samples showed higher absorption coefficient in high frequency range (1200–1600 Hz), and the maximum value was up to 0.8. It revealed the superior absorption performance of wood-rubber materials. Fig. 4.14(b) shows the comparison of transmission loss between the hybrid fiber metal laminated panels (i.e., sample MLSP-I and MLSP-II) (Pai et al., 2021) and the proposed wood-rubber composite sample (1:1, 25 mm).



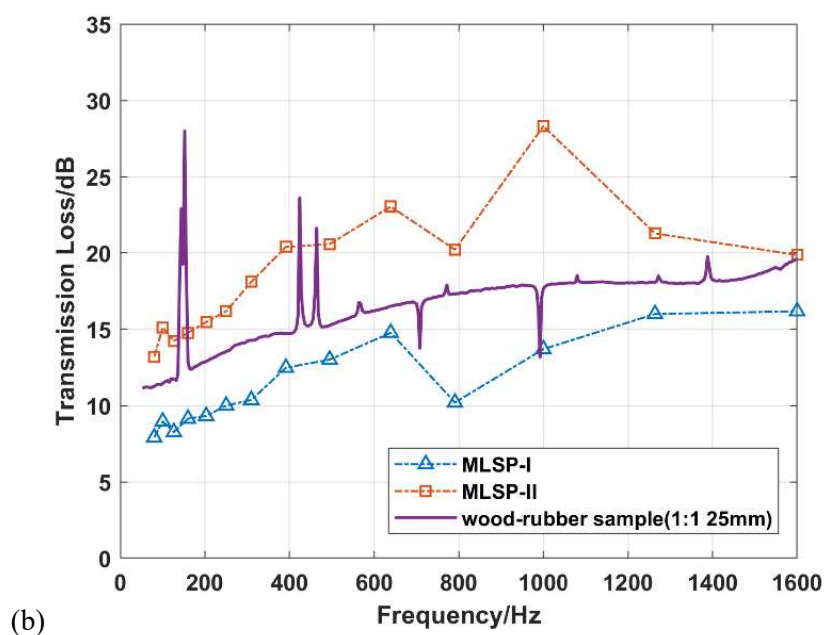


Fig. 4.14: Acoustic performance comparison. (a) Absorption coefficient index: including kenaf fiber specimen (Lim et al., 2018), paper-polyethylene specimen (Buratti et al., 2016), wool-paper specimen (Buratti et al., 2016), waste paper specimen (Buratti et al., 2016), extruded polystyrene panel (Buratti et al., 2016)) and recycled wood-rubber composite sample (i.e., thickness 25mm, wood-rubber ratio 2:1 and thickness 25mm, wood-rubber ratio 1:1), and (b) Transmission loss index: including hybrid fiber metal laminate panels (MLSP-I and MLSP-II) (Pai et al., 2021) and recycled wood-rubber composite samples (i.e., 1:1 and 25 mm).

4.3 Characterization of the PVDF thin-film materials

4.3.1 Fabrication of a PVDF thin-film speaker

PVDF film materials are considered as a secondary source in ANC system herein. Compared to conventional electromagnetic speakers, the former provides higher flexibility and transparency at a smaller scale. As a thin-film speaker, it is structurally suitable for coupling with the composite panels to form a dual-function barrier. The section below outlines the frequency response measurement of a PVDF thin-film speaker. The sound pressure of a piezoelectric polymer sheet at a certain distance is directly proportional to the applied electric field strength. For a given voltage, the thinner the film is, the higher the sound pressure can be generated (Bies, 2018). The SPL can be expressed as:

$$P_s = \sqrt{\frac{1}{T} \int_0^T p^2(t) dt} \quad (4.17)$$

$$SPL = 20 \log_{10} \left(\frac{P_s}{P_{ref}} \right) \text{ (dB)} \quad (4.18)$$

where $p(t)$ is the instantaneous sound pressure, T is the sampling time, P_s is the time-averaged pressure determined over a measured time interval T at a certain distance from the sound source, and $P_{ref} = 20 \times 10^{-6}$ Pa. Noted that the SPL value is measured by the sound level meter.

Fig. 4.15 shows the structure of the proposed speaker fabricated with a plastic film diaphragm (i.e., PET thin-film) and piezoelectric polymer (i.e., PVDF thin-film). Its configuration covers three main parts: a vibrating PVDF diaphragm coated by silver ink as electrodes, a PET thin-film and a supporting structure made of acrylic

materials. The supporting frame is used to secure the PVDF thin-film. In this study, a 28- μm thickness PVDF thin-film was used, see Fig. 4.15(b). Silver ink paints were coated on the surface of the PVDF thin-film as electrodes. By feeding a voltage supply, it can create a mechanical strain to generate sound waves.

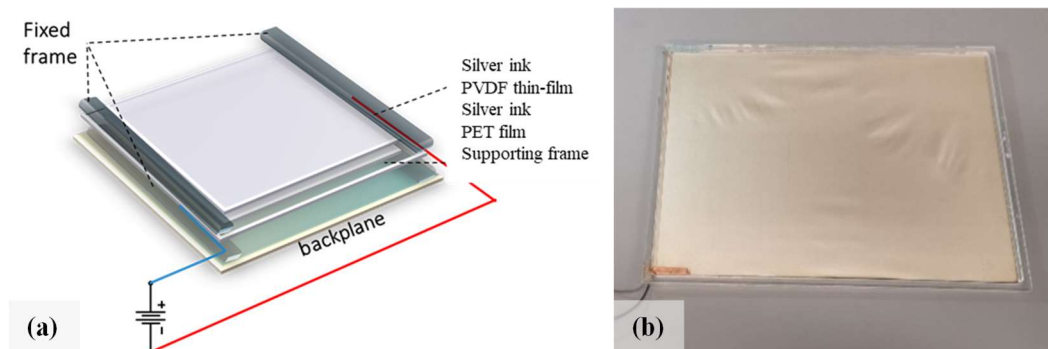


Fig. 4.15: (a) Schematic diagram of a PVDF thin-film speaker; and (b) A fabricated PVDF thin-film speaker.

4.3.2 Experimental setup and testing condition

Fig. 4.16 shows the experimental setup for frequency response measurement. Herein, three important factors are identified (Sugimoto et al., 2009; Ohga et al., 2010), namely (i) the steady-state response (SSR) and harmonic distortion (HD); (ii) the SPL responses versus input voltage levels; and (iii) the directivity effect. The following are the hardware and software used for acoustic measurement.

- Laboratory environment: In-house semi-anechoic chamber.
- Instruments: Microphones (*B&K 1/2 in. type 4189*), Pre-amplifier (*ENDEVCO model 4416b*), Oscilloscope (*Keysight DSOX3014T*), Signal generator (*Keysight 33500*), High-speed voltage amplifier (*NF-HSA 4014*); and Sound level meter (*SVAN 985*).
- Software: *SVANPC++*.
- Measurement distance: 1 m.

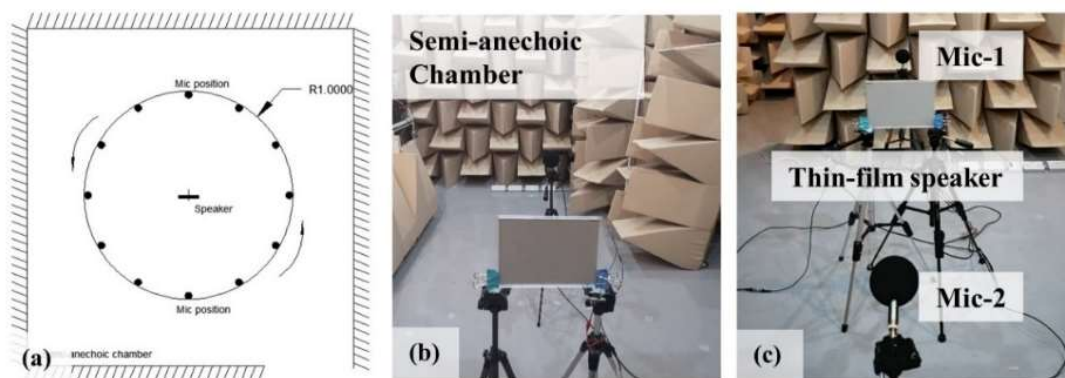


Fig. 4.16: Experimental setup for acoustic response testing of the PVDF thin-film speaker. (a) Schematic diagram of setup; (b) and (c) Pictures of microphones and the PVDF thin-film speaker position within the semi-anechoic chamber.

4.3.3 Response analysis of PVDF thin-film speaker

To obtain the steady-state responses, the output from loudspeakers often suffers from linear and non-linear distortions. Linear distortion can be seen as a non-flat frequency response and/or a non-flat group delay. Non-linear distortion is mainly due to the phenomenon of a non-linear relationship between the “input” and “output” signals. To measure these distortion effects, a specific frequency (e.g., fundamental frequency) plays a critical role at a particular voltage power level. By sweeping the input signals to obtain the fundamental frequency, we can reveal the frequency-dependent harmonic distortion relationship.

Harmonic distortion can be expressed in terms of decibel (dB) unit or a percentage (Dubois, 1996). Theoretically, the second-order harmonic distortion is generally caused by asymmetries in the system. The third-order harmonic distortion is generally caused by the “clipping” effect in the system, which can originate from the components in the electronics hardware. Odd-order harmonics can generally result in effects with greater severity than even-order harmonics (Morse, 1976; Sugimoto et al., 2009). In addition, the severity of these effects at high-order harmonics is

generally considered lower than the second- and third-order harmonics. It can be considered as reasonably low levels in a well-designed system. Ideally, the lower the harmonic distortion is, the perceived sound generates greater clarity and more transparency as created from the loudspeaker output. In terms of the frequency range division, we consider 30–150 Hz, 150–500 Hz (low-to-mid frequency range) and 500–5000 Hz (mid-to-high frequency range). Above 5000 Hz, it is regarded as high frequencies. The effect of harmonic distortion is generally non-linear in nature, and an increase of 10 dB in the test signal typically results in a far greater increase in the level of harmonic distortion. In general, large-sized loudspeakers may suffer from less harmonic distortion than smaller ones when they are played under the same levels and conditions.

Fig. 4.17 depicts the steady-state response and harmonic distortion of the PVDF thin-film speaker. In Fig. 4.17(a), the red line denotes the steady-state response corresponding to the driven frequency. As we can essentially consider the acoustic performance of PVDF speakers at low and middle frequencies, therefore the steady-state responses were thus measured in the range of 50–4000 Hz. In Fig. 4.17(b), the relationship between the input audio signals (i.e., amplitudes shown in the signal generator) and the harmonic distortion levels are presented. Typically, the distortion level of the loudspeakers is highly dependent on input signal levels. A frequency of input signal levels at 1 kHz was chosen in this study. The red line represents steady-state responses SPL by increasing the input signal levels. As PVDF thin-films are high-impedance materials, a high input voltage level is required. A higher input signal level can contribute to the steady-state response, however the second- and third-order harmonic distortion are relatively large. Noted that the applied voltage is stepped up to 36 V (peak-to-peak), which was measured by an oscilloscope.

Fig. 4.18 shows the output SPL with increasing input signal power. With an input voltage by audio signal generator (i.e., 4 , 8 and 10 V), the interesting frequency range

is from 100 to 1600 Hz. The amplifier gain is similar as aforementioned. A polynomial curve fitting is adopted to express the developing trend. Basically, a higher driving voltage lead to a flat SPL output at low frequency range. For instance, an input voltage of 10 V (i.e., green dotted-line curve) can provide a flat frequency response from 400 to 1200 Hz. The results imply that the speaker can be controlled by adjusting the input voltage.

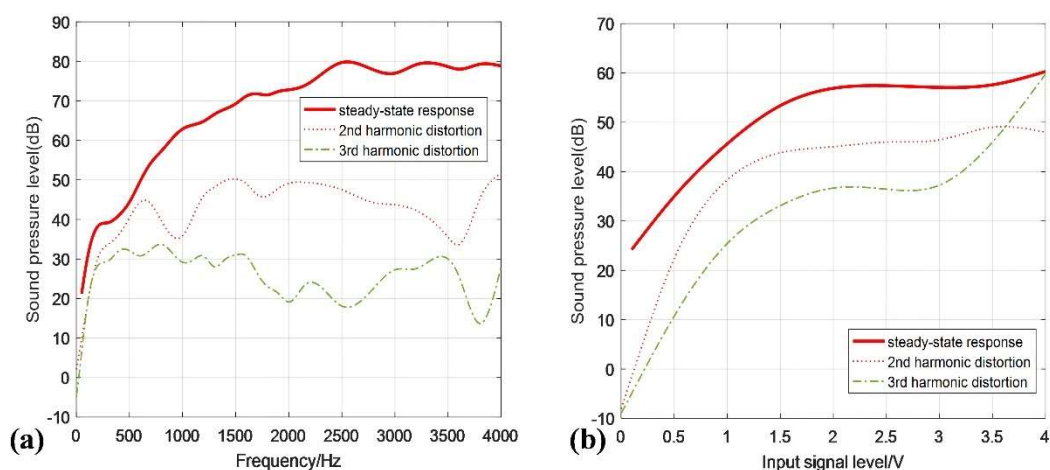


Fig. 4.17: (a) Steady-state responses and harmonic distortion of the PVDF thin-film speaker; and (b) Relationship between input signals (at 1 kHz) and harmonic distortion levels of a PVDF thin-film speaker.

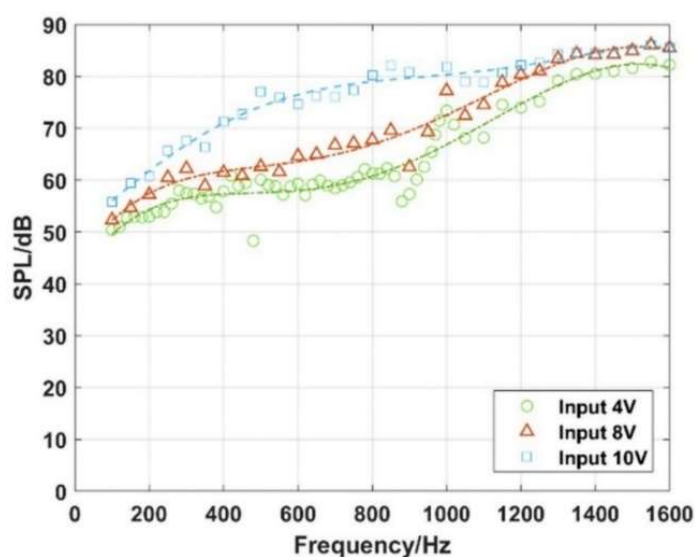


Fig. 4.18: Frequency response curves of a PVDF thin-film speaker.

Directivity is a term used to describe the change of SPL responses of speakers at off-axis angles. A wide-directivity speaker can generate a consistent SPL between the on-axis and off-axis. However, the SPL output of a narrow directivity speaker is substantially different between the on-axis and off-axis. According to the ISO standard (ISO, 2010), the directivity of speakers is defined as an angle of coverage of the speaker output, which can be used to show the acoustic performance of speakers in various directions. For effective noise control, it is desirable in high-quality design that a speaker can generate sound fields equally in all directions, such that a uniform noise mitigation within a space can be achieved.

Fig. 4.19 presents directivity measurement of a PVDF film speaker at a measurement distance of 1 m. The results show that all of the measured positions are Over 50 dB, which reveals a smooth pattern. The symmetry between the upper- and lower-bound hemispheres is slightly different. Although the SPLs are higher in the lower-bound hemisphere, the directivity curve is almost circular in the whole range with a decent directivity. This confirms omnidirectional performance of the proposed speaker.

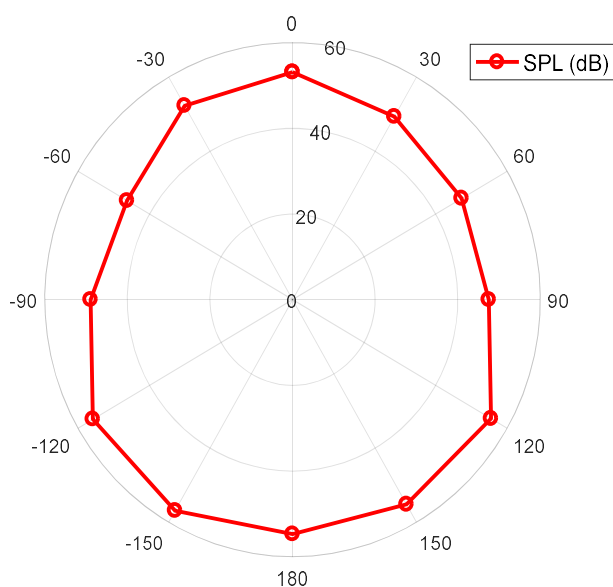


Fig. 4.19: Directivity of PVDF thin-film speaker.

4.4 Design and implementation of scale-down model

4.4.1 Sound field simulation

A simplified two-dimensional numerical simulation is carried out to show the sound fields in the presence of a noise barrier. The present numerical simulation results are used to offer some guidelines for the preparation of a scale-down model, while the effectiveness of the barrier is further demonstrated via the in-house laboratory test.

Fig. 4.20 shows the general configuration of the numerical model with an air domain of 1.8 m (in length) and 0.8 m (in height). A monopole point source is used as a sound source. The separation distance (i.e., d_1 as shown in Fig. 4.20), which is the distance between the point source and the passive noise barrier, is a variable. A parametric study is conducted to determine an appropriate barrier position to achieve a better shielding effect. The dimensions of the barrier (i.e., the white area in Fig. 4.20) are 0.46 m (in height) and 0.025 m (in thickness), respectively.

The outer domain of the air field (see Fig. 4.20) is a perfect match layer (PML) to avoid the reflection of sound fields (Ng, 2019; COMSOL, Ver. 5.4). PML is a region to isolate the computational domain from outer interference. It is an additional domain which can absorb all the incident wave energy without producing reflection. The principle of PML is based on a formulation that can transform the complex coordinate to the actual coordinate. Noted that the wave impedance issue is not considered during the transformation process (Ng, 2019). For the incident wave within the coordinate ξ , the transformation is given by:

$$\xi' = \text{sign}(\xi - \xi_0) |\xi - \xi_0|^n \frac{1}{\partial \xi^n} (1 - i) \quad (4.19)$$

where L is the scaled width of PML, ξ_0 is the coordinate of the inner PML boundary, $\partial \xi$ is the actual width of PML and n is the scaling exponent for each PML. The imaginary coordinate can be seen as a buffer zone, which is to extend the actual width of PML during the calculation process. The energy of incident wave would occur dissipation within the buffer zone, thereby resulting in little or even no reflection wave generated by the outer boundary.

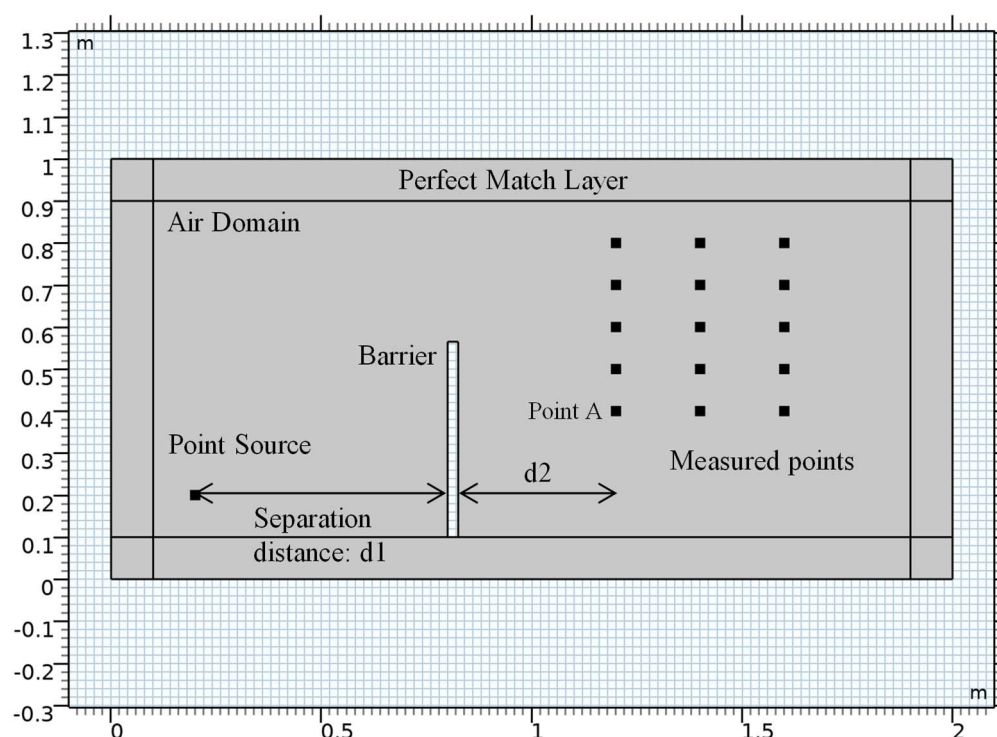


Fig. 4.20: General configuration in the numerical model.

The Helmholtz equation is then used to compute the SPL distribution in the frequency domain under a quiescent background condition (Moffett, 1970; Temkin, 1994; Blackstock and Atchley, 2001), which is given by:

$$\nabla \cdot \left(-\frac{1}{\rho_c} (\nabla p_t - q_d) \right) - \left(\frac{\omega}{c_c} \right)^2 \frac{p_t}{\rho_c} = Q_m \quad (4.20)$$

where ρ_c refers to the density of medium and c_c is the speed of sound in a medium, q_d

denotes the dipole domain source that is zero in this study, Q_m is a monopole domain source, p_t is the total pressure of sound (the total pressure p_t includes the acoustic variations to the ambient pressure and background pressure), and ω is the angular frequency.

Consider the environment of the semi-anechoic chamber, the boundary conditions of air domain are assumed to be non-reflective (Ng, 2019). The ground surface is considered as reflective surface. We assume the noise barrier surface is an absorptive thin layer backed by a thick one. With reference to the absorption coefficient of the composite wood-rubber sample (25-mm thick), we assume the normal absorptive coefficient $\alpha_n=0.25$. The governing equation can be expressed as (COMSOL, Ver. 5.4):

$$-n \cdot \left(-\frac{1}{\rho_c} (\nabla p_t - q_d) \right) = -\frac{i\omega p_t}{Z_i}$$

$$Z_i = \rho_c c_c \frac{1+R}{1-R} \quad (4.21)$$

$$R = e^{i\phi} \sqrt{1-\alpha_n}$$

where α_n is the normal absorption coefficient, Z_i is the acoustic impedance, p_t is the total pressure of sound, and R is the reflection coefficient. The point source is placed to generate sound under various frequencies. The sound intensity to consider the monopole amplitude can be expressed by (COMSOL, Ver. 5.4):

$$S = e^{i\phi} \sqrt{\frac{2\rho_c \omega I_{rms} d_{src}}{2\pi}}$$

$$Q_m = \frac{4\pi}{\rho_c} S \delta(x - x_0) \quad (4.22)$$

where d_{src} denotes the distance from the source where the sound intensity I_{rms} is

specified, and ϕ is the phase of the source, $\delta(x-x_0)$ is the delta function in two dimensions, and S is the monopole amplitude. Mesh grids used in this numerical study are free triangular shapes. The size of the maximum element is smaller than one fifth of the wavelength (i.e., 6.86 mm), while the size of the minimum element was smaller than one sixth of wavelength (i.e., 5.72 mm) (Ng, 2019; Won and Choe, 2020; COMSOL, Ver. 5.4). Consider the frequency sweeping in the range of 50–10000 Hz, the initial amplitude of the monopole source is set as 90 dB as a point source.

4.4.2 Barrier implementation and measurement setup

A scale-down model was prepared for the in-house laboratory test. The scale ratio was selected at 1:4 as a miniaturized model for the laboratory test. A prototype was built in the semi-anechoic chamber to characterize the performance. A 3-by-3 array frame structure was prepared to form the laminated components (i.e., a wood-rubber panel with an embedded piezoelectric thin-film) together. Prefabricated and demountable components can be used to simplify the assembly procedures. We used a metal holding frame to provide sufficient mechanical stiffness as a supporting frame. Card slots were predesigned in the holding frame, which can allow the prefabricated components to fit the holding frame along the tracks. This setup is similar to modular structures for easy manufacturing and installation.

Fig. 4.21 presents the schematic diagram of the barrier. It is a U-like supporting frame with an inserted wood-rubber composite panel and an embedded PVDF thin-film speaker. Each rectangular wood-rubber panel was prepared as 200 mm (length) \times 140 mm (width) \times 25 mm (thickness). Fig. 4.21(b) shows the assemble structure with an overall height of 465mm. Three major procedures to form a dual-function barrier included: (i) prefabricating composite panels and PVDF thin-film speakers independently; (ii) inserting the recycled composite panels and embedded PVDF thin-film into the U-like supporting frame; and (iii) fixing the integrated modulus into

the holding frame.

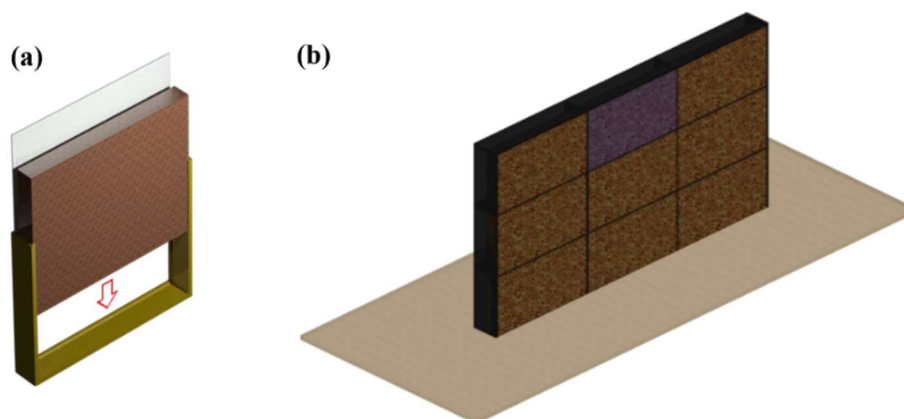


Fig. 4.21: Schematic diagram of dual-function barrier. (a) A U-like supporting frame with an inserted wood-rubber composite panel and an embedded PVDF thin-film speaker and (b) Schematic diagram of a 3-by-3 array dual-function noise barrier.

Referring to the relevant standards (ISO, 1997), we conducted a “*direct method*” to measure the SPLs at the monitor position and the receiver positions for both “before” and “after” the barrier installation. To simplify the measurement, we assumed that the noise barrier can be extended infinitely. Measurements were carried out on the wave propagation direction at distances to align along the central axis from the loudspeaker. The dependence of the emitted waves with respect to height was obtained by varying distance from the sound source and the height of the microphone array. Under this testing circumstance, the attenuation magnitude in terms of sound pressure level and the cover range of the barrier in terms of distance and height can be determined to demonstrate the barrier performance. Utilizing a simplified two-dimensional profile between distance and height, the shadow zone representing areas of sound attenuation can be determined along the central axis from the noise barrier.

The insertion loss (IL), which can be defined as the difference in SPLs with and without the presence of a passive noise barrier, can be expressed as (ISO, 1997; Dragonetti et al., 2003; FHWA, 2018,2021):

$$D_{IL} = (L_{m,A} - L_{m,B}) - (L_{r,A} - L_{r,B}) \quad (4.23)$$

where $L_{m,A}$ (“after the barrier installation”) and $L_{m,B}$ (“before the barrier installation”) are the SPLs at the monitor position with and without the barrier, respectively. $L_{r,A}$ and $L_{r,B}$ are the SPLs at the receiver positions with and without the barrier, respectively. Noted that the monitor position was used to assess the uncertainty of measurements.

Fig. 4.22 presents the experimental setup of the barrier. A loudspeaker was performed as a noise source and a microphone array was used for data acquisition. The distance between the loudspeaker and the noise barrier was set as d_1 , while d_2 was determined as the distance between the noise barrier and the measurement points (see Fig. 4.22). A sound field profile was measured along the central line of the noise barrier, as shown in Fig. 4.22(b). The microphone array was placed on different positions with various distance (d_2) along the central line of the barrier for data acquisition. The microphone height was ranged specifically from 0.3 to 0.6 m, namely channels 1, 2, 3, and 4, respectively. Two microphones were set lower than the barrier top (i.e., channels 1 and 2), while two microphones were set higher than the barrier wall (i.e., channels 3 and 4). To simulate the situation of an infinite barrier preferably, highly absorptive wedge boundaries (i.e., two lines of triangle absorptive wedges as shown in Fig. 4.22(c)) were placed along both sides of the noise barrier. This arrangement can minimize the effects of reflection disturbance and sound leakage. Using highly absorptive wedge boundaries along both sides of the noise barrier also can eliminate the effects of various sound-propagation paths.

To characterize the effectiveness of the barrier, the study of sound field includes two parts. To demonstrate the high-frequency noise control (i.e., above 1500 Hz), measurement is conducted under two scenarios, namely: (i) without any barrier; and (ii) with the passive barrier (i.e., wood-rubber composite panel). Gaussian noise with wide-frequency bandwidth and flat power spectrum was considered as sound source.

The insertion loss (IL) index can be used to identify the sound insulation performance of the passive barrier. To further investigate the feasibility of low-frequency control (i.e., 800–1500 Hz), measurement was conducted under three scenarios, namely: (i) without any barrier; (ii) with the passive barrier (i.e., wood-rubber composite panel); and (iii) with the dual-function barrier (i.e., integrating the wood-rubber composite panel and the PVDF thin-film speaker together). Peak and narrowband noise at a specific frequency (e.g., a sinusoidal signal) combined with Gaussian noise was considered as sound source. Phases of the secondary source were manually tuned (Sharifzadeh Mirshekarloo et al., 2018) to optimize the control effect at the measurement points.

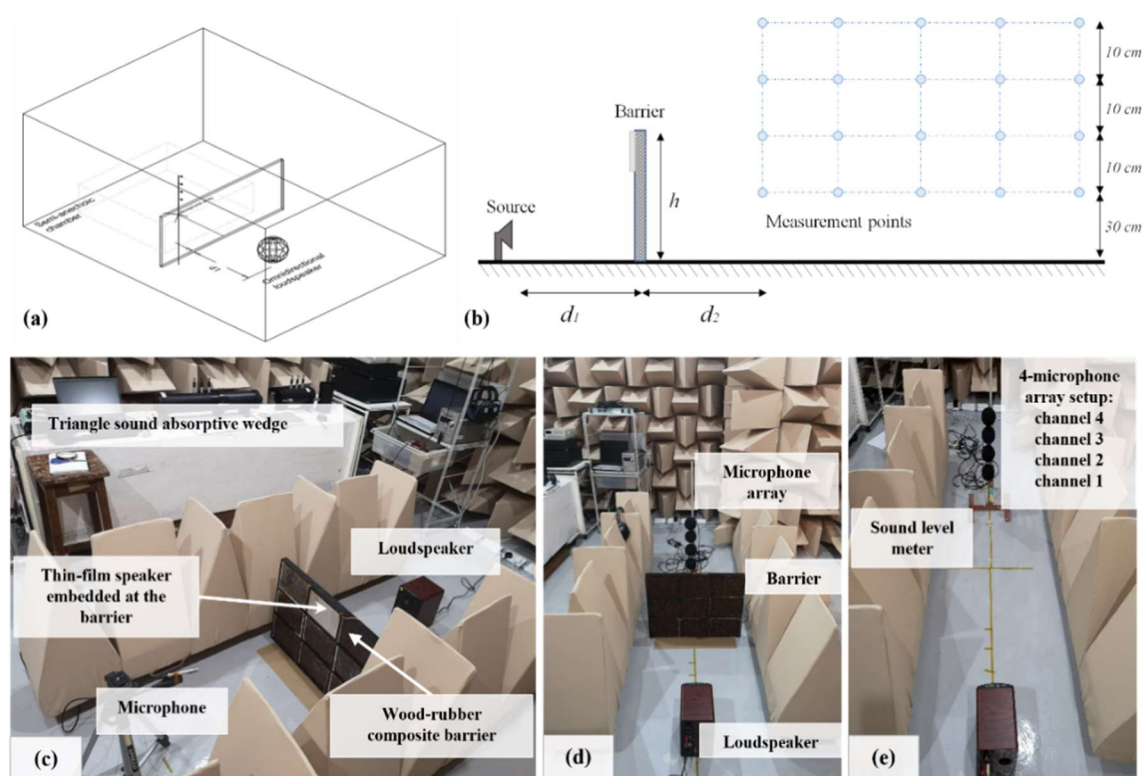


Fig. 4.22: Experimental setup of scale-down model: (a) and (b) Schematic diagram of a scale-down model setup for performance identification of the dual-function noise barrier; (c) and (d) A dual-function barrier setup in the semi-anechoic chamber; and (e) Acoustic measurement for the scale-down model experiment.

4.4.3 Effectiveness of barrier

4.4.3.1 Sound field analysis

Rebuilding a realistic scene, the sound generation and diffusion effect can be visually observed for analysis. Then, an optimal scheme at the specific context can be determined. A two-dimensional acoustic pressure model is presented herein to show the effect of the separation distance (i.e., d_1) and to visualize the variation of sound fields in frequency domain. The displaying position of passive noise barriers may affect the diffraction angle of sound waves (EPD, 2003; Sahraei and Ghaemi, 2013), thereby decreasing the shielding effects of barrier (EPD, 2003; Fan et al., 2013; FHWA, 2018,2021). The separation distance d_1 was set in the ranged of 0.1–0.5 m. In Fig. 4.23, various SPL profiles versus frequencies obtained at point A are presented (as shown in Fig. 4.20), where was 0.5 m from the barrier and 0.3 m from the floor. The blue solid line represents the SPLs without a barrier, while the dash lines reveal the SPL profiles with the presence of barrier. A noise reduction can be observed as shown in the orange shadow region. The reduction can be realized by 10–20 dB.

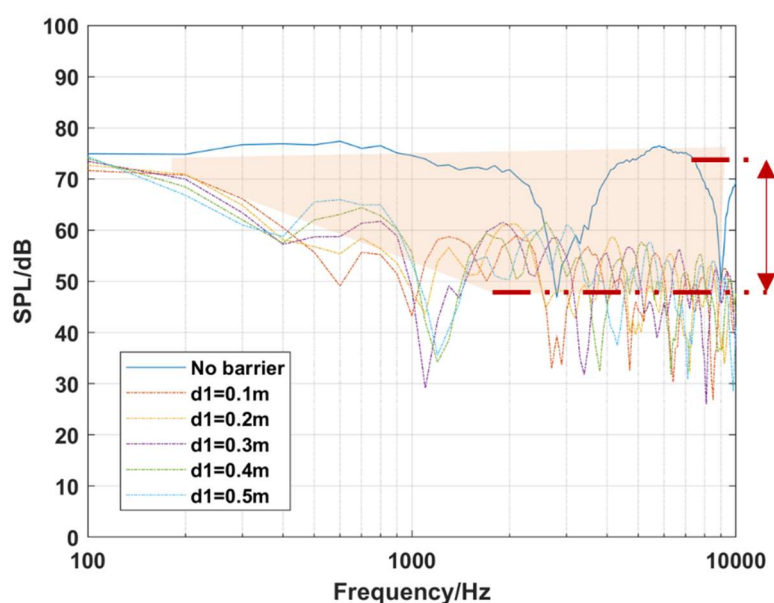


Fig. 4.23: SPLs at measurement point A with different separation distance (d_1).

Fig. 4.24 presents the contour plot of sound fields at 1500 Hz with and without a passive noise barrier. According to the diffraction theory (Maekawa, 1968), we can draw a straight line from the noise source to the top edge of the noise barrier, so called straight path. A shadow zone can be formed between the straight path and the ground floor, as shown in Fig. 4.24(b).

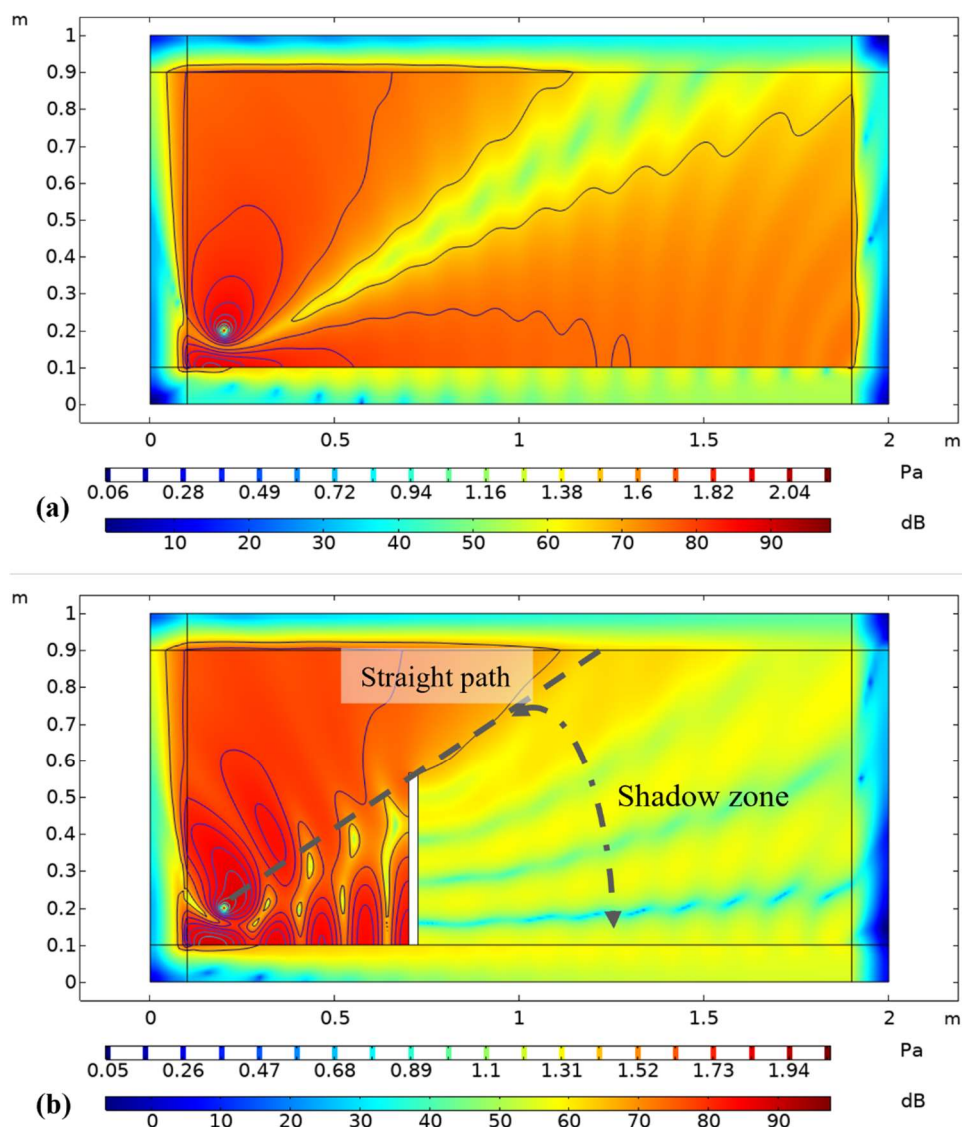


Fig. 4.24: Numerical simulation of sound fields at 1500 Hz: (a) without a passive noise barrier; and (b) with a passive noise barrier.

4.4.3.2 SPL measurement results and discussions

According to the sound field analysis, a scale-down model was implemented to measure the SPL difference before and after the barrier installation. The distance between the barrier and noise source was set as $d_1=0.5$ m.

By comparing with the testing results with and without presence of barrier, the passive control performance at high-frequency range can be demonstrated. Fig. 4.25 presents the insertion loss in the presence of the passive barrier with various distances between the barrier and measurement points (i.e., d_2). The results indicate a significant sound insulation performance of passive barrier, especially in the middle- and high-frequency range (e.g., above 1500 Hz). A maximum noise attenuation occurred at microphone height 0.3m (as shown in blue line) with an insertion loss up to 20 dB, which reveals the shielding effects of the passive barrier. For the range less than 1000 Hz, the sound reduction was 2–8 dB.

To further illustrate the sound field distribution, Fig. 4.26 presents the contour maps above 2000 Hz for two illustrative cases (i.e., without any barrier and with the passive barrier) at the specific measurement range (i.e., 0.3–0.6m in height and 0.5–1.0m in distance d_2). According to the comparison results, a global noise attenuation can be achieved in presence of the passive barrier. The maximum SPL reduction can be up to 24 dB by displaying a wood-rubber composite barrier. In general, the recycled materials (i.e., wood-rubber material) can illustrate fairly good sound insulation performance as an absorptive-type passive barrier.

To further consider low-frequency noise components with peak and narrowband characteristics, a piezoelectric thin-film is investigated as an auxiliary part. The SPLs measurement was conducted for three illustrative cases (i.e., without any barrier; with the passive barrier only; and with the dual-function noise barrier). A narrowband sinusoidal wave with gaussian noise was generated for the test. Figs. 4.27–4.30

present the variation of SPLs at each measurement point at the frequency range of 800–1500 Hz. The black line represents the measured SPLs without any barrier between the sound source and the receiver. The green line indicates the SPLs with displaying passive barrier only. The red line shows the optimal results in the presence of the dual-function barrier. Noted that phases of the secondary source were manually tuned. The results indicate that an induced anti-noise source (i.e., flexible PVDF thin-film speaker) is feasible to further reduce SPLs on basis of the passive insulation (up to 3–5 dB) at some measurement points. The insertion loss results (i.e., SPLs difference) are presented in Figs. 4.31–4.34. The presence of the wood-rubber passive barrier is capable of reducing 10 dB or even more at mid- and high- frequency range. Enhance performance can be observed at narrowband frequency range. The limited effectiveness at a frequency range of 800–1100 Hz shall be due to the insufficient SPL response of thin-film speaker. Yet, due to the interference effect, deviations would inevitably occur, resulting in the fluctuation and disturbance of sound field. In general, using the ANC method via PVDF thinfilm is only available for narrowband frequency and a small-scale point control (e.g., at measurement point with height 30cm and distance 50 cm).

Contour maps are plotted along the centre axis of the barrier, which is to evaluate the variation of SPLs in a two-dimensional sound field between the distance and height. Two important metrics that can affect the SPLs in sound fields are the measuring distance (d_2) and frequency. Fig. 4.35 presents the contour maps of SPL distribution separately with frequency of 1100–1500 Hz. Three different cases are indicated in order from left to right: (i) without any barrier, (ii) with the passive barrier only, and (iii) with the dual-function barrier. In general, the reduction of SPLs can be achieved above 10 dB using the passive barrier only. Further attenuation of 3 dB can be observed at some measurement points with assistance of active control, but a part of measurement space would be compromised. For example, we can

observe a lower SPL at the separation distance of 50 cm in the presence of active control, however, the effect of constructive interference occurs at 120 and 130 cm.

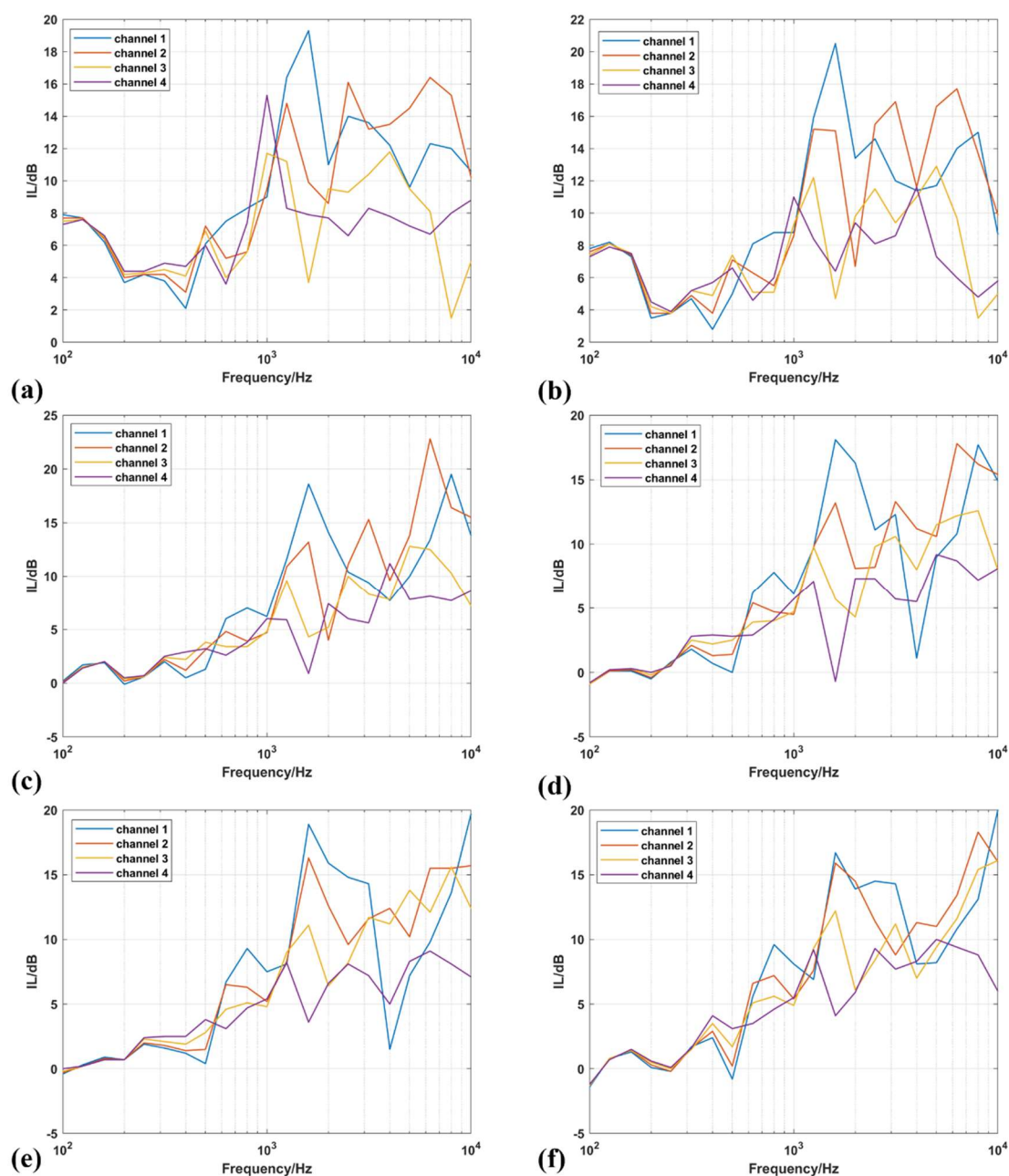
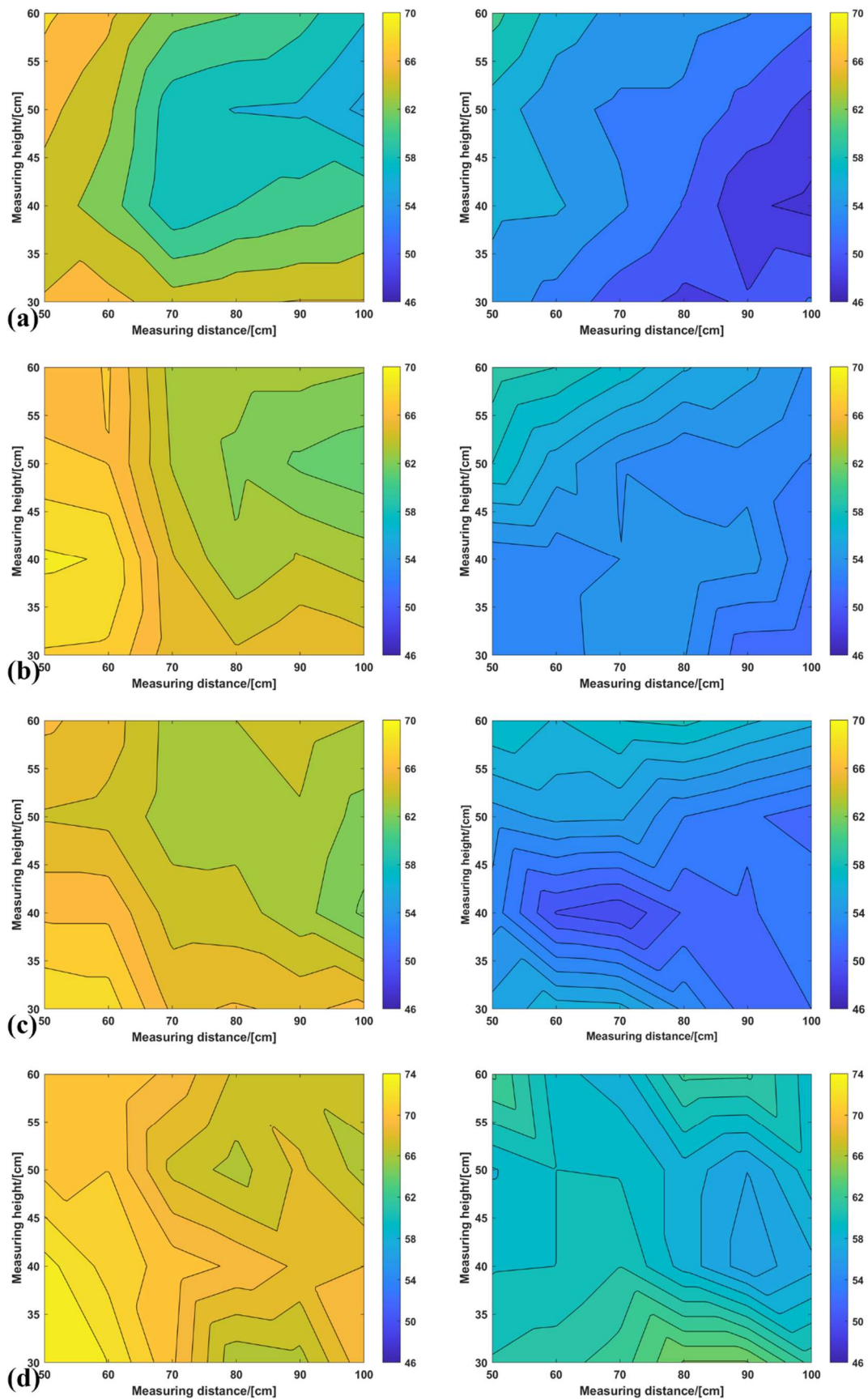


Fig. 4.25: Insertion loss with presence of a passive noise barrier (0.1–10 kHz). (a) Distance from the barrier 0.5 m; (b) Distance from the barrier 0.6 m; (c) Distance from the barrier 0.7 m; (d) Distance from the barrier 0.8 m; (e) Distance from the barrier 0.9 m, and (f) Distance from the barrier 1.0 m.



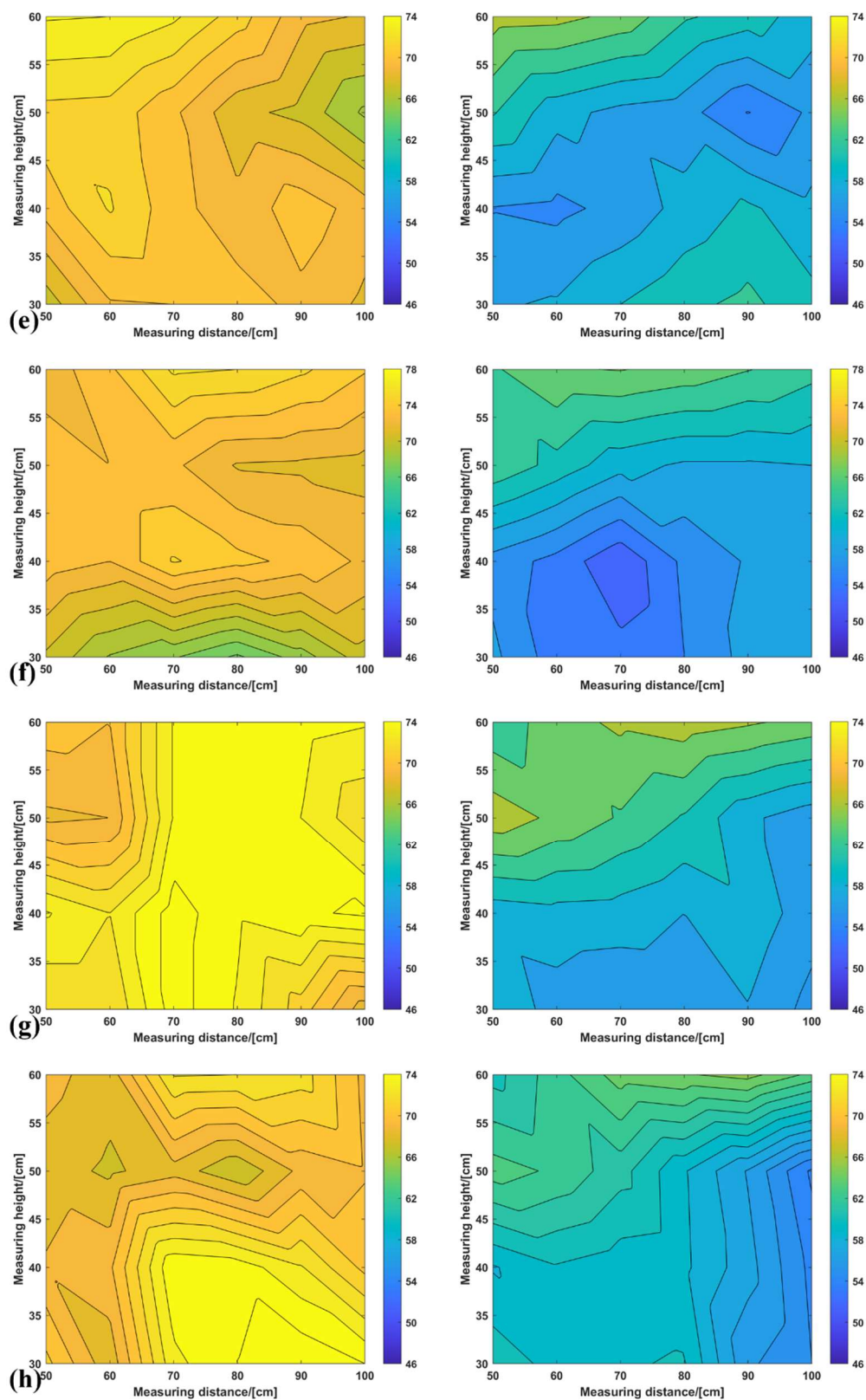


Fig. 4.26: Contour profiles of SPL distribution under two cases: (i) without any barrier; and (ii) with a passive barrier only at (a) 2000 Hz, (b) 2500 Hz, (c) 3150 Hz, (d) 4000 Hz, (e) 5000 Hz, (f) 6300 Hz, (g) 8000 Hz, and (h) 10000 Hz.

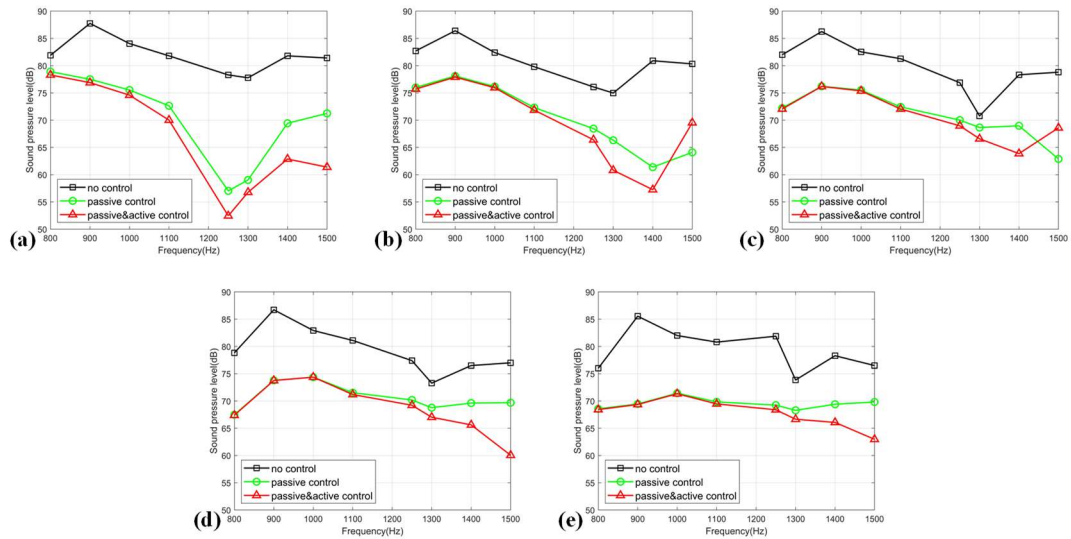


Fig. 4.27: Variation of SPLs at microphone height 0.3 m under three various conditions at different separation distance between the sound barrier and the microphone: (a) 0.5 m, (b) 0.7 m, (c) 0.9 m, (d) 1.1 m, and (e) 1.3 m.

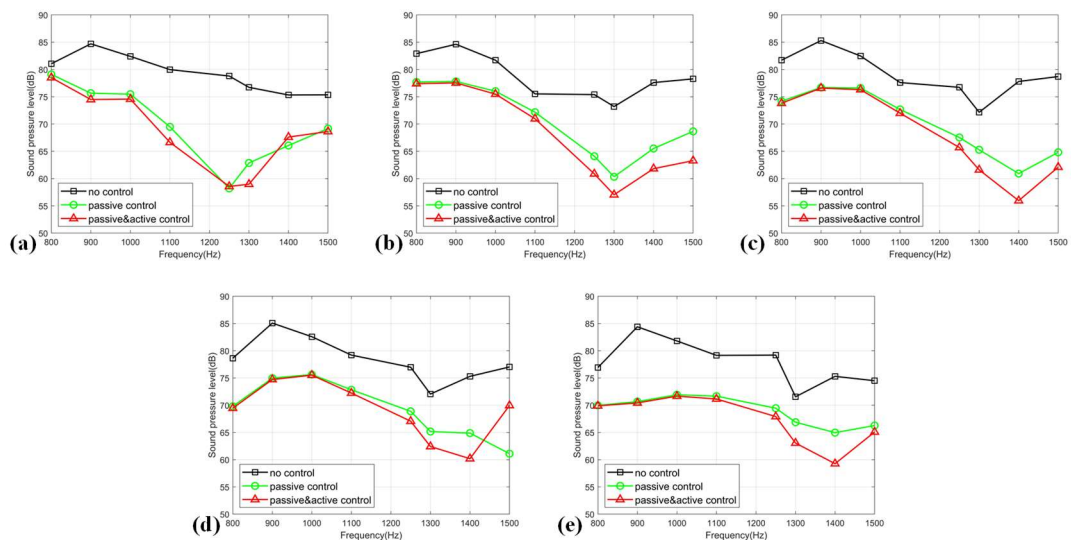


Fig. 4.28: Variation of SPLs microphone height 0.4 m under three various conditions at different separation distance between the sound barrier and the microphone: (a) 0.5 m, (b) 0.7 m, (c) 0.9m, (d) 1.1m, and (e) 1.3 m.

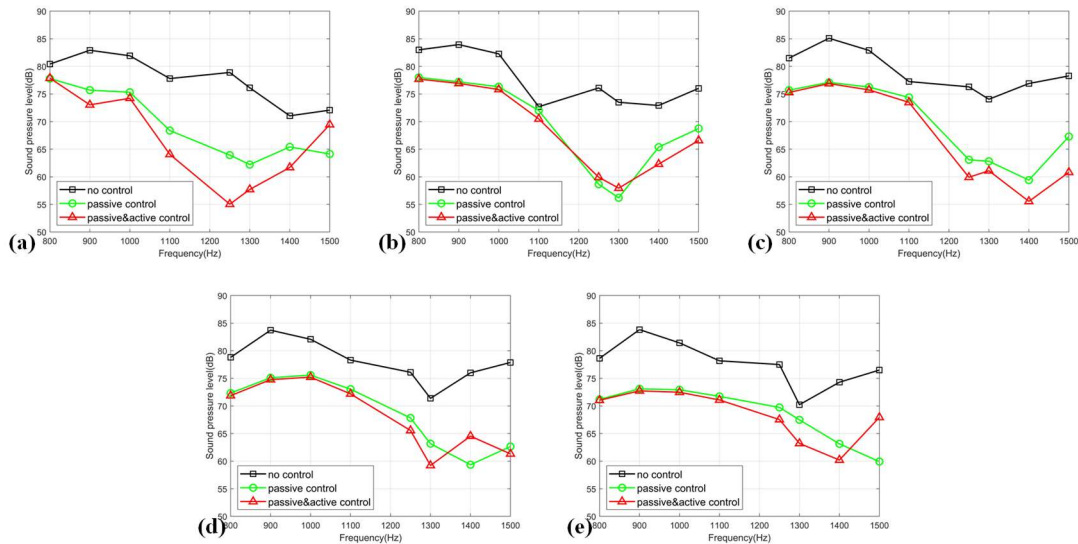


Fig. 4.29: Variation of SPLs at microphone height 0.5 m under three various conditions at different separation distance between the sound barrier and the microphone: (a) 0.5 m, (b) 0.7 m, (c) 0.9 m, (d) 1.1 m, and (e) 1.3 m.

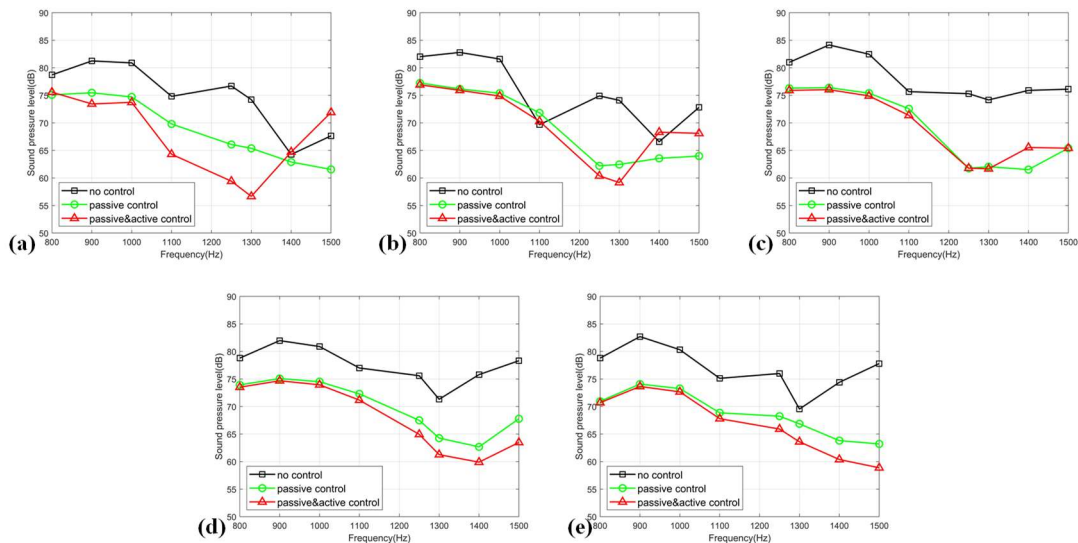


Fig. 4.30: Variation of SPLs at microphone height 0.6 m under three various conditions at different separation distance between the sound barrier and the microphone: (a) 0.5 m, (b) 0.7 m, (c) 0.9 m, (d) 1.1 m, and (e) 1.3 m.

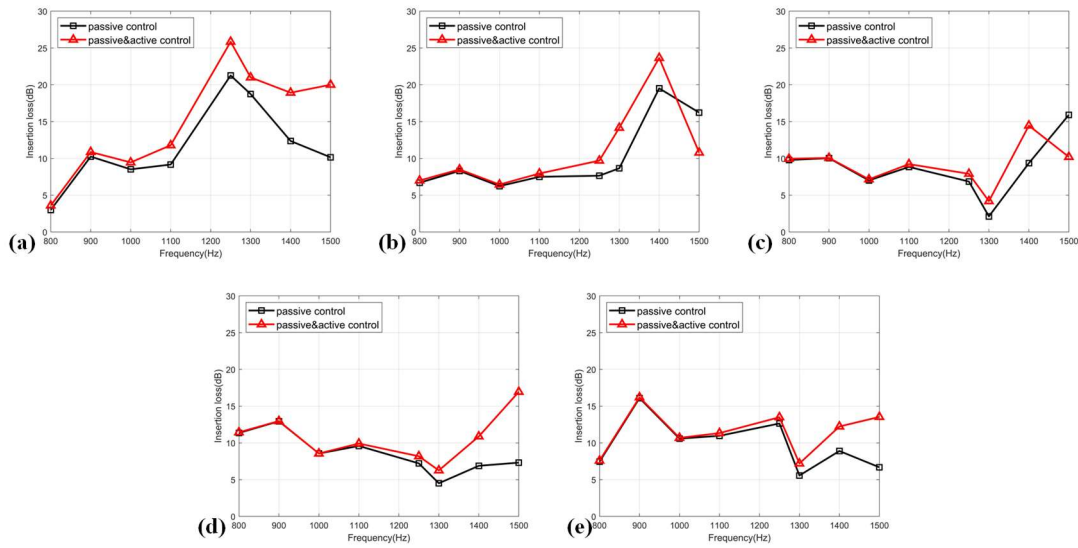


Fig. 4.31: Variation of insertion loss results at microphone height 0.3 m under three various conditions at different separation distance between the sound barrier and the microphone: (a) 0.5 m, (b) 0.7 m, (c) 0.9 m, (d) 1.1 m, and (e) 1.3 m.

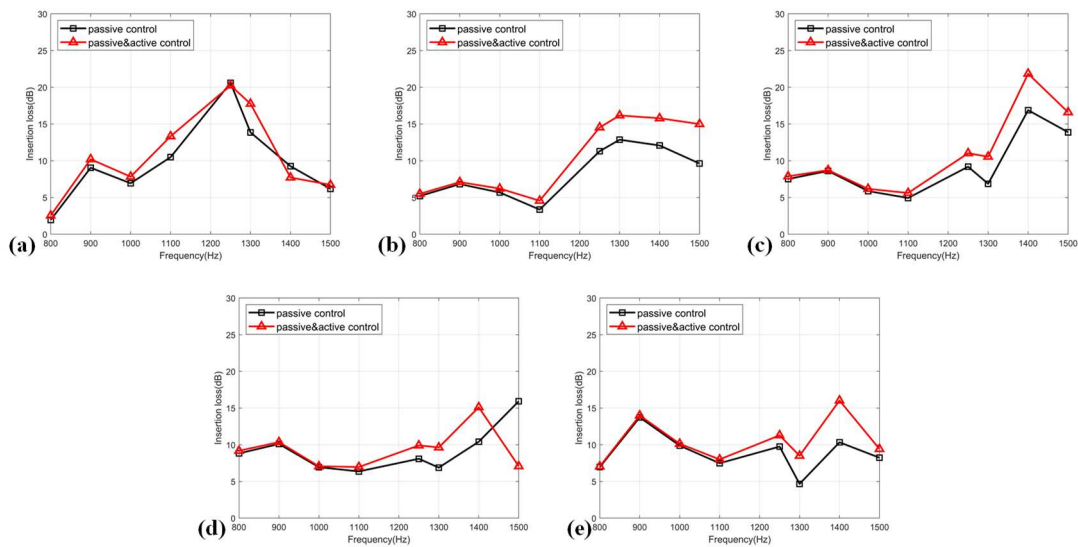


Fig. 4.32: Variation of insertion loss results at microphone height 0.4 m under three various conditions at different separation distance between the sound barrier and the microphone: (a) 0.5 m, (b) 0.7 m, (c) 0.9 m, (d) 1.1 m, and (e) 1.3 m.

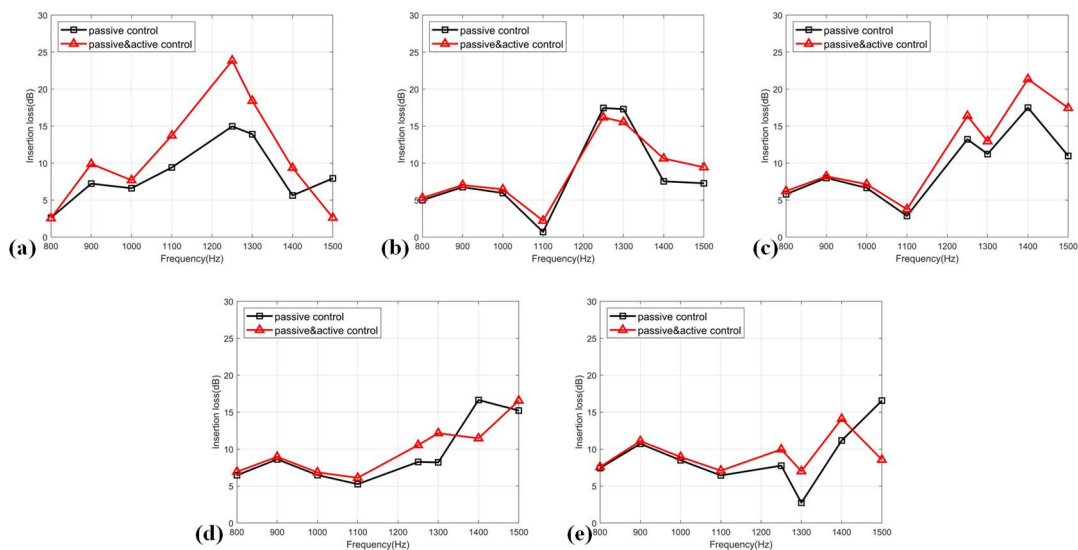


Fig. 4.33: Variation of insertion loss results at microphone height 0.5 m under three various conditions at different separation distance between the sound barrier and the microphone: (a) 0.5 m, (b) 0.7 m, (c) 0.9 m, (d) 1.1 m, and (e) 1.3 m.

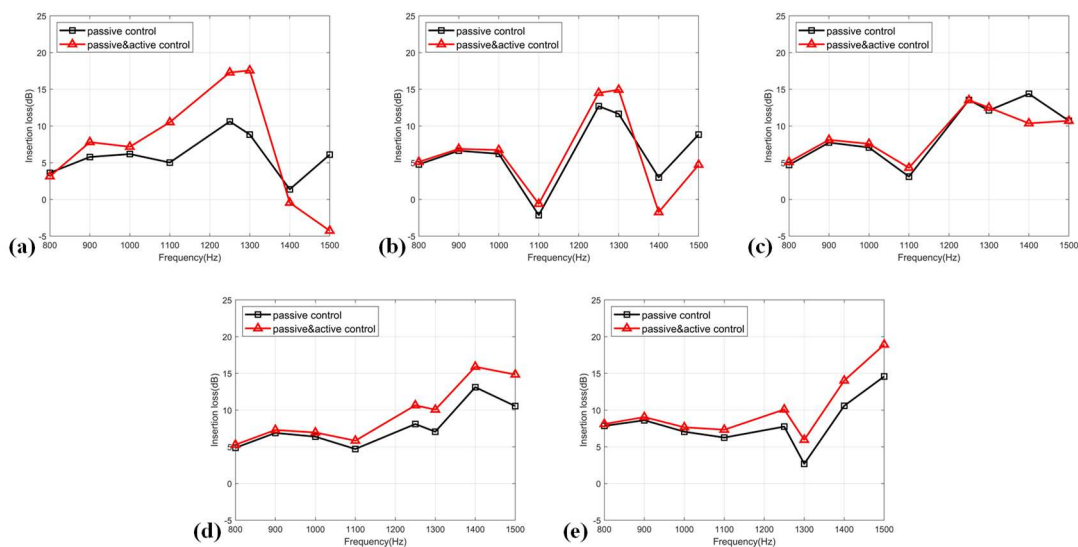


Fig. 4.34: Variation of insertion loss results at microphone height 0.6 m under three various conditions at different separation distance between the sound barrier and the microphone: (a) 0.5 m, (b) 0.7 m, (c) 0.9 m, (d) 1.1 m, and (e) 1.3 m.

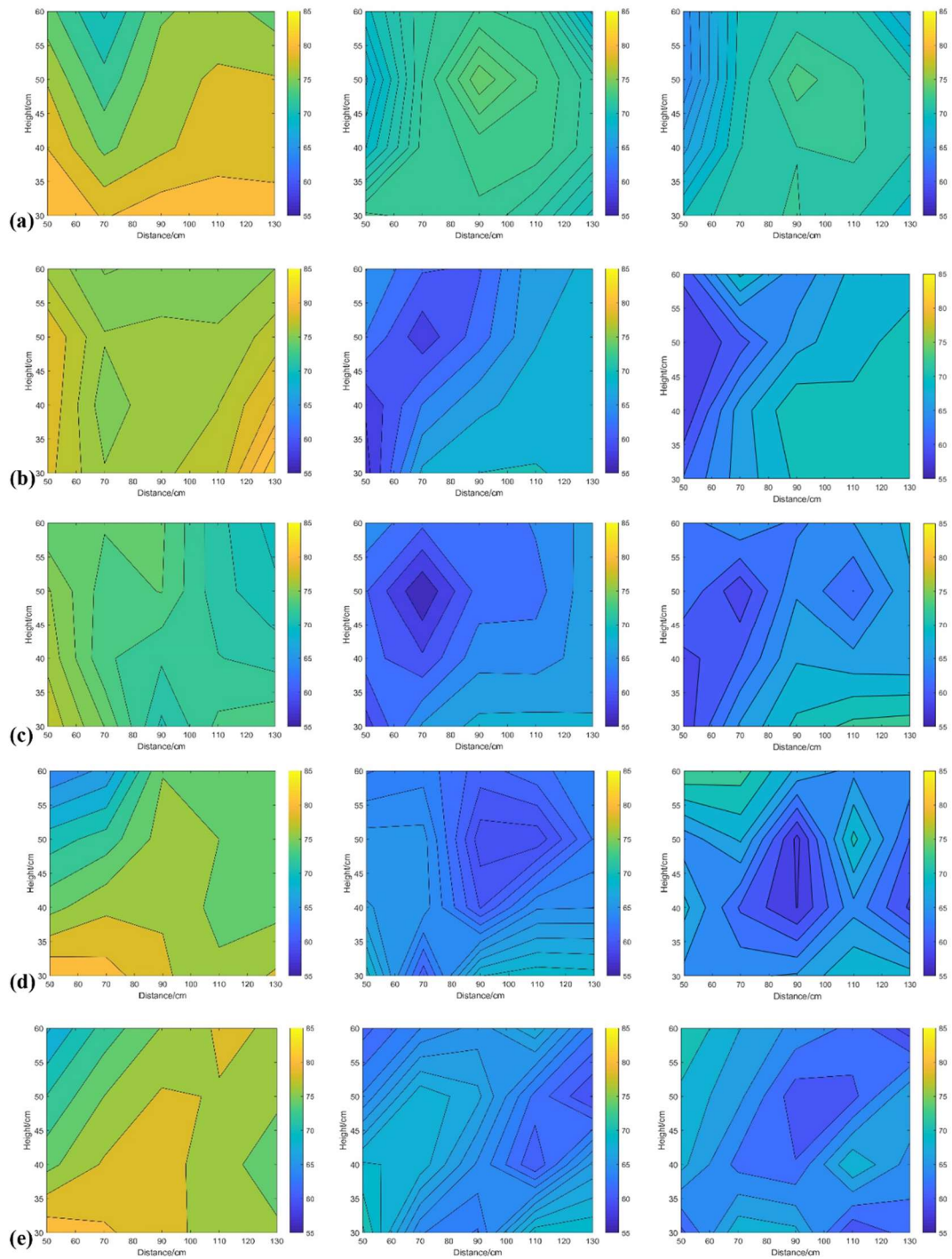
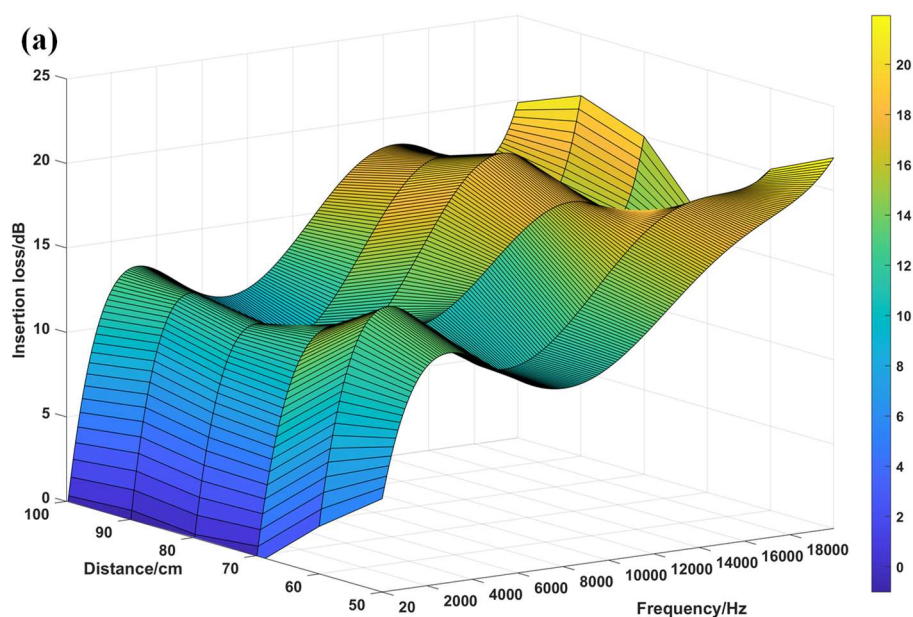


Fig. 4.35: Contour profiles of SPL distribution under three cases: (i) without any barrier; (ii) with the passive barrier only; and (iii) with the dual-function noise barrier at (a) 1100 Hz, (b) 1250 Hz, (c) 1300 Hz, (d) 1400 Hz, and (e) 1500 Hz.

4.4.3.3 Overall assessments

To further demonstrate the overall performance of the proposed barrier, the fitting trend diagrams based on the measurement results at high-frequency range (i.e., above 2000 Hz) and at low-to-medium frequency range (i.e., 800–1500 Hz) are plotted in Fig. 4.36(a) and 4.36(b), respectively. These results illustrate the relationship between SPL reductions and two important factors (i.e., frequency and measured distance) in the presence of the passive barrier only and the dual-function barrier, respectively. It is noted that the measurement microphone height was at 0.3m (i.e., channel 1), which can reveal the optimal shielding effect of the proposed barrier. In general, the reduction of 5–10 dB can be realized at low-to-medium frequency range, while a significant noise reduction can be identified in the high-frequency range (i.e., 10–15 dB at 2–10 kHz and above 15dB at 10–20 kHz).



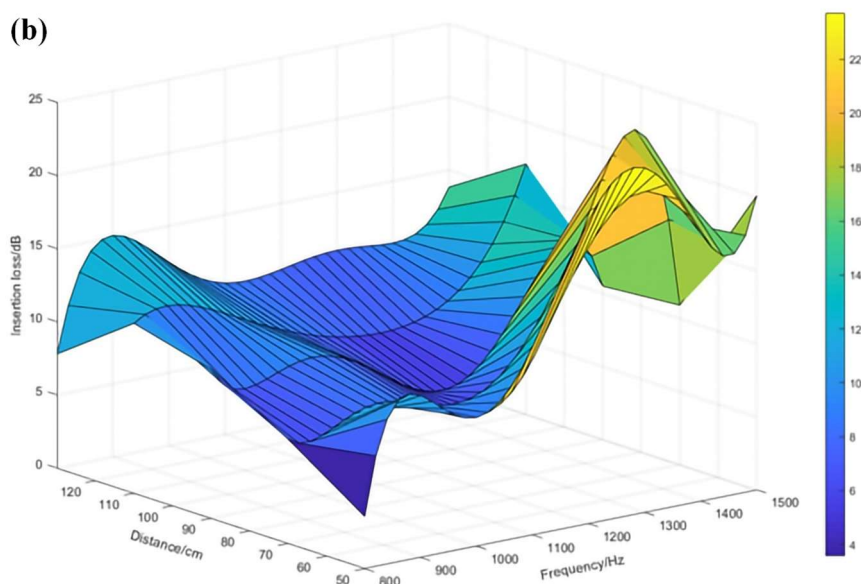


Fig. 4.36: Overall assessment results: the SPL reduction profiles (a) at high-frequency range; and (b) at low-to-medium frequency range.

4.5 Concluding remarks

In this work, a comprehensive assessment for the soundproofing properties of wood-rubber composites is presented. As a recycled waste, wood-rubber composites are low-cost and environmental-friendly, which provides an alternative in construction noise barrier design. In addition, it is with significant sound insulation performance (high absorption coefficient and transmission loss index). The thin-film piezoelectric material, PVDF, is considered as an auxiliary part to mitigate the peak narrowband low-frequency noise component. An acoustic response study about the thin-film speakers is illustrated. By integrating the composite panel and thin-film layer, a laminated barrier configuration is studied and examined as a dual-function barrier. The major findings of this composite barrier are summarized as below:

- The soundproofing performance of the wood-rubber samples is mainly dominated by two parameters including thickness and wood-rubber ratio. With increasing thickness, the absorption coefficient and transmission loss increase

accordingly. A higher wood proportion leads to a higher absorption coefficient, while a higher rubber proportion can be beneficial to the transmission loss.

- The flexible and lightweight piezoelectric film shows potential as an sound-generation device to couple with passive-type barriers. Through the radiation measurements, it shows flat response above medium frequency range, which is an alternative for sound generation. Further modification is focused on the reduction of harmonic distortion in low-frequency range.
- By implementing a scale-down model, the effectiveness of proposed barrier reveals good performance in noise attenuation. The highest insertion loss (*IL*) value can fetch up to 20 dB. The reduction of 5–10 dB can be realized at low-to-medium frequency range, while 10–15 dB can be identified at high-frequency range.

Although an in-situ measurement of the proposed barrier is not presented, the new configuration of a laminated structure by combining recycled composites and piezoelectric thin-film shows potential application as a detachable design. Yet, the arrangement of multiple control sources is still absence, which directly restricts the final performance of active control. The size of quiet zone created by the control system is relied on the synergetic effects between the primary source, secondary source, and sensors. The global attenuation is still restricted in ANC method, and inevitable interference effects occur. The active control approach is limited at some measurement points, then the passive control is still dominant and inimitable in this work. A refined study will continuously focus on the development of piezoelectric thin-film speakers and their optimization (e.g., reduce the harmonic distortion effect). Furthermore, the implementation of digital signal processing platform and multiple control sources will be considered to enhance the active control efficiency.

CHAPTER 5

ACOUSTIC-MANIPULATED DEVICE TO ENHANCE FILTRATION REMOVAL OF SUB-MICRON PARTICLES

5.1 Introduction

Indoor air quality is a crucial issue that deserves greater concern, particularly because public awareness of pollution is dramatically changing people's views towards their health. Heating, ventilation, and air conditioning (HVAC) systems have been proposed to maintain a healthy environment in commercial offices and hospital wards not only by providing thermal comfort to the occupants but also by improving resistance to infection (Qian et al., 2006; Sha and Qi, 2020). Viruses can spread through the air on dust, fibers, and other microscopic particles because air is the primary carrier of contaminants and airborne particulates in buildings (Li et al., 2007; Khankari, 2016), as shown in Fig. 5.1. Epidemiological evidence has shown that a good ventilation practice is recognized as a means of reducing the possibility of airborne viral transmission in confined indoor spaces and associating with the decreased risk of viral infection transmission (Morawska et al., 2020; Qian et al., 2021). Hence, the development of advanced technologies to improve ventilation and filtration needs is of great research interest.

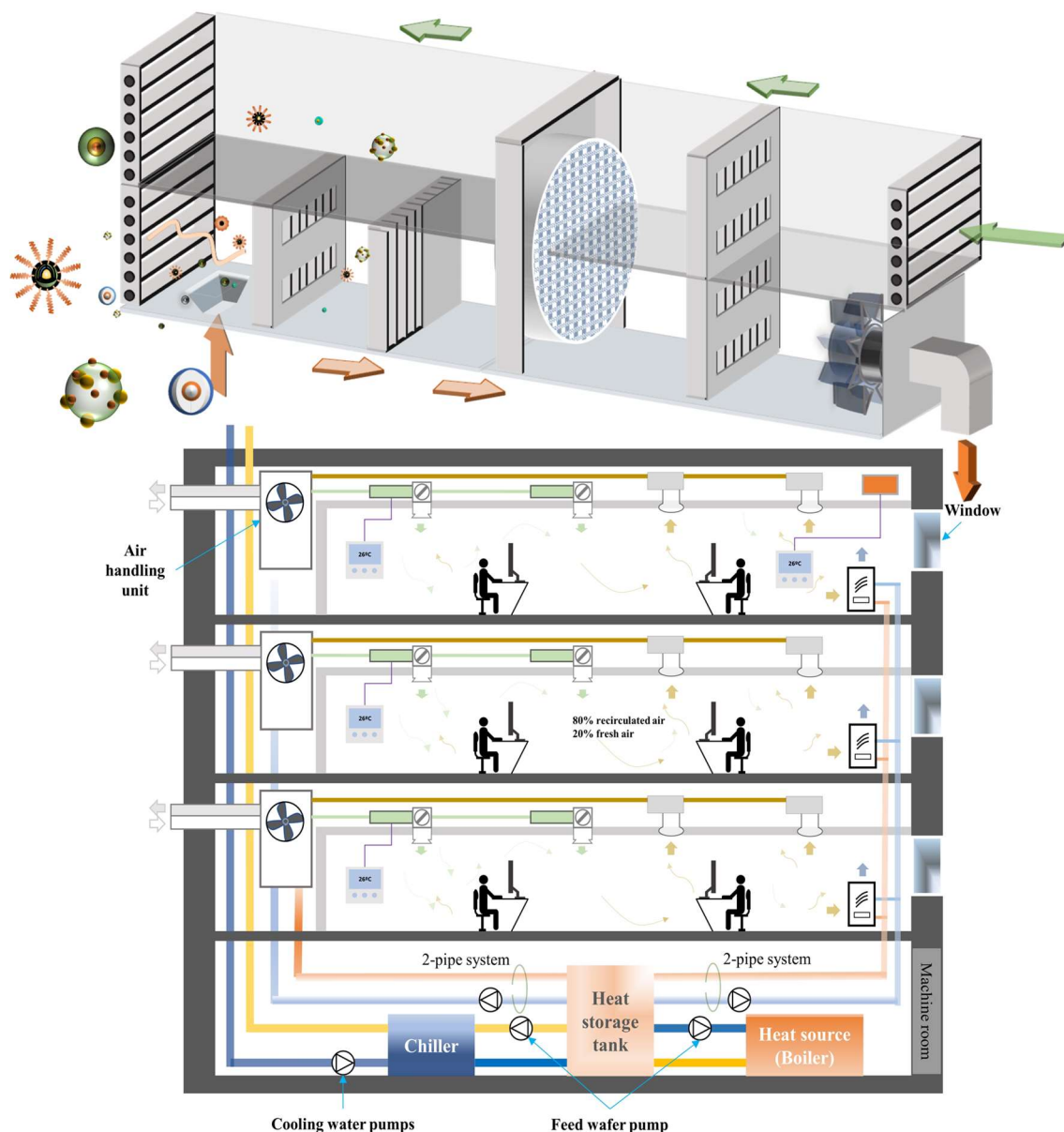


Fig. 5.1: A typical schematic diagram of HVAC system in commercial building (Zheng et al., 2021).

Low-grade filters (e.g., minimum efficiency rating value (MERV) of 6–9) are generally installed inside air ventilation ductworks. However, they are not effective for capturing fine or ultrafine particles at a sub-micrometer scale. The use of high-efficiency particulate air (HEPA) filters is a promising way to achieve better capturing efficiency, however this inevitably reduces the maximum airflow rate, which must be offset by greater extraction fan power in a ventilation system. HEPA filters must also

be replaced frequently, as they become ineffective beyond their lifetime to result in a polluted environment. The capital and replacement costs of HEPA filters are thus higher. Hence, there is a need for an innovative device not only to effectively remove fine particles from indoor air, and also to meet long-term sustainability targets (Manisalidis et al., 2020) and environmental regulations (Veeck, 2008).

Acoustic trapping is an active but contact-free manipulation technique under research of capturing particles (e.g., aerosols, dust, and hazardous objects) in a fluid flow (Brandt, 2001; Evander and Laurell, 2012). By achieving a standing wave field, fine particles can be forced to reside and trapped into a specific zone/region, which can enhance a filtering function. Furthermore, as particulates accumulate, the use of acoustic pressure prompts these particulates to form larger structures by collision and adhere them together, i.e., acoustic agglomeration.

Both theoretical studies (Riera-Franco de Sarabia and Gallego-Juárez, 1986; Temkin, 1994; Hoffmann, 2000; Liu and Li, 2020) and independent experiments (Clair, 1949; Mednikov, 1965; Ng et al., 2017) have been examined. These studies showed that acoustic agglomeration can be achieved by sound pressure fields, via acoustic streaming and acoustic radiation force. Reports in the literature for simulating the acoustic manipulation of airborne particles have been investigated by Fu et al. (2015) and Lei et al. (2013) on a Rayleigh streaming flow under an acoustic radiation force. Yuen et al. (2014, 2016) also experimentally investigated the removal filtration efficiency for removing aerosols between 0.3 to 6 μm sizes using a 100W power transducer, which removed 12–20% at 90 L/min. Further, they explained that the removal efficiency is proportional to the duration that the aerosols exposed to the acoustic fields, while maintaining a negligible pressure drop, thus minimizing power consumption. They also studied an acoustic streaming effect, which induces aerosol depositions through a hanging plate platform type ultrasonic transducer oscillating at 19 kHz vertically under a 44W power. Aerosols that aggregate into 6- μm diameter

particles can experience strong acoustic radiation force against drag and gravitational forces (Yuen et al., 2017).

In practice, 15–30% of the energy consumption would be generally applied to air distribution by mechanical-driven fans to overcome pressure drop in ventilation ducts and across filters in building systems (Ng et al., 2017). According to the feasibility studies as aforementioned, a combination of acoustic-driven pre-filtering techniques and commercial coarse filters should be a promising way to enhance filtration efficiency and simultaneously maintain a relatively unobstructed flow condition. Yet, most of investigations demonstrate significant achievements under high SPLs (i.e., 130–140 dB, see (Ng et al., 2017) and the references therein). The problem of high SPLs is a potential barrier to restrict the application of acoustic-driven techniques in actual building scenes. Hence, a further study and notable breakthrough, to improve the removal efficiency of airborne fine particles (especially for sub-micron particles) under lower SPLs, is of current focus.

Using the concept of “acoustic trapping”, we develop a simple U-shaped device (i.e., double resonant acoustic chambers) that can work at lower SPLs to enhance the filtration efficiency of low-grade filters in submicron particles. This technique is based on a unique airflow configuration (i.e., fluid flows in the device are in parallel, but sound waves are in opposite directions) in a ventilation duct. In this study, we attempt to introduce an overall understanding of the acoustic effects exerting on particles. A working principle about acoustic radiation force and secondary radiation force is explained in Section 5.2. To offer some design guidelines for the preparation and fabrication of experimental work, we conduct a simplified numerical analysis using the commercial software COMSOL Multiphysics®. Relevant discussion and experimental results are presented in Section 5.3. In the experimental part, a testing prototype is assembled to examine the filtration efficiency of sub-micron particles in the presence of acoustic wave. We also show that a higher filtration efficiency can be

achieved as the acoustic-driven technique is used along with a commercial MERV-grade filter. We discuss how the PM filtration can be achieved by the acoustic-based pre-filter. To further illustrate the acoustic effect on the fine particles within the acoustic-driven device, the microscopic observation is used to show the particle precipitations at the bottom of resonant acoustic chambers. A conclusion of major finding is presented in Section 5.4.

5.2 Theoretical analysis and experimental studies

5.2.1 Working principle

To understand the operating principles of acoustic-driven techniques, the basis of acoustic-particle interactions is briefly reviewed in this section. Using such techniques, it is generally achieved by the creation of a one-dimensional standing wave field in a medium, which can create differential pressure regions. Due to the pressure gradient, moving particles can be trapped at pressure nodes, where can strengthen the microscopic interaction of particles.

5.2.1.1 Configuration of acoustic-manipulated device

Fig. 5.2 shows two schematic diagrams of acoustic-driven configurations. Fig. 5.2(a) is a common design of high intensity acoustic-based particle treatments with a loudspeaker mounted at the top of a ventilation duct. Particles within the airflow appear to coincide with the flow fields. This case requires a high-intensity acoustic energy to force the particles gathering, as the moving direction of such particles is perpendicular to acoustic waves (Qiao et al., 2015; Yuen et al., 2016; Qiao et al., 2017; Shi et al., 2017; Yuen et al., 2017). However, in this configuration, the acoustic energy is dispersed in the whole ventilation duct, as no physical boundary is present to concentrate the emitted sound waves.

We propose a novel configuration as shown in Fig. 5.2(b). A confined chamber to facilitate particle trapping is designed, in which acoustic waves emitted from a loudspeaker is in an opposite direction against an incoming airflow. The present acoustic resonant chamber with incoming airflow enables a better utilization of sound energy, which can be verified via the numerical simulation of particle trajectories in Section 5.2.2. The resonant acoustic chamber forms a one-dimensional standing wave to create acoustic pressure nodes at a specific region. This forces the sound waves propagating in one dimension, and thus effectively minimizes the spread of sound waves from the loudspeaker source. Airborne particles moving inside the resonance tube can be captured by the pressure nodes by using the full extent of the enclosure without dispersing the sound pressure fields. The above two design approaches illustrate how different geometries and speaker locations can affect the residence time effect of airborne particles under sound pressure fields. In the present design configuration, the emitted sound waves are confined and reflected off the hard boundary walls of the chamber. It is thus favorable to induce a trapping region at lower SPLs to enhance utilization of sound energy for particle treatment as a pre-filtering technique.

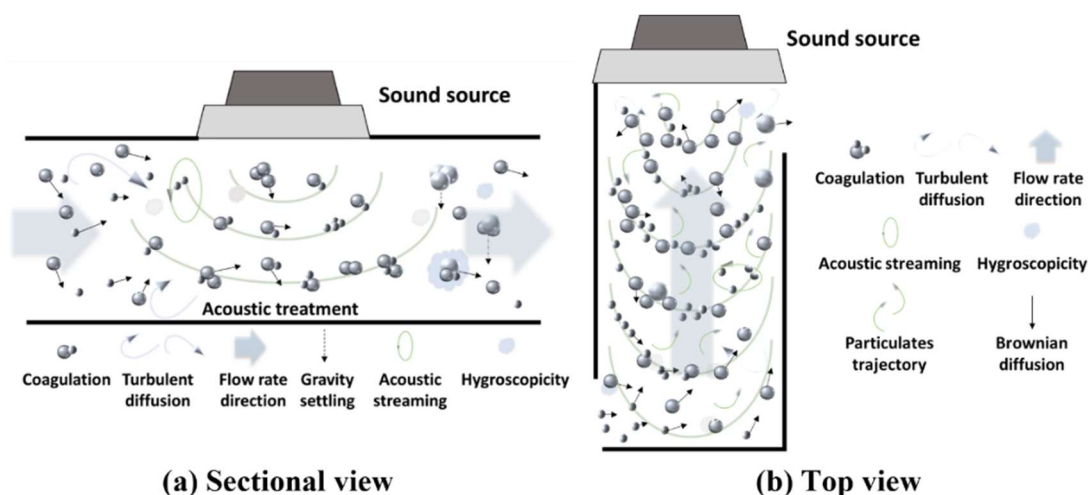


Fig. 5.2: Illustration of aerosol particulate transport under the acoustic effects: (a) A loudspeaker is mounted at the top of a ventilation duct (Ng et al., 2017); and (b) A loudspeaker is mounted at the sidewall of a ventilation duct.

Consider a closed tube, the acoustic frequency can be calculated as follows (Qiao et al., 2015,2017):

$$f = \frac{mc}{2L}, \quad m = 1, 2, 3 \dots \quad (5.1)$$

Acoustic pressure (i.e., the force of sound exerting on a surface area) is the main quantity to characterize acoustic fields. In this study, the acoustic pressure model is simplified as a two-dimensional (2D) acoustic enclosure driven at a constant frequency and same phase. To determine the effect of acoustic intensity, we define ‘‘SPL’’ as the following standard logarithmic form:

$$\text{SPL} = 20 \log_{10} \left(\frac{P_{rms}}{P_{ref}} \right) \quad (\text{dB}) \quad (5.2)$$

where P_{rms} is the root-mean-square sound pressure and P_{ref} is the reference sound pressure ($= 20 \times 10^{-6}$ Pa).

5.2.1.2 Acoustic radiation force

The first process in particle manipulation with sound is an orthokinetic process (Ng et al., 2017), which is the acoustic radiation force (or referred as the primary radiation force) acting on a particle under a sound pressure field (Yasui, 2011). As the size of particles is much smaller than the wavelength of acoustic wave (Foresti et al., 2012), the acoustic radiation force F_a acting on a small particle can be expressed as (Gor'kov, 1962; Qiao et al., 2015):

$$F_a = -(4\pi R^3 / 3) \nabla \left[P_A^2 / (4\rho_p c_p^2) \phi_1 - 3\rho_p v_A^2 / 8\phi_2 \right] \quad (5.3)$$

$$\phi_1 = 1 - \frac{\rho_p c_p^2}{\rho_0 c_0^2}$$

$$\phi_2 = \frac{2(\rho_0 - \rho_p)}{(2\rho_0 + \rho_p)}$$

where R is the equivalent radius of small spherical particles; P_A and v_A are the sound pressure amplitude and the velocity amplitude in acoustic standing waves, respectively; ϕ_1 and ϕ_2 are the acoustic contrast factors; ρ_p and c_p are the density and velocity of the particle, respectively; and ρ_0 and c_0 are the density and speed of sound in the carrier medium, respectively. The Gor'kov equations are applicable to sound pressure fields where a standing wave is sustained (Gor'kov, 1962), but not to the scenarios involving traveling waves.

Under a steady-state condition, particles within a carrier medium (typically air) are influenced by acoustic waves, they can be gathered in sound pressure nodes and anti-nodes (Qiao et al., 2015). Greenhall et al. (2013) used a modified acoustic contrast factor Φ to replace the original acoustic contrast factors ϕ_1 and ϕ_2 , which can be used to identify the attraction of particles at the pressure nodes or anti-nodes. The acoustic contrast factor (Φ) is given by (Karpul et al., 2010; Greenhall et al., 2013):

$$\Phi = \frac{5\rho_p - 2\rho_0}{2\rho_p + \rho_0} \frac{\beta_p}{\beta_0} \quad (5.4)$$

where $\beta_p = 1/(\rho_p c_p^2)$ and $\beta_0 = 1/(\rho_0 c_0^2)$ represent the compressibility of the particles and the air carrier medium, respectively. If $\Phi > 0$, particles are driven to the nearest pressure nodes, and if $\Phi < 0$, particles are driven to the nearest pressure anti-nodes (Karpul et al., 2010; Greenhall et al., 2013; Qiao et al., 2015). The acoustic contrast factor may be utilized for further analysis of the acoustic radiation force, which

generally creates traction on particles within a sound pressure field (Haake and Dual, 2002; Habibi et al., 2017). Particles may reside in an acoustic pressure antinode with a spatial location where may effectively reduce the particles' velocity as the pressure is maintained.

5.2.1.3 Secondary radiation force

The second process in particle manipulation with sound involves an aerodynamic mechanism (González et al., 2003), which describes collisions due to viscous interactions between particles and the carrier medium (air). Specifically, this mechanism describes the relationship between the angular velocity of two particles that may collide within the anti-nodal and nodal locations (Saeidi et al., 2020). This interaction is expressed as follows, which is also called as the secondary radiation force (Weiser et al., 1984; Benes et al., 2001; Laurell et al., 2007; Ahn et al., 2015; Qiao et al., 2017):

$$F_s = 4\pi R^6 \left[\overbrace{\frac{(\rho_p - \rho_0)^2 (3 \cos^2 \theta - 1)}{6\rho_0 d^4} v_p^2(x)}^{\text{Particle Velocity Term}} - \overbrace{\frac{\omega^2 \rho_0 (\beta_p - \beta_0)}{9d^2} p_s^2(x)}^{\text{Sound Pressure Term}} \right] \quad (5.5)$$

and the general form of the sound pressure $p_s(x)$ (i.e., the superposition of the forward (incident) and backward (reflected) sinusoidal waves) is (Qiao et al., 2017)

$$p_s(x) = p_i \sin\left(\frac{m\pi x}{L} - 2\pi ft\right) + p_r \sin\left(\frac{m\pi x}{L} + 2\pi ft\right) \quad (5.6)$$

where F_s consists of a particle velocity term and a sound pressure term to represent the particle's trajectory, θ is the angle between the angular velocity from the center of two particles and the propagation direction of an acoustic wave, d is the distance between particles, $v_p(x)$ is the velocity of particles, ω is the angular velocity of the air carrier

medium, p_i is the sound pressure amplitude of the incident wave, p_r is the sound pressure amplitude of the reflected wave, x is a spatial variable, and t is a temporal variable. The effect of the secondary radiation force on a particle entering within the sound pressure field relates to the magnitude of F_s , especially its polarity (represented by a positive or negative number) (Benes et al., 2001). If F_s is negative, the interaction between two particles is considered to be attractive, which will promote particle coagulation via a collision process. However, if F_s is positive, the interaction between two particles is repulsive, and thus separation will likely occur as their respective numerical vectors diverge in the localized sound pressure field (Weiser et al., 1984).

5.2.2 Numerical modeling

Studies of the mechanisms of acoustic-particle interaction have been identified by numerical methods. For example, Zhang et al. (2018a) investigated a three-dimensional discrete element model of the acoustic agglomeration of sprayed aerosol droplets that considered orthokinetic interaction, the acoustic wake effect, gravity force, and the Brownian random force. Liu and Li (2020) implemented a parallel computing strategy, including acoustic particle interaction mechanisms and a particle collision process, to predict the trapping rate under various influencing factors. To provide a theoretical understanding, 2D simplified numerical models (i.e. acoustic pressure model, turbulence model) are utilized to illustrate the flow pattern and sound pressure profile within the ventilation duct via a finite element method.

5.2.2.1 *Governing equations of continuous airflow*

Consider the Reynolds-averaged Navier–Stokes (RANS) equations, it is utilized for the present numerical simulation (Wilcox, 2000; Alfonsi, 2009). Using tensor notations, the RANS equations are expressed by (Alfonsi, 2009)

$$\frac{\partial \bar{u}_i}{\partial x_i} = 0 \quad (5.7)$$

$$\frac{\partial \bar{u}_i}{\partial t} + \bar{u}_j \frac{\partial \bar{u}_i}{\partial x_j} = -\frac{\partial \bar{p}}{\partial x_i} + \nu \frac{\partial^2 \bar{u}_i}{\partial x_j \partial x_j} - \frac{\partial \tau_{ij}}{\partial x_j} \quad (5.8)$$

where \bar{u}_i is the mean flow velocity, \bar{p} is the mean pressure of a fluid flow, ν is the fluid kinematic viscosity, and τ_{ij} is the Reynolds-stress term. As we mainly focus on the flow patterns and acoustic effects inside the U-shaped device, the boundary conditions of the ventilation duct model are set as a velocity inlet and an arbitrary outlet for numerical analysis.

In addition, a standard k - ε turbulence model (Shi et al., 2020) can be used to calculate the dynamic viscosity, i.e., $\mu_T = \rho C_\mu k^2 / \varepsilon$ where k denotes the turbulent kinetic energy, and ε denotes the turbulent dissipation rate, and C_μ is a constant (= 0.09). The transport equations of this model, in a simple form, can be written as follows (Rodi, 2017; Shi et al., 2020)

$$\rho_0 \frac{\partial k}{\partial t} + \rho_0 u \cdot \nabla k = \nabla \cdot \left[\left(\mu_0 + \frac{\mu_T}{\sigma_k} \right) \nabla k \right] + P_k - \rho_0 \varepsilon \quad (5.9)$$

$$\rho_0 \frac{\partial \varepsilon}{\partial t} + \rho_0 u \cdot \nabla \varepsilon = \nabla \cdot \left[\left(\mu_0 + \frac{\mu_T}{\sigma_\varepsilon} \right) \nabla \varepsilon \right] + C_{\varepsilon 1} \frac{\varepsilon}{k} P_k - C_{\varepsilon 2} \rho_0 \frac{\varepsilon^2}{k} \quad (5.10)$$

where u is the average flow velocity, ρ_0 is the fluid density, μ_0 is the fluid viscosity, and P_k is the production term. In the above equations, the non-dimensional constants $C_{\varepsilon 1}$, $C_{\varepsilon 2}$, σ_k and σ_ε can be set as 1.44, 1.92, 1.0, and 1.3, respectively. Readers may refer to Refs. (Wilcox, 2000; Alfonsi, 2009; Shi et al., 2020) for details.

5.2.2.2 Governing equation of acoustic pressure field

The acoustic field can be described by one variable, the pressure p , and is governed by the following wave equation (COMSOL, Ver 5.4):

$$\frac{\partial^2 p}{\partial t^2} - c^2 \frac{\partial^2 p}{\partial x^2} = 0 \quad (5.11)$$

where t is time, and c is the speed of sound. The wave equation can be solved into harmonic components via Fourier series. The wave equation can be solved in the frequency domain for one frequency at a time. A harmonic solution has the form $p(x, t) = p(x)e^{i\omega t}$. Using the assumption for the pressure field, the time-dependent wave equation can be expressed by the Helmholtz equation (Shi et al. 2020):

$$\nabla \cdot \left(-\frac{1}{\rho_0} (\nabla p_t - q_d) \right) - \frac{\omega^2}{\rho_0 c^2} p_t = Q_m \quad (5.12)$$

where ρ_0 is the density of the fluid, p_t is the total pressure, ω is the angular frequency, q_d and Q_m denote dipole and monopole domain sources, respectively.

5.2.2.3 Dynamic motion of particles under fluid flow

To simplify the numerical model as a 2D model in Fig. 5.2, the motion of particles is investigated with the turbulence model and acoustic model separately. In the turbulence model, we mainly discuss the motion of particles that is affected by a continuous airflow (see Eqs. (5.7) – (5.10)). The acoustic effect acting on the released particles is induced by the acoustic radiation force, (see Eq. (5.3)). According to Newton's second law, the motion of particles can be written as (Kim and Zydney, 2004; Shi et al., 2020)

$$\frac{d}{dt} (m_p v) = F_a + F_g + F_d \quad (5.13)$$

where m_p denotes the particle mass, v denotes the particle velocity, F_g is the gravitational force, and F_d is the drag force. In the equation, F_a is the acoustic radiation force acting on the released particles. The drag force with Oseen's correction (Oseen, 1910; Shi et al., 2020) can be expressed as follows:

$$F_d = \frac{1}{8} C_d \rho_p S |u - v| (u - v), \quad (5.14)$$

$$C_d = \frac{24}{\text{Re}_r} \left(1 + \frac{3}{16} \text{Re}_r \right), \quad \text{Re}_r = \frac{\rho_0 U_r d_p}{\mu_0}$$

where C_d is the drag coefficient, Re_r is the relative Reynolds number, U_r is the relative velocity between airflow and particle, ρ_0 is the fluid density, d_p is the particle diameter, ρ_p is the density of particles, μ_0 is the fluid viscosity, and S denotes the projection area of the particle perpendicular to the direction of propagation of acoustic waves.

As the dynamic behavior of particles under the action of flow fields and the effect of acoustic radiation force is quite complex, we assume that: (i) the air medium is incompressible; (ii) the air temperature is constant; (iii) the attenuation of acoustic waves in air is ignored; (iii) the flow is assumed lossless and adiabatic; and (iv) the particle size is much smaller than the wavelength of acoustic waves. In the numerical analysis, a freeze-wall boundary condition (Shi et al., 2020) is adopted for the U-shaped enclosure, it implies that moving particles would be frozen to have an unchanged position and velocity once they collide the chamber wall surface.

5.2.3 Device fabrication and experimental setup

5.2.3.1 Filtration efficiency measurement to determine the effectiveness of U-shaped acoustic-driven device

To investigate the synergetic effect of particle trapping in the U-shaped design configuration under acoustic and flow fields, we fabricated a prototype to measure the particle concentration with and without an acoustic force, as shown in Fig. 5.3. We

also designed a ventilation duct model coupled by the U-shaped acoustic-driven device for experimental studies, see Figs. 5.3(d) and 5.3(c). In this section, we describe the fabrication procedures of the experimental setup to demonstrate and validate the performance of the proposed acoustic-driven device. In this design, we fabricated two acoustic resonance chambers by partitioning a cubic transparent acrylic material into two rectangular sections. Two circular sections were cut out of the tube walls in the resonant chambers, and two loudspeakers (*TANBX, TB-412, 4-inch coaxial audio loudspeaker*) were embedded into the circular holes. Stainless-steel sound reflectors were deployed in the opposite direction of the loudspeakers, as shown in Fig. 5.3(b). The loudspeakers were operated at the same frequency, and the occurrence of interference effects can be minimized due to the presence of interior wall. In addition, appropriate sealant materials were applied to the acoustic chambers to minimize sound leakage. Small open gaps are used to allow the airflow to pass. A full experimental prototype was constructed to investigate the acoustic effects under various ventilation scenarios, as shown in Figs. 5.3(d) and 5.3(e). PM generated by an aerosol generator can be released into the duct, and the particles are allowed to flow into the chamber inlet and through the device to undergo a trapping process. A power supply was connected to the electrical equipment (i.e., power fan, loudspeakers, aerosol generator, and particle size analyzer).

According to the experimental setup, we conducted experiment without a MERV filter to analyze the performance of the acoustic-driven device as a pre-filter, and then tested the performance of the setup in combination with a commercial MERV-6-graded filter (*PureFit, Pleated Filter MERV 6 Furnace Filter*). The filtration performance was measured by generating PM aerosols with a particle generator (*TSI, Model 8026*) using a sodium chloride (*NaCl*) source. The diameters of sprayed particles range from 0.01 μm to 1.0 μm (*GRIMM series 5400*), as shown in Fig. 5.4. According to the comprehensive review aforementioned, the diameter of indoor house dust mite allergens is mainly at the range of 0.1–10 μm . Larger particles can be easily

captured by a low-grade filter, but finer particles (0.1–1.0 μm) are often difficult for removal. The concentration versus particle distribution profile was measured with a particle counter (*METONE, BT-620, operating flow rate 1.0 cfm*) between 108 and 116 dB. The maximum operating SPL was 116 dB. Airflow was induced with an extraction fan (*APC-10, diameter 100 mm, 2800 r/min, 150 m³/h*) at the tube end, and the fan speed was controlled (between 0.45 and 0.75 m/s) by a controllable frequency inverter circuit. An airflow meter probe (*Testo, Model 435-4*) was used to measure the air velocity at room temperature.

To optimize the filtration efficiency, we analyzed the filtration performance by examining three important parameters. We examined the loudspeaker-operating frequency, the applied SPL (in dB), and the airflow rate of the ventilation tube under various particle sizes (i.e., 0.3–10 μm) (Ng et al., 2017). The efficiency with which a filter removes particles from an airflow represents its effectiveness in reducing the particle concentration within the airflow. Therefore, a removal coefficient that also represents the filtration efficiency (α) is expressed by the following equation (Qiao et al., 2015,2017):

$$\alpha = \left(\frac{C_1 - C_2}{C_1} \right) \times 100\% \quad (5.15)$$

where C_1 represents the particle concentration in the absence of the acoustic effect, and C_2 represents the particle concentration in the presence of acoustic effect. This equation can be used to determine the overall performance of the device.

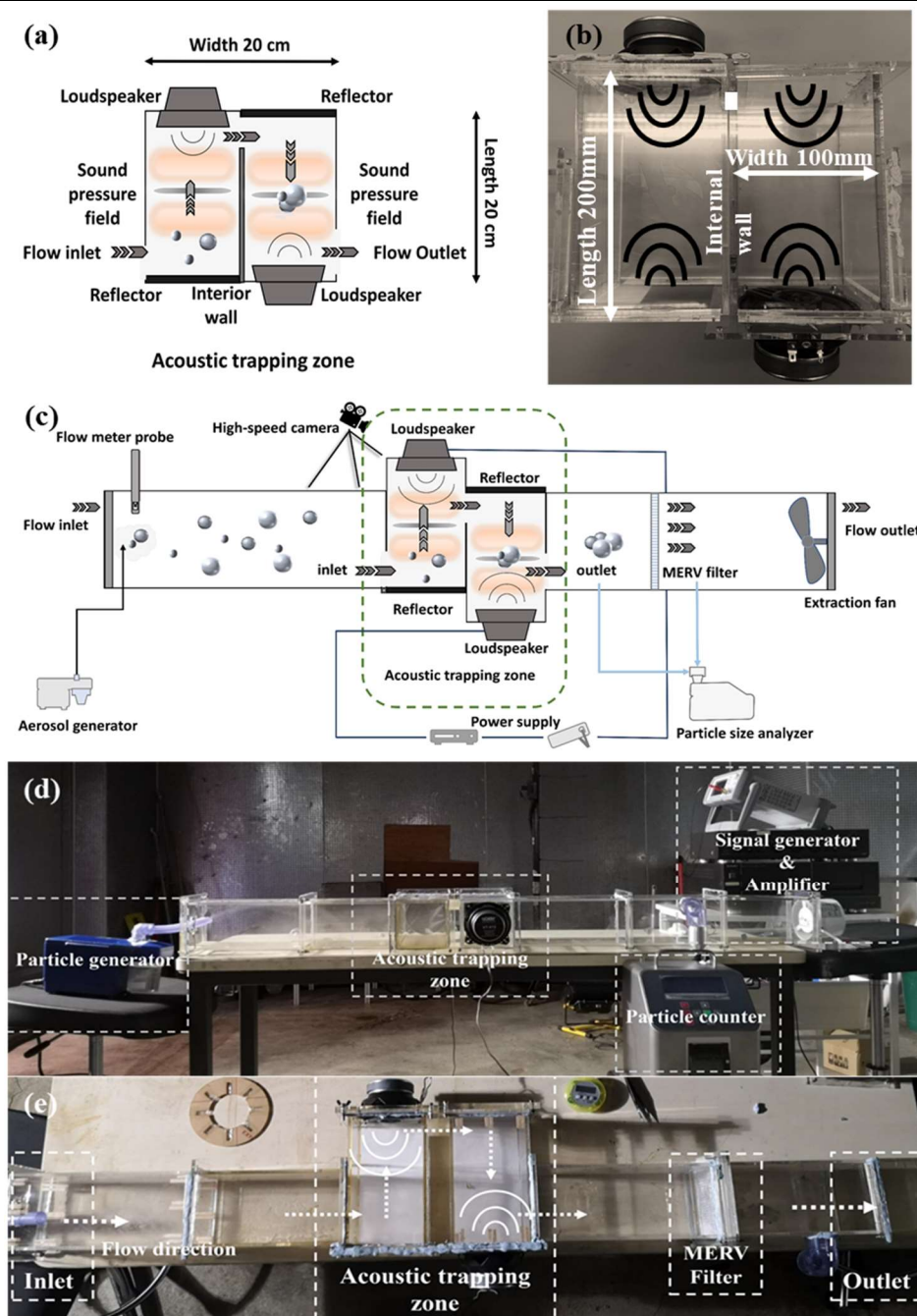


Fig. 5.3: (a) Schematic diagram (top view) of the U-shaped acoustic-driven device; (b) Photo of the fabricated acoustic-driven device (top view); (c) Schematic diagram of a ventilation duct with the U-shaped acoustic-driven device (top view); (d) Experimental setup (side view) of a ventilation tube with the U-shaped acoustic-driven device; (e) Experimental setup (top view) comprises of an aerosol source, a trapping zone, a MERV commercial filter (*PureFit, Pleated Filter MERV 6 Furnace Filter*) and a power fan.

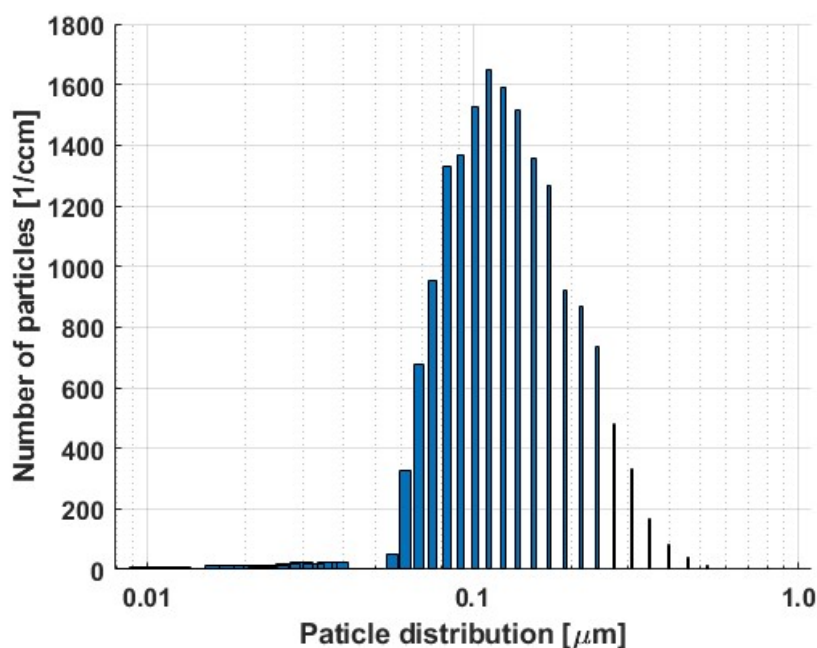


Fig. 5.4: Measured distribution of sprayed particles from aerosol generator.

5.2.3.2 *Microscopic observation of particles precipitation at the bottom of acoustic-driven device*

Adhesive force plays an important role in the process of particle aggregation (Chang et al., 2017), such as acoustic radiation force (Boulaud et al., 1984; Zhou et al., 2015), London-van der Waals force (Park et al., 1999; Peng et al., 2010), liquid bridge force (Zhang et al., 2018a; Kim and Lee, 2020), etc. When two particles are in a very short distance relative to their dimensions, the London-van der Waals force can act as an attractive force to cohere particles (Chang et al., 2017), which the London-van der Waals force is from 1×10^{-9} to 1×10^{-7} N at a particle diameter of 0.01–10 μm . When two particles tend to collide (assuming the particle diameter distribution of 0.006–10 μm), the distance between the particles is about 4×10^{-4} μm (Kulkarni et al., 2011; Marshall and Li, 2014). In addition to the aforementioned adhesive forces, turbulent agglomeration is another promising way to improve fine particles interaction. The vortexes in the turbulent field can reduce the Stoke number (St_k) (a variable to determine the motion of a particle in turbulent flow) and the relative velocity of particles, which cause a significant agglomeration effect for fine particles (Chen et al.,

2019; Sun et al., 2020).

Directly observations of the microscopic morphology of particles can deepen and aid understanding the acoustic effect on particles interaction. Lu et al. (2019) utilized a high-speed camera system to capture the position of fly-ash particles per 1/20,000 second. According to the captures, the average velocities of particles can be estimated through measuring the changes of distance between two adjacent images. However, a direct observation for the morphology of particles within a sound field is still difficult because it relies on the high-resolution of instruments. As a compromise to visualize the acoustic-particle effect in a microscopic way, Qiao et al. (2015,2017), who proposed two acoustic-driven devices for acoustic agglomeration, observed the particle sedimentations at the bottom of the acoustic resonant chambers. The particle precipitations appear to be stripe shapes and gather near to the position of pressure nodes. Besides, Liu et al. (2009a) used a sticky square film (i.e., 0.5×0.5 cm) to collect the particles deposited at the bottom of the vertical agglomeration chamber. Using scanning electronic microscope, most of the aggregates have one or several coarse particles as cores to adhere many finer ones. Therefore, one aggregate can consist of a certain number of fine particles.

In this work, the U-shaped acoustic-driven device is supposed to trap and affect the particles' movement. Due to the acoustic-particle interaction, particles in the acoustic-driven device may occur collision and adhesion, thereby resulting in some sedimentations at the bottom. To observe the morphology of particle precipitations, a simple sampling method is described herein. The morphology images can be shown via SEM images, which allows to further understand acoustic effects on particles.

Fig. 5.5 shows the proposed sampling method. Thin aluminium sheets were cut into 10-by-10-mm squares to collect the particle precipitations at the bottom of the acoustic-driven device. Each small sample sheet was dipped into ethanol solution for

cleaning, following by deionized water rinse. The sample sheets were attached on a polytetrafluoroethylene (PTFE) thin-film, see Fig. 5.5(b), then the PTFE thin-film was placed at the bottom of the acoustic resonant chamber as shown in Fig. 5.5(c). The aluminium sheets were marked and numbered by L1–L7 as row numbers and C1–C3 as column numbers.

Spray particles were continuously injected into the acoustic-driven device. An optimal loudspeaker-operating frequency (i.e., 836 Hz) was used to form a standing wave field. Thus, a pressure node was formed in the center of the resonant chamber (at the position of 10 cm). The overall operating time of incident sound wave was about 30 min. The sampling process was repeated for sufficient specimens. The collected sample sheets were divided into three groups according to their testing conditions, i.e., (i) sample sheets cleaned by ethanol as a control group; sample sheets placed at the bottom of the device: (ii) with spray particles but in the absence of acoustic effect; and (iii) with spray particles in the presence of an acoustic effect. Noted that the sample sheets were placed in sealed petri dishes to avoid contamination before and after sampling. Comparative analysis was thereby conducted between the sample sheets in three groups. For instance, two collected specimens in the same position (e.g., L5C2) but with different testing conditions (e.g., with and without acoustic effect) were used for comparison.

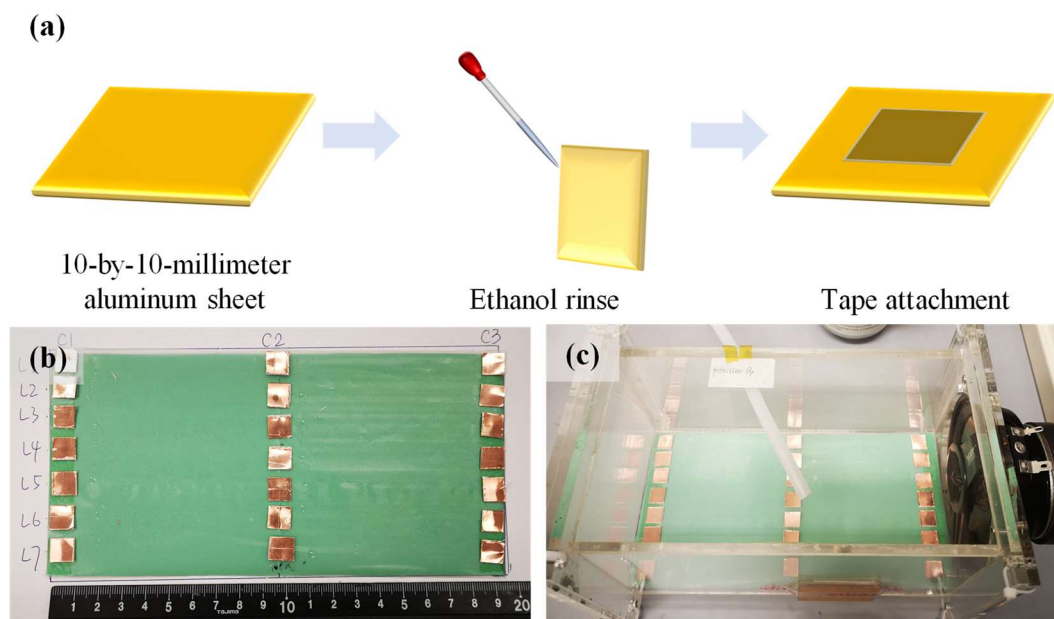


Fig. 5.5: (a) Preparation of a sample sheet (10-by-10-mm square sample sheet); (b) Attaching the sample sheets on a PTFE thin-film; and (c) Placing the PTFE thin-film at the bottom of the acoustic-driven device.

5.3 Results and discussion

5.3.1 Numerical analysis

According to the schematic diagrams of acoustic-driven configurations (see Fig. 5.2), the common design is mounted a loudspeaker at the top of a ventilation duct (as shown in Fig. 5.2(a)) (Ng et al., 2017). To achieve an acoustic-based particulates manipulation under lower SPLs, we propose a novel configuration based on Fig. 5.2(b) for particulates treatment. To provide the relevant numerical analysis about these two different configurations, two case studies are presented in subsequent sections, i.e., (i) a loudspeaker mounted at the top of ventilation duct, and (ii) a combined resonant chamber with loudspeaker mounted at the side wall. Using numerical analysis, we can obtain the preliminary understanding about the sound standing wave field distribution, flow pattern of turbulence field and the underlying conditions which may affect the

moving trajectories of particles.

5.3.1.1 Case I: Loudspeaker mounted at the top of ventilation duct

We investigate acoustic behavior in a 2D ventilation duct model with a length of 120 cm. The schematic diagram is shown as Fig. 5.6, which illustrates a cross-sectional diagram of a typical ventilation system with the loudspeaker considered as an acoustic emitter. The diagram illustrates the airflow direction originating from an inlet to an outlet via an acoustic radiation region (Ng et al., 2017), which is designed to affect the aerosol particles. In the numerical model, the wall boundaries at the top and bottom are constructed of rigid sound surface. Both inlet and outlet are set with a flow speed of 0–0.5 m/s. To ensure sufficient computational accuracy, the maximum element edge length is smaller than one-sixth of the wavelength (Muller et al., 2012; Peng et al., 2020; Rokad and Pandya, 2020). The simulation shows that standing waves can be sustained under resonance at a minimum sound pressure level of 70 dB, which can be also maintained at the 9th harmonic frequency of 10287 Hz.

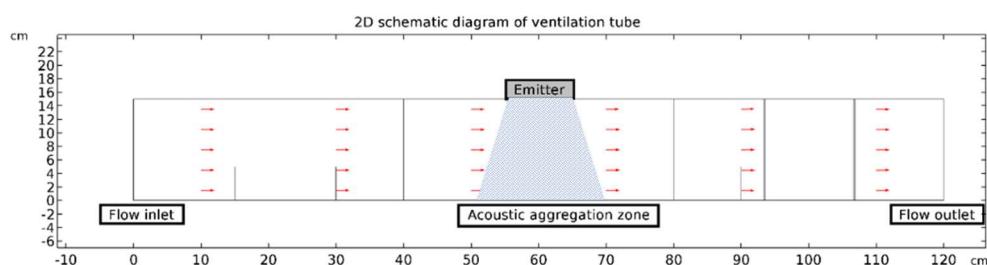


Fig. 5.6: A schematic diagram of ventilation ducting with 120 cm length for simulation.

In Fig. 5.7, we investigate the effect on the tube size, whereby the cross-sectional height was varied from 10, 15 to 20 cm. We select a 15-cm height for the tube as similar to Ng et al. (2017) and the emitter generates the standing wave at the middle as indicated by a 60-cm mark. As seen in the figure, the emitter generates an acoustic wave profile that can extent to the tube covering a triangular area according to an

acoustic angular spread. Using a linear extrapolation, the acoustic angular spread can be evaluated by two sides of the acoustic field lines. Under different height dimensions, the acoustic angular spread values are 56.1° , 55.1° , and 47.9° , respectively.

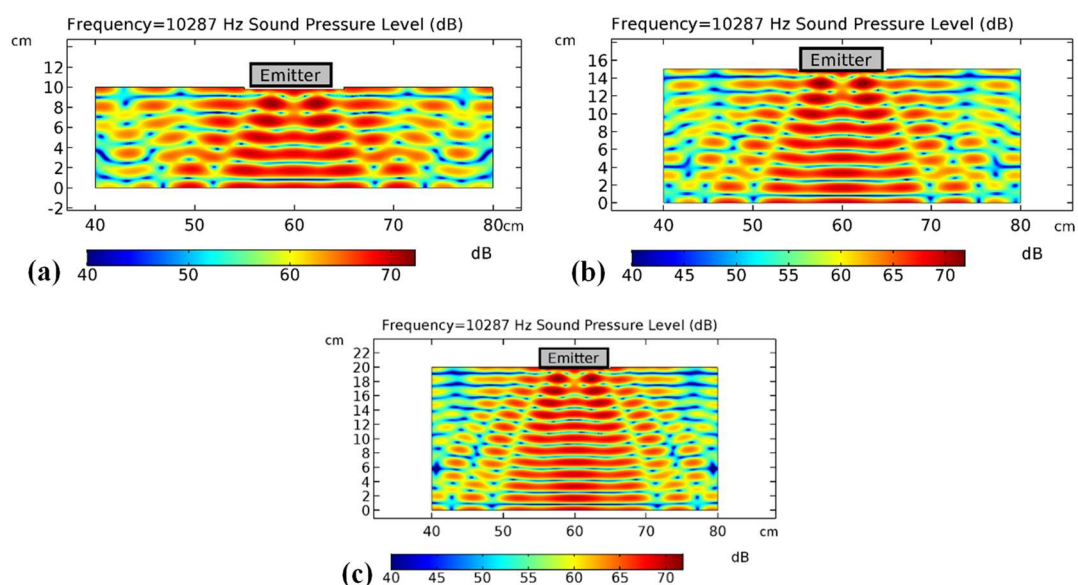


Fig. 5.7: A 2D model simulation of a ventilation duct of different height: (a) 10 cm, (b) 15 cm and (c) 20 cm under 10287 Hz.

Fig. 5.8 shows the numerical simulations in a 15-cm cross-sectional tube at three different resonant frequencies, i.e., 6858 Hz, 10287 Hz and 20574 Hz. In this case, the acoustic angular spread values are 56.1° , 55.1° , and 47.9° , respectively. The results indicate that the angle of the emission spread decreases proportionally with increasing frequency. Operating with lower frequencies, however, does not guarantee that a high sound pressure level can be sustained by an emitter (Tu et al., 2019). To enhance the trapping effect, extending the residence time of particles in the agglomeration region is highly desired. Therefore, in this 15 cm cross-sectional tube design, the fabrication of such devices can achieve an acoustic spread of 55° with an operating frequency at around 10 kHz.

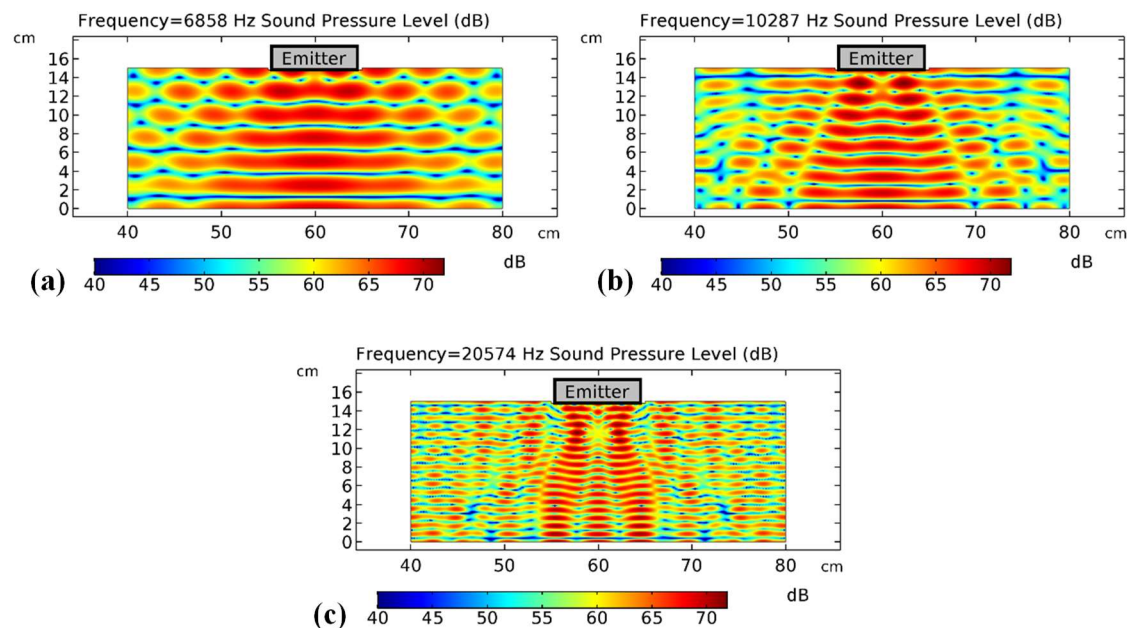


Fig. 5.8: A 2D model simulation of a ventilation duct at 15cm size at different frequencies: (a) 6858 Hz, (b) 10287 Hz and (c) 20574 Hz.

We further investigate the acoustic agglomeration effect towards particulate matter (PM10) by inserting aerosol particles at a size of $10\ \mu\text{m}$ and operating the emitter at an SPL of 160 dB (Liu et al., 2021). In the simulation, we insert a concentration of 10,000 particles to the tube randomly. The airflow rate is set as 0, 0.1, 0.3 and 0.5 m/s, as shown in Fig. 5.9. The results from the numerical simulations indicate that acoustic aggregation can affect the particles by trapping them in the acoustic zone. Four different airflow rates are presented, it is observed that an acoustic spread of 55° is retained in the presence of airflow.

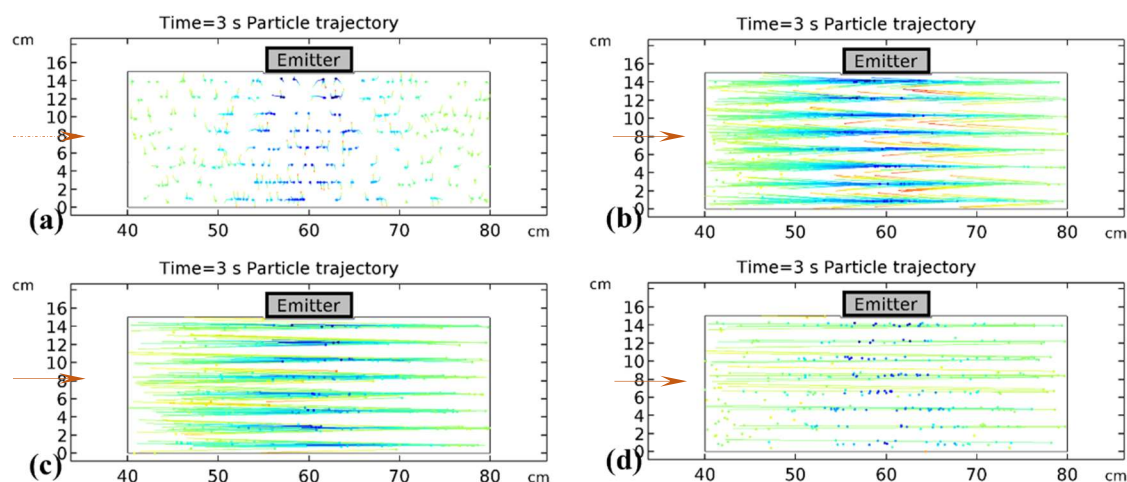


Fig. 5.9: A 2D model showing the particle trajectory of PM10 sized matter as introduced into the tube at a flow rate of (a) 0, (b) 0.1, (c) 0.3 and (d) 0.5 m/s. Arrows indicate the direction of moving particles across the tube and a snapshot is captured at 3s.

5.3.1.2 Case II: Combined resonant chambers with loudspeaker mounted at the side wall

We perform the numerical investigation of the trapping process in the acoustic resonant chamber based on the proposed configuration in Fig. 5.2(b). Simulations of sound pressure fields, flow fields and particle trajectories are used to visualize the moving trajectories of particle under different dominant effects in the acoustic resonant chambers. Two simplified 2D models (i.e., an acoustic pressure model and a fluid flow model) are implemented separately utilizing COMSOL, which is to offer some guidelines for experimental setup. The acoustic pressure model is used to study the SPL profile, while the turbulent flow model is used to illustrate the flow pattern within the acoustic-manipulated device. Particles are released in both models to reveal the particle trajectories under different dominant forces. Based on the acoustic wave theory, the distribution of sound pressure in a standing wave can be obtained by Eq. (5.6), which is a summation of the forward and backward propagation waves. Under a standing wave, an abrupt pressure change at the pressure nodes can be created within

the resonant chambers. To illustrate the trajectory of particles under an acoustic field, the effect of acoustic radiation force (Eq. (5.3)) is studied to investigate the motion of particles. A total number of 10,000 particles are released to the acoustic resonant chambers from 0 to 0.3 m/s, where the density and diameter of the particles are 100 kg/m^3 and $5 \times 10^{-6} \text{ m}$, respectively. In addition, the RANS equations (Eqs. (5.7) and (5.8)) can be utilized to solve the continuous flow inside the device. Then, the $k-\varepsilon$ turbulence model (Eqs. (5.9) and (5.10)) is adopted to consider the turbulence effect within the resonant chambers (Shi et al., 2020). In the flow field simulation, we consider the drag force (i.e., F_d) in Eq. (5.13) that is a dominant effect to act against the motion of particles by using the built-in functions of the numerical simulation software. Particles are released to show their movements under the flow field.

According to the previous study (Ng et al., 2017) and the references therein, the particle number concentration can be reduced under the conditions of an SPL of 140 dB and an average flow speed of 0.15 m/s. Hence, we only expect that moving particles with a relatively low speed along the fluid field are possible to be blocked under the coupling effects of the turbulent flow and standing wave. To investigate the overall coupling effects, we conduct an experiment to examine the filtration efficiency of the proposed acoustic-driven pre-filtering device. The overall assessment of the acoustic-driven device for low-graded filters improvement is discussed in the subsequent section.

Fig. 5.10 shows a two-dimensional cross-sectional simulation that is used to examine the airflow pathway and the influence of the two-chamber enclosure structure in the absence of acoustic effects. The airflow pathway and speed contour simulated under a steady-state condition within the two chambers. The boundary condition for the “*flow inlet*” is designated as 0.75 m/s, and the “*flow outlet*” is set at an arbitrary interface. Noted that the location of “*flow inlet*” and “*flow outlet*” are shown in Fig. 5.3(c). In these diagrams, there is a significant increase in speed at the

gap between two chambers, and at the region near the outlet. Fig. 5.10(a) shows the profile of flow speed within the U-shaped resonant chambers. Fig. 5.10(b) presents the trajectory of the airflow with respect to speed. We observe that there is mainly a laminar airflow in the first and second chambers, but a turbulent airflow is also induced at the low velocity regions, due to airflow resistance resulting in the two chambers. Since the pressure nodes have a lower SPL, so particles would be trapped in these regions.

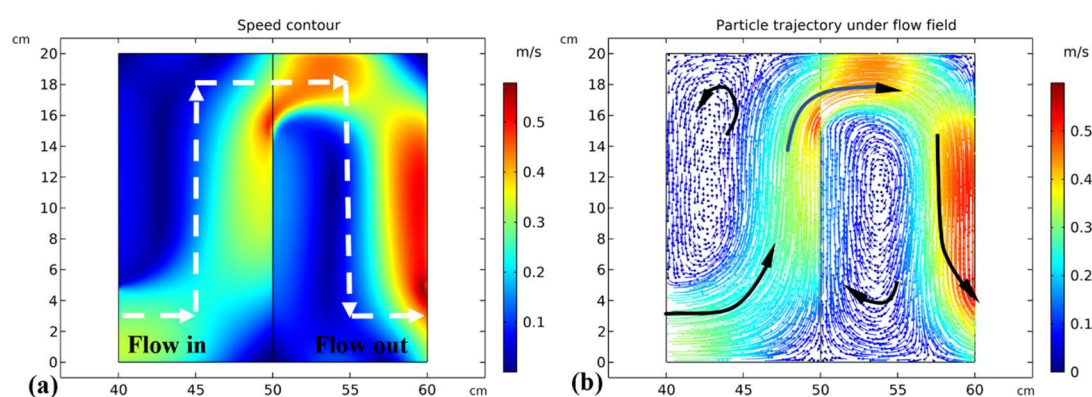


Fig. 5.10: A 2D numerical simulation. (a) the airflow speed contour map under a steady-state condition; and (b) the particle trajectory of a laminar flow occurs within the chambers with a minimal airflow resistance.

Fig. 5.11 shows a 2D numerical simulation that consists of two resonance chambers, which was used to investigate the acoustic device. In Fig. 5.11(a), the sound pressure field region is formed by the sound waves emitted from the loudspeakers at a resonant frequency that corresponds to the dimensions of the chamber. It shows the respective locations of the nodes and anti-nodes, which indicate the highest and lowest SPLs. This creates a pressure differential, resulting in the trapping of particles as they pass from the inlet to the outlet via two sound field regions. By using the acoustic pressure model as shown in Fig. 5.11(a), we can obtain the sound pressure within the U-shaped device. Then, the “*Particle Tracing for Fluid Flow*” interface function in COMSOL was used to trace the motion of particles. In

addition, Fig. 5.11(b) presents the variation of sound pressure along the length direction of the resonant chamber at 836 Hz, and Fig. 5.11(c) shows the trapping of particles at the pressure nodes under acoustic fields.

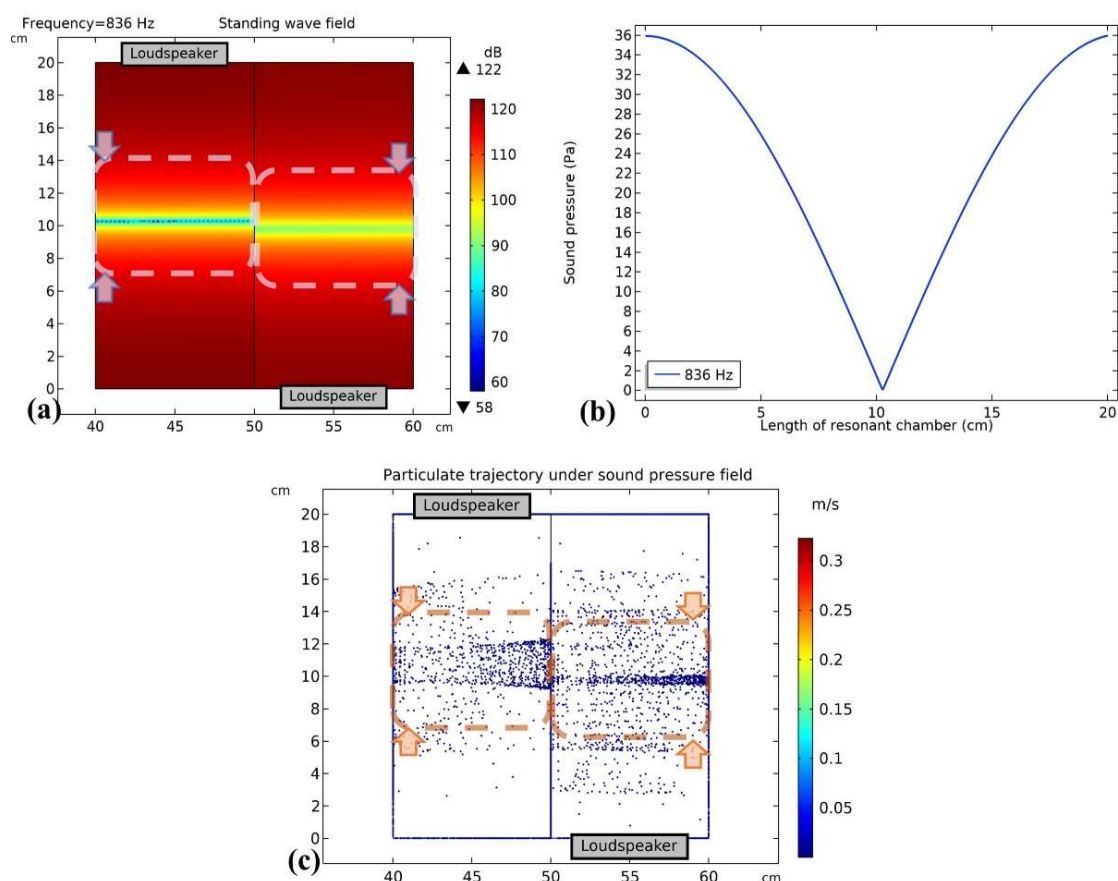


Fig. 5.11: A 2D numerical simulation of the device operating at 836 Hz and 116 dB: (a) Formations of a standing wave and a pressure differential (at 10 cm location) to facilitate particle trapping; (b) Variation of sound pressure along the length direction of the resonant chambers at 836 Hz; and (c) Trapping of particles at the pressure nodes.

5.3.2 Experimental results

We designed an experimental prototype for verification of this pre-filtering technique by a particle concentration measurement. The filtration of aerosol particles of certain sizes was optimized, to verify the proposed simulation parameters and

boundary conditions. The loudspeakers provided specific acoustic pressure waves with a certain dependence on frequency, and we illustrated how this can influence the aerosol concentration of fine particles (0.3–1.0 μm) and coarse particles (2.5–10 μm).

In a preliminary testing, particles were generated by sandpapering balsa wood (*Ochroma pyramidale*; density = 116 kg/m^3), and were introduced into the chamber via a sidewall, as it was horizontally oriented. Fig. 5.12(a) is a resonant particle acoustic pattern under the influence of a standing wave. Figs. 5.12(b) and 5.12(c) are enlarged images to show the concentration of particles in the center of the resonance chamber, i.e., the location of the pressure node inside the chamber. It can be seen that the wood powders can be forced and gathered at the center of the resonant tube under 116 dB and 836 Hz. At the pressure node, such powders were aligned to a uniform and multi-line pattern, and the interval between two lines was around 2.43 mm. By using this test, it can help reflect the effect of acoustic force on the lightweight particles under an acoustic field.

To study the acoustic effects, we systematically examined the performance of the device in terms of the reduction in the particle concentration and the removal coefficient, and thereby determined its filtration efficiency. Three case studies were examined to determine the dependence of the device performance on the frequency, SPL, and airflow rate. These parameters are the critical variables to determine the effectiveness of the present device. The findings that support our theoretical simulations of the particle trapping effect are also discussed in this section.

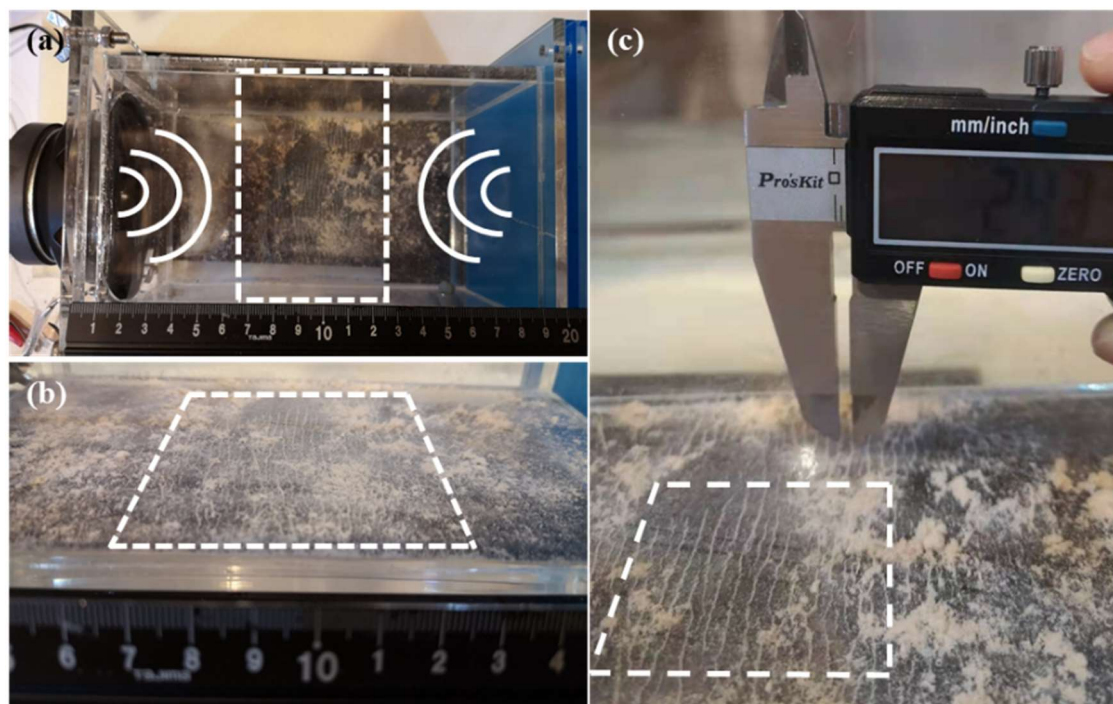


Fig. 5.12: Preliminary test of wood powders generated from sandpapering balsa wood (*Ochroma pyramidale*; density = 116 kg/m^3): (a) Balsa wood within the resonant chamber under 116 dB and 836 Hz; (b) Particles concentrated at the pressure node; and (c) A multi-line pattern of wood powders under acoustic standing waves within the resonant chamber (the interval between two lines $\sim 2.43 \text{ mm}$).

5.3.2.1 Frequency dependence on PM reduction

To examine the frequency dependence on PM reduction in our experiment, we considered the resonant frequencies of 836, 1637, 2510, 3346, and 4183 Hz under an SPL of 116 dB for the enclosure with a length of 20 cm.

Fig. 5.13 shows a plot of the particle concentration with an airflow of 0.75 m/s, as these particles were introduced into the tube. The measured particle concentrations, for fine and coarse particles, during the trapping process under various frequencies are presented. At 836 Hz (the lowest frequency that was applied), there was a 61% reduction in the particle concentration, which was the strongest trapping effect that was observed. In contrast, at 4183 Hz (the highest frequency that was applied), there

was only a 1% reduction in the particle concentration, which was the lowest reduction that was achieved. These data show that acoustic waves in the enclosure induced a significant reduction in particle concentration, and that the greatest reduction occurred at a particle size of 1.0 μm , which is similar to the findings in (Qiao et al., 2017). This is equal to a removal coefficient of up to 61%. In contrast, the lowest reduction occurred at a particle size of 2.5 μm . This suggests that the particle size resists the trapping effect, due to the influence of the particle velocity and acoustic pressure.

Fig. 5.14 shows that, under an optimal fundamental resonant frequency of 836 Hz, the reduction in the concentration of fine particles is the highest among others (as shown by the green solid line), and would decrease thereafter, with particles greater than 2.5 μm in size. This trend can also be observed at other resonant frequencies (from 1637 to 4183 Hz) that form a standing wave. However, the particle-reduction trend would decrease when we increased the frequency, as shown by the efficiency of removal of 1.0- μm particles.

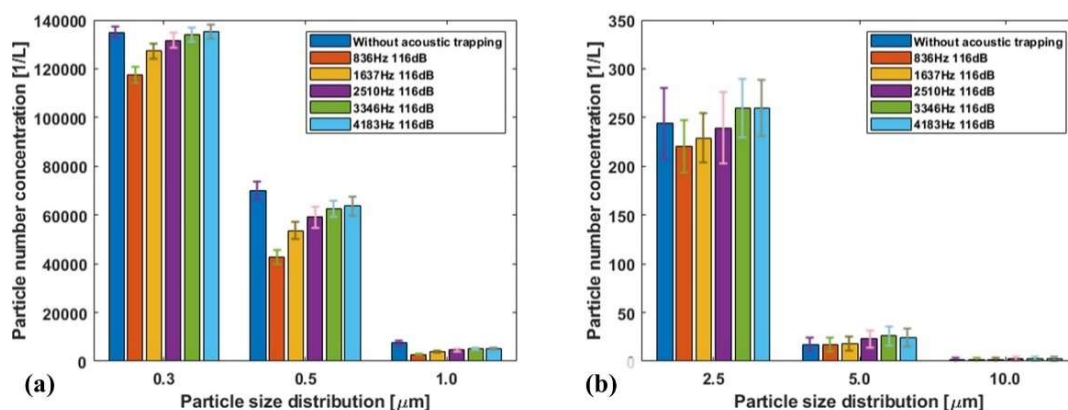


Fig. 5.13: Particle number concentration under various operating frequencies (836–4183 Hz) and 116 dB: (a) fine particles (0.3 to 1.0 μm); and (b) coarse particles (2.5 to 10.0 μm).

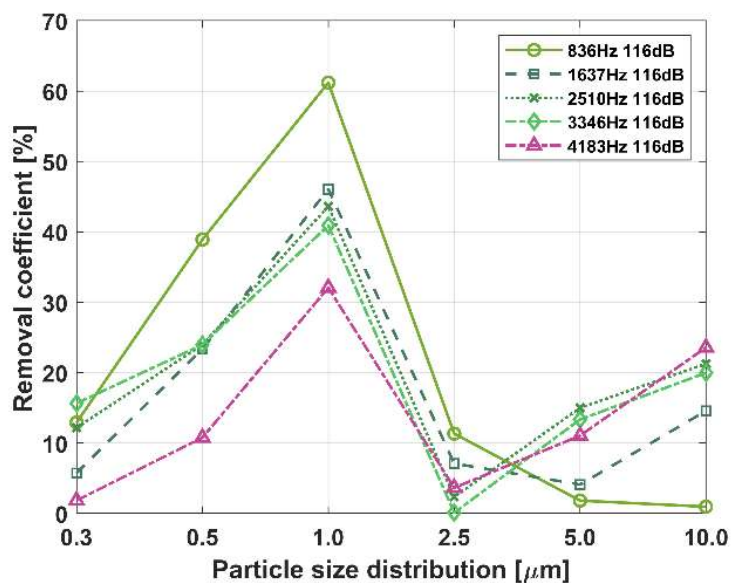


Fig. 5.14: Removal coefficient of under various resonant frequencies (between 836 Hz and 4183 Hz) at 116 dB.

5.3.2.2 SPL dependence on PM reduction

In the first case study, we determined that 836 Hz was the most effective frequency to promote particle trapping. In the second case study, we examined the effects of the SPL on particle reduction. Fig. 5.15 shows a plot of the particle concentration under the acoustic effect, which was applied at an optimized frequency of 836 Hz and an SPL between 108 and 116 dB. Figs. 5.15(a) and 5.15(b) show the measured particle concentration for the fine and coarse particle distributions, respectively.

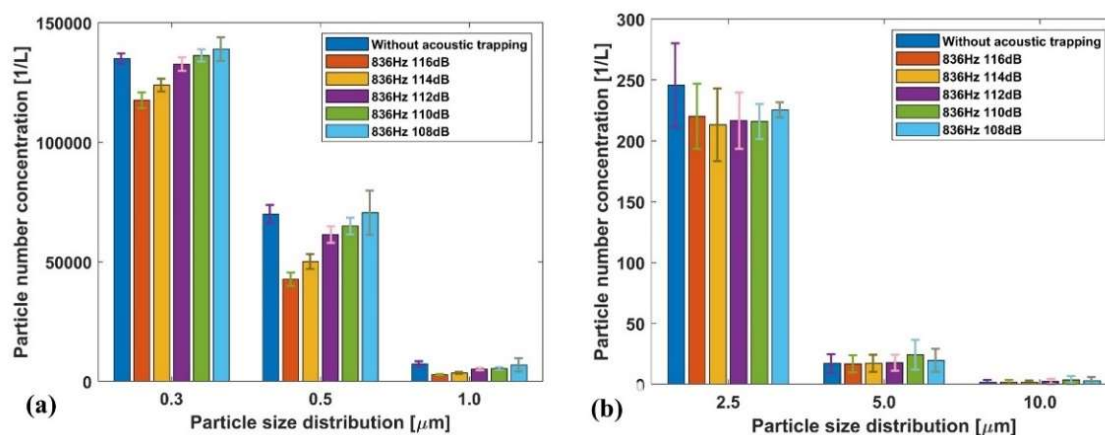


Fig. 5.15: Influence of particle size distributions with and without the acoustic effect under 836 Hz and 108–116 dB: (a) fine particle (0.3 to 2.5 μm); and (b) coarse particle (2.5 to 10.0 μm).

Fig. 5.16 shows the removal coefficient determined for the acoustic-driven device operated at various SPLs. Similar maximum removal coefficients for 1-μm particles were found for SPLs greater than 108 dB. At 108 dB, a linearly increasing trend can be seen as the removal coefficient increases from 3% to 21%, which may indicate insufficiency in the supply of a sound pressure field for the promotion of particle trapping. At SPLs of 110–116 dB, the effectiveness of acoustic effect is clearly observed, as the removal-coefficient trends similar to those in Fig. 5.14. The maximum removal coefficient for 1-μm particles was again 61%, whereas for >2.5-μm particles, an SPL of 110 dB increased the removal coefficient from 14% to 34%. Because the removal of finer particles is more difficult, it was optimal to operate the loudspeakers at 116 dB to maximize the trapping effect.

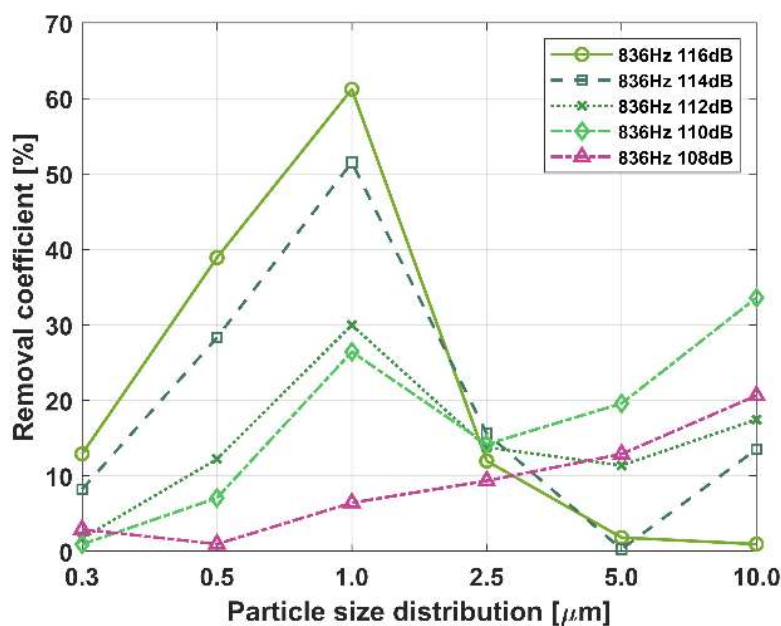


Fig. 5.16: Removal coefficient of particles at 836 Hz under different SPLs.

5.3.2.3 Airflow dependence on PM reduction

In this case, we further examined the dependence of acoustic effect on airflow while applying a loudspeaker frequency of 836 Hz at an SPL of 116 dB. Fig. 5.17 shows the removal coefficient at a flow speed from 0.45 to 0.75 m/s. Noted that the flow speed is measured at the flow inlet of the acoustic resonant chambers as shown in Fig. 5.3(a). The results show a maximum removal coefficient trend that is similar to those in Figs. 5.14 and 5.16 with respect to the particle size distribution. According to the numerical simulations, it is possible that an increase in the flow rate allows the particle trajectory to provide a recirculating airflow within the chambers and allows particles to reside within the sound pressure field for a longer period. Therefore, as more incoming particles enter into the chamber, the greater airflow can induce a greater recirculating flow within the vertical enclosure and thus cause a greater number of particles to undergo the trapping effect. The results are consistent with the numerical simulation results. However, further investigation is required to obtain more conclusive data.

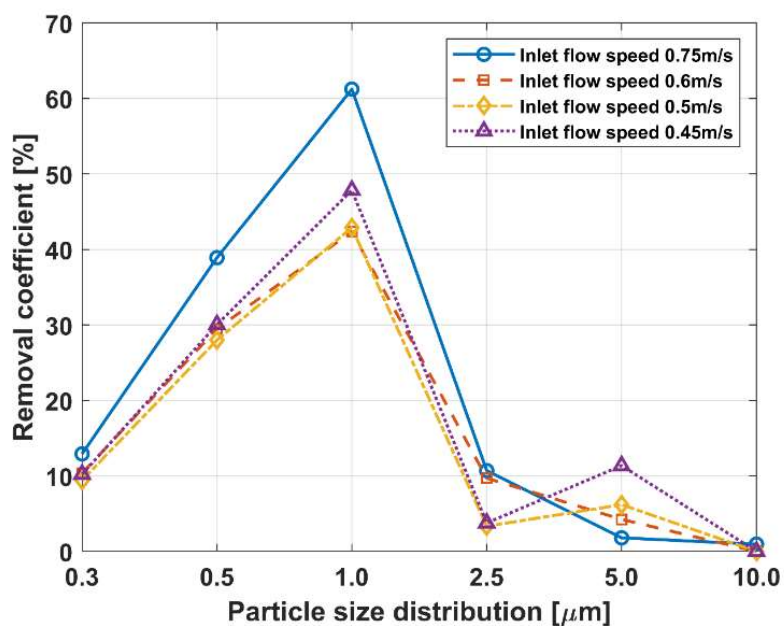


Fig. 5.17: Removal coefficient of particles under the inlet flow speed ranged from 0.45–0.75 m/s.

In Table 5.1, we summarize the filtration efficiency of particle concentrations under various critical parameters (i.e., frequency, SPL and airflow rate). In addition, a further investigation is presented in the next section to obtain more data that are conclusive.

Table 5.1: Filtration efficiency of particle concentrations under various parameters.

Under various operating frequencies			
Operating Frequency	Operating SPL	Inlet flow speed	Removal coefficient for PM 1.0
836 Hz	116 dB	0.75 m/s	61.4%
1637 Hz			46.1%
2510 Hz			37.3%
3346 Hz			30.7%
4183 HZ			30.6%
Under various SPLs			
Operating Frequency	Operating SPL	Inlet flow speed	Removal efficiency for PM 1.0
836 HZ	116 dB	0.75 m/s	61.4%
	114 dB		51.7%
	112 dB		30.3%
	110 dB		26.7%
	108 dB		6.8%
Under various inlet flow conditions			
Operating Frequency	Operating SPL	Inlet flow speed	Removal efficiency for PM 1.0
836 HZ	116 dB	0.75 m/s	61.4%
		0.6 m/s	42.8%
		0.5 m/s	43.0%
		0.45 m/s	47.0%

5.3.2.4 *Acoustic-based pre-filtering system*

In the previous sections, we analyzed the acoustic effect of the U-shaped device and the optimization of its operating parameters. In this section, we will discuss the improvement provided by the acoustic-driven pre-filter in terms of the overall filtration efficiency. To test and calibrate this device for practical use, we examined the effectiveness of a commercial MERV-6 grade coarse filter when combined with the present technique.

Fig. 5.18 shows a comparison of the particle concentration with respect to size (0.3–10 μm) and with respect to the presence of a MERV-6 filter, and a MERV-6 filter combined with the acoustic-driven pre-filter. Figs. 5.18(a) and 5.18(b) show the concentrations of fine particles (0.3–2.0 μm), while Figs. 5.18(c) and 5.18(d) present the concentrations of coarse particles (2.5–10.0 μm). It can be seen that when the MERV-6 filter was used, the particle reduction would increase as we increased the particle size. With the presence of this acoustic-driven device, it can further increase the particle reduction in all cases, especially for the case of 0.3–1.0 μm . These data indicate that the present pre-filtering technique is more effective to remove fine particles than coarse particles. Therefore, an acoustic-based pre-filtration technique complements MERV-6 filters can be designed for the removal of fine particles. This also shows that the combination of the present technique with MERV-6 filters may generate a cost effectiveness and long-use filtration device.

Fig. 5.19 shows the removal performance pertaining to a MERV-6 coarse filter, the present technique, and a MERV-6 filter combined with the present technique. The MERV-6 filter achieved an average reduction in the concentration for coarse particles (>2.5 μm) of 50%, corresponding to the *PureFit Pleated Filter* specifications (i.e., a filtration efficiency up to 60% for 0.3–10.0 μm particles). However, the filtration performance of the MERV-6 filter considerably decreased for particles smaller than 0.8 μm , which was expected. Therefore, significantly improved filtration performance

can be obtained when the MERV-6 filter was used in combination with the acoustic-driven pre-filtering technique. Furthermore, the acoustic-based pre-filtration technique can compensate for the ineffective fine-particle removal rate by the MERV-6 filter, resulting in a maximum removal coefficient of up to 89%. If the MERV-6 filter was absent, the present technique can still achieve a maximum removal coefficient of up to 61% efficiency for particle sizes approaching 1.0 μm . These data indicate that the present pre-filtering technique is more effective to remove fine particles than coarse particles. Therefore, an acoustic-based pre-filtration technique complements MERV-6 filters can be designed for the removal of fine particles. This also shows that the combination of the present technique with MERV-6 filters may generate a cost effectiveness and long-use filtration device.

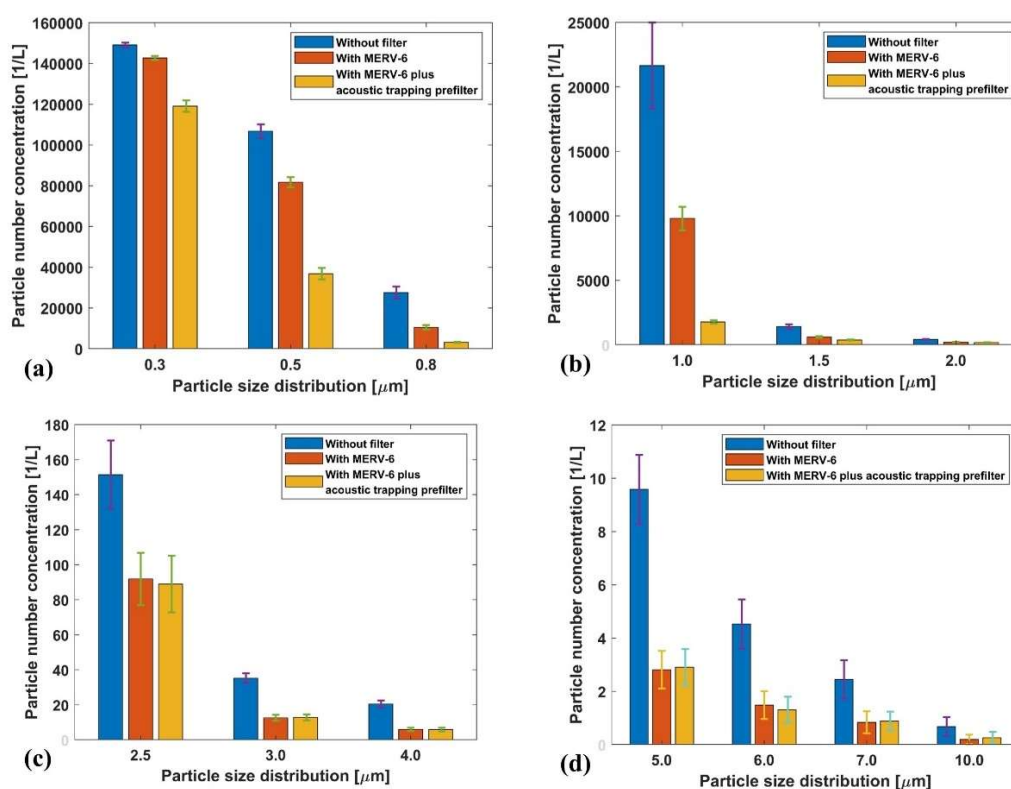


Fig. 5.18: Influence of particle size distributions with and without a MERV filter under 116 dB and 836 Hz: fine particles between (a) 0.3–0.8 μm , (b) 1.0–2.0 μm ; and coarse particles between (c) 2.5–4.0 μm and (d) 5.0–10.0 μm .

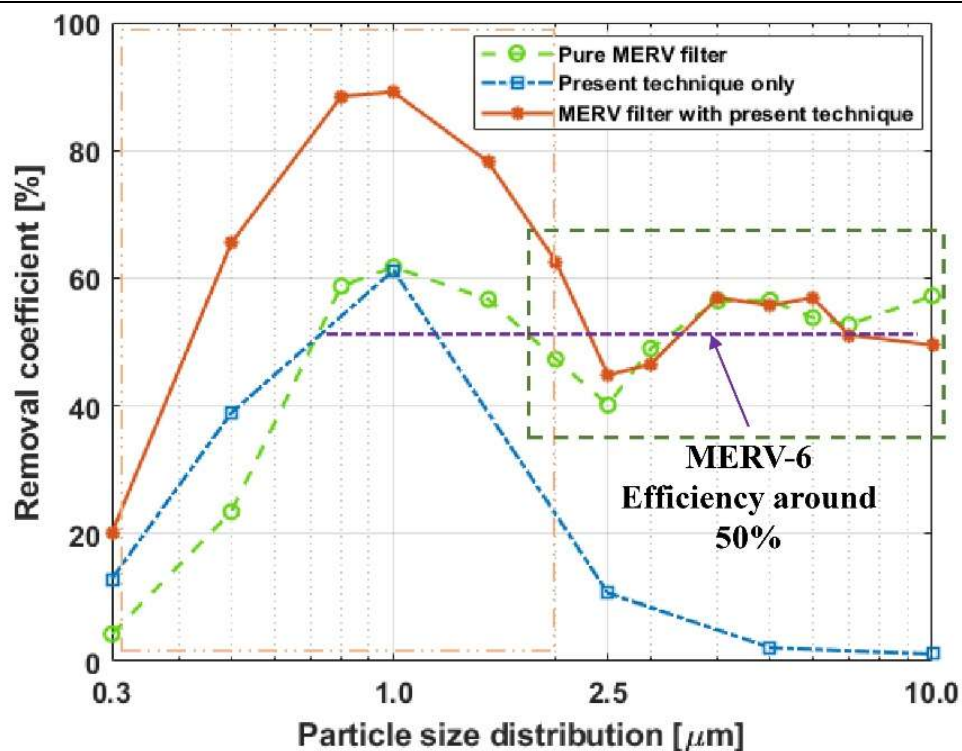


Fig. 5.19: Removal coefficient as determined from a MERV-6 filter (green dash line), present technique (blue dash line), and a MERV filter with the present technique (red solid line).

To benchmark our results with those in the literature, Fig. 5.20 depicts the filtration efficiency for the present pre-filtering technique combined with a low-grade MERV-6 filter for comparison. To demonstrate the working performance, we selected a common HVAC filter (MERV-6 filter) for analysis. Our device achieved a high performance of up to 89% efficiency, which indicates that it is an effective method for the removal of fine particles. Notably, our device was more than 100% better for filtering 0.3–2.0 μm particles than cabin filters, which are often implemented in vehicle-based applications (Xu et al., 2011). Compared to the high-grade MERV-13 filter as tested by Dols et al. (2020), our achieved efficiency was also consistent with the MERV-13 filter for a particle size of 0.4–1.0 μm. This finding indicates that if a MERV-6 graded filter is replaced with high-grade filters, the filtration performance will be further increased, without the need to rely solely on very high-performance-

based HEPA-type filters. Compared to the fine-particle filter (F6-class) (Zhao et al., 2020), our device can present a better removal efficiency rate at a region of 0.3–1.0 μm . Notably, our device also exhibited better performance than those low-grade HVAC filters (NIOSH, 2003). The removal efficiency of the present technique would decrease when the particle size is larger than 1.0 μm due to the interaction of acoustic strength. In reality, it is rather difficult to filter the sub-micron particles than the super-micron particles, the present filtration technique provides an effective avenue for this issue.

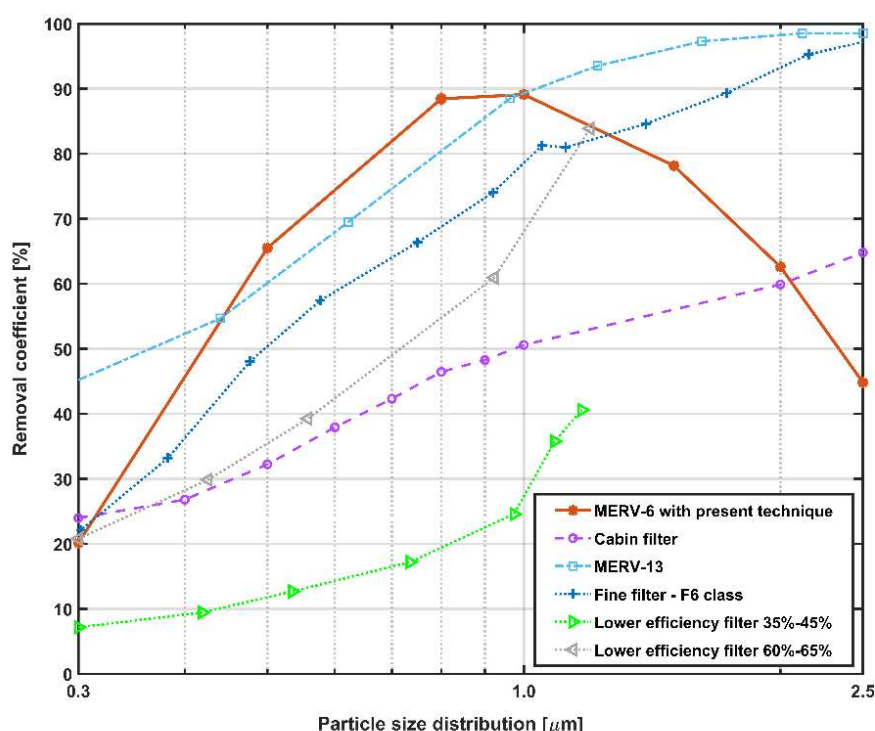


Fig. 5.20: Performance comparison between MERV-6 filter coupling with the present U-shaped device, cabin filter (Xu et al., 2011), MERV-13 filter (Dols et al., 2020), fine filter (F6 class) (Zhao et al., 2020), and low-grade filter (35–45% and 60–65%) (NIOSH, 2003).

In addition to indoor air quality, it is known that reducing airborne transmission of virus in enclosed areas requires effective control measures, including ventilation and air filtration (Morawska et al., 2020). Recent epidemiological studies (Liu et al.,

2020) indicated that aerosol transmission of SARS-CoV-2 mainly includes two size ranges, one is in the sub-micron range (0.25–1.0 μm) and the other one is in the super-micron range ($> 2.5 \mu\text{m}$). The study presented herein shows good results for the sub-micron range (0.3–1.0 μm). Hence, the potential application of this engineering design is a promising approach to reduce the possibility of airborne viral transmission in ventilated indoor spaces. The present investigation also provides insights into the improved design of a non-invasive pre-filtering approach in ventilation systems, as the design possesses a high level of flexibility to work with various filter types.

5.3.2.5 Morphological features of particle precipitation with or without sound application

The SEM images of particle precipitations are shown in Fig.5.21. The underlying colors, i.e., blue, yellow and pink, are used to classify the samples under three different testing conditions corresponding to the control group, sampling without a sound effect, and sampling with a sound effect, respectively. Fig. 5.21(a) shows the SEM images of clean aluminium sample sheets as reference, in which the magnification is ranged from 331x to 5.05kx. Cleaning by the ethanol solution, no particle or dust can be observed on the surface of the sample sheets.

To illustrate the acoustic effect on aerosol particles, we mainly discuss the sample sheets tested under two conditions, i.e., sampling without a sound effect and sampling with a sound effect. Fig. 5.21(b) shows the morphological images of particle precipitations without an acoustic effect, which are enlarged from 5.23kx to 9.56kx. According to the images, two kinds of morphologies can be observed such as spheroidal particles and cumulated particle clusters. Due to the turbulence-induced disturbance and Brownian motion, the heavy particles may be deposited under the force of gravity. The distribution of particle sedimentations is relatively independent. The diameters of the spheroidal particles are about 1.79 μm and 2.47 μm . The cumulated particle clusters ($\sim 3 \mu\text{m}$ in diameter) are also observed, see the white

arrows and yellow circles marked in Fig. 5.21(b).

Fig. 5.21(c) shows the morphological images of particle precipitations in the presence of an acoustic effect (i.e., pink background section). The magnifications are from 861x to 56.0kx. According to the SEM images, we observe various morphological forms of particle sedimentations, which is different from the patterns in Fig. 5.21(b). A multi-line pattern can be observed, in which the particle sedimentations present stripe-like shapes (see the white square marked in Fig. 5.21(c)). The width of the stripe-sedimentation particles is $\sim 2.65 \mu\text{m}$ and the length is $\sim 11.35 \mu\text{m}$. The interval between stripe-sedimentation particles is about $7.30 \mu\text{m}$. In addition, we also observe some larger particle clusters with irregular shapes under a magnification of 13.0 kx. The approximate length of the regular stripe-shape aggregates is from $0.93 \mu\text{m}$ to $2.86 \mu\text{m}$. Some stripe-shape particle clusters are larger than $5 \mu\text{m}$ in length. It implies that the particle precipitations can be observed without an acoustic effect, however, regular and larger stripe-shape particle precipitations can be formed under the effect of acoustic waves. In general, the SEM images are the supportive evidence to show the acoustic impact on fine particles within the U-shaped acoustic-driven device.

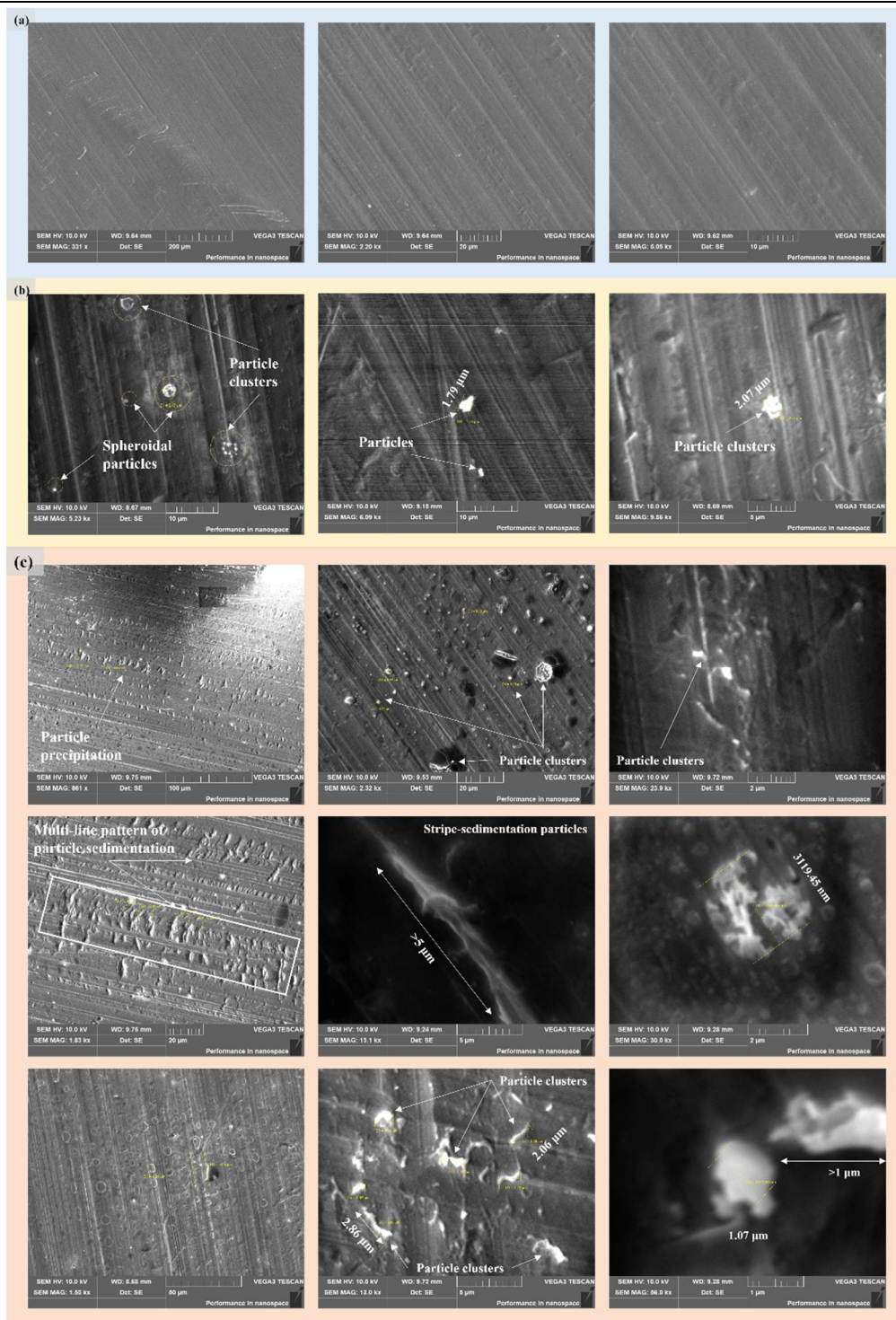


Fig. 5.21: SEM images of particles precipitation at the bottom of the U-shaped acoustic resonant chamber: (a) Clean sample sheets as a control group; (b) Sample sheets placed at the bottom of the acoustic-driven device without an acoustic effect; and (c) Sample sheets placed at the bottom of the acoustic-driven device with an acoustic effect.

5.4 Concluding remarks

The implementation of an acoustic-based manipulation device can improve particle removal filtration efficiency inside mechanical ventilation systems. The major findings of this work are summarized as follows:

- A simple U-shaped acoustic-driven resonating device that can enhance the filtration rate of coarse filters for the sub-micron particles under a lower SPL has been proposed. To facilitate the trapping effect, loudspeakers were deployed at the sidewall positions of the resonant chambers, where the generation of acoustic waves is in an opposite direction against an incoming airflow.
- To verify the proposed technique, a prototype was fabricated, and experimental tests were conducted to investigate the extent of trapping fine particles with various sizes. Parametric studies of the device performance on acoustic frequency, SPL and flow speed were investigated. As a standalone device, it can achieve a filtration efficiency of 61% and operate at a lower incident SPL (116 dB).
- Coupling with a MERV-6 graded coarse filter, the acoustic effect could reduce the presence of particles at the sub-micron range of 0.3–1.0 μm , with up to 89% efficiency for the removal coefficient of 1.0- μm particles. The removal efficiency can be flexibly enhanced by coupling the present design with high-grade filters.
- Using a microscopic observation, some morphological forms of particle precipitation can be observed, this is the supportive evidence to illustrate the occurrence of acoustic-particle interaction within the resonant chambers.

Although this work does not provide a direct observation of collision and interaction of sub-micron particles, the present design has shown potential to perform as an effective prefilter air-cleaning strategy. Yet, the U-shaped configuration utilizing

double resonant chambers may restrict the flow rate within the ventilation duct. Consider the practical flow rate (e.g., 6 m/s) in mechanical ventilation ducts, this device works under a small-scale flow rate. A refined study will focus on the influence of greater airflow rates on the working efficiency. Further research emphasis will also focus on the aggregation modes of particles within the acoustic-driven zone and the sensitivity of acoustic frequencies on various particle sizes.

CHAPTER 6

FABRICATION AND CHARACTERIZATION OF NANO-THINFILM THERMO-ACOUSTIC DEVICES

6.1 Introduction

Current research efforts in novel acoustic devices focus on the study of alternative electroacoustic transducers having no moving parts (Hu et al., 2010; Kontomichos et al., 2012; Tiwatane and Barve, 2014; Chen et al., 2021), which can be achieved by utilizing a thermo-acoustic (TA) effect. Unlike the conventional pressure-velocity variation mechanism, the TA effect that came from the thermophone concept (Arnold and Crandall, 1917) can be created by a temperature-position displacement for generating sound waves. Despite its availability for a century ago, this technology has been hindered due to the lack of smart materials and fabrication methods. In the 1990s, the first TA device, made of a 30-nm-thick aluminium film placed on a micro-porous silicon layer for sound generation, was reported (Shinoda et al., 1999). Nevertheless, most of the thermal energy generated by the aluminium film leaked to the substrate, greatly reducing its working performance. Advanced nanotechnology opens up new visions for exponential progress in acoustic engineering fields. Following the discovery of carbon nanotubes (CNTs) (Iijima, 1991), graphene is the most recently discovered carbon allotrope (Novoselov et al., 2004; Novoselov et al.,

2005).

By bonding carbon atoms in various ways, a number of allotropic forms can be obtained, including graphite, diamond, fullerenes, CNTs and graphene. Their morphologies and synthetic methods can affect their mechanical, thermal and electrical properties, in which CNTs and graphene have the best combination of properties and benefits (Filchakova and Saik, 2021). Fig. 6.1(a) shows the structure of graphene, which is a single sheet (monolayer) of carbon atoms arranged in a honeycomb hexagonal lattice. Due to the one-atom-thick structure, it is also known as a two-dimensional (2D) material. In Fig. 6.1(b), the structure of a single-walled carbon nanotube (SWCNT) is presented. This structure can be conceptualized by wrapping a graphene sheet into a seamless cylinder (Onorato, 2011; Vidu et al., 2014). Based on advanced nanotechnology, using the TA technique only requires a direct connection to an electrical source (alternating current (AC)) with sufficient power to achieve acoustic wave emission.

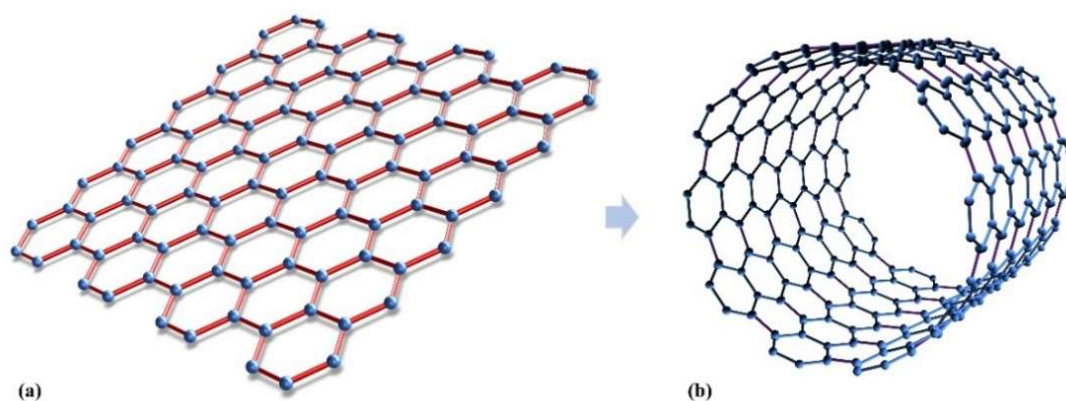


Fig. 6.1: (a) Graphene: a monolayer of carbon atoms tightly bound in a hexagonal honeycomb lattice and (b) Single-walled carbon nanotube (SWCNT): a graphene layer seamlessly rolled into a tubular structure (Onorato, 2011; Vidu et al., 2014; Yan et al., 2019).

The transduction process of the TA effect is the transformation of thermal energy

into acoustic energy. A local vibration of air molecules can be formed by periodic heat emissions from TA transducers, resulting in a proportional air pressure gradient of surrounding air. Using such TA transducers to generate acoustic waves enables to avoid a traditional moving piston or other comparable mechanisms, thereby reducing manufacturing costs and structural complexities associated with conventional piezoelectric- and electromagnetic-type loudspeakers. Conventional loudspeakers often consist of a moving cone, a voice coil, a permanent magnet and an enclosure. The intricate structure of conventional loudspeakers may restrict their applications in miniaturized precision instruments. Fortunately, TA devices with a lightweight and compact structure (Tian et al., 2012; Aliev et al., 2015), there is no mechanical movement of the devices involved in sound generation, so that no resonance peaks are produced. This results in a broadband frequency response range that is unachievable by mechanically driven devices (Hu et al., 2012a; Wei et al., 2013). TA devices are a fascinating technology in a new generation of speakers that have revolutionized the fundamental mechanism of conventional mechanical electro-acoustic devices. Hence, it shows great advantage as a practical magnet-free speaker (Xiao et al., 2008).

To theoretically understand the TA performance, Guiraud et al. (2019) developed a numerical model for describing an arbitrary multilayered structure to illustrate the sound generation of a thermophone structure, which is a general model based on the classical conservation law. To gain an in-depth understanding of CNT materials, Tong et al. (2014) considered the mirage effect induced from a heated CNT thin film. They (Lim et al. (2013), Tong et al. (2015)) also developed a series of accurate analytical models for explaining the radiation of near- and far-field TA waves from a suspended CNT thin-film device. Moreover, analytical solutions are also available for various TA devices, including a gas-filled encapsulated TA transducer (Tong et al., 2013), a solid cylindrical TA transducer (Tong et al., 2016), and a free-standing nano-thinfilm structure in a fluid medium (Mao et al., 2019a). More recently, Lai et al. (2019) derived a theoretical model to investigate the optical behavior of vertically aligned

CNT arrays under different polarized incident light effects. Zhou et al. (2021) utilized the boundary element method to predict the surrounding acoustic field of a CNT thin film in an arbitrary 3D configuration. To understand the variation of TA responses, Tong et al. (2017) also developed a theoretical study based on the Fourier transformation by feeding different input signals (e.g., square root signal, triangular wave signal and rectangular pulse signal) to TA devices. To enhance the sound pressure output, Mao et al. (2019b; 2021) further considered the use of a magnetic field to enhance the sound pressure output of TA devices under a periodic AC power supply.

To develop a TA device, it requires advanced materials with specific properties such as the low heat capacity per unit area (HCPUA) and high thermal conductivity (Kumar et al., 2021). In terms of experimental studies, a significant breakthrough on CNT-based TA loudspeakers was reported by Xiao et al. (2008) with exemplary sound emitting properties. A CNT single-layer film was directly drawn out from CNT arrays and aligned onto a 4-inch wafer, which presented a wide frequency response range within 1 MHz and up to 100 dB loudness. Thereafter, Nasibulin et al. (2011) reported an aerosol chemical vapor deposition (CVD) synthesis method to prepare a free-standing SWCNT film via direct deposition. This method not only can control the good performance of SWCNT thin films, but also its thickness in a few micrometers. Barnard et al. (2013) roughly discussed the feasibility of CNT-based TA speakers to achieve a high sound pressure output from four aspects, including the numerical non-dimensional analysis, gaseous immersion effects, multiple-film stacking and different input signal conditions. In addition, a novel TA chip, which fabricated by a suspending CNT thin yarn array, was developed by Wei et al. (2013). The TA chip consisted of a silicon base with periodic grooves (900- μm in pitch and 150- μm in depth). The sound pressure generated by a suspended CNT thin yarn array chip relied on the depth of the periodic grooves and the thermal wavelength. Aliev et al. (2015) also compared the TA performance of various CNT-formed TA devices, including

multi-walled CNT (MWCNT) thin films, graphene sponges and gold-coated poly(acrylonitrile) nanofibers.

Recently, another intensive focus has turned to graphene (Suk et al., 2011; Tian et al., 2011a; Suk et al., 2012) and Ti_3C_2 (Gou et al., 2019), which are highly effective materials with high mechanical strength, good electrical mobility and superior thermal conductivity (Tu et al., 2019). Tian et al. (2011a) fabricated three different thickness graphene sheet samples and measured their responses and efficiency. They mentioned that the HCPUA of graphene materials and the thermal properties of substrates are the key factors for sound generation. Subsequently, Tian et al. (2012) developed a single-layer graphene sound-emitting device by using a high porosity anodic aluminum oxide (AAO) template, resulting in higher sound pressure output up to 0.6 Pa with an input power of 0.25 W. Sbrockey et al. (2018) proposed a graphene-based TA device with a flexible plastic substrate (i.e., 0.002 inch-thick Kapton), which can achieve an SPL of 60 dB under a 7 V power input. Although both graphene and CNT materials are proposed as TA devices, there are still some limitations during the fabrication processes. Experimental investigations on the acoustic performance of CNT- and graphene-based TA devices supported by different substrates are still insufficient.

As a single-element thin-film speaker, TA devices could make possible change of daily audio-visual experience. The key point is the mechanical and thermal properties of materials. Graphene, a very thin and flexible structure, possesses various superior material properties as aforementioned. It is not only the most durable material, and also extremely malleable and elastic. Because of its one-atom-thick, graphene is nearly transparent. However, the use of graphene as a free-standing material is still challenging. As an ultra-thin film, the problematic issues of mechanical brittleness and adhesive interfacing contact can directly lead to the reduction of performance.

In terms of material preparation and cultivation, chemical vapor deposition

(CVD) method is a promising and inexpensive way for the synthesis of graphene thin films (Mattevi et al., 2011; Wang et al., 2020a). Owing to the growth of graphene sheets is commonly deposited on the base of copper (Cu) (Li et al., 2009b), nickel (Ni) (Reina et al., 2009), and iridium (Ir) (Coraux et al., 2008), etc. Therefore, cultivated graphene sheets need to be transferred onto a non-conductive substrate for practical applications, which is the main drawback of using CVD graphene thin films. It is imperative that the quality of graphene remains preserved during the transfer process. A fast and reliable method to transfer graphene thin films from a conductive substrate to a targeted one is another critical step. During this transfer process, various polymers (e.g., polymethyl methacrylate (PMMA) and polydimethylsiloxane (PDMS)) are widely used as a supportive layer. Deokar et al. (2015) reported a high crystalline quality monolayer graphene growth and its transfer method. According to Deokar et al. (2015), they provided three modified steps for maintaining the quality of graphene, i.e., Cu etching solution choice, trapped water removal and PMMA residual removal method. Li et al. (2009a) also developed an improved transfer process by adding a second layer of PMMA for material transfer, which can achieve a lower density of cracks and tears. Using the double layer PMMA for material transfer, Borin Barin et al. (2015) further investigated an optimized transfer method by considering the influence of various transfer parameters, for example PMMA concentration, temperature and baking time. As a supportive layer-based transfer, the usage and removal of PMMA during the process can either enhance or degrade the final quality of graphene. In addition, Suk et al. (2011) presented a novel dry transfer technique by utilizing PDMS as a supportive layer. Her et al. (2013) also proposed a transfer procedure utilizing acetic acid to replace the acetone treatment approach in PMMA removal, resulting in less contaminants on the surface of graphene sheets.

CNT thin films are of several orders thicker than a monolayer graphene sheet. With a structure of entire tube (or stack of tubes), it can maintain itself as a free-standing material. As a strong and robust structure, CNTs are claimed as an

appropriate candidate for fabricating TA chips, which can be formed by a suspended yarn structure (Wei et al., 2013). A gap distance between the nano-thinfilm and the substrate conduces to higher and reliable sound emissions (Tong et al., 2015). CNT yarns have showed a much higher mechanical strength than a fresh CNT film (Liu et al., 2009b) and thin yarns can possibly achieve a faster thermal response (Wei et al., 2012). According to the relevant numerical analytical models (Tong, 2015; Tong et al., 2015), a few-micrometer gap separation can enhance the sound performance of CNT-based TA devices.

Considering CNT- and graphene-based TA devices, we attempt to provide a feasibility study in this work. With reference to the theoretical study of a gap separation effect on TA devices, a 50- μm gap separation between thinfilm and substrate can contribute to sound output and structural stability (Tong et al., 2015). We design and prepare a substrate with a 50- μm -gap utilizing wafer treatment technology. As aforementioned, CVD-grown graphene materials are still challenging in the arbitrary substrate transfer and residual removal processes. In this connection, we examine a transfer process for graphene-based TA devices. Also, a CNT-based TA device is fabricated. Sound measurement for both TA devices is conducted to illustrate their SPL profiles. To understand the gap separation effect of nano-thinfilms, a simple reviewed about the theoretical model is presented in Section 6.2. Experimental procedures about the fabrication process are described in Section 6.3. Results and discussion are then presented in Section 6.4. Finally, the major findings of this work and limitations are stated in Section 6.5.

6.2 Gap effects for nano-thinfilm TA device

When an electric power is applied to a CNT thin film, the surrounding medium (gas or fluid) is heated periodically. An oscillating temperature field is induced in the medium, resulting in thermal expansion and contraction of the medium to generate

acoustic waves. During the periodic heating process, the material properties of a substrate have great impact on thermal waves (e.g., material porosity (Tian et al., 2012) and thermal diffusivity of the substrate (Tong et al., 2015)). When a gap separation between the nano-thinfilm and substrate, there is a potentiation of sound output as a thermal wave that can reflect back into the medium (Tong et al., 2015). Utilizing CNT thin films with low HCPUA, typically ranging from $1.5 \times 10^{-1} \text{ J}/(\text{m}^2 \cdot \text{K})$ to $7.7 \times 10^{-3} \text{ J}/(\text{m}^2 \cdot \text{K})$ (Tian et al., 2011a), the thermal energy can be transferred within an ultra-short time period, resulting in the rapid generation of acoustic waves. Aiming at improving the sound output performance, a suspended-on-substrate TA structure has been investigated by the analysis of the gap separation effect, as shown in Fig. 6.2. Fig. 6.2(a) illustrates the schematic diagram of a TA device suspended on a silicon substrate. Two external electrodes and two holding bars are used to fix the nano-thinfilm. Fig. 6.2(b) presents the structure of a four-TA-transducer shunt-wound array, which can be used to address the higher requirement of sound output.

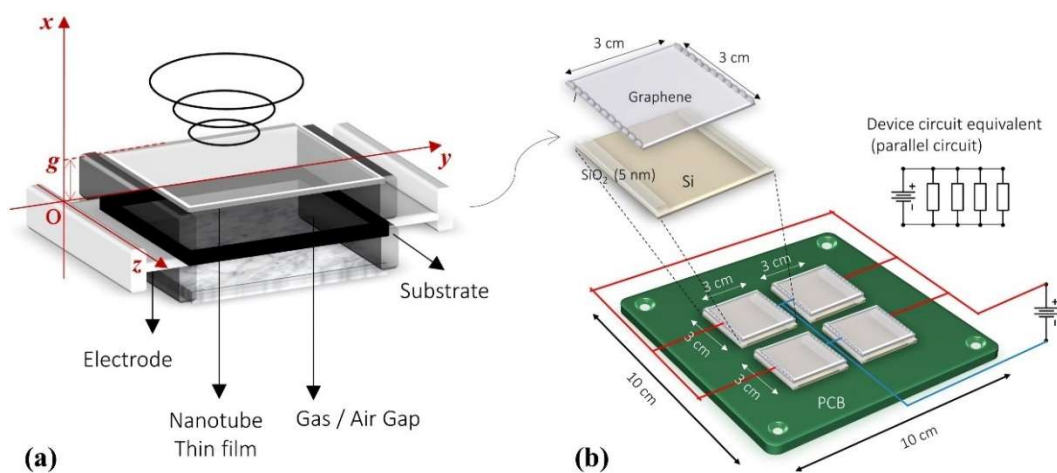


Fig. 6.2: (a) Schematic diagram of an encapsulated TA transducer; and (b) Schematic diagram of a four-TA-transducer shunt-wound array.

When a nano-thinfilm TA device is driven by an AC signal, the produced Joule power can be expressed by (Vesterinen et al., 2010):

$$P_j(t) = \bar{P}_j [1 + \exp(-2i\omega t)] \quad (6.1)$$

where \bar{P}_j is the average electric power and ω is the angular frequency. In the context of linear and non-viscous thermo-acoustic theory, the temperature field (T) and acoustic pressure field (P) can be solved via the following coupled equations (Vesterinen et al., 2010; Tong et al., 2015):

$$\nabla^2 T_1 - \frac{1}{\alpha_1} \frac{\partial T_1}{\partial t} = -\frac{S_1}{\kappa_1} - \frac{1}{\kappa_1} \frac{\partial P_1}{\partial t} \quad (6.2a)$$

where α_1 is the diffusion constant of medium (typically air), κ_1 is heat conductivity of medium, S_1 is the heat source with unit W/m^3 , P_1 is the acoustic pressure and t is time. Eq. (6.2a) is the diffusion equation of temperature. The coupling term $-\frac{1}{\kappa_1} \frac{\partial P_1}{\partial t}$ in Eq. (6.2a) has only a small effect on the final result of temperature (T), which can be neglected (McDonald and Wetsel, 1978; Vesterinen et al., 2010; Tong et al., 2015).

By ignoring the coupled term $-\frac{1}{\kappa_1} \frac{\partial P_1}{\partial t}$ in Eq. (6.2a), the acoustic pressure field (P)

can be expressed as (Vesterinen et al., 2010; Tong et al., 2015):

$$\nabla^2 P - \frac{1}{C_0^2} \frac{\partial^2 P}{\partial t^2} = -\frac{\alpha_1 \rho_0}{\kappa_1 T_0} \frac{\partial (\kappa_1 \nabla^2 T_1 + S_1)}{\partial t} \quad (6.2b)$$

where P is the acoustic pressure, ρ_0 is the density of surrounding medium, T_0 is the ambient temperature of medium, and C_0 is the isothermal speed of sound. With a harmonic AC input signal, the heat source (suspended-on-substrate nano-thinfilm) can

be expressed by (Vesterinen et al., 2010):

$$S_1 = \frac{P_{in}}{a} \delta(x-g) \exp(j\omega t) \quad (6.3)$$

where P_{in} is the effective input power, a is the thin-film area, $\delta(x-g)$ denotes the Dirac Delta function, x represents perpendicular direction to the thin-film surface, and g is the gap distance between the thin film and the substrate. The coordinate axis diagram is shown in Fig. 6.2(a). Here we consider the nano-thinfilm with thickness of the order of a few tens of nanometers, while the gap separation distance (g) is far large compared to the thickness of nano-thinfilm. There is a concentration of Joule heat at the position of nano-thinfilm (i.e., $x=g$). j is the imaginary number (i.e., $j = \sqrt{-1}$) and ω is the angular frequency. Assuming the CNT thinfilm is an infinite impedance plane in the acoustic near-field. Hence, the temperature field is only dependent on the x -direction, see Fig. 6.2(a). According to the analytical model presented by Tong et al. (2015), the explicit expression of the thermal wave in a medium (typically air) as:

$$\bar{T}_1(x) = \frac{P_{in}}{a} \frac{1}{2\lambda_1\kappa_1} \{R \cdot \exp[-\lambda_1(x+g)] + \exp(-\lambda_1|x-g|)\} \quad (6.4)$$

where $\lambda_1 = \sqrt{\frac{j\omega}{\alpha_1}}$. R denotes the reflection coefficient of the thermal wave, which is

related to the thermal diffusivity. It can be expressed as $R = \frac{(\sqrt{\alpha_2} - \sqrt{\alpha_1})}{\sqrt{\alpha_2} + \sqrt{\alpha_1}}$, in which α_1

is the diffusion constant of the surrounding medium (typically air) and α_2 is the thermal diffusivity of the substrate. In Eq. (6.4), two important parts are involved in the thermal wave. The first part represents the influence of the substrate on the

thermal field, while the second part directly comes from the heat source.

To further investigate the gap separation effect on the acoustic near- and far-field, the sound pressure output can be resolved by the analytical model (Tong et al., 2015). Consider Eq. (6.4), the output sound pressure along the perpendicular direction to the thin-film surface (i.e. x -direction) can be expressed as (Tong et al., 2015):

$$\bar{P}(x) = -\frac{C_0}{T_0 C_p} \frac{P_{in}}{2a} [(R-1) \cdot \exp(-\lambda_1 g) + \exp(-jkg) + 1] \cdot \exp(-jkx) \quad (6.5)$$

where $k = \omega / C_0$. The far-field sound pressure is thus given by (Tong et al., 2015):

$$\bar{P}(x) = -\frac{C_0}{T_0 C_p} \frac{P_{in}}{2a} [(R-1) \cdot \exp(-\lambda_1 g) + \exp(-jkg) + 1] \cdot \exp(-jkx) \cdot \frac{R_0}{x-g} \quad (6.6)$$

where R_0 is the Rayleigh distance (i.e., $R_0 = af / C_0$), and f is the frequency of sound.

There are two cases to illustrate the gap separation effect on the sound pressure output in Eqs. (6.5) and (6.6).

In the higher frequency range and a large gap (i.e., $|\exp(-\lambda_1 g)| \sim 0$), we have $(R-1) \cdot \exp(-\lambda_1 g) \sim 0$. Consider $n = 0, 1, 2, 3, \dots$, when the angular frequency satisfies the condition of $\omega = [(2n+1)\pi C_0] / g$, the terms in the square bracket can be derived as “ $\exp(-jkg) + 1 = 0$ ”, resulting in the sound pressure $\bar{P}(x) = 0$. When the angular frequency meets the condition of $\omega = (2n\pi C_0) / g$, the terms in the square bracket can be written as “ $\exp(-jkg) + 1 = 2$ ”, resulting in the maximum value of the sound

pressure $\bar{P}(x)$. In the low frequency range or a small gap, we obtain $|\exp(-\lambda_1 g)| \sim 1$, thereby resulting in “ $(R-1) \cdot \exp(-\lambda_1 g) + 2$ ”. According to the definition of the reflection term R , it is a constant (smaller than 1). An inference can be presented that the amplitude of acoustic pressure decreases with reducing the gap distance. The critical point of the gap separation effect occurs at $g = 45 \mu\text{m}$ (Tong et al., 2015).

To examine the performance of a suspended-on-substrate nano thin-film TA device, we design and prepare a $3 \text{ cm} \times 3 \text{ cm}$ silicon substrate. A silicon substrate is prepared for holding the nano thin film. To enhance the output performance of sound pressure, a $50\text{-}\mu\text{m}$ gap separation is provided to form an interference of thermal wave between the nano thin film and the silicon substrate. Two extensional electrodes are used to mount on either side of the silicon substrate for power feeding. The fabricated procedures are illustrated in the subsequent section.

6.3 Experimental procedures

6.3.1 Substrate preparation

In this section, the preparation procedures of a silicon substrate are presented in Fig. 6.3. Two 5-inch masks were designed, in which one is for photolithography and the other is for the physical vapor deposition (PVD), see Fig. 6.3(a). Referring to the schematic diagram of a suspended-on-substrate nano-thinfilm (see Fig. 6.2(a)), we designed two holding bars on both sides of the silicon substrate. A thin layer of silicon dioxide was deposited on the top of the holding bars for insulation purpose. Two extensional electrode layers were then deposited on the edge of the holding bars by the gold sputtering technique.

The procedures of a 4-inch silicon wafer treatment through the photolithography process is presented in Fig. 6.3(b). A thoroughly cleaned and dried silicon wafer can

serve as a substrate of the TA device. Photoresist was spun on to the wafer utilizing a spin coater (*Sawatec SM-180-BT*). A mask aligner (*Mask Aligner System*) was used to pass a controllable amount of ultraviolet (UV) light through the mask onto the coated wafer. UV exposure can make the patterned area insoluble in developer solution. Using developer solution can remove exposed resist and leave behind a final pattern onto the silicon. With the cover of photoresist, the silicon substrate was formed a 50- μm gap by utilizing a physical dry etching process, which is a high-energy beam to etch off the substrate atoms. When the silicon atoms were knocked out from the substrate, the silicon material can evaporate simultaneously. Thereafter, a thin layer of SiO_2 was deposited onto the holding bar to form an insulated interface. Gold sputtering was used for coating a thin gold layer as electrodes. During the sputtering process, gold was bombarded with high-energy ions in a vacuum chamber, resulting in the gold atoms or molecules being ‘sputtered’ into the vapor and condensing on the substrate to be coated. Using a 4-inch wafer, four substrates can be obtained, then it was cut by a dicing saw as a 3-by-3-centimeter square. The 50- μm gap Si/ SiO_2 substrates are presented in Fig. 6.3. Subsequently, the etched silicon substrates were cleaned by chemical solvent, followed by a deionized water rinse. Solvent can clean oil and organic residues that may appear on glass surfaces. The target substrate was sonicated for 20 minutes in acetone, followed by immersion in isopropyl alcohol for 30 minutes. After that, deionized water was used again for the substrate rinse and then dried by a nitrogen blowing.

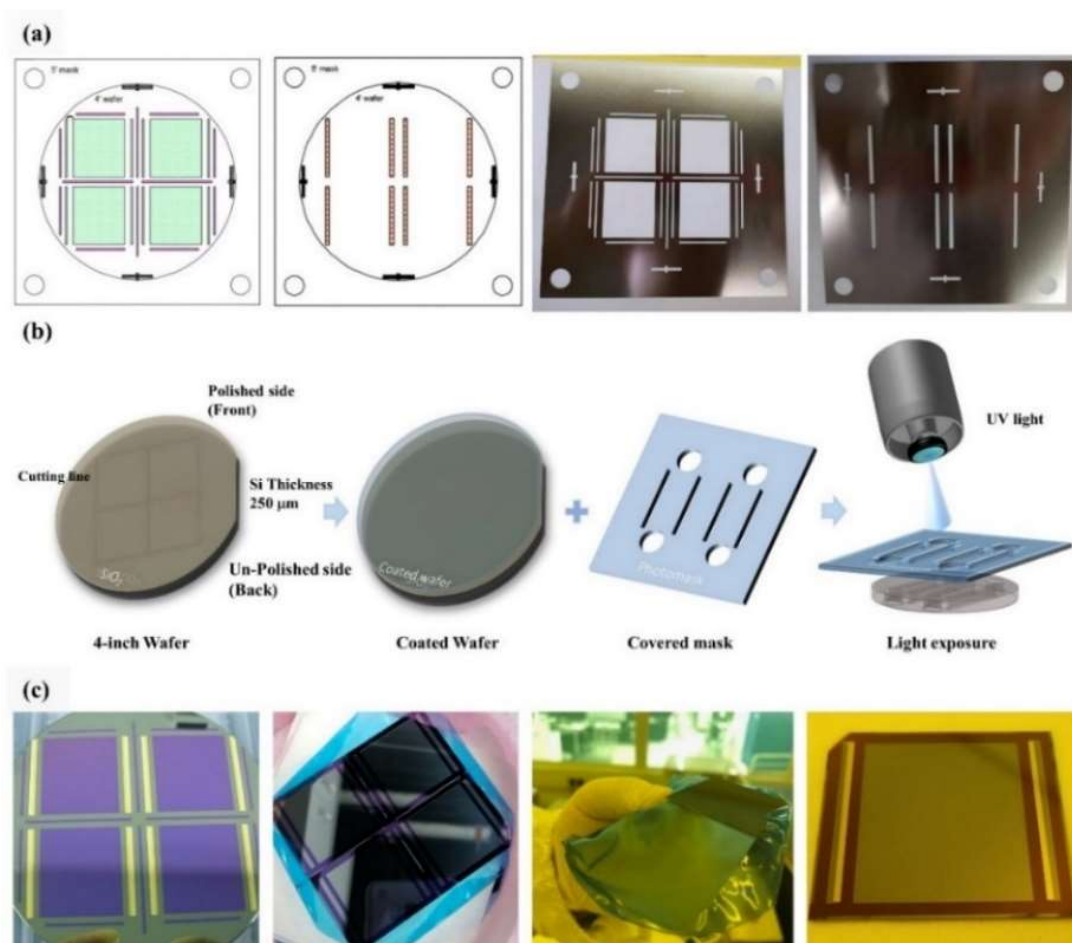


Fig. 6.3: A 50-μm gap silicon substrate preparation. (a) a 5-inch covered mask design for photolithography and physical vapor deposition; (b) Procedure of wafer treatment including wafer coating and photolithography; and (c) a 4-inch wafer cutting into four substrates (3 cm×3 cm).

6.3.2 TA device fabrication

Graphene has extraordinary physical and electrical properties (Novoselov et al., 2005; Chen et al., 2008; Morozov et al., 2008). Since it is only one-atom thick, graphene is nearly transparent, however, it is also an excellent electrical and thermal conductor. The thermal conduction of a suspended single-layer graphene is around 5000 W/(m·K) (Balandin et al., 2008; Ghosh et al., 2008; Prasher, 2010). Graphene also has a huge electrical mobility of about 200,000 cm²/(V·s) at room temperature

(Lin et al., 2010). There are many potential applications of using graphene as a transparent conductor in photovoltaic cells and flexible electronic devices. Moreover, the larger surface area to mass ratio of graphene makes it excellent for energy storage or chemical sensing (Xu et al., 2014). Fig. 6.4(a) shows the SEM image of a graphene sheet with a hexagonal mesh structure.

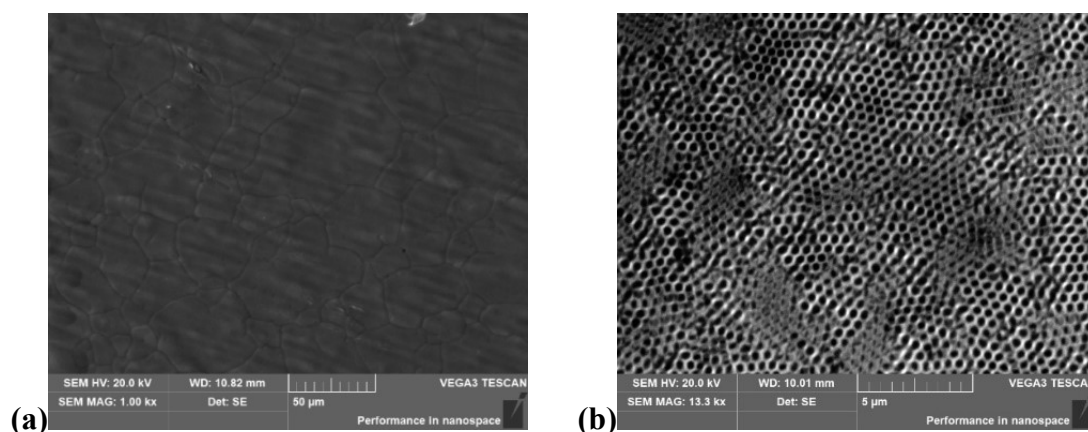


Fig. 6.4: (a) SEM image of a graphene thin-film layer; and (b) SEM image of an anodic aluminum oxide template.

Due to the low thermal conductivity, anodic aluminum oxide (AAO) templates can act as a substrate to achieve a high acoustic emission efficiency (Tian et al., 2012). The SEM image of an AAO template is presented in Fig. 6.4(b) to show its internal structure that is a highly porous layer. The aperture of the AAO template is about 350 nm in diameter with a 90% porosity ratio. With a porous structure, the AAO template is able to meet the requirement of high thermal diffusivity, which is possible to improve the TA performance (Tong et al., 2015). A periodic heating process acting on graphene can quickly heat up the surrounding air in the near field. Therefore, this porous substrate is a promising way to improve the sound intensity of graphene-based TA devices. Depending mainly on the nature of the anodizing electrolyte (Diggle et al., 1969), AAO films can be performed in two different morphologies, they are non-porous barrier-type oxide films and porous-type oxide films (Lee and Park, 2014).

The porous AAO type has a honeycomb-like structure formed by a high-density array with uniform and parallel pores, which can be grown on aluminum. This porous oxide film contains mutually parallel nanopores (Keller et al., 1953). Each cylindrical nanopore and its surrounding oxide region can constitute a hexagonal cell aligned normal to the metal surface. Under specific electrochemical conditions, the oxide cells can self-organize into a hexagonally close-packed arrangement, forming a honeycomb-like structure. The pore diameter and density of self-ordered porous AAOs are tunable in wide ranges by properly choosing anodization conditions: the pore diameter ranging from 10–400 nm and the pore density from 10^8 – 10^{10} pores/cm² (Lee and Park, 2014). The novel and tunable structural features of porous AAOs have been intensively exploited for synthesizing a diverse range of nanostructured materials in the form of nanodots, nanowires and nanotubes.

As aforementioned, the use of graphene as a free-standing material is still difficult, a special template is required to host it as a platform due to its fragility. To maintain a small gap-suspending design, we utilized an AAO template as an underlayer between the graphene layer and the Si/SiO₂ gap substrate. Fig. 6.5 presents the schematic structure of an AAO template onto a 50- μ m gap Si/SiO₂ substrate. Adhesive was utilized to fix the edges of the AAO template and the gap substrate. The pitch of holes in the AAO template was about 450 nm, and the thickness was about 50 μ m. With the similar 50- μ m thickness, the AAO template can be perfectly fixed within the gap of Si/SiO₂ gap substrate, as shown in the cross-section schematic diagram in Fig. 6.5.

Generally, the synthesis of graphene is typically achieved by CVD growth methods and later transferred onto a device platform with a specifically designed structure. To achieve a high-quality graphene, many fabrication parameters during the growth stages are essential for high precision control, for example annealing process, substrate temperature, gas flow rate and cooling down settling process. To consider

various fabrication requirements, CVD-grown graphene sheets need to be transferred on a non-conducting substrate (Han et al., 2014). During the transfer process of CVD graphene to an arbitrary substrate, it is possible to cause defects, doping and scattering by metallic or polymer residues (Deokar et al., 2015). The conventional wet chemical transfer process involves the use of polymer as a temporary supporting layer. With reference to the wet transfer method of copper-based graphene thin films, we conducted the transfer process of graphene thin films onto the prepared substrate, as shown in Fig. 6.5. The graphene sheet used here is a commercial product (*Monolayer graphene on polymer film, Graphenea*). Li et al. (2009a) proposed a double-layer PMMA transfer method, which can be used to maintain the quality of graphene. Due to the deposition of the second layer, it makes the first layer attached to the graphene thin film, resulting in a more flexible graphene thin film. With reference to the PMMA supporting layer transfer method, the detailed operation processes are presented in the next section.

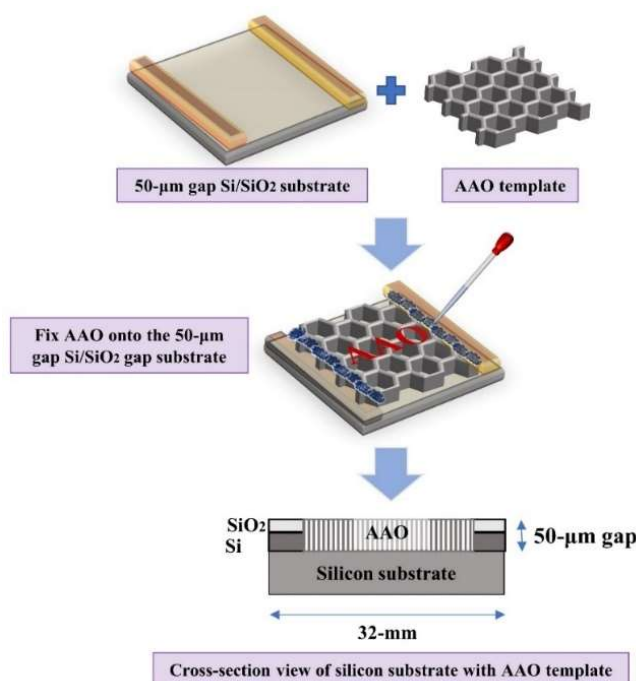


Fig. 6.5: Schematic structure of an AAO template onto a 50- μm gap Si/SiO₂ substrate.

Fig. 6.6 illustrates the transfer process of graphene sheets. Poly (methyl methacrylate) (PMMA) was used as a supporting layer to assist the transfer process. In summary, the following procedural steps are involved:

- 1) Utilized a magnetic stirrer to prepare 2% PMMA solution. Anisole was used as solvent. The stirring time was about 24 hours.
- 2) Extracted a thin layer of a PMMA by spin coating. The roughness of the spin coated PMMA was less than 1.5 nm, resulting in a smooth and uniform layer. The spin coater was set as 500 rpm for 10 s, and 1500 rpm for 20 s to uniformly coat a thin PMMA on the top of graphene. The PMMA layer, only a few tens of nanometers, can support the graphene thin film during the transfer process. After coating, the PMMA/graphene/polymer stack was placed in the oven for solidifying the PMMA layer under 100°C for 10 min.
- 3) Immersed the stack into deionized water slowly for a while. Then, the PMMA/graphene layer was gradually released from the polymer base. Later, the polymer base sank below the water surface. The PMMA/graphene stack would float on the deionized water surface.
- 4) Released the polymer layer, the prepared substrate was immersed into deionized water. Polytetrafluoroethylene (PTFE) cassette was used to hold the substrate. Slightly tilted the substrate 45°, aligned the PMMA/graphene stack on the center of the prepared substrate, and gently lifted the PMMA/graphene/substrate stack up from below.
- 5) Took the PMMA/graphene/substrate stack out carefully and dried it in air. Annealed the stack on a hot plate at 150°C for one hour. It is helpful to evaporate the surface moisture and also to improve the compactness of contact surface between the PMMA/graphene stack and the prepared substrate.
- 6) Placed the whole stack into a vacuum chamber for 24-hour storage to further ensure the interface connection between the graphene layer and the target substrate.

- 7) Removed the PMMA layer, the PMMA/graphene/substrate stack was placed into acetone and water bath at 50°C for 30 min, then immersed into iso-propyl alcohol for removing acetone for another 1 hour. Used deionized water for rinse the residual and dried the stack on the hot plate under 100°C for 30 min.
- 8) Put the graphene/substrate stack into a vacuum box for another 48-hour storage to improve the interface connection.
- 9) Stored the graphene/substrate stack in a sealed petri dish. Before acoustic performance test, the graphene/substrate stack was placed into the drying oven to remove moisture that may attach on the material surface.
- 10) Dripped conductive silver adhesive on either side of graphene edge, which can lock the graphene thin film at the target substrate. The curing time of conductive silver adhesive was about 28 hours. The prepared graphene-based TA device was then connected to a breadboard for test measurement.

Fig. 6.7 shows the pictures for transfer experiment. We transferred the graphene thin film based on the wet method, deionized water was used to separate the graphene thin film from the polymer base. During the transfer process, it is difficult to align the graphene thin film on the center of the prepared substrate, which may lead to the occurrence of folds and cracks. Another issue is the interfacial problem between the graphene thin film and the substrate. Instability may still exist even a vacuum treatment was conducted to enhance the connection between the graphene thin film and the prepared substrate. These issues should be further considered in the future development as it can affect the performance of TA devices.

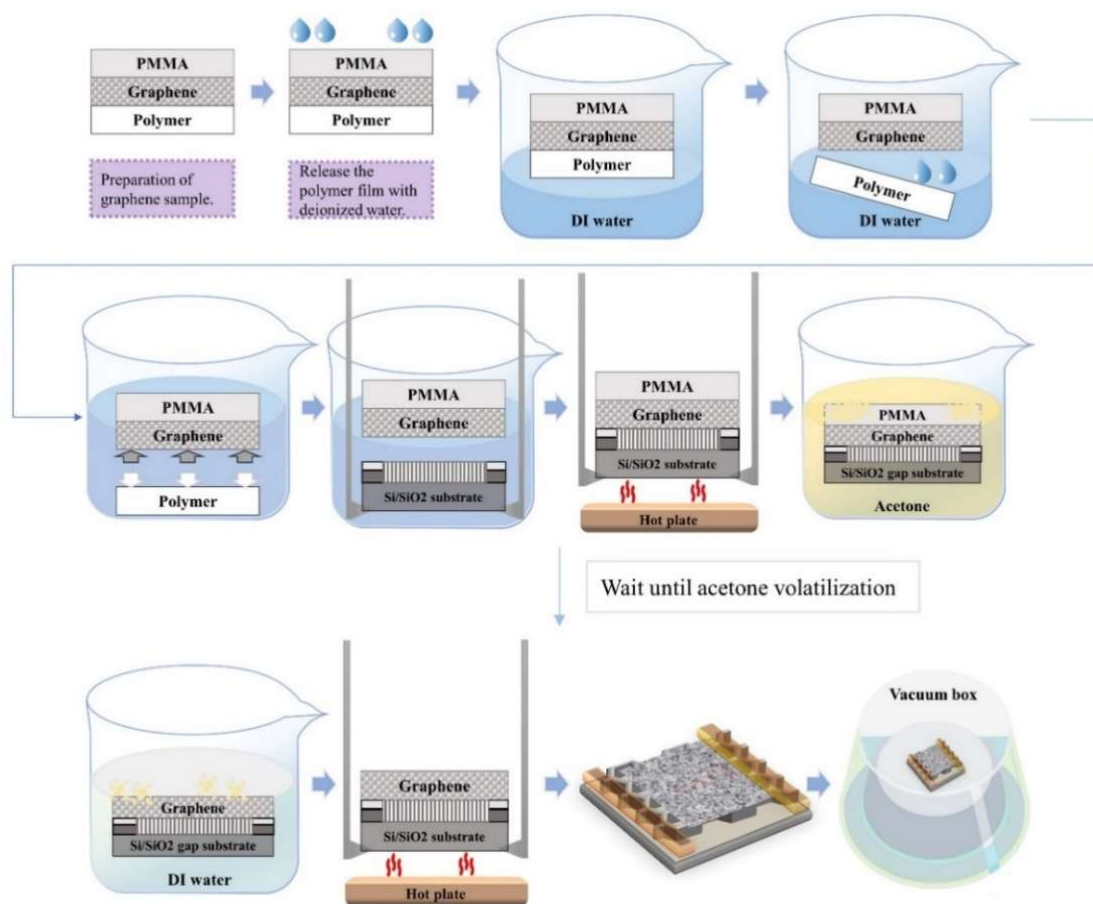


Fig. 6.6: Transfer procedures of a graphene thin film from a polymer substrate to a 50- μm gap Si/SiO₂ substrate.



Fig. 6.7: Procedures of graphene thin-film layer transfer onto a prepared substrate (50- μm gap Si/SiO₂ substrate with AAO template) in the in-house Cleanroom.

CNT sheets are relatively strong and highly conductive for heat and electricity (Abdallah et al., 2020). It has a high aspect ratio and robust structure, which makes it a perfect choice as TA loudspeakers (Wei et al., 2013). Here, we test the TA sound generation ability of a suspended-on-substrate CNT, and the SEM image of a CNT sheet is shown in Fig. 6.8. The fabrication procedures of a CNT-based TA device are presented in Fig. 6.9. The drawn CNT thin film was directly put on two bars that were held by a flat vise. The flat vise was fixed on the one-directional sliding platform. A lifting platform was used to hold the Si/SiO₂ 50- μ m gap substrate to attach at the undersurface of the CNT thin film. Conductive silver adhesive was used as electrodes at two sides. The CNT-based TA device was then connected to a breadboard for acoustic testing.

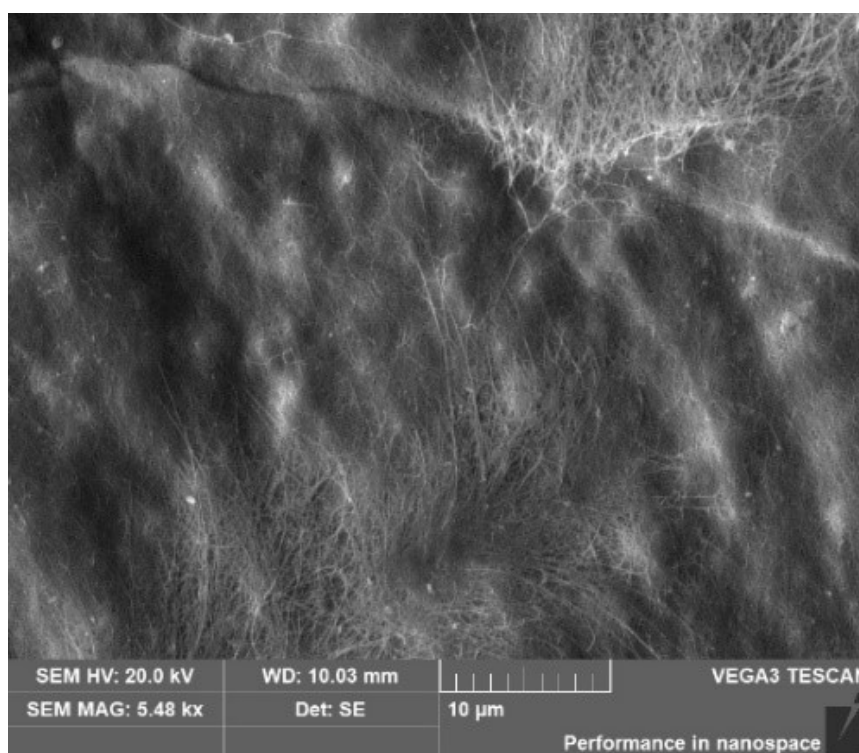


Fig. 6.8: SEM image of a CNT thin film.



Fig. 6.9: Fabrication procedures of a CNT-based TA device.

6.3.3 Sound measurement setup

Fig. 6.10 presents the acoustic performance test in the in-house semi-anechoic chamber. In the figure, a microphone (*B&K 4189*) and a thermal camera (*FLIR E65*) were used to monitor the variations of sound and temperature levels during the test. Fig. 6.10(c) shows the CNT-based TA device connected to a breadboard with input power and resistance. A signal generator (*Keysight 33500*) and an audio amplifier (*Sony CMT-M33NT*) were used to generate audio signals. The background SPL within the semi-anechoic chamber was about 29 dB, which can be measured by the same equipment setup. Sound output results were then measured by a high-quality microphone at various distance levels away from the device surface.

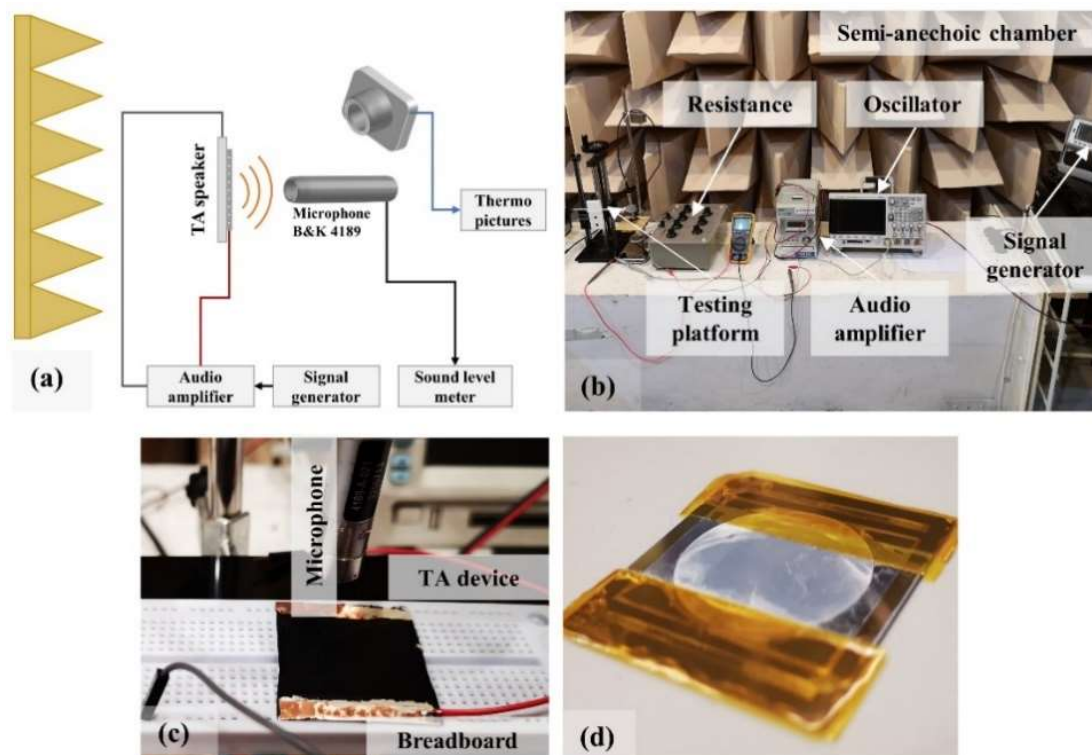


Fig. 6.10: Acoustic performance testing: (a) Schematic of the experimental setup; (b) measurement equipment; (c) CNT-based TA device; and (d) graphene-based TA device.

6.4 Results and discussion

Fig. 6.11 shows the SPL profile of the CNT-based TA device in the range of 20 Hz–20 kHz. The resistance of the CNT-based TA device was around 30 Ω . The input power was 2.83W. In the low-frequency region (i.e., $f < 20$ kHz), the device exhibited a linear SPL spectrum. In this figure, the relatively low-frequency range, the measured SPL was near to the background noise level. Above 600 Hz, the measured SPLs increased linearly along with increasing frequency. Referring to the previous study for CNT thin-film speakers (Aliev et al., 2015), the sound pressure spectra of F-MWNT-F were reviewed (see the purple and yellow dash lines) for comparison. The fabricated CNT-based TA device was still limited in high SPL output comparing with the existing publications.

Fig. 6.12 shows the SPL profiles under different microphone positions (i.e., 1, 3, 6, and 9 cm) away from the CNT-based TA speaker at 1 kHz. We observe that the SPLs can reach at 67 dB under a high-power supply. Fig. 6.13 plots the temperature variation under various input power levels. Increasing the input power, the temperature of the TA device would increase dramatically in the early stage until to a stable level. However, excessive input power may induce overheated problem. To avoid adverse effect, a relatively low input power is suggested here as the high temperature may cause damage of the thin-film based on the experience. In Fig. 6.14, the measured SPL profiles of the graphene-based TA device are presented. The measured frequency range was from 1–10 kHz. Due to the brittle reason, the structure of the graphene-based TA device was unstable, resulting in an instable sound output. In the transfer process, the graphene thin-film layer can be easier to fold. Compared to the CNT-based TA device, the SPL of the graphene one was relatively lower, i.e., the maximum SPL is at about 50 dB. Compared with the previous studies (Tian et al., 2012; Kim et al., 2016; Bian et al., 2017), the sound intensity is still a major concern and further performance enhancement is required.

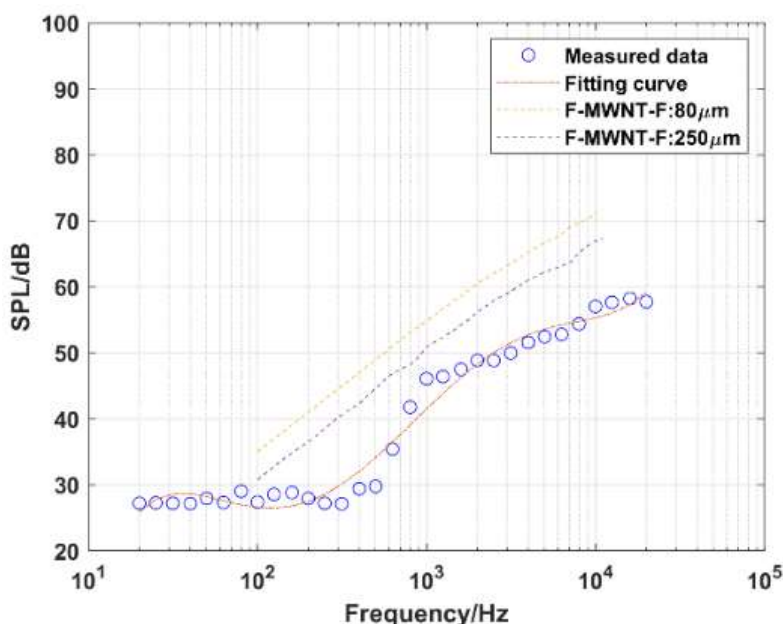


Fig. 6.11: Sound pressure levels of a CNT-based TA device measured at a distance of 1 cm and comparison with F-MWNT-F TA device (Aliev et al., 2015).

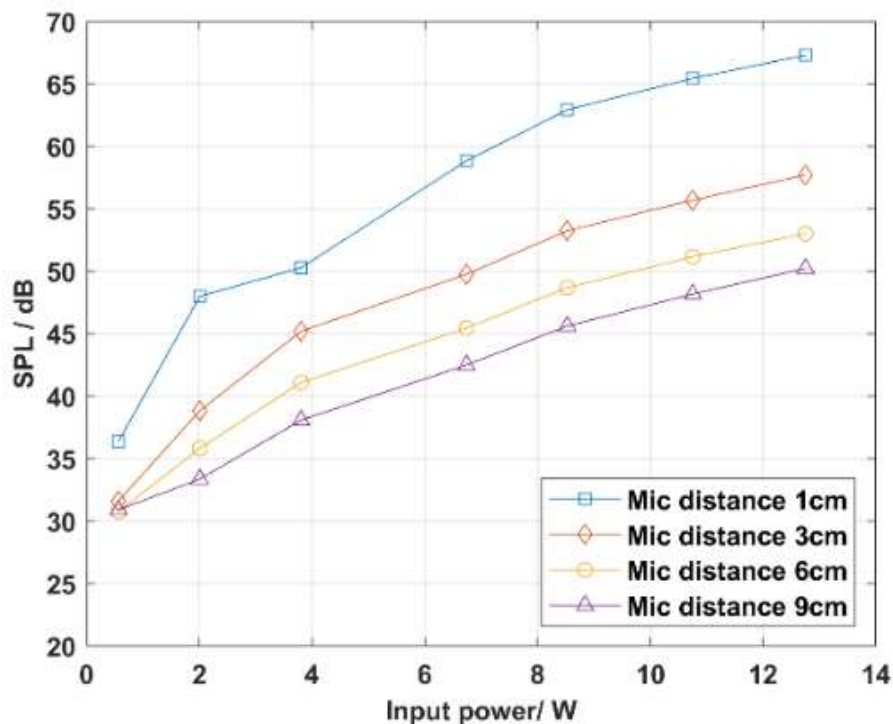


Fig. 6.12: Sound pressure levels under various AC power with different microphone distances.

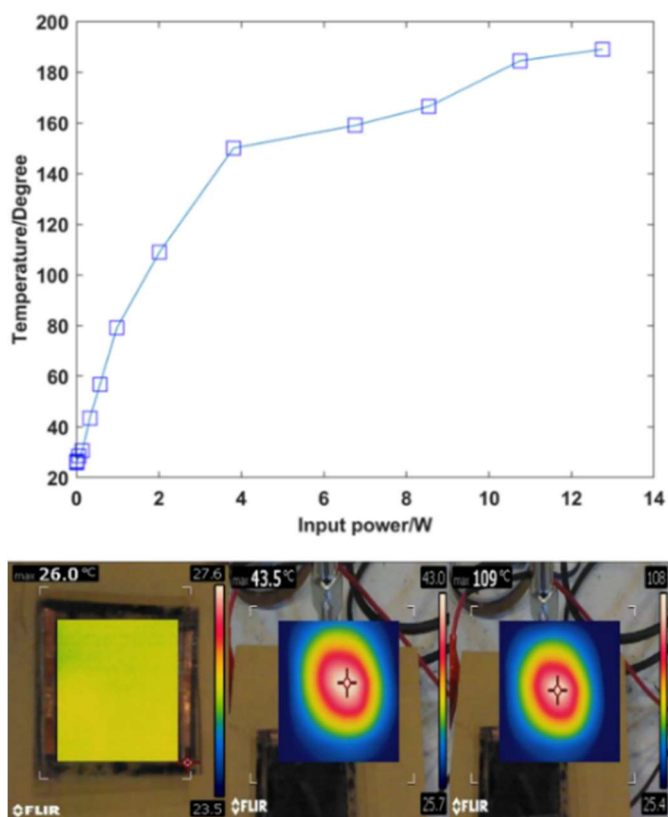


Fig. 6.13: Temperature variation of a CNT-based TA device with different input power levels.

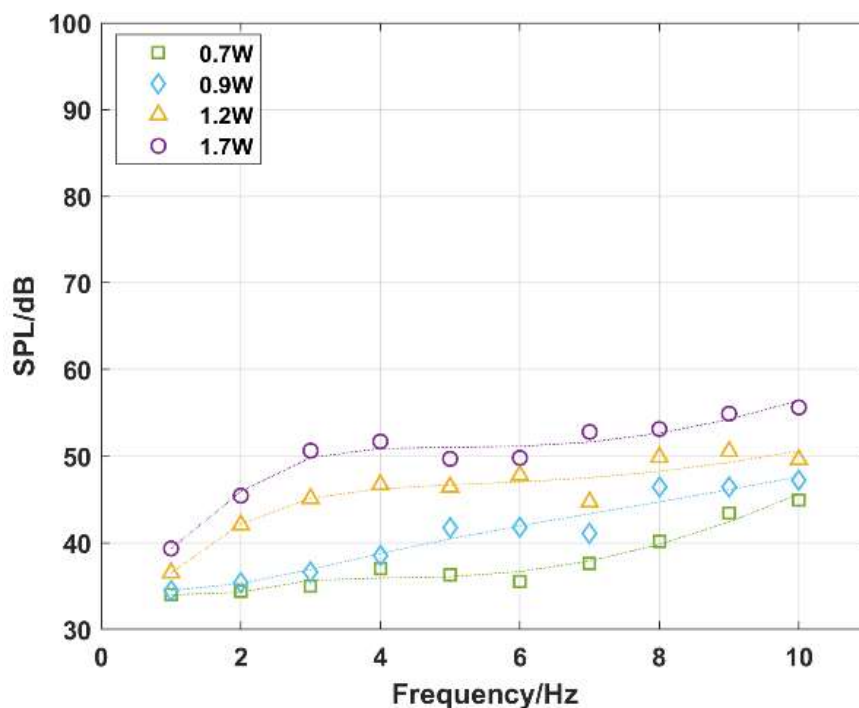


Fig. 6.14: Sound pressure levels of a graphene-based TA device with various input power.

6.5 Concluding remarks

TA devices made of nanomaterials were investigated. The fabrication process of TA devices was described in this work. The SPL profiles of the devices were simply measured and discussed. The major findings of this work are summarized herein.

- Both CNT- and graphene-based TA devices deployed on a 50- μm gap silicon substrate were fabricated for experimental studies. According to the measurement results, the highest SPL value of the CNT-based TA device can be up to 67 dB, while the graphene-based TA device is around 55 dB. Due to ultrathin thickness of graphene, it is still challenging to maintain high quality of the graphene layer in the transferring process.
- Since CNT materials are of several orders thicker than graphene, it can maintain itself as a free-standing material. It can be interfaced and contacted with an

electrical power supply to emit higher and more stable sound output. The ultrathin graphene layer is still challenging in the transferring process. A completely suspended design is difficult. As a compromise, a high-porosity AAO template is used as a supporting platform to stabilize the graphene layer. After the transferring, a vacuum treatment is necessary to enhance the interface connection between the graphene thin-film layer and the supporting template.

Although the two TA devices were fabricated, further investigations about nano-thinfilm-based TA devices are still required. Due to the mechanical properties of graphene (e.g., thickness, hardness and brittleness), it leads to the performance reduction of graphene thin-film materials. The PMMA layer was used as a supporting layer for easier transfer. Yet, the residue of PMMA should be another reason to degrade the quality of the thinfilm. According to the aforementioned experience, further investigations about graphene-based TA device are the on-going work. The main concern about the TA devices is the sound output improvement and structural stability. A systematic comparison and comprehensive study will be delivered. In general, to go beyond the limitations of conventional vibration-based speakers, TA devices shows their unique advantages, such as flat frequency responses, high sensitivities, compact structures, and miniaturization designs, which can be an alternative in the next generation of acoustic devices.

CHAPTER 7

CONCLUSIONS AND RECOMMENDATIONS

7.1 Conclusions

This project has been devoted to investigating the behavior of acoustic waves and its potential applications in two engineering fields, i.e., noise mitigation and air filtration. Both of them are relevant to our daily life and even public health. In this work, we have developed innovative acoustic-based technologies, which can be adopted as alternatives in the existing mitigation measures.

The first part focused on investigating the acoustic characteristics and the noise reduction strategies. A data-driven method was considered for improvement of ANC system. In addition, a composite barrier was fabricated to achieve noise control. To further investigate the potential applications, the second part aimed to investigate the feasibility of an acoustic-based particle-manipulation technique; and to develop a new-generation TA speaker. The important findings in this research are summarized as follows:

1. A learning and forecasting method, i.e., Bayesian inference based on a dynamic liner model approach, was utilized as a means of raw signal pretreatment in the ANC system. By coupling with a conventional FxLMS algorithm and a new C-FxLMS/F algorithm, different types of reference noise signals, i.e., (i) Gaussian noise; (ii) sinusoidal signal with Gaussian noise; and (iii) in-situ measurement construction noise data, were investigated. With the characteristic of “*forecast-*

observation-analysis” loop, such a learning and forecasting method showed advantages in the implementation of signal processing. The case studies showed that the pre-processing system can achieve a higher convergence speed of ANC systems. Consider the cost of secondary path in control systems, this forecasting method may provide a short-time step compensation by utilizing the prediction function of the Bayesian theory.

2. To explore the use of recycled composite materials for global control of medium- and high-frequency noise, wood-rubber composite samples were prepared and tested for an all-inclusive analysis. The material tests indicated that the wood-rubber composites show superior performance in sound insulation. To allow better flexibility, a PVDF thin-film speaker was studied to replace conventional speakers as an anti-noise source. A dual-function barrier prototype, coupling the recycled composites and the piezoelectric thinfilm, was then investigated for noise control. By implementing a scale-down model for experiment, a significant reduction of SPLs can be observed in the presence of barrier.
3. A novel U-shaped acoustic-driven device was proposed, which can greatly enhance the removal efficiency of low-grade filters in submicron particles (0.3–1.0 μm). Such a U-shaped configuration enables to form a standing wave field and to utilized synergetic effects of turbulence and acoustic waves. A prototype was well prepared for verification. As a standalone device, it shows a decent efficiency of filtration up to 61% (at 1.0 μm) when the device was driven by a relatively lower incident SPL (116 dB) comparing previous literatures. Coupling with a coarse MERV-6 commercial filter, the acoustic effect can reduce the presence of particles at the submicron range of 0.3–1.0 μm , with up to 89% efficiency for the removal coefficient of 1.0- μm particles. The removal efficiency can be flexibly enhanced by coupling the proposed design with high-grade filters. Furthermore, using microscopic observation, various morphological forms of

particle precipitation were observed, which is supportive to show the acoustic-particle interaction within the acoustic-driven device.

4. New-generation TA devices were investigated, e.g., a CNT-based and a graphene-based TA device, to provide a feasibility study. The gap separation effect was reviewed, such that a 50- μm gap substrate was prepared for TA device structure. We went through fabrication process of TA devices and measured their acoustic output. Yet, due to the ultrathin thickness, we found out that it is still technically difficult for the fully suspension of graphene thinfilm. Thereby, a high-porosity (up to 90%) anodic aluminum oxide template was used to maintain the ultrathin layer. According to the measurement results, the highest SPL output of the CNT- and graphene-based TA devices can be up to 67 dB and 55 dB, respectively.

7.2 Limitations and recommendations for future work

In this project, we provided an in-depth understanding of the acoustic waves and its potential applications, which may offer some guidelines to industrial applications. Despite the important works as aforementioned, there is still ample room for further investigation. The following problems should be considered in the future study.

In this research, a pre-processing approach coupling with an adaptive control algorithm is investigated. Although it can improve the convergence speed, the pre-processing system is only valid for information inference within a short-step period. Hence, further investigation will extend to the time period issue of this pre-processing system. On the other hand, the computational effort would be increased when the Bayesian-based approach is incorporated with an ANC system. With development, this problem may be fixed by designing an *ad-hoc* intelligent controller that can reduce the computational complexity with the use of Bayesian inference. Therefore,

increasing the computational complexity can be compensated to achieve a better adaptation system in real-engineering environments.

On the other hand, although a dual-function barrier design is considered in this work, there are still obstacles in achieving a global noise attenuation via ANC. To create a larger quiet zone whilst minimizing the adverse impact to other areas is still a challenge. The reason is that there are uncertainties for ANC systems when they are adopted in open-space applications. To achieve a capacious quiet zone, the required number of secondary sources for sound attenuation would increase geometrically (Hu, 2019; Hu and Tang, 2019), thereby resulting in design and installation difficulties (Kuo, 1996). According to the proposed approach, an optimization design is required to progressively alleviate these issues. For instance, the optimization of the number and position of secondary source will be critical to enhance performance. Moreover, another issue is to investigate the flat and stable frequency responses of PVDF thin-film speakers with lower high-order harmonic distortion. In general, the use of ANC systems has great potential in future applications, but it also contains realistic limitations. At this stage, the passive control is still dominant.

Although a U-shaped acoustic-driven device has been presented, it sacrifices a portion of air flow rate within the mechanically ventilated systems. By presenting the physical boundaries, the proposed configuration can achieve particles manipulation under lower SPL requirements, unfortunately, the air flow rate is inevitably reduced. In practical application, the velocity of airflow for ventilation main ducts in various use classifications, e.g., hospitals, theatres, and offices etc., is usually in the range of 5–15.2 m/s (Grondzik et al., 2009). Targeting at this issue, we will attempt to further investigate an embedded U-shaped array device, which can achieve particle filtration using the synergistic effect (i.e., turbulence effects and acoustic trapping). This design should maintain a sufficient flow rate within the ventilation ducts. Not limited to this issue, we will also consider the influence of higher airflow rates on the working

efficiency, and the sensitivity of acoustic frequency on various particle sizes. To realize an intelligent control in ventilation systems, an adaptive feed-forward control mechanism, consisting of flow sensors, actuators and controllers, can be used to integrate with the acoustic-driven device.

Finally, in the experimental process of CNT- and graphene-based TA devices, a precision operation process still needs to be further explored to maintain the quality of nano-thinfilms during the process. To provide a uniform distribution of graphene across Si/SiO₂ substrate, Raman spectroscopy and optical microscopy with lower magnification should be performed. Moreover, the persistence of acoustic performance of the CNT- and graphene-based TA devices is another crucial point that is worth studying in the future work. In general, the investigation of such a new-generation TA acoustic device is an irreversible trend as it contains various superior properties, e.g., flat-band frequency responses, high-intensity outputs, compact structures, and miniaturized systems. To meet all of the requirements for realizing practical applications, extensive investigations are required in the future work.

REFERENCES

- Abdallah, B., Elhissi, A. M. A., Ahmed, W., et al. (2020), Chapter 16 - Carbon nanotubes drug delivery system for cancer treatment, In *Advances in Medical and Surgical Engineering*, Academic Press, 313-332.
- Åbom, M. (1991), Measurement of the scattering-matrix of acoustical two-ports, *Mechanical Systems and Signal Processing*, 5(2), 89-104.
- Ahn, K. H., Ahn, J., Kim, I. T., et al. (2015), Separation of fine particles at different frequencies and HRTs using acoustic standing waves, *Environmental technology*, 36(1-4), 302-309.
- Akhtar, M. T. and Mitsuhashi, W. (2011), Improving robustness of filtered- x least mean p-power algorithm for active attenuation of standard symmetric- α -stable impulsive noise, *Applied Acoustics*, 72(9), 688-694.
- Al Omour, A. M., Zidouri, A., Iqbal, N., et al. (2016), Filtered-X least mean fourth (FXLMF) and leaky FXLMF adaptive algorithms, *EURASIP Journal on Advances in Signal Processing*, 2016(1), 1-20.
- Alfonsi, G. (2009), Reynolds-Averaged Navier-Stokes Equations for Turbulence Modeling, *Applied Mechanics Reviews*, 62(4), 1-20.
- Aliev, A. E., Mayo, N. K., Jung De Andrade, M., et al. (2015), Alternative Nanostructures for Thermophones, *ACS Nano*, 9(5), 4743-4756.
- ANSI/ASHRAE, (1999), Standard 52.2-1999: Method of Testing General Ventilation Air-Cleaning Device for Removal Efficiency by Particle Size.
- ANSI/ASHRAE, (2019), Standard 62.1-2019: Ventilation for Acceptable Indoor Air Quality.
- Ardekani, I., Zhang, X., Sharifzadeh, H., et al. (2017), Maximum a posteriori adjustment of adaptive transversal filters in active noise control, *2017 Asia-Pacific Signal and Information Processing Association Annual Summit and Conference (APSIPA ASC)*, 118-123.

References

- Ardekani, I. T., Kaipio, J. P., Nasiri, A., et al. (2016), A Statistical Inverse Problem Approach to Online Secondary Path Modeling in Active Noise Control, *IEEE/ACM Transactions on Audio, Speech, and Language Processing*, 24(1), 54-64.
- Arenas-Garcia, J., Martinez-Ramon, M., Gomez-Verdejo, V., et al. (2003), Multiple plant identifier via adaptive LMS convex combination, *IEEE International Symposium on Intelligent Signal Processing*, 137-142.
- Arenas-Garcia, J., Martinez-Ramon, M., Navia-Vazquez, A., et al. (2006), Plant identification via adaptive combination of transversal filters, *Signal Processing*, 86(9), 2430-2438.
- Arenas, C., Leiva, C., Vilches, L. F., et al. (2013), Use of co-combustion bottom ash to design an acoustic absorbing material for highway noise barriers, *Waste Management*, 33(11), 2316-2321.
- Arnold, H. D. and Crandall, I. B. (1917), The Thermophone as a Precision Source of Sound, *Physical Review*, 10(1), 22-38.
- Asdrubali, F., Schiavoni, S., and Horoshenkov, K. V. (2012), A Review of Sustainable Materials for Acoustic Applications, *Building acoustics*, 19(4), 283-311.
- Asgarisabet, M. and Barnard, A. (2017), Multi-Physics Simulation of Ultra-Lightweight Carbon Nanotube Speakers, *Sae International Journal of Materials and Manufacturing*, 10(3), 395-401.
- Asgarisabet, M., Barnard, A. R., and Bouman, T. M. (2016), Near field acoustic holography measurements of carbon nanotube thin film speakers, *Journal of the Acoustical Society of America*, 140(6), 4237-4245.
- Assouar, B., Oudich, M., and Zhou, X. (2016), Acoustic metamaterials for sound mitigation, *Comptes Rendus Physique*, 17(5), 524-532.
- ASTM E2611-09, (2009), Standard Test Method for Measurement of Normal Incidence Sound Transmission of Acoustical Materials Based on the Transfer Matrix Method, ASTM International, West Conshohocken.
- ASTM E1050-10, (2010), Standard Test Method for Impedance and Absorption of Acoustical Material Using a Tube, Two Microphones and a Digital Frequency Analysis System, ASTM International, West Conshohocken.

References

- ASTM E596-96, (2016), Standard Test Method for Laboratory Measurement of Noise Reduction of Sound-Isolating Enclosures, ASTM International, West Conshohocken.
- Avent, A. W. and Bowen, C. R. (2015), Principles of thermoacoustic energy harvesting, *The European Physical Journal Special Topics*, 224(14), 2967-2992.
- Brüel & Kjær, (2007), Technical Review: Transmission Loss in a Standing Wave Tube.
- Balandin, A. A., Ghosh, S., Bao, W., et al. (2008), Superior Thermal Conductivity of Single-Layer Graphene, *Nano Letters*, 8(3), 902-907.
- Baliatsas, C., Van Kamp, I., Van Poll, R., et al. (2016), Health effects from low-frequency noise and infrasound in the general population: Is it time to listen? A systematic review of observational studies, *Science of The Total Environment*, 557-558, 163-169.
- Barnard, A. R., Jenkins, D. M., Brungart, T. A., et al. (2013), Feasibility of a high-powered carbon nanotube thin-film loudspeaker, *The Journal of the Acoustical Society of America*, 134(3), EL276-EL281.
- Benes, E., Groschl, M., Nowotny, H., et al. (2001), Ultrasonic separation of suspended particles, *IEEE Ultrasonics Symposium. Proceedings. An International Symposium (Cat. No.01CH37263)*, 649-659.
- Berardi, U. and Iannace, G. (2015), Acoustic characterization of natural fibers for sound absorption applications, *Building and Environment*, 94, 840-852.
- Bershad, N. J. (1991), Adaptive Recovery of a Chirped Sinusoid in Noise, Part 2: Performance of the LMS Algorithm, *IEEE Transactions on Signal Processing*, 39(3), 595-602.
- Berthilsson, S., Barkefors, A., and Sternad, M. (2012), MIMO design of Active Noise Controllers for car interiors: Extending the silenced region at higher frequencies, *2012 American Control Conference (ACC)*, 6140-6147.
- Bian, A., Li, S., Xing, Q., et al. (2017), Thermo-acoustic theory of graphene films considering heat transfer of substrate materials, *Acta Acustica*, 42, 755-761, (In Chinese).
- Bies, D. A. (2018), Engineering noise control, 5th Edition, Boca Raton : CRC Press, Taylor & Francis Group.

References

- Blackstock, D. T. and Atchley, A. A. (2001), Fundamentals of Physical Acoustics, *The Journal of the Acoustical Society of America*, 109(4), 1274-1276.
- Bolton, J. S., Yun, R. J., Pope, J., et al. (1997), Development of a New Sound Transmission Test for Automotive Sealant Materials, *SAE Transactions*, 106, 2651-2658.
- Borin Barin, G., Song, Y., De Fátima Gimenez, I., et al. (2015), Optimized graphene transfer: Influence of polymethylmethacrylate (PMMA) layer concentration and baking time on graphene final performance, *Carbon*, 84, 82-90.
- Bouchard, M. and Quednau, S. (2000), Multichannel recursive-least-square algorithms and fast-transversal-filter algorithms for active noise control and sound reproduction systems, *IEEE Transactions on Speech and Audio Processing*, 8(5), 606-618.
- Bouchard, M. and Yu, F. (2001), Inverse structure for active noise control and combined active noise control/sound reproduction systems, *IEEE Transactions on Speech and Audio Processing*, 9(2), 141-151.
- Boucher, C. C., S. J. Elliott, and P. A. Nelson. (1991), The effects of modeling errors on the performance and stability of active noise control systems, *Proc. Recent Advances in Active Control of Sound Vibration*, 290-301.
- Boulaud, D., Frambourt, C., Madelaine, G., et al. (1984), Experimental study of the acoustic agglomeration and precipitation of an aerosol, *Journal of Aerosol Science*, 15(3), 247-252.
- Brandt, E. H. (2001), Suspended by sound, *Nature*, 413(6855), 474-475.
- Buratti, C., Belloni, E., Lascaro, E., et al. (2016), Sustainable Panels with Recycled Materials for Building Applications: Environmental and Acoustic Characterization, *Energy procedia*, 101, 972-979.
- Burgess, J. C. (1981), Active adaptive sound control in a duct: A computer simulation, *The Journal of the Acoustical Society of America*, 70(3), 715-726.
- Chakravarthy, S. R. and Kuo, S. M. (2006), Application of Active Noise Control for Reducing Snore, *IEEE International Conference on Acoustics Speech and Signal Processing Proceedings*, V-V.

References

- Chang, Q., Zheng, C., Yang, Z., et al. (2017), Electric agglomeration modes of coal-fired fly-ash particles with water droplet humidification, *Fuel*, 200, 134-145.
- Chen, G., Tang, L., Mace, B., et al. (2021), Multi-physics coupling in thermoacoustic devices: A review, *Renewable and Sustainable Energy Reviews*, 146, 111170.
- Chen, J.-H., Jang, C., Xiao, S., et al. (2008), Intrinsic and extrinsic performance limits of graphene devices on SiO₂, *Nature Nanotechnology*, 3(4), 206-209.
- Chen, W., Rao, W., Min, H., et al. (2011), An active noise barrier with unidirectional secondary sources, *Applied Acoustics*, 72(12), 969-974.
- Chen, Z., You, C., Wang, H., et al. (2019), Experimental study on the synergetic removal of fine particles by wet flue gas desulfurization tower with a flow pattern control device, *Powder Technology*, 343, 122-128.
- Chou, K. H., Lee, P. S., and Shaw, D. T. (1980), Acoustically induced turbulence and shock waves under a traveling-wave condition, *The Journal of the Acoustical Society of America*, 68(6), 1780-1789.
- Chung, J. Y. and Blaser, D. A. (1980a), Transfer function method of measuring in-duct acoustic properties. I. Theory, *The Journal of the Acoustical Society of America*, 68(3), 907-913.
- Chung, J. Y. and Blaser, D. A. (1980b), Transfer function method of measuring in-duct acoustic properties. II. Experiment, *The Journal of the Acoustical Society of America*, 68(3), 914-921.
- Clair, H. W. S. (1949), Agglomeration of Smoke, Fog, or Dust Particles by Sonic Waves, *Industrial & Engineering Chemistry*, 41(11), 2434-2438.
- COMSOL, (Ver. 5.4), Acoustic Module User's Guide.
- Coraux, J., N'diaye, A. T., Busse, C., et al. (2008), Structural coherency of graphene on Ir(111), *Nano Letters*, 8(2), 565-570.
- De Diego, M., Gonzalez, A., Ferrer, M., et al. (2004), Multichannel active noise control system for local spectral reshaping of multifrequency noise, *Journal of Sound and Vibration*, 274(1-2), 249-271.
- DEFRA. (2006), Update of Noise Database for Prediction of Noise on Construction and Open Sites, Department for Environment Food and Rural Affairs, U.K.

References

- Deokar, G., Avila, J., Razado-Colambo, I., et al. (2015), Towards high quality CVD graphene growth and transfer, *Carbon*, 89, 82-92.
- DESAPD. (2019), Revision of World Population Prospects, Department of Economic and Social Affairs Population Dynamics, U.S.
- Diggle, J. W., Downie, T. C., and Goulding, C. W. (1969), Anodic oxide films on aluminum, *Chemical Reviews*, 69(3), 365-405.
- Dols, W., Polidoro, B., Poppendieck, D., et al. (2020), A Tool to Model the Fate and Transport of Indoor Microbiological Aerosols (FaTIMA), *Technical Note (NIST TN)*, Gaithersburg, MD.
- Dong, S., Lipkens, B., and Cameron, T. M. (2006), The effects of orthokinetic collision, acoustic wake, and gravity on acoustic agglomeration of polydisperse aerosols, *Journal of Aerosol Science*, 37(4), 540-553.
- Dragonetti, R., Iannace, G., and Ianniello, C. (2003), Insertion loss of a heap of gravel outdoors, *Acta Acustica*, 89, S56-S57.
- Duhamel, D., Sergent, P., Hua, C., et al. (1998), Measurement of active control efficiency around noise barriers, *Applied Acoustics*, 55(3), 217-241.
- Eder, J., Hanselka, J., and Sachau, D. (2017), Experimental Comparison on the Effect of the Number of System Components of an Active Noise Blocker, *Proceeding Inter-noise 2017*, Hong Kong, China, 1687-1696.
- Elliot, S. J. and Nelson, P. A. (1985), The application of adaptive filtering to the active control of sound and vibration.
- Elliott, S. J., Cheer, J., Bhan, L., et al. (2018), A wavenumber approach to analysing the active control of plane waves with arrays of secondary sources, *Journal of Sound and Vibration*, 419, 405-419.
- EPD. (1997), Technical Memorandum on Noise from Percussive Piling, Environmental Protection Department, Hong Kong.
- EPD. (1998), Technical Memorandum on Noise from Construction Work other than Percussive Piling, Environmental Protection Department, Hong Kong.
- EPD. (2001), Technical Memorandum on Noise from Construction Work in Designated Areas, Environmental Protection Department, Hong Kong.

References

- EPD. (2003), Guidelines on design of noise barriers, Environmental Protection Department, Hong Kong.
- EPD. (2018), Cap. 400 Noise Control Ordinance, Environmental Protection Department, Hong Kong.
- EPD. (2019), Pollution Complaint Statistics, Environmental Protection Department, Hong Kong.
- EPD. (2021), An overview on challenges for waste reduction and management in Hong Kong, Environmental Protection Department, Hong Kong.
- Ersoy, S. and Küçük, H. (2009), Investigation of industrial tea-leaf-fibre waste material for its sound absorption properties, *Applied Acoustics*, 70(1), 215-220.
- Evander, M. and Laurell, T. (2012), Acoustic Trapping, In *Encyclopedia of Nanotechnology*, Springer Netherlands, 41-45.
- Fan, F., Zhang, M., Peng, Z., et al. (2017), Direct Simulation Monte Carlo Method for Acoustic Agglomeration under Standing Wave Condition, *Aerosol and Air Quality Research*, 17(4), 1073-1083.
- Fan, R., Su, Z., and Cheng, L. (2013), Modeling, analysis, and validation of an active T-shaped noise barrier, *The Journal of the Acoustical Society of America*, 134(3), 1990-2003.
- Feldman, K. T. (1968), Review of the literature on Rijke thermoacoustic phenomena, *Journal of Sound and Vibration*, 7(1), 83-89.
- Ferrer, M., Gonzalez, A., Diego, M. D., et al. (2013), Convex Combination Filtered-X Algorithms for Active Noise Control Systems, *IEEE Transactions on Audio, Speech, and Language Processing*, 21(1), 156-167.
- FHWA. (2018), HEP-18-065: Noise Measurement Handbook, Department of Transportation Federal Highway Administration, U.S.
- FHWA. (2021), Measurement of Highway-Related Noise: Highway Barrier Insertion Loss Measurement, Department of Transportation Federal Highway Administration, U.S.

References

- Filchakova, M. and Saik, V. (2021). Single-walled carbon nanotubes: structure, properties, applications, and health and safety, Web page: <https://tuball.com/articles/single-walled-carbon-nanotubes>.
- Foresti, D., Nabavi, M., and Poulidakos, D. (2012), On the acoustic levitation stability behaviour of spherical and ellipsoidal particles, *Journal of Fluid Mechanics*, 709, 581-592.
- Foresti, D., Sambatakakis, G., Bottan, S., et al. (2013), Morphing Surfaces Enable Acoustophoretic Contactless Transport of Ultrahigh-Density Matter in Air, *Scientific Reports*, 3(1), 3176.
- Friot, E. (2017), Time-domain versus frequency-domain effort weighting in active noise control design, *The Journal of the Acoustical Society of America*, 141(1), EL11-EL15.
- Fu, S.-C., Yuen, W.-T., Wu, C., et al. (2015), Finite-difference lattice Boltzmann simulation on acoustics-induced particle deposition, *Comptes rendus - Mécanique*, 343(10-11), 589-598.
- Gallego-Juarez, J., Riera, E., and Corral, G. (1996), Pilot scale acoustic preconditioning of coal combustion fumes to enhance electrostatic precipitator performance, *High Temperature Gas Cleaning*, 60-68.
- Gallego-Juárez, J. A., Riera-Franco De Sarabia, E., Rodríguez-Corral, G., et al. (1999), Application of Acoustic Agglomeration to Reduce Fine Particle Emissions from Coal Combustion Plants, *Environmental Science & Technology*, 33(21), 3843-3849.
- Gentry-Grace, C. A. (1998), A Study of Smart Foam for Noise Control Applications, PhD. Thesis, Virginia Polytechnic Institute & State University.
- George, N. V. and Gonzalez, A. (2014), Convex combination of nonlinear adaptive filters for active noise control, *Applied Acoustics*, 76, 157-161.
- George, N. V. and Panda, G. (2012), On the development of adaptive hybrid active noise control system for effective mitigation of nonlinear noise, *Signal Processing*, 92(2), 509-516.
- Ghofrani, M., Ashori, A., Rezvani, M. H., et al. (2016), Acoustical properties of plywood/waste tire rubber composite panels, *Measurement*, 94, 382-387.

References

- Ghosh, S., Calizo, I., Teweldebrhan, D., et al. (2008), Extremely high thermal conductivity of graphene: Prospects for thermal management applications in nanoelectronic circuits, *Applied Physics Letters*, 92(15), 151911.
- Gil-Lopez, T., Medina-Molina, M., Verdu-Vazquez, A., et al. (2017), Acoustic and economic analysis of the use of palm tree pruning waste in noise barriers to mitigate the environmental impact of motorways, *The Science of the total environment*, 584-585, 1066-1076.
- González, I. A., Gallego-Juárez, J. A., and Riera, E. (2003), The influence of entrainment on acoustically induced interactions between aerosol particles—an experimental study, *Journal of Aerosol Science*, 34(12), 1611-1631.
- Gor'kov, L. P. (1962), On the Forces Acting on a Small Particle in an Acoustical Field in an Ideal Fluid, *Soviet Physics Doklady*, 6, 773.
- Gou, G. Y., Jin, M. L., Lee, B. J., et al. (2019), Flexible Two-Dimensional Ti₃C₂ MXene Films as Thermoacoustic Devices, *ACS Nano*, 13(11), 12613-12620.
- Greenhall, J., Guevara Vasquez, F., and Raeymaekers, B. (2013), Continuous and unconstrained manipulation of micro-particles using phase-control of bulk acoustic waves, *Applied Physics Letters*, 103(7), 074103.
- Grondzik, W. T., Kwok, A. G., Reynolds, J. S., et al. (2009), *Mechanical and Electrical Equipment for Buildings*, 13th Edition, Hoboken: Wiley.
- Guigou, C. and Fuller, C. R. (1999), Control of aircraft interior broadband noise with foam-PVDF smart skin, *Journal of Sound and Vibration*, 220(3), 541-557.
- Guiraud, P., Giordano, S., Bou-Matar, O., et al. (2019), Multilayer modeling of thermoacoustic sound generation for thermophone analysis and design, *Journal of Sound and Vibration*, 455, 275-298.
- Guo, Q., Yang, Z., and Zhang, J. (2012), Influence of a combined external field on the agglomeration of inhalable particles from a coal combustion plant, *Powder Technology*, 227, 67-73.
- Haake, A. and Dual, J. (2002), Micro-manipulation of small particles by node position control of an ultrasonic standing wave, *Ultrasonics*, 40(1), 317-322.

References

- Habibi, R., Devendran, C., and Neild, A. (2017), Trapping and patterning of large particles and cells in a 1D ultrasonic standing wave, *Lab on a Chip*, 17(19), 3279-3290.
- Hahad, O., Prochaska, J. H., Daiber, A., et al. (2019), Environmental Noise-Induced Effects on Stress Hormones, Oxidative Stress, and Vascular Dysfunction: Key Factors in the Relationship between Cerebrocardiovascular and Psychological Disorders, *Oxidative Medicine and Cellular Longevity*, 2019(18), 1-13.
- Hall, A., Gaston, J., Wolde, W., et al. (2014), Signal conditioning of carbon nanotube thin film loudspeakers, *14th IEEE International Conference on Nanotechnology*, 668-671.
- Han, N. and Qiu, X. (2007), A study of sound intensity control for active noise barriers, *Applied Acoustics*, 68(10), 1297-1306.
- Han, R., Wu, M., Liu, F., et al. (2019), A narrowband active noise control system with a frequency estimator based on Bayesian inference, *Journal of Sound and Vibration*, 455, 299-311.
- Han, Z., Kimouche, A., Kalita, D., et al. (2014), Homogeneous Optical and Electronic Properties of Graphene Due to the Suppression of Multilayer Patches During CVD on Copper Foils, *Advanced Functional Materials*, 24(7), 964-970.
- Hansen, C. H. (2013), Active control of noise and vibration, 2nd Edition, Boca Raton, FL : CRC Press.
- Helmholtz, H. (1878), The Theory of Sound, *Nature*, 19(476), 117-118.
- Helzner, E. P., Patel, A. S., Pratt, S., et al. (2011), Hearing Sensitivity in Older Adults: Associations with Cardiovascular Risk Factors in the Health, Aging and Body Composition Study, *Journal of the American Geriatrics Society*, 59(6), 972-979.
- Her, M., Beams, R., and Novotny, L. (2013), Graphene transfer with reduced residue, *Physics Letters A*, 377(21), 1455-1458.
- Hoffmann, T. L. (2000), Environmental implications of acoustic aerosol agglomeration, *Ultrasonics*, 38(1), 353-357.
- Hoffmann, T. L., Chen, W., Koopmann, G. H., et al. (1993), Experimental and Numerical Analysis of Bimodal Acoustic Agglomeration, *Journal of Vibration and Acoustics*, 115(3), 232-240.

References

- Hoffmann, T. L. and Koopmann, G. H. (1994), A new technique for visualization of acoustic particle agglomeration, *Review of Scientific Instruments*, 65(5), 1527-1536.
- Hoffmann, T. L. and Koopmann, G. H. (1996), Visualization of acoustic particle interaction and agglomeration: Theory and experiments, *The Journal of the Acoustical Society of America*, 99(4), 2130-2141.
- Hong, J. Y. and Jeon, J. Y. (2014), The effects of audio–visual factors on perceptions of environmental noise barrier performance, *Landscape and Urban Planning*, 125, 28-37.
- Hosur, S. and Tewfik, A. H. (1997), Wavelet transform domain adaptive FIR filtering, *IEEE Transactions on Signal Processing*, 45(3), 617-630.
- Hu, H., Wang, Y., and Wang, Z. (2012a), Wideband flat frequency response of thermo-acoustic emission, *Journal of Physics D: Applied Physics*, 45(34), 345401.
- Hu, H., Zhu, T., and Xu, J. (2010), Model for thermoacoustic emission from solids, *Applied Physics Letters*, 96(21), 214101.
- Hu, Q. (2019), Active control of the sound radiation from a finite line source using novel directional secondary sources, PhD. Thesis, The Hong Kong Polytechnic University.
- Hu, Q. and Tang, S. K. (2019), Active cancellation of sound generated by finite length coherent line sources using piston-like secondary source arrays, *The Journal of the Acoustical Society of America*, 145(6), 3647-3655.
- Hu, S., Rajamani, R., and Yu, X. (2012), Invisible speakers in home windows for simultaneous auxiliary audio playback and active noise cancellation, *Mechatronics*, 22(8), 1031-1042.
- Hu, S., Rajamani, R., and Yu, X. (2013), Directional cancellation of acoustic noise for home window applications, *Applied Acoustics*, 74(3), 467-477.
- Huang, H., Qiu, X., and Kang, J. (2011), Active noise attenuation in ventilation windows, *The Journal of the Acoustical Society of America*, 130(1), 176-188.
- Iannace, G., Ciaburro, G., and Trematerra, A. (2021), Metamaterials acoustic barrier, *Applied Acoustics*, 181, 108172.

References

- Iijima, S. (1991), Helical microtubules of graphitic carbon, *Nature*, 354(6348), 56-58.
- Iniesta, C., Olazagoitia, J., Vinolas, J., et al. (2018), Review of travelling-wave thermoacoustic electric-generator technology, *Proceedings of the Institution of Mechanical Engineers Part A Journal of Power and Energy*, 232, 940-957.
- Ise, S., Yano, H., and Tachibana, H. (1991), Basic study on active noise barrier, *J.Acoust.Soc.Jpn (E)*, 12(6), 299-306.
- Ishizuka, T. and Fujiwara, K. (2004), Performance of noise barriers with various edge shapes and acoustical conditions, *Applied Acoustics*, 65(2), 125-141.
- ISO, (1997), Acoustics - *In-situ* determination of insertion loss of outdoor noise barriers of all types, International Organization for Standardization.
- ISO, (1998), Acoustics - Determination of sound absorption coefficient and impedance in impedance tubes - Part 2: Transfer-function method, International Organization for Standardization.
- ISO, (2010), Acoustics - Determination of sound power levels and sound energy levels of noise sources using sound pressure - Engineering methods for an essentially free field over a reflecting plane, International Organization for Standardization.
- Jaakkola, J. J. K., Reinikainen, L. M., Heinonen, O. P., et al. (1991), Indoor air quality requirements for healthy office buildings: Recommendations based on an epidemiologic study, *Environment International*, 17(4), 371-378.
- Jang, C. M., Kim, D. W., and Lee, S. Y. (2008), Performance characteristics of turbo blower in a refuse collecting system according to operation conditions, *Journal of Mechanical Science and Technology*, 22(10), 1896-1901.
- Jin, T., Huang, J., Feng, Y., et al. (2015), Thermoacoustic prime movers and refrigerators: Thermally powered engines without moving components, *Energy*, 93, 828-853.
- Kačianauskas, R., Rimša, V., Kačeniauskas, A., et al. (2018), Comparative DEM-CFD study of binary interaction and acoustic agglomeration of aerosol microparticles at low frequencies, *Chemical Engineering Research and Design*, 136, 548-563.

References

- Karpul, D., Tapson, J., Rapson, M., et al. (2010), Limiting factors in acoustic separation of carbon particles in air, *The Journal of the Acoustical Society of America*, 127(4), 2153-2158.
- Kawai, H. (1969), The piezoelectricity of Poly (vinylidene Fluoride), *Japanese Journal of Applied Physics*, 8(7), 975-976.
- Keller, F., Hunter, M. S., and Robinson, D. L. (1953), Structural Features of Oxide Coatings on Aluminum, *Journal of The Electrochemical Society*, 100(9), 411.
- Kelly, F. J. and Fussell, J. C. (2019), Improving indoor air quality, health and performance within environments where people live, travel, learn and work, *Atmospheric Environment*, 200, 90-109.
- Khankari, K. (2016), Patient room HVAC: Airflow path matters, *ASHRAE Journal*, 58(6), 16-26.
- Kim, C. S., Hong, S. K., Lee, J.-M., et al. (2016), Free-Standing Graphene Thermophone on a Polymer-Mesh Substrate, *Small*, 12(2), 185-189.
- Kim, D. and Lee, S. J. (2020), Effect of water microdroplet size on the removal of indoor particulate matter, *Building and Environment*, 181(107097).
- Kim, H., Yang, W., and No, K. (2012), Improvement of low-frequency characteristics of piezoelectric speakers based on acoustic diaphragms, *IEEE Transactions on Ultrasonics, Ferroelectrics and Frequency Control*, 59.
- Kim, J., Yun, G.-Y., Kim, J.-H., et al. (2011), Piezoelectric electro-active paper (EAPap) speaker, 25(11), 2763-2768.
- Kim, M.-M. and Zydney, A. L. (2004), Effect of electrostatic, hydrodynamic, and Brownian forces on particle trajectories and sieving in normal flow filtration, *Journal of Colloid and Interface Science*, 269(2), 425-431.
- Kinsler, L. E. (2000), *Fundamentals of acoustics*, 4th Edition, New York : John Wiley.
- Kontomichos, F., Koutsioubas, A., Mourjopoulos, J., et al. (2012), Testing and simulation of a thermoacoustic transducer prototype, *126th Audio Engineering Society Convention*, 2.
- Kozlov, M. E., Haines, C. S., Oh, J., et al. (2009), Sound of carbon nanotube assemblies, *Journal of Applied Physics*, 106(12), 124311.

References

- Krahe, D. (2005), A MIMO-system for a 2-dimensional active noise control application, *The Fourth International Workshop on Multidimensional Systems*, 123-128.
- Kramers, H. A. (1949), Vibrations of a gas column, *Physica*, 15(11), 971-984.
- Kulkarni, P., Baron, P. A., and Willeke, K. (2011), *Aerosol Measurement: Principles, Techniques, and Applications* Hoboken: John Wiley & Sons, Incorporated.
- Kumar, P., Sriramdas, R., Aliev, A. E., et al. (2021), Understanding the low frequency response of carbon nanotube thermoacoustic projectors, *Journal of Sound and Vibration*, 498, 115940.
- Kuo, S. M. (1995), Adaptive active noise control systems: algorithms and digital signal processing (DSP) implementations, *SPIE's 1995 Symposium on OE/Aerospace Sensing and Dual Use Photonics*, 27.
- Kuo, S. M. (1996), *Active noise control systems : algorithms and DSP implementations* New York : Wiley.
- Kuo, S. M. and Gireddy, R. (2007), Real-time experiment of snore active noise control, *2007 IEEE International Conference on Control Applications*, 1342-1346.
- Kuo, S. M. and Ji, M. (1996), Passband disturbance reduction in periodic active noise control systems, *IEEE Transactions on Speech and Audio Processing*, 4(2), 96-103.
- Kuo, S. M. and Morgan, D. R. (1999), Active noise control: a tutorial review, *Proceedings of the IEEE*, 87(6), 943-973.
- Kuo, S. M., Yenduri, R. K., and Gupta, A. (2008), Frequency-domain delayless active sound quality control algorithm, *Journal of Sound and Vibration*, 318(4), 715-724.
- Kurakata, K., Mizunami, T., Sato, H., et al. (2008), Effect of Ageing on Hearing Thresholds in the Low Frequency Region, *JOURNAL OF LOW FREQUENCY NOISE, VIBRATION AND ACTIVE CONTROL*, 27(3), 175-184.
- Kurian, N. C., Patel, K., and George, N. V. (2017), Robust active noise control: An information theoretic learning approach, *Applied Acoustics*, 117, 180-184.

References

- Labašová, E. and Ďuriš, R. (2019), Measurement of the Acoustic Absorption Coefficient by Impedance Tube, *Research Papers Faculty of Materials Science and Technology Slovak University of Technology*, 27, 94-101.
- Lai, S. K., Tong, L. H., and Lim, C. W. (2019), On the reflection and diffraction of carbon nanotube array thin film, *Wave Motion*, 90, 196-204.
- Lai, S. K. and Zhang, Y. T. (2019), Real-time prediction of noise signals for active control using a Bayesian inference approach, *Inter-Noise 2019 Congress*, Madrid, Spain.
- Lam, B., Gan, W.-S., Shi, D., et al. (2021), Ten questions concerning active noise control in the built environment, *Building and Environment*, 200, 107928.
- Lam, B., Shi, C., and Gan, W.-S. (2017), Active noise control systems for open windows: Current updates and future perspectives, *24th International Congress on Sound and Vibration*, London, U.K.
- Laurell, T., Petersson, F., and Nilsson, A. (2007), Chip integrated strategies for acoustic separation and manipulation of cells and particles, *Chemical Society reviews*, 36(3), 492-506.
- LCPD. (2016), Hong Kong 2030+: Towards a Planning Vision and Strategy Transcending 2030., Legislative Council Panel of Development, Hong Kong.
- Lee, H. M., Wang, Z., Lim, K. M., et al. (2020), Investigation of the effects of sample size on sound absorption performance of noise barrier, *Applied Acoustics*, 157, 106989.
- Lee, J.-K., Kim, J., Rhee, C.-J., et al. (2002), Noise reduction of passive and active hybrid panels, *Smart Materials and Structures*, 11(6), 940-946.
- Lee, P. S., Cheng, M. T., and Shaw, D. T. (1981), The Influence of Hydrodynamic Turbulence on Acoustic Turbulent Agglomeration, *Aerosol Science and Technology*, 1(1), 47-58.
- Lee, S. C., Hong, J. Y., and Jeon, J. Y. (2015), Effects of acoustic characteristics of combined construction noise on annoyance, *Building and Environment*, 92, 657-667.

References

- Lee, W. and Park, S.-J. (2014), Porous Anodic Aluminum Oxide: Anodization and Templated Synthesis of Functional Nanostructures, *Chemical Reviews*, 114(15), 7487-7556.
- Lei, J., Glynn-Jones, P., and Hill, M. (2013), Acoustic streaming in the transducer plane in ultrasonic particle manipulation devices, *Lab Chip*, 13(11), 2133-2143.
- Leventhall, H. G. (2004), Low frequency noise and annoyance, *Noise Health*, 6(23), 59-72.
- Li, X., Zhu, Y., Cai, W., et al. (2009a), Transfer of Large-Area Graphene Films for High-Performance Transparent Conductive Electrodes, *Nano Letters*, 9(12), 4359-4363.
- Li, X. S., Cai, W. W., An, J. H., et al. (2009b), Large-Area Synthesis of High-Quality and Uniform Graphene Films on Copper Foils, *Science*, 324(5932), 1312.
- Li, Y., Leung, G. M., Tang, J. W., et al. (2007), Role of ventilation in airborne transmission of infectious agents in the built environment - a multidisciplinary systematic review, *Indoor Air*, 17(1), 2-18.
- Li, Y., Wang, Y., and Jiang, T. (2016), Norm-adaption penalized least mean square/fourth algorithm for sparse channel estimation, *Signal Processing*, 128, 243-251.
- Lim, C. W., Tong, L. H., and Li, Y. C. (2013), Theory of suspended carbon nanotube thinfilm as a thermal-acoustic source, *Journal of Sound and Vibration*, 332(21), 5451-5461.
- Lim, S. J. and Harris, J. G. (1997), Combined LMS/F algorithm, *Electronics Letters*, 33(6), 467-468.
- Lim, Z. Y., Putra, A., Nor, M. J. M., et al. (2018), Sound absorption performance of natural kenaf fibres, *Applied Acoustics*, 130, 107-114.
- Lin, Y. M., Dimitrakopoulos, C., Jenkins, K. A., et al. (2010), 100-GHz Transistors from Wafer-Scale Epitaxial Graphene, *Science*, 327(5966), 662.
- Lipowsky, H., Staudacher, S., Bauer, M., et al. (2009), Application of Bayesian Forecasting to Change Detection and Prognosis of Gas Turbine Performance, *Journal of Engineering for Gas Turbines and Power*, 132(3).

References

- Lipowsky, H., Staudacher, S., Bauer, M., et al. (2010), Application of Bayesian Forecasting to Change Detection and Prognosis of Gas Turbine Performance, *Journal of Engineering for Gas Turbines and Power*, 132(3), 31602.
- Liu, C., Zhao, Y., Tian, Z., et al. (2021), Numerical Simulation of Condensation of Natural Fog Aerosol under Acoustic Wave Action, *Aerosol and Air Quality Research*, 21(4), 200361.
- Liu, J. and Li, X. (2020), A computational investigation of particle acoustic agglomeration in a resonance tube, *Powder Technology*, 374, 82-94.
- Liu, J., Wang, J., Zhang, G., et al. (2011), Frequency comparative study of coal-fired fly ash acoustic agglomeration, *Journal of Environmental Sciences*, 23(11), 1845-1851.
- Liu, J., Zhang, G., Zhou, J., et al. (2009a), Experimental study of acoustic agglomeration of coal-fired fly ash particles at low frequencies, *Powder Technology*, 193(1), 20-25.
- Liu, J. C. C. and Niu, F. (2008), Study on the analogy feedback active soft edge noise barrier, *Applied Acoustics*, 69(8), 728-732.
- Liu, K., Sun, Y., Zhou, R., et al. (2009b), Carbon nanotube yarns with high tensile strength made by a twisting and shrinking method, *Nanotechnology*, 21, 045708.
- Liu, Y., Ning, Z., Chen, Y., et al. (2020), Aerodynamic analysis of SARS-CoV-2 in two Wuhan hospitals, *Nature*, 582(7813), 557-560.
- Lolla, D., Gorse, J., Kisielowski, C., et al. (2016), Polyvinylidene fluoride molecules in nanofibers, imaged at atomic scale by aberration corrected electron microscopy, *Nanoscale*, 8(1), 120-128.
- Lu, M., Fang, M., He, M., et al. (2019), Insights into agglomeration and separation of fly-ash particles in a sound wave field, *RSC advances*, 9(9), 5224-5233.
- Maekawa, Z. (1968), Noise reduction by screens, *Applied Acoustics*, 1(3), 157-173.
- Magri, L. and Juniper, M. (2013), Sensitivity analysis of a time-delayed thermo-acoustic system via an adjoint-based approach, *Journal of Fluid Mechanics*, 719.

References

- Maknickas, A., Markauskas, D., and Kačianauskas, R. (2016), Discrete element simulating the hydrodynamic effects in acoustic agglomeration of micron-sized particles, *Particulate Science and Technology*, 34(4), 453-460.
- Manisalidis, I., Stavropoulou, E., Stavropoulos, A., et al. (2020), Environmental and Health Impacts of Air Pollution: A Review, *Frontiers in Public Health*, 8(14).
- Mao, Y., Lim, C. W., and Li, T. (2019a), Thermo-acoustic radiation of free-standing nano-thin film in viscous fluids, *International Journal of Engineering Science*, 139, 11-23.
- Mao, Y., Lim, C. W., and Li, T. (2019b), Multi-field coupling thermo-acoustic radiation using free-standing nano-thin films in a static magnetic field, *Journal of Thermal Stresses*, 42(6), 769-786.
- Mao, Y., Lim, C. W., Li, T., et al. (2021), Thermo-magnetic induced monodirectional periodic acoustic emission from free-standing nano-thin film, *Journal of Sound and Vibration*, 490, 115569.
- Markauskas, D., Kačianauskas, R., and Maknickas, A. (2015), Numerical particle-based analysis of the effects responsible for acoustic particle agglomeration, *Advanced Powder Technology*, 26(3), 698-704.
- Marshall, J. S. and Li, S. (2014), *Adhesive Particle Flow: A Discrete-Element Approach* Cambridge University Press.
- Mattevi, C., Kim, H., and Chhowalla, M. (2011), A review of chemical vapour deposition of graphene on copper, *Journal of Materials Chemistry*, 21(10), 3324-3334.
- Max, B. (2019), *Principles of optics, Seventh anniversary edition, 60th anniversary edition..* Cambridge : Cambridge University Press.
- Mcdonald, F. A. and Wetsel, G. C. (1978), Generalized theory of the photoacoustic effect, *Journal of Applied Physics*, 49(4), 2313-2322.
- Mednikov, E. P. (1965), *Acoustic Coagulation and Precipitation of Aerosols: Authorized Translation from the Russian by Chas. V. Larrick Consultants Bureau.*
- Mirowska, M. and Mroz, E. (2000), Effect of low-frequency noise at low levels on human health in light of questionnaire investigation, *The 29th International Congress and Exhibition on Noise Control Engineering*, Nice, France.

References

- Mital, A. and Ramakrishnan, A. S. (1997), Effectiveness of noise barriers on an interstate highway: a subjective and objective evaluation, *J Hum Ergol (Tokyo)*, 26(1), 31-38.
- Moffett, M. B. (1970), Theoretical Acoustics. Philip M. Morse and K. Uno Ingard. McGraw-Hill, New York, 1968. xxii, 938 pp., illus. \$23. International Series in Pure and Applied Physics, *Science (American Association for the Advancement of Science)*, 170(3954), 156-157.
- Morawska, L., Tang, J. W., Bahnfleth, W., et al. (2020), How can airborne transmission of COVID-19 indoors be minimised?, *Environ Int*, 142, 105832.
- Morgan, S. and Kay, D. (2001), Selection of noise barrier material, *Transportation Research Record*, 1756, 63-67.
- Morozov, S. V., Novoselov, K. S., Katsnelson, M. I., et al. (2008), Giant Intrinsic Carrier Mobilities in Graphene and Its Bilayer, *Physical Review Letters*, 100(1), 016602.
- Morse, P. M. (1976), Vibration and sound New York : American Institute of Physics.
- Muller, P. B., Barnkob, R., Jensen, M. J. H., et al. (2012), A numerical study of microparticle acoustophoresis driven by acoustic radiation forces and streaming-induced drag forces, *Lab on a Chip*, 12(22), 4617-4627.
- Munjal, M. L. (2014), Acoustics of Ducts and Mufflers New York: John Wiley & Sons, Incorporated.
- Murao, T., Nishimura, M., and Gan, W.-S. (2019), A hybrid approach to active and passive noise control for open windows, *Applied Acoustics*, 155, 338-345.
- Murao, T., Nishimura, M., Sakurama, K., et al. (2016), Basic study on active acoustic shielding (Improving the method to enlarge the AAS window), *Mechanical Engineering Journal*, 3(1), 15-00322-00315-00322.
- Murphy, E. and King, E. A. (2014), Chapter 6 - Industrial and Construction Type Noise, In *Environmental Noise Pollution*, Elsevier, 173-201.
- Nasibulin, A. G., Kaskela, A., Mustonen, K., et al. (2011), Multifunctional Free-Standing Single-Walled Carbon Nanotube Films, *ACS Nano*, 5(4), 3214-3221.

References

- Nechita, P. and Năstac, S. (2018), Foam-formed cellulose composite materials with potential applications in sound insulation, *Journal of Composite Materials*, 52(6), 747-754.
- Neithalath, N., Marolf, A., Weiss, W., et al. (2005), Modeling the Influence of Pore Structure on the Acoustic Absorption of Enhanced Porosity Concrete, *Journal of Advanced Concrete Technology*, 3(1), 29-40.
- Nelson, P. A. (1993), Active control of sound London : Academic Press.
- NFPA-96, (2021), Standard for Ventilation Control and Fire Protection of Commercial Cooking Operations.
- Ng, B. F., Xiong, J. W., and Wan, M. P. (2017), Application of acoustic agglomeration to enhance air filtration efficiency in air-conditioning and mechanical ventilation (ACMV) systems, *PLOS ONE*, 12(6).
- Ng, H. T. (2019), Acoustically driven air vibration in cavity and its application to sound barriers, PhD. Thesis, The Hong Kong Polytechnic University.
- Ni, J. and Li, F. (2010), Adaptive combination of subband adaptive filters for acoustic echo cancellation, *IEEE Transactions on Consumer Electronics*, 56(3), 1549-1555.
- Nilsson, M. E. and Berglund, B. (2006), Noise annoyance and activity disturbance before and after the erection of a roadside noise barrier, *The Journal of the Acoustical Society of America*, 119(4), 2178-2188.
- NIOSH. (2003), Guidance for filtration and air-cleaning systems to protect building environments from protect building environments from airborne chemical, biological, or radiological attacks.
- Niu, M., Shen, F., Zhou, F., et al. (2020), Indoor air filtration could lead to increased airborne endotoxin levels, *Environment International*, 142, 105878.
- Nobile, M. A. (1984), The two-microphone transfer function method for measuring absorption coefficients and impedance: Some limitations and precautions, *The Journal of the Acoustical Society of America*, 75, S55.
- Novoselov, K. S., Geim, A. K., Morozov, S. V., et al. (2005), Two-dimensional gas of massless Dirac fermions in graphene, *Nature*, 438(7065), 197-200.

References

- Novoselov, K. S., Geim, A. K., Morozov, S. V., et al. (2004), Electric Field Effect in Atomically Thin Carbon Films, *Science*, 306(5696), 666-669.
- Ohga, J., Takei, T., and Moriyama, N. (2010), Wideband piezoelectric rectangular loudspeakers using a tuck shaped PVDF bimorph, *IEEE Transactions on Dielectrics and Electrical Insulation*, 17(4), 1074 - 1078.
- Olivieri, O., Bolton, J. S., and Yoo, T. (2006), Measurement of transmission loss of materials using a standing wave tube, *INTER-NOISE 2006*, HAWAII, USA.
- Omoto, A. and Fujiwara, K. (1993), A study of an actively controlled noise barrier, *The Journal of the Acoustical Society of America*, 94(4), 2173-2180.
- Omoto, A., Takashima, K., Fujiwara, K., et al. (1997), Active suppression of sound diffracted by a barrier: An outdoor experiment, *The Journal of the Acoustical Society of America*, 102(3), 1671-1679.
- Onorato, P. (2011), Transport Properties in Carbon Nanotubes, In, Vol. 179, 45-109.
- Oseen, C. W. (1910), Uber die Stokes' sche Formel und Uber eine verwandte Aufgabe in der Hydrodynamik, *Ark. Mat. Astron. Fysik.*, 9, 1-20.
- Padhi, T., Chandra, M., Kar, A., et al. (2018), A new hybrid active noise control system with convex combination of time and frequency domain filtered-x LMS algorithms, *Circuits, Systems, and Signal Processing*, 37(8), 3275-3294.
- Pai, A., Satish Shenoy, B., Kini, R. C., et al. (2021), The scope of acoustic impedance matching of hybrid fiber metal laminates for shielding applications, *Journal of King Saud University - Engineering Sciences*.
- Pàmies, T., Romeu, J., Genescà, M., et al. (2014), Active control of aircraft fly-over sound transmission through an open window, *Applied Acoustics*, 84, 116-121.
- Park, S. H., Lee, K. W., Otto, E., et al. (1999), The log-normal size distribution theory of brownian aerosol coagulation for the entire particle size range: Part I— analytical solution using the harmonic mean coagulation kernel, *Journal of Aerosol Science*, 30(1), 3-16.
- Patel, V., Cheer, J., and George, N. V. (2017), Modified Phase-Scheduled-Command FxLMS Algorithm for Active Sound Profiling, *IEEE/ACM Transactions on Audio, Speech, and Language Processing*, 25(9), 1799-1808.

References

- Patterson, H. S. and Cawood, W. (1931), Phenomena in a Sounding Tube, *Nature*, 127(3209), 667-667.
- Pawlaczyk-Luszczyńska, M., Dudarewicz, A., Waszkowska, M., et al. (2005), The impact of low-frequency noise on human mental performance, *International journal of occupational medicine and environmental health*, 18(2), 185-198.
- Pedreño-Rojas, M. A., Morales-Conde, M. J., Pérez-Gálvez, F., et al. (2017), Eco-efficient acoustic and thermal conditioning using false ceiling plates made from plaster and wood waste, *Journal of Cleaner Production*, 166, 690-705.
- Peng, L. (2017), Chapter 13-Sound absorption and insulation functional composites, In *Advanced High Strength Natural Fibre Composites in Construction*, 333-373.
- Peng, X., He, W., Xin, F., et al. (2020), The acoustic radiation force of a focused ultrasound beam on a suspended eukaryotic cell, *Ultrasonics*, 108(106205).
- Peng, Z., Doroodchi, E., and Evans, G. (2010), DEM simulation of aggregation of suspended nanoparticles, *Powder Technology*, 204, 91-102.
- Pervaiz, M. and Sain, M. M. (2003), Carbon storage potential in natural fiber composites, *Resources, Conservation and Recycling*, 39(4), 325-340.
- Pierce, A. D. and Beyer, R. T. (1990), Acoustics: An Introduction to Its Physical Principles and Applications. 1989 Edition, *The Journal of the Acoustical Society of America*, 87(4), 1826-1827.
- Podgornik, R., Holm, C., and Kekicheff, P. (2000), *Electrostatic Effects in Soft Matter and Biophysics* Boston : Kluwer Academic Publishers.
- Pole, A. (1994), *Applied Bayesian forecasting and times series analysis*, 1st Edition, New York : Chapman and Hall.
- Prasher, R. (2010), Graphene Spreads the Heat, *Science*, 328(5975), 185.
- Prevenslik, T. (2010), Thermophones by quantum mechanics, *12th IEEE Intersociety Conference on Thermal and Thermomechanical Phenomena in Electronic Systems*, 1-5.
- Putra, A., Abdullah, Y., Efendy, H., et al. (2013), Utilizing Sugarcane Wasted Fibers as a Sustainable Acoustic Absorber, *Procedia engineering*, 53, 632-638.

References

- Qian, H., Li, Y., Nielsen, P. V., et al. (2006), Dispersion of exhaled droplet nuclei in a two-bed hospital ward with three different ventilation systems, *Indoor Air*, 16(2), 111-128.
- Qian, H., Miao, T., Liu, L., et al. (2021), Indoor transmission of SARS-CoV-2, *Indoor Air*, 31(3), 639-645.
- Qiao, Y., Gou, G., Wu, F., et al. (2020), Graphene-Based Thermoacoustic Sound Source, *ACS Nano*, 14(4), 3779-3804.
- Qiao, Z., Huang, Y., Vincenzo, N., et al. (2015), Aerosol manipulation by acoustic tunable phase-control at resonant frequency, *Powder Technology*, 281, 76-82.
- Qiao, Z., Huang, Y., Vincenzo, N., et al. (2017), Aerosol manipulation through modulated multiple acoustic wavepackets with a pair of resonators, *Powder Technology*, 322, 24-31.
- Qiu, Z., Lee, C. M., Xu, Z. H., et al. (2016), A multi-resolution filtered-x LMS algorithm based on discrete wavelet transform for active noise control, *Mechanical Systems and Signal Processing*, 66-67, 458-469.
- Rabl, A., Spadaro, J. V., and Zoughaib, A. (2008), Environmental impacts and costs of solid waste: a comparison of landfill and incineration, *Waste Management & Research*, 26(2), 147-162.
- Raj, M., Fatima, S., and Tandon, N. (2020), A study of areca nut leaf sheath fibers as a green sound-absorbing material, *Applied Acoustics*, 169, 107490.
- Rayleigh, J. W. S. B. (1945), *The theory of sound*, 2nd Edition, New York : Dover publications.
- Rees, L. E. and Elliott, S. J. (2006), Adaptive algorithms for active sound-profiling, *IEEE Transactions on Audio, Speech, and Language Processing*, 14(2), 711-719.
- Reina, A., Jia, X., Ho, J., et al. (2009), Large Area, Few-Layer Graphene Films on Arbitrary Substrates by Chemical Vapor Deposition, *Nano Letters*, 9(1), 30-35.
- Remington, P. J., Knight, J. S., Hanna, D., et al. (2005), A hybrid active/passive exhaust noise control system for locomotives, *The Journal of the Acoustical Society of America*, 117(1), 68-78.

References

- Riera-Franco De Sarabia, E. and Gallego-Juárez, J. A. (1986), Ultrasonic agglomeration of micron aerosols under standing wave conditions, *Journal of Sound and Vibration*, 110(3), 413-427.
- Rodi, W. (2017), *Turbulence Models and Their Application in Hydraulics*, 3rd Edition, Routledge Press.
- Rokad, V. and Pandya, D. H. (2020), Development of 3D improved acoustic transient model for vibro cleaner using COMSOL multiphysics, *Materials Today: Proceedings*, 44, 732-736.
- Rott, N. (1969), Damped and thermally driven acoustic oscillations in wide and narrow tubes, *Zeitschrift für angewandte Mathematik und Physik ZAMP*, 20(2), 230-243.
- SAE Recommended Practice, (1976), Exterior Sound Level Measurement Procedure for Powered Mobile Construction Equipment.
- Saeidi, D., Saghafian, M., Haghjooy Javanmard, S., et al. (2020), A Quantitative Study of the Secondary Acoustic Radiation Force on Biological Cells during Acoustophoresis, *Micromachines*, 11(2), 152.
- Sahraei, M. A. and Ghaemi, S. (2013), Influence of Height and Distance of Traffic Noise barriers for Noise Mitigation.
- Samsudin, E., Ismail, L., and Abdul Kadir, K. (2016), A review on physical factors influencing absorption performance of fibrous sound absorption material from natural fibers, *Journal of Engineering and Applied Sciences*, 11, 3703-3710.
- Sánchez-Dehesa, J., Garcia-Chocano, V. M., Torrent, D., et al. (2011), Noise control by sonic crystal barriers made of recycled materials, *The Journal of the Acoustical Society of America*, 129(3), 1173-1183.
- Sbrockey, N. M., Salagaj, T., Tompa, G. S., et al. (2018), Synthesis and characterization of graphene based thermoacoustic devices, *Journal of Crystal Growth*, 493, 41-44.
- Schiavi, A., Pavoni Belli, A., Corallo, M., et al. (2006), Acoustical Performance Characterization of Sustainable Materials used under Floating Floors in Dwellings.

References

- Secchi, S., Asdrubali, F., Cellai, G., et al. (2016), Experimental and environmental analysis of new sound-absorbing and insulating elements in recycled cardboard, *Journal of Building Engineering*, 5, 1-12.
- Sha, H. and Qi, D. (2020), A Review of High-Rise Ventilation for Energy Efficiency and Safety, *Sustainable Cities and Society*, 54(101971).
- Sharifzadeh Mirshekarloo, M., Tan, C. Y., Yu, X., et al. (2018), Transparent piezoelectric film speakers for windows with active noise mitigation function, *Applied Acoustics*, 137, 90-97.
- Sharifzadeh Mirshekarloo, M., Zhang, L., Chen, S., et al. (2016), Transparent piezoelectric film speakers for active noise mitigation, *INTER-NOISE and NOISE-CON Congress and Conference Proceedings*, 253(5), 3102-3107.
- Shen, G., Huang, X., He, C., et al. (2018), Experimental study of acoustic agglomeration and fragmentation on coal-fired ash with different particle size distribution, *Powder Technology*, 325, 145-150.
- Shi, C.-H., Zhang, J., Zhao, Y., et al. (2017), Acoustic Agglomeration Process of Fine Particles in a Resonance Structure, *IOP Conference Series: Earth and Environmental Science*, 78, 012001.
- Shi, Y., Wei, J., Bai, W., et al. (2020), Numerical investigations of acoustic agglomeration of liquid droplet using a coupled CFD-DEM model, *Advanced Powder Technology*, 31(6), 2394-2411.
- Shinoda, H., Nakajima, T., Ueno, K., et al. (1999), Thermally induced ultrasonic emission from porous silicon, *Nature*, 400(6747), 853-855.
- Sim, J. S. T., Zulkifli, R., Elwaleed, A. K., et al. (2014), Recycled Paper Fibres as Sound Absorbing Material, *Applied mechanics and materials*, 663, 459-463.
- Song, B. H. and Bolton, J. S. (2000), A transfer-matrix approach for estimating the characteristic impedance and wave numbers of limp and rigid porous materials, *J Acoust Soc Am*, 107(3), 1131-1152.
- Song, L., Koopmann, G. H., and Hoffmann, T. L. (1994), An Improved Theoretical Model of Acoustic Agglomeration, *Journal of Vibration and Acoustics*, 116(2), 208-214.

References

- Song, P. and Zhao, H. (2018), Filtered-x generalized mixed norm (FXGMN) algorithm for active noise control, *Mechanical Systems and Signal Processing*, 107, 93-104.
- Song, P. and Zhao, H. (2019), Filtered-x least mean square/fourth (FXLMS/F) algorithm for active noise control, *Mechanical Systems and Signal Processing*, 120, 69-82.
- Sugimoto, T., Ono, K., Ando, A., et al. (2009), PVDF-driven flexible and transparent loudspeaker, *Applied Acoustics*, 70(8), 1021-1028.
- Suk, J. W., Kirk, K., Hao, Y., et al. (2012), Thermoacoustic Sound Generation from Monolayer Graphene for Transparent and Flexible Sound Sources, *Advanced Materials*, 24(47), 6342-6347.
- Suk, J. W., Kitt, A., Magnuson, C. W., et al. (2011), Transfer of CVD-Grown Monolayer Graphene onto Arbitrary Substrates, *ACS Nano*, 5(9), 6916-6924.
- Sun, G., Li, M., and Lim, T. (2015), A family of threshold based robust adaptive algorithms for active impulsive noise control, *Applied Acoustics*, 97, 30-36.
- Sun, X., Kuo, S. M., and Meng, G. (2006), Adaptive algorithm for active control of impulsive noise, *Journal of Sound and Vibration*, 291(1), 516-522.
- Sun, Z., Yang, L., Wu, H., et al. (2020), Agglomeration and removal characteristics of fine particles from coal combustion under different turbulent flow fields, *Journal of Environmental Sciences*, 89, 113-124.
- Suzuki, K., Sakakibara, S., Okada, M., et al. (2011), Study of Carbon-Nanotube Web Thermoacoustic Loud Speakers, *Japanese Journal of Applied Physics*, 50, 01BJ10.
- Swift, G. W. (1988), Thermoacoustic engines, *The Journal of the Acoustical Society of America*, 84(4), 1145-1180.
- Tahir Akhtar, M. and Mitsuhashi, W. (2009), Improving performance of FxLMS algorithm for active noise control of impulsive noise, *Journal of Sound and Vibration*, 327(3), 647-656.
- Tang, X. L. and Lee, C. M. (2012), Time–frequency-domain filtered-x LMS algorithm for active noise control, *Journal of Sound and Vibration*, 331(23), 5002-5011.

References

- Tartibu, L. K. (2019), Developing more efficient travelling-wave thermo-acoustic refrigerators: A review, *Sustainable Energy Technologies and Assessments*, 31, 102-114.
- Temkin, S. (1994), Gasdynamic agglomeration of aerosols. I. Acoustic waves, *Physics of Fluids*, 6(7), 2294-2303.
- Temkin, S. and Ecker, G. Z. (1989), Droplet pair interactions in a shock-wave flow field, *Journal of Fluid Mechanics*, 202, 467-497.
- Thai, Q. B., Chong, R. O., Nguyen, P. T. T., et al. (2020), Recycling of waste tire fibers into advanced aerogels for thermal insulation and sound absorption applications, *Journal of Environmental Chemical Engineering*, 8(5), 104279.
- Thomas, D., Contal, P., Renaudin, V., et al. (1999), Modelling pressure drop in HEPA filters during dynamic filtration, *Journal of Aerosol Science*, 30(2), 235-246.
- Tian, H., Ren, T. L., Xie, D., et al. (2011a), Graphene-on-Paper Sound Source Devices, *ACS Nano*, 5(6), 4878-4885.
- Tian, H., Xie, D., Yang, Y., et al. (2011b), Flexible, ultrathin, and transparent sound-emitting devices using silver nanowires film, *Applied Physics Letters*, 99(25), 253507.
- Tian, H., Xie, D., Yang, Y., et al. (2011c), Transparent, flexible, ultrathin sound source devices using Indium Tin oxide films, *Applied Physics Letters*, 99(4), 043503.
- Tian, H., Xie, D., Yang, Y., et al. (2012), Single-layer graphene sound-emitting devices: experiments and modeling, *Nanoscale*, 4(7), 2272-2277.
- Timmer, M. a. G., De Blok, K., and Van Der Meer, T. H. (2018), Review on the conversion of thermoacoustic power into electricity, *The Journal of the Acoustical Society of America*, 143(2), 841-857.
- Tiuc, A. E., Vermeşan, H., Gabor, T., et al. (2016), Improved Sound Absorption Properties of Polyurethane Foam Mixed with Textile Waste, *Energy procedia*, 85, 559-565.
- Tiwary, R., Reethof, G., and Mcdaniel, O. H. (1984), Acoustically generated turbulence and its effect on acoustic agglomeration, *The Journal of the Acoustical Society of America*, 76(3), 841-849.

References

- Tiwatane, T. and Barve, D. S. (2014), Thermoacoustic Effect: the Power of Conversion of Sound Energy & Heat Energy: Review, *International Journal for Research in Technological Studies*, 1(4), 20-28.
- Tong, L. H. (2015), Theoretical Study and Numerical Analysis on Thermo- and Opto-Acoustic Characteristics and Mirage Effect of Carbon Nanotube Thin-Films, PhD. Thesis, City University of Hong Kong.
- Tong, L. H., Lai, S. K., and Lim, C. W. (2017), Broadband signal response of thermoacoustic devices and its applications, *The Journal of the Acoustical Society of America*, 141(4), 2430-2430.
- Tong, L. H., Lim, C. W., Lai, S. K., et al. (2015), Gap separation effect on thermoacoustic wave generation by heated suspended CNT nano-thin film, *Applied Thermal Engineering*, 86, 135-142.
- Tong, L. H., Lim, C. W., and Li, Y. C. (2013), Gas-Filled Encapsulated Thermal-Acoustic Transducer, *Journal of Vibration and Acoustics*, 135(5).
- Tong, L. H., Lim, C. W., Li, Y. C., et al. (2014), Generation of mirage effect by heated carbon nanotube thin film, *Journal of Applied Physics*, 115(24), 244905.
- Tong, L. H., Lim, C. W., Zhao, X. S., et al. (2016), Theory and modeling of cylindrical thermo-acoustic transduction, *Physics Letters A*, 380(25), 2123-2128.
- Torraca, P., Bobinger, M., Servadio, M., et al. (2018), On the Frequency Response of Nanostructured Thermoacoustic Loudspeakers, *Nanomaterials (Basel)*, 8(10), 833.
- Tu, T., Ju, Z.-Y., Li, Y.-T., et al. (2019), A novel thermal acoustic device based on vertical graphene film, *AIP Advances*, 9(7), 075302.
- Tu, Y. and Fuller, C. R. (2000), MULTIPLE REFERENCE FEEDFORWARD ACTIVE NOISE CONTROL PART I: ANALYSIS AND SIMULATION OF BEHAVIOR, *Journal of Sound and Vibration*, 233(5), 745-759.
- UWE. (2015), Thematic issue: Noise impacts on health, University of the West of England.
- Veeck, A. C. (2008), Air filtration: Guidelines and standards for using air filters, *Filtration & Separation*, 45(1), 28-30.

References

- Vesterinen, V., Niskanen, A. O., Hassel, J., et al. (2010), Fundamental Efficiency of Nanothermophones: Modeling and Experiments, *Nano Letters*, 10(12), 5020-5024.
- Vidu, R., Rahman, M., Mahmoudi, M., et al. (2014), Nanostructures: A Platform for Brain Repair and Augmentation, *Frontiers in systems neuroscience*, 8, 91.
- Wang, J., Ren, Z., Hou, Y., et al. (2020a), A review of graphene synthesis at low temperatures by CVD methods, *New Carbon Materials*, 35(3), 193-208.
- Wang, X., Koba, Y., Ishikawa, S., et al. (2015), Hybrid active noise barrier with sound masking (Experiment for verifying the noise attenuation performance in an office room and evaluation of maskers by listening experiments), *44th International Congress and Exposition on Noise Control Engineering, INTER-NOISE 2015*, San Francisco, United States.
- Wang, Y. S., Guo, H., Li, Y. R., et al. (2020b), Active control for vehicle interior noise based on DWT-FxLMS algorithm using a piezoelectric feedback system, *Applied Acoustics*, 167, 107409.
- Wang, Y. W. and Ni, Y. Q. (2020c), Bayesian dynamic forecasting of structural strain response using structural health monitoring data, *Structural Control and Health Monitoring*, 27(8), e2575.
- Wang, Y. W., Ni, Y. Q., and Wang, X. (2017), Detection of performance deterioration of high-speed train wheels based on Bayesian dynamic model, *Proceedings of the 11th International Workshop on Structural Health Monitoring*, 2808-2815.
- Wang, Y. W., Ni, Y. Q., and Wang, X. (2020d), Real-time defect detection of high-speed train wheels by using Bayesian forecasting and dynamic model, *Mechanical Systems and Signal Processing*, 139, 106654.
- Weber, J. K. R., Rey, C. A., Neufeind, J., et al. (2009), Acoustic levitator for structure measurements on low temperature liquid droplets, *Review of Scientific Instruments*, 80(8), 083904.
- Wei, Y., Lin, X., Jiang, K., et al. (2013), Thermoacoustic Chips with Carbon Nanotube Thin Yarn Arrays, *Nano Lett.*, 13(10), 4795-4801.
- Wei, Y., Liu, P., Jiang, K., et al. (2012), A Display Module Implemented by the Fast High-Temperature Response of Carbon Nanotube Thin Yarns, *Nano Letters*, 12(5), 2548-2553.

References

- Weiser, M., Apfel, R., and Neppiras, E. (1984), Intersparticle force on red-cells in a standing wave field, *Acta Acustica united with Acustica*, 56(2), 114-119.
- West, M. and Harrison, J. (1997), Bayesian Forecasting and Dynamic Models, 2nd Edition, New York, NY: Springer New York.
- Wheatley, J., Hofler, T., Swift, G. W., et al. (1983), Experiments with an Intrinsically Irreversible Acoustic Heat Engine, *Physical Review Letters*, 50(7), 499-502.
- WHO. (2011), Burden and disease from environmental noise - Quantification of healthy life years lost in Europe, Europe.
- Widrow, B., Glover, J. R., Mccool, J. M., et al. (1975), Adaptive noise cancelling: Principles and applications, *Proceedings of the IEEE*, 63(12), 1692-1716.
- Widrow, B., Larimore, M. G., Johnson, C. R., Jr., et al. (1976), Stationary and Nonstationary Learning Characteristics of the LMS Adaptive Filter, *Proceedings of the IEEE*, 64(8), 1151-1162.
- Widrow, B., Shur, D., and Shaffer, S. (1981), On adaptive inverse control, *Fifteenth Asilomar Conference on Circuits, Systems, and Computers*, 185-189.
- Widrow, B. and Stearns, S. D. (1985), Adaptive signal processing Englewood Cliffs, N.J. : Prentice-Hall.
- Wilcox, D. C. (2000), Turbulence modeling for CFD, 3rd Edition, La Cañada, Calif. : DCW Industries.
- Won, K.-S. and Choe, J. (2020), Transmission loss analysis in a partitioned duct with porous boundaries based on combination of FEM and measurement of sound absorption coefficients, *Applied Acoustics*, 165, 107291.
- Xiao, L., Chen, Z., Feng, C., et al. (2008), Flexible, Stretchable, Transparent Carbon Nanotube Thin Film Loudspeakers, *Nano Letters*, 8(12), 4539-4545.
- Xiao, L., Liu, P., Liu, L., et al. (2011), High frequency response of carbon nanotube thin film speaker in gases, *Journal of Applied Physics*, 110, 084311-084311.
- Xu, B., Liu, S., Liu, J., et al. (2011), Effects of Vehicle Cabin Filter Efficiency on Ultrafine Particle Concentration Ratios Measured In-Cabin and On-Roadway, *Aerosol Science and Technology*, 45(2), 234-243.

References

- Xu, Y., Lin, Z., Zhong, X., et al. (2014), Holey graphene frameworks for highly efficient capacitive energy storage, *Nature Communications*, 5(1), 4554.
- Yan, J., Chen, L., and Yang, L. (2016), Combined effect of acoustic agglomeration and vapor condensation on fine particles removal, *Chemical Engineering Journal*, 290, 319-327.
- Yan, J. W., Lai, S. K., and He, L. H. (2019), Nonlinear dynamic behavior of single-layer graphene under uniformly distributed loads, *Composites Part B: Engineering*, 165, 473-490.
- Yang, H. S., Kim, D. J., and Kim, H. J. (2003), Rice straw-wood particle composite for sound absorbing wooden construction materials, *Bioresource Technology*, 86(2), 117-121.
- Yang, M. and Sheng, P. (2017), Sound Absorption Structures: From Porous Media to Acoustic Metamaterials, *Annual Review of Materials Research*, 47(1), 83-114.
- Yao, Q., Li, S. Q., Xu, H. W., et al. (2010), Reprint of: Studies on formation and control of combustion particulate matter in China: A review, *Energy*, 35(11), 4480-4493.
- Yasui, K. (2011), Fundamentals of Acoustic Cavitation and Sonochemistry, In *Theoretical and Experimental Sonochemistry Involving Inorganic Systems*, Springer Netherlands, 1-29.
- Yu, X., Rajamani, R., Stelson, K. A., et al. (2007), Active Control of Sound Transmission Through Windows With Carbon Nanotube-Based Transparent Actuators, *IEEE Transactions on Control Systems Technology*, 15(4), 704-714.
- Yuen, K. V. (2010), Bayesian Methods for Structural Dynamics and Civil Engineering.
- Yuen, W. T., Fu, S. C., and Chao, C. Y. H. (2016), The correlation between acoustic streaming patterns and aerosol removal efficiencies in an acoustic aerosol removal system, *Aerosol Science and Technology*, 50(1), 52-62.
- Yuen, W. T., Fu, S. C., and Chao, C. Y. H. (2017), The effect of aerosol size distribution and concentration on the removal efficiency of an acoustic aerosol removal system, *Journal of Aerosol Science*, 104, 79-89.

References

- Yuen, W. T., Fu, S. C., Kwan, J. K. C., et al. (2014), The Use of Nonlinear Acoustics as an Energy-Efficient Technique for Aerosol Removal, *Aerosol Science and Technology*, 48(9), 907-915.
- Zabalza Bribián, I., Valero Capilla, A., and Aranda Usón, A. (2011), Life cycle assessment of building materials: Comparative analysis of energy and environmental impacts and evaluation of the eco-efficiency improvement potential, *Building and Environment*, 46(5), 1133-1140.
- Zhang, G., Liu, J., Wang, J., et al. (2012), Numerical simulation of acoustic wake effect in acoustic agglomeration under Oseen flow condition, *Chinese Science Bulletin*, 57(19), 2404-2412.
- Zhang, G. X., Wang, J. Q., Chi, Z. H., et al. (2018a), Acoustic agglomeration with addition of sprayed liquid droplets: Three-dimensional discrete element modeling and experimental verification, *Chemical Engineering Science*, 187, 342-353.
- Zhang, G. X., Zhang, L. L., Wang, J. Q., et al. (2018b), A new model for the acoustic wake effect in aerosol acoustic agglomeration processes, *Applied Mathematical Modelling*, 61, 124-140.
- Zhang, L. H., Wang, Y. W., Ni, Y. Q., et al. (2018c), Online condition assessment of high-speed trains based on Bayesian forecasting approach and time series analysis, *Smart Structures and Systems*, 21(5), 705-713.
- Zhang, S., Wang, Y. S., Guo, H., et al. (2019), A normalized frequency-domain block filtered-x LMS algorithm for active vehicle interior noise control, *Mechanical Systems and Signal Processing*, 120, 150-165.
- Zhang, X. and Qiu, X. (2017), Performance of a snoring noise control system based on an active partition, *Applied Acoustics*, 116, 283-290.
- Zhao, B., An, N., and Chen, C. (2020), Using air purifier as a supplementary protective measure in dental clinics during the COVID-19 pandemic, *Infection Control and Hospital Epidemiology*.
- Zhao, J., Wang, X. M., Chang, J. M., et al. (2010), Sound insulation property of wood-waste tire rubber composite, *Composites science and technology*, 70(14), 2033-2038.

References

- Zheng, W., Hu, J., Wang, Z., et al. (2021), COVID-19 Impact on Operation and Energy Consumption of Heating, Ventilation and Air-Conditioning (HVAC) Systems, *Advances in Applied Energy*, 3, 100040.
- Zhou, D., Luo, Z., Fang, M., et al. (2017), Numerical calculation of particle movement in sound wave fields and experimental verification through high-speed photography, *Applied Energy*, 185, 2245-2250.
- Zhou, D., Luo, Z., Fang, M., et al. (2015), Preliminary Experimental Study of Acoustic Agglomeration of Coal-fired Fine Particles, *Procedia engineering*, 102, 1261-1270.
- Zhou, Y. L., Yin, Y. X., and Zhang, Q. Z. (2013), An optimal repetitive control algorithm for periodic impulsive noise attenuation in a non-minimum phase ANC system, *Applied Acoustics*, 74(10), 1175-1181.
- Zhou, Z., Li, H., Wang, J., et al. (2021), BEM modeling and experiment verification for thermoacoustic response of suspended nano thin films, *Engineering Analysis with Boundary Elements*, 130, 10-19.
- Zhu, X., Kim, B.-J., Wang, Q., et al. (2013), Recent Advances in the Sound Insulation Properties of Bio-based Materials, *BioResources*, 9(1), 1764-1786.
- Zolpakar, N. A., Mohd-Ghazali, N., and Hassan El-Fawal, M. (2016), Performance analysis of the standing wave thermoacoustic refrigerator: A review, *Renewable and Sustainable Energy Reviews*, 54, 626-634.